



The Interplay of Viscoelasticity, Water Transport, and Adhesion in Skin Adhesives under Wet Conditions

Eiler, Johannes

Publication date:
2020

Document Version
Publisher's PDF, also known as Version of record

[Link back to DTU Orbit](#)

Citation (APA):
Eiler, J. (2020). *The Interplay of Viscoelasticity, Water Transport, and Adhesion in Skin Adhesives under Wet Conditions*. Technical University of Denmark.

General rights

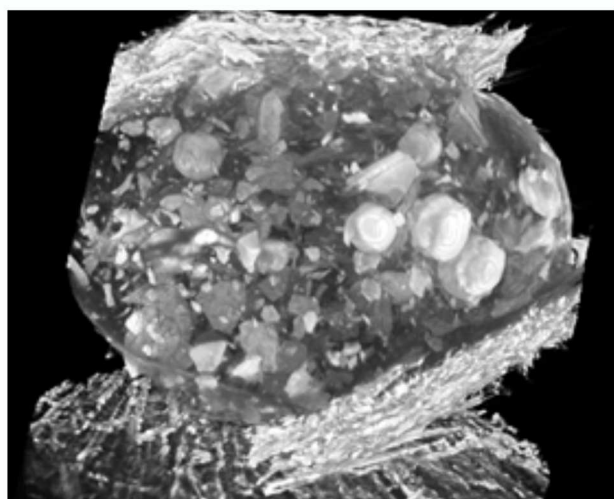
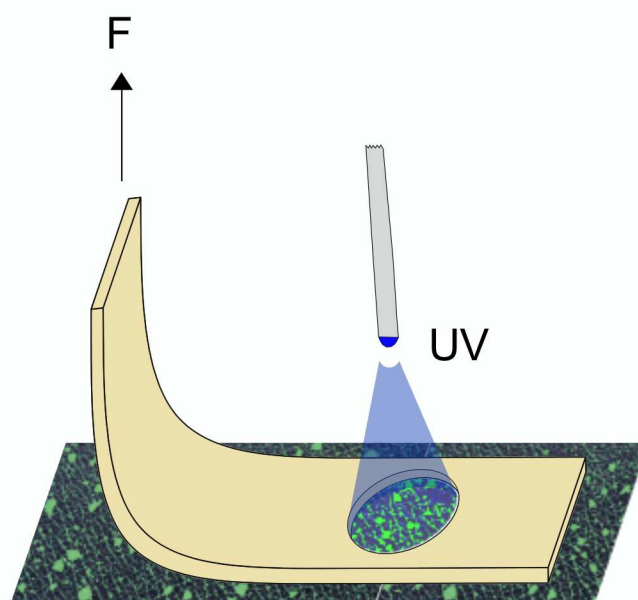
Copyright and moral rights for the publications made accessible in the public portal are retained by the authors and/or other copyright owners and it is a condition of accessing publications that users recognise and abide by the legal requirements associated with these rights.

- Users may download and print one copy of any publication from the public portal for the purpose of private study or research.
- You may not further distribute the material or use it for any profit-making activity or commercial gain
- You may freely distribute the URL identifying the publication in the public portal

If you believe that this document breaches copyright please contact us providing details, and we will remove access to the work immediately and investigate your claim.

The Interplay of Viscoelasticity, Water Transport, and Adhesion in Skin Adhesives under Wet Conditions

PhD Dissertation



Preface

This thesis is the result of an industrial PhD study conducted in collaboration between Coloplast A/S and the Technical University of Denmark (DTU). The study received funding from the Innovation Fund Denmark and was part of the Grand Solutions Project # 6151-00007B entitled "Smart sweat removal from human skin for prolonged ostomy bag adhesion and increased substantivity of topical formulations (SROT)". Besides Coloplast A/S and DTU a third partner (Riemann A/S) was also involved in the project. I conducted the PhD study over a period of 3 years, during which I could flexibly conduct laboratory experiments and office tasks at either institution. My main supervisor was Professor Esben Thormann (DTU) and my co-supervisors were Bahar Bingöl (Technology Project Manager at Coloplast A/S) and Professor Kristoffer Almdal (DTU). During the PhD study, I went on two external research stays (one month each) at the Novel Devices Lab at the University of Cincinnati (OH, USA). The external stays have been instrumental in the development of the perspiration simulator, which was a key technique to evaluate the performance of skin adhesives during perspiration.

Acknowledgements

I have thoroughly enjoyed the past three years working on my PhD project. It has been a remarkable development with many steep learning curves. I thank my supervisor Esben Thormann for the guidance throughout the project and the many scientific discussions. I especially appreciate that you have always had an open door and taken the time to give constructive feedback. I also thank my industrial supervisor Bahar Bingöl as well as Kristoffer Hansen who have also always taken their time to give constructive feedback. There were many great scientific discussions with an even higher number of questions, which in turn induced countless interesting experiments during the study. I also thank my great friend and colleague during the SROT project, Daniel Hansen. We were both PhD students and managed to work in an extremely synergistic way. Additionally, I also thank all my colleagues at Coloplast and DTU for making it two great places to work. I also thank Professor Jason Heikenfeld and the entire Novel Devices Lab at the University of Cincinnati for welcoming and helping me during my external stay. On a personal level, I also thank Amalie Modvig and my family for their support not only during my PhD study but also in everyday life.

Abstract

Worldwide, there are millions of people living with an ostomy, which is typically created during a life-saving surgical procedure. Thereafter, ostomates use a removable pouch to collect and dispose of urine and faeces from their abdomen. An integral part of the pouch system is the adhesive, which holds the pouch in place during wear. Importantly, the adhesive should be strong enough to avoid undesired detachment while also being easy to remove upon changing of the pouch. Finding the right balance of adhesion is especially challenging during wet conditions, where moisture from the skin or from the ostomy may interfere with the adhesive bonds.

To allow an active lifestyle for ostomates without worrying about the adhesion of the pouch, this project aims to understand the processes leading to a loss of adhesion and subsequently identify strategies to maintain adhesion instead. First, the mechanism for water transport within skin adhesives is investigated through a microstructural analysis of these polymer composites. Different approaches are then evaluated to tune the water transport within skin adhesives from changes in their effect on the viscoelastic properties is determined. Next, skin adhesives are systematically designed to decouple the effects of changes in their water absorption capabilities and in their viscoelastic properties during perspiration. For this purpose, a perspiration simulator is developed, which mimics human skin in some key characteristics, to achieve controlled and reproducible perspiration conditions. Finally, the learnings about the interplay of the viscoelastic properties, the water absorption capabilities, and the peel adhesion are used to develop new skin adhesive formulations with an improved performance during perspiration.

Resumé

På verdensplan lever der millioner af mennesker med en stomi som konsekvens af et livsreddende kirurgisk indgreb. Disse mennesker bruger en aftagelig pose til at opsamle og bortskaffe deres urin og fæces direkte fra tarmen. En vigtig del af posesystemet er hudklæberen der holder stomiposen på plads. Mens hudklæberen skal klæbe stærkt nok til at bære vægten af stomiposen så skal den også let kunne fjernes ved udskiftning af stomiposen. Det er afgørende at finde den rigtige klæbebalance og det er særligt udfordrende under våde forhold, hvor fugt fra huden eller stomien kan nedsætte klæbeevnen.

For at mennesker med stomi kan føre en aktiv livsstil uden bekymringer om vedhæftning af deres stomipose, undersøges i dette projekt processerne som fører til tab af klæbeevne og der identificeres strategier til at modvirke disse processer. Først undersøges mekanismen for vandtransport i hudklæbere gennem en mikrostrukturel analyse af disse polymerkompositter. Så justeres vandtransportegenskaberne på forskellige måder og effekten af disse forandringer på hudklæbernes viskoelastiske egenskaber evalueres. Derefter designes hudklæbere systematisk for at kunne adskille effekten af forandringer i deres viskoelastiske egenskaber fra forandringer i deres vandtransportegenskaber på deres klæbeevne efter at svede. Til dette formål udvikles en svedesimulator som efterligner menneskelig hud i nogle relevante egenskaber mens den garanterer kontrollerede og reproducerbare svedebetingelser. Til sidst bruges læring om samspillet mellem de viskoelastiske egenskaber, vandtransportegenskaber og klæbeevnen til at udvikle nye hudklæbere med forbedret ydelse efter at svede.

Publications

Appended Publications

- I. Eiler, J.; Simonsen, S. B.; Hansen, D.; Bingöl, B.; Hansen, K.; Thormann, E. Water Transport in Polymer Composites through Swelling-Induced Networks of Hydrogel Particles. *Soft Matter* 2020, <https://doi.org/10.1039/D0SM01103G>
- II. Eiler, J.; Hansen, D.; Bingöl, B.; Hansen, K.; Thormann, E. Tuneable and Responsive Formation of Swelling-Induced Hydrogel Networks for Water Transport in Polymer Composites (submitted)
- III. Eiler, J.; Hansen, D.; Bingöl, B.; Hansen, K.; Heikenfeld, J.; Thormann, E. In Vitro Evaluation of Skin Adhesives during Perspiration. *International Journal of Adhesion and Adhesives* 2020, 99, 102574, <https://doi.org/10.1016/j.ijadhadh.2020.102574>
- IV. Eiler, J.; Hansen, D.; Bingöl, B.; Hansen, K.; Thormann, E. How the Viscoelastic and Sweat Absorbing Properties of Skin Adhesives Affect their Performance during Perspiration (submitted)

Related Publications

- Hansen, D.; Brewer, J. R.; Eiler, J.; Komjani, N. M.; Hansen, K.; Thormann, E. Water Diffusion in Polymer Composites Probed by Impedance Spectroscopy and Time-Resolved Chemical Imaging. *ACS Applied Polymer Materials* 2020, 2, 837, <https://doi.org/10.1021/acsapm.9b01107>
- Hansen, D.; Zajforoushan Moghaddam, S.; Eiler, J.; Hansen, K.; Thormann, E. Performance of Polymeric Skin Adhesives during Perspiration. *ACS Applied Polymer Materials* 2020, 2, 1535, <https://doi.org/10.1021/acsapm.9b01214>
- Chiaula, V.; Mazurek, P.; Eiler, J.; Nielsen, A. C.; Skov, A.L. Glycerol-silicone adhesives with excellent fluid handling and mechanical properties for advanced wound care applications. *International Journal of Adhesion and Adhesives* 2020, 102, 102667, <https://doi.org/10.1016/j.ijadhadh.2020.102667>

Contents

Preface	i
Acknowledgements	iii
Abstract	v
Resumé	vii
Publications	ix
I Introduction, Background, and Methods	1
1 Introduction	3
1.1 What is an Ostomy?	3
1.2 Ostomy Care Adhesives	4
1.2.1 Adhesion Requirements for Ostomy Care Adhesives	4
1.2.2 Skin Health Requirements for Ostomy Care Adhesives	6
1.3 Aim of the Project	7
2 Background	9
2.1 The Basics of Adhesion	9
2.1.1 Definition of Cohesion and Adhesion	9
2.1.2 Adhesion Mechanisms	10
2.2 Pressure-Sensitive Adhesives	12
2.2.1 Viscoelastic Materials	13
2.2.2 Rheology: Evaluating Viscoelasticity	15
2.2.3 Viscoelastic Properties and Adhesive Performance	17
2.2.4 Tuning the Viscoelastic Properties	18
2.3 PSAs and Water	20
2.3.1 Removal of Water from the Interface	21
2.3.2 Bio-inspired Adhesives	22

3	Project Definition	25
3.1	State of the Art	25
3.2	Commercial Adhesives on Human Skin	26
3.2.1	Commercial Adhesives on Human Skin at Rest	26
3.2.2	Commercial Adhesives on Human Skin during Exercise	27
3.3	Project Plan	31
4	Materials and Methods	33
4.1	Raw Materials for Adhesive Composites	33
4.2	Processing of Raw Materials into Adhesive Composites	34
4.3	Methods for Characterisation	34
4.3.1	Characterisation of Raw Materials	36
4.3.2	Characterisation of Adhesive Composites	39
4.3.3	Characterisation of Artificial Skin Substrates	41
4.4	Adhesion to Human Skin	41
II	Results and Discussion	43
5	Water Transporting Networks	45
5.1	Particle Networks in Skin Adhesives (<i>Paper I</i>)	45
5.1.1	Analysis of X-ray μ CT Data	45
5.1.2	X-ray μ CT of Additional Composition	48
5.1.3	Summary of <i>Paper I</i>	49
5.2	Adhesive Design Considerations for Water Transport (<i>Paper II</i>)	51
5.3	Key Conclusions	53
6	Adhesive Performance during Perspiration	55
6.1	Development of a Perspiration Simulator	55
6.1.1	First iteration (<i>Paper III</i>)	57
6.1.2	Second iteration	61
6.2	Adhesive Performance Testing	67
6.2.1	The Impact of the Viscoelastic Properties and Sweat Absorption Capabilities (<i>Paper IV</i>)	67
6.2.2	Excessive Absorption of Sweat	68
6.3	Comparison with Adhesive Behaviour on Human Skin	72
6.3.1	Non-Absorbing Adhesives	73
6.3.2	Absorbing Adhesives	73
6.4	Key Conclusions	76
7	New Skin Adhesive Formulations with Prolonged Resistance to Perspiration	77
7.1	Design of New Skin Adhesive Formulations	77

7.1.1	Tuning the Polymer Matrix	77
7.1.2	Tuning the Particle Loading	79
7.2	Performance of New Skin Adhesive Formulations	80
7.2.1	Characterisation of New Skin Adhesive Formulations	80
7.2.2	Peel Adhesion of New Skin Adhesive Formulations on Perspiration Simulator	81
7.2.3	Comparison with Adhesive Performance on Human Skin	86
7.3	Key Conclusions	88
III	Concluding Remarks	89
8	Conclusions	91
9	Outlook	93
10	Appendix	99
10.1	Calculation of the Critical Modulus for Cold Flow of Viscoelastic Materials	99
10.2	The Impact of the Bonding Conditions on the Performance of Skin Adhesives during Perspiration	101
	Bibliography	102
	Manuscripts	111
	Paper I - Water Transport in Polymer Composites through Swelling-Induced Networks of Hydrogel Particles	113
	Paper II - Tuneable and Responsive Formation of Swelling-Induced Hydrogel Networks for Water Transport in Polymer Composites	130
	Paper III - In Vitro Evaluation of Skin Adhesives during Perspiration	152
	Paper IV - How the Viscoelastic and Sweat Absorbing Properties of Skin Adhesives Affect their Performance during Perspiration	160

Part I

Introduction, Background, and Methods

1 Introduction

1.1 What is an Ostomy?

An ostomy constitutes an artificial opening in the abdomen, which is used to redirect the natural path of the urinary or digestive system. It is usually created in a life-saving procedure against serious medical conditions such as cancer, inflammatory bowel disease, and diverticulitis. After the formation of an ostomy, a pouch is typically attached to the skin with an adhesive in order to collect the faeces directly from the ostomy. Several studies have shown that the formation of an ostomy is associated with a reduced quality of life due to complications including skin irritations, leakage, and odour[1–3]. Such complications do not only impact ostomates physically but can also cause emotional and psychological distress. Therefore, the development and continuous improvement of ostomy care products is of paramount importance to ensure a high quality of life for people with an ostomy.

In Denmark, a regional database has been established to document the formation of ostomies in the capital region. Nearly 100 % of patients from Bispebjerg Hospital, Herlev Hospital, Hvidovre Hospital, Nordsjællands Hospital, and Rigshospitalet are entered into the database with a combined catchment area covering approx. 1.7 million people[4]. At the time of writing, annual reports for the years 2010 - 2015 had been created by the Steering Group of the Surgical Nurses in the Capital Region of Denmark and made publicly available [5–10]. The reports show that an average of 1138 ± 96 ostomy formations occurred every year in the capital region of Denmark. Even though ostomy formation occurred across all ages, most ostomies were created for patients in the age groups 60 - 69 and 70 - 79 (see Fig. 1.1a). 46 % of ostomies were created for female patients, while 54 % were created for male patients (see Fig. 1.1b). Moreover, the annual reports reveal that approx. 64 % of the annually created ostomies were permanent and the remaining 36 % were temporary (see Fig. 1.1c). Since there is no national register for the formation of ostomies in Denmark, the Steering Group of the Surgical Nurses in the Capital Region of Denmark can only estimate the number of ostomates in Denmark to 10 000 - 12 000 (2015)[10]. In Europe, the number of ostomates is estimated to approx. 700 000 (2012), while the number of ostomates in the US is estimated to exceed 1 000 000 (2014)[1].

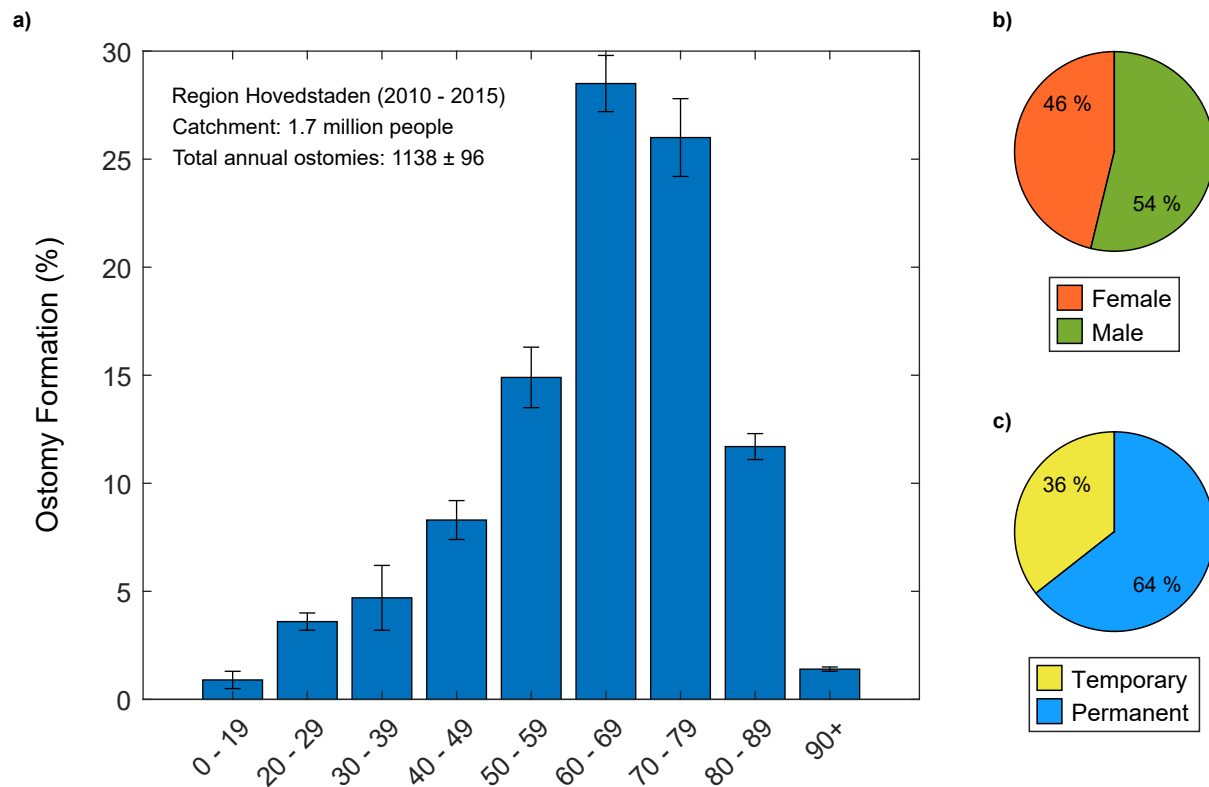


Figure 1.1: Data from the stoma database in the capital region of Denmark between 2010 and 2015. a) The distribution of ostomy formation is shown for different age groups. Most ostomies are created at the ages 60 - 79. b) Ostomy formation is more prevalent in male (54 %) than in female (46 %) patients. c) 64 % of all ostomies created were permanent, while 36 % were temporary.

1.2 Ostomy Care Adhesives

Adhesives for ostomy care products are used to attach a pouch to the abdomen so that the faeces can be collected directly from the ostomy. The adhesive thereby sits on the skin and secures the pouch during wear.

1.2.1 Adhesion Requirements for Ostomy Care Adhesives

The requirements for skin adhesives in ostomy care products are manifold. Primarily, the adhesive should hold the ostomy pouch in place during the entire wear time. The

type of product that is used strongly affects the wear time of the adhesives. In one-piece products, the adhesive connects to the pouch, while in two-piece products, the adhesive connects to a flange, which can be separated from the pouch (see Fig. 1.2a and 1.2b). From a statistical analysis among some users in Denmark, the changing frequency for a one-piece product was determined as approximately 10.6 ± 7.1 times per week, while the adhesives in two-piece products are changed 3 ± 2 times per week[11]. The wear times of such adhesives are therefore anywhere between 9 h and 168 h.

Ideally, the adhesive should be able to withstand daily activities such as working, exercising, showering, and sleeping. This requires that the adhesion during wear is always sufficiently strong to carry the weight of the pouch. In addition to good adhesion, the adhesive also needs to exhibit sufficiently high shear strength in order to support an ostomy pouch.

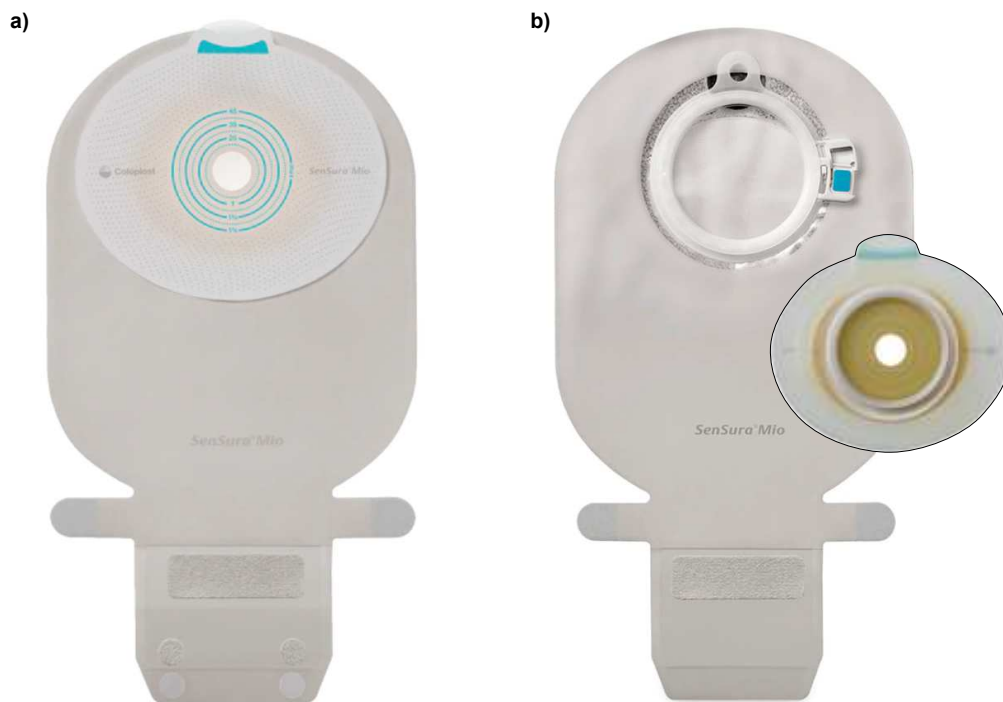


Figure 1.2: Images of ostomy care pouches from Coloplast. a) A one-piece product, where the adhesives attaches directly to the pouch. b) A two-piece product, where the adhesive attaches to a flange, which can be decoupled from the pouch.

1.2.2 Skin Health Requirements for Ostomy Care Adhesives

The skin is one of the largest human organs and acts as a protective layer for the body. It consists of several layers, all of which serve a particular function. The outermost layer, called epidermis, is the most relevant for adhesion as it is in direct contact with the adhesive. Because of its exposure to the environment, the epidermis is a barrier for infections and also regulates the water loss from the body. The epidermis itself also consists of several layers, with the outermost layer being called stratum corneum. The stratum corneum comprises several layers of cells, which are incorporated into a matrix of lipids[12]. The thickness of the stratum corneum varies between different body parts but is in the order of approximately 10 μm [13]. The thickness changes dramatically with skin hydration and can swell to several times the original thickness upon exposure to water[14, 15]. Besides thickness, skin hydration also influences parameters such as the surface energy, roughness, or mechanical properties of the stratum corneum, all of which greatly influence adhesion[16–19]. The stratum corneum hydrates when water is transported from the body and evaporation from the skin surface is slowed down or even prevented e.g. due to high relative humidities or occlusion[20–22]. Prolonged hyperhydration has been associated with damage to the skin and should therefore be avoided[23, 24]. Consequently, adhesives for prolonged wear should allow for the evaporation of moisture from the stratum corneum in order to keep skin healthy.

Since the output from an ostomy is highly corrosive for the skin, the adhesive should also act as a barrier to prevent any contact and subsequent skin irritations. This implies that soft adhesives are required, which are able to flow into the crevices of the skin and create a good seal. While a good seal is important to protect the skin from faeces, such a seal may conversely occlude the skin and cause moisture accumulation below the adhesive and the properties need to be carefully balanced. Finally, while being able to withstand daily activities, the adhesives should be easily removable without leaving any residue or causing any trauma to the underlying tissue. This poses a limit for the adhesion in order to avoid damage to the skin.

1.3 Aim of the Project

In my thesis entitled "The Interplay of Viscoelasticity, Water Transport, and Adhesion in Skin Adhesives under Wet Conditions", I am looking to gain a fundamental understanding of the processes leading to a loss of adhesion on human skin. One of the challenges for such applications is that adhesion is readily lost in the presence of water[25, 26]. When wearing adhesives, moisture is not only supplied externally, e.g. during showering or swimming, but also internally from the skin through perspiration. Therefore, in order for people to pursue an active lifestyle while wearing these adhesives, it becomes paramount that skin adhesives can retain adhesion in wet environments. Consequently, I am looking to identify different strategies to maintain adhesion on human skin in wet environments in order to aid the development of improved skin adhesive formulations.

2 Background

2.1 The Basics of Adhesion

The basics of adhesion are elucidated in the following section. This will help to understand how adhesion to skin can be achieved in the first place and also highlight challenges as well as improvement possibilities.

2.1.1 Definition of Cohesion and Adhesion

Cohesion is defined as the affinity of two surfaces of a similar material. The thermodynamic work of cohesion, W_c , is the work that is required to cleave a homogeneous material with surface energy, γ_1 (see illustration in Fig. 2.1a). This means that the work of cohesion is equal to the work required to create two new surfaces of one single material:

$$W_c = 2 \cdot \gamma_1 \quad (2.1)$$

On the other hand, adhesion is the phenomenon of two different materials sticking to each other when brought into proximity. Here, two dissimilar materials with surface energies γ_1 and γ_2 are in contact and form an interface with a corresponding energy of γ_{12} . Cleaving therefore requires the creation of the new surfaces as well as the disappearance of an interface (see illustration in Fig. 2.1b). The thermodynamic work of adhesion, W_a , is therefore defined as:

$$W_a = \gamma_1 + \gamma_2 - \gamma_{12} \quad (2.2)$$

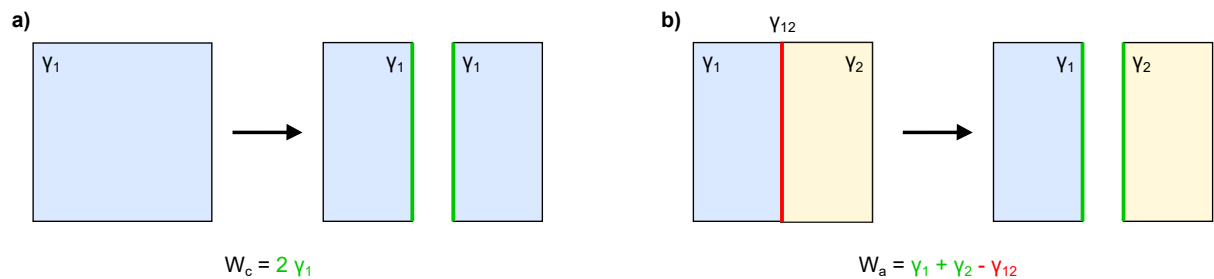


Figure 2.1: Schematic illustration of a) the work of cohesion and b) the work of adhesion.

2.1.2 Adhesion Mechanisms

Adhesion between two surfaces may be provided through different mechanisms. In Fig. 2.2a - e, five common mechanisms are illustrated, which will be further explained in the following section.

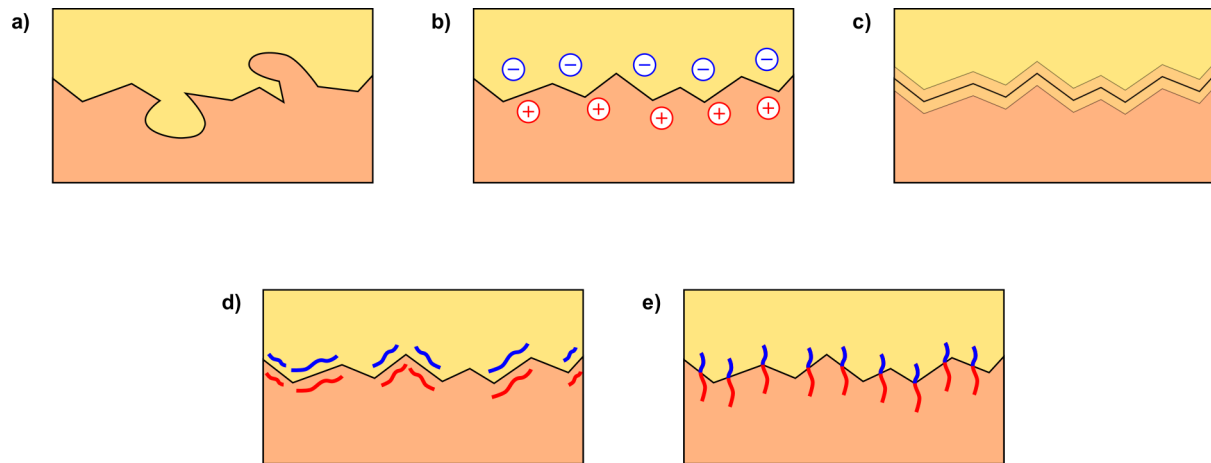


Figure 2.2: Five different adhesion mechanisms are schematically illustrated. a) Mechanical adhesion due to interlocking. b) Electrostatic adhesion due to electrostatic forces between two charged surfaces. c) Diffusive adhesion is based on the interdiffusion of the materials at the surface, creating a strong interphase. d) Dispersive adhesion is based on dispersive interactions between two surfaces. e) Chemical adhesion requires the formation of covalent, ionic, or hydrogen bonds across the interface.

Mechanical Adhesion

Mechanical adhesion does not involve any intermolecular forces and is solely based on physical interlocking of two surfaces (see Fig. 2.2a). This could potentially be achieved by a material that flows into the crevices of a surface, subsequently hardens, and therefore is locked.

Electrostatic Adhesion

Electrostatic adhesion (also called electroadhesion) occurs as a consequence of attractive electrostatic forces that may be strong enough to hold surfaces together (see Fig. 2.2b). An electroadhesive pad typically consists of electrodes embedded in a polymer matrix. When the pad is in contact with a substrate, an alternating potential can be applied between the electrodes to create an electric field, which in turn induces charges within the surface. The opposing charges in the pad and the substrate then create an adhesive force.

Researches are working to use electrostatic adhesion to create robots that can climb walls and for potential applications in space[27, 28].

Diffusive Adhesion

Diffusive adhesion involves interdiffusion of one material into the other at their common interface (see Fig. 2.2c). This requires some degree of mobility as well as miscibility of the two phases and can increase adhesion strongly. Diffusive adhesion plays a crucial role in sintering processes, where metal or ceramic particles are fused together at elevated temperatures below their melting points. In nature, diffusive adhesion is responsible for the strong bonding between calcified cartilage and bones in the human body[29].

Dispersive Adhesion

Dispersive adhesion occurs due to non-specific interactions between two surfaces, where van der Waals interactions are responsible for the attraction (see Fig. 2.2d). Dispersive adhesion can be used to create removable adhesives, since all interactions are physical in nature. Popular examples of products that take advantage of dispersive adhesion include various tapes, labels, and sticky notes. In nature, geckos are a very prominent example of this mechanism of adhesion. It has been shown that van der Waals interactions are responsible for the ability of geckos to climb vertically along walls[30, 31]. However, since van der Waals forces are typically considered as weak interactions, geckos must maximise the contact area in order to support their weight during climbing. A structural analysis of the foot of the gecko revealed that a single gecko toe has approximately 150 000 setae which in turn each consists of hundreds of spatulae [32]. With maximum adhesive forces around 200 μN for every single seta, a projected adhesive force of approximately 100 N per foot can therefore be achieved[30]. Crucially, these van der Waals interactions can be perturbed easily through crack propagation at the interface because the individual bonds are rather weak. Therefore, in order to detach their feet, geckos use a complex motion, where the pressure is concentrated on a small number of setae at any point in order to break the van der Waals bonds[33].

While adhesion may be strong under dry conditions, a trend towards lower adhesion was found in the presence of water. The shear adhesion of gecko feet on glass plates under different toe and substrate wetting conditions was investigated by Stark et al.[34]. As water prohibited intimate contact formation, softened the gecko toes, and perturbed the van der Waals interactions, a reduction in adhesive forces was observed. Indeed, some studies suggest reduced gecko activity during rainfall [35, 36] and therefore support these findings from the laboratory.

Chemical Adhesion

Chemical adhesion is achieved through the formation of bonds between the two contacting surfaces (see Fig. 2.2e). Thereby, hydrogen bonding can lead to good adhesion, while covalent and ionic bonding provide even stronger interactions. Chemical adhesion is limited to specific combinations of substrates and can be utilised in structural or dental adhesives as the respective bonds are strong and able to withstand harsh environments. In the natural world, mussels also take advantage of chemical adhesion in order to cling to surfaces under water. Waite has summarised how mussels achieve strong adhesion in four points[37]. Firstly, a potential film of water between the adhesive and the substrate needs to be replaced. Secondly, the adhesive needs to wet the substrate and create intimate contact. Thirdly, many strong interactions need to be created between the adhesive and the substrate. Thereby, the mussel adhesive is based on a polyphenolic protein, which consists of repeated peptide units with hydroxy-alkyl, amino-alkyl, and phenolic functional groups. A large part of the phenolic groups (approx. 75 %) is thereby classified as catechoyls such as the amino acid 3,4-dihydroxy-L-phenylalanine (DOPA). These groups can form hydrogen bonds, metal-ligand complexes, Michael-type addition compounds, and charge-transfer complexes, which all represent highly energetic interactions and enable strong bonding. Lastly, the adhesive needs to cure/set in order to achieve sufficient cohesion. This way, mussels can adhere to rocks in wet environments and harsh conditions to withstand great forces.

2.2 Pressure-Sensitive Adhesives

Pressure-sensitive adhesives (PSAs) are materials that are typically used to create a removable, non-permanent bond between two surfaces. Like with geckos, their adhesion mechanism is often based on dispersive interactions, which means that PSAs can stick to almost any surface[38]. Unlike with geckos, in order to ensure that such adhesives do not delaminate at small shear stresses, a mechanism for energy dissipation is utilised, which originates from the viscoelastic nature of these materials. The concept of viscoelasticity, its evaluation, and consequences for adhesives will be explained in the following sections.

2.2.1 Viscoelastic Materials

In order to understand viscoelasticity, materials with either fully elastic or fully viscous behaviour are considered first. Elastic behaviour is characterised by the immediate occurrence of a strain, ϵ , in response to an applied stress, σ (see — in Fig. 2.3a). Upon relieving the stress, the elastic strain is also released and the material returns to its original conformation without permanent deformation. Consequently, after application of a given strain to an elastic material, the corresponding stress is immediately built up and remains constant until the material is released (see — in Fig. 2.3b). Elastic deformation occurs in solid materials and is directly associated with a stretching of chemical bonds at the molecular level. It does not involve any energy dissipation and therefore a linear relationship between the applied stress and the resulting strain is observed (see — in Fig. 2.3c). The proportionality constant is thereby called the elastic modulus.

On the other hand, viscous materials are fluids that flow after application of a stress (see — in Fig. 2.3a). The deformation is irreversible as the molecules in the liquid can move freely. The viscosity, η , is thereby a measure of the resistance to flow. Upon application of a given strain to such a viscous fluid, the stress is dissipated in the form of heat while the strain remains (see — in Fig. 2.3b).

Viscoelasticity is the combination of elastic and viscous properties in one material. This type of behaviour is often observed in polymeric materials, where the individual polymer chains have some freedom of movement to enable viscous dissipation. When a viscoelastic material is subject to a stress, immediate elastic deformation occurs along with a time-dependent viscous deformation (see — in Fig. 2.3a). Upon relief of the stress, the elastic strain is released instantaneously, while the remaining viscoelastic strain may be recovered over time. On the other hand, when a constant strain is applied to a viscoelastic material, a stress occurs immediately, which is subsequently relieved through a rearrangement of the polymer chains (see — in Fig. 2.3b). Upon relief of the strain, an opposing stress remains, which will in turn be dissipated again through rearrangement of the chains. This behaviour gives rise to a hysteresis loop in the stress-strain diagram (see — in Fig. 2.3c). The area within the loop thereby corresponds to the energy that has been dissipated during deformation of the material.

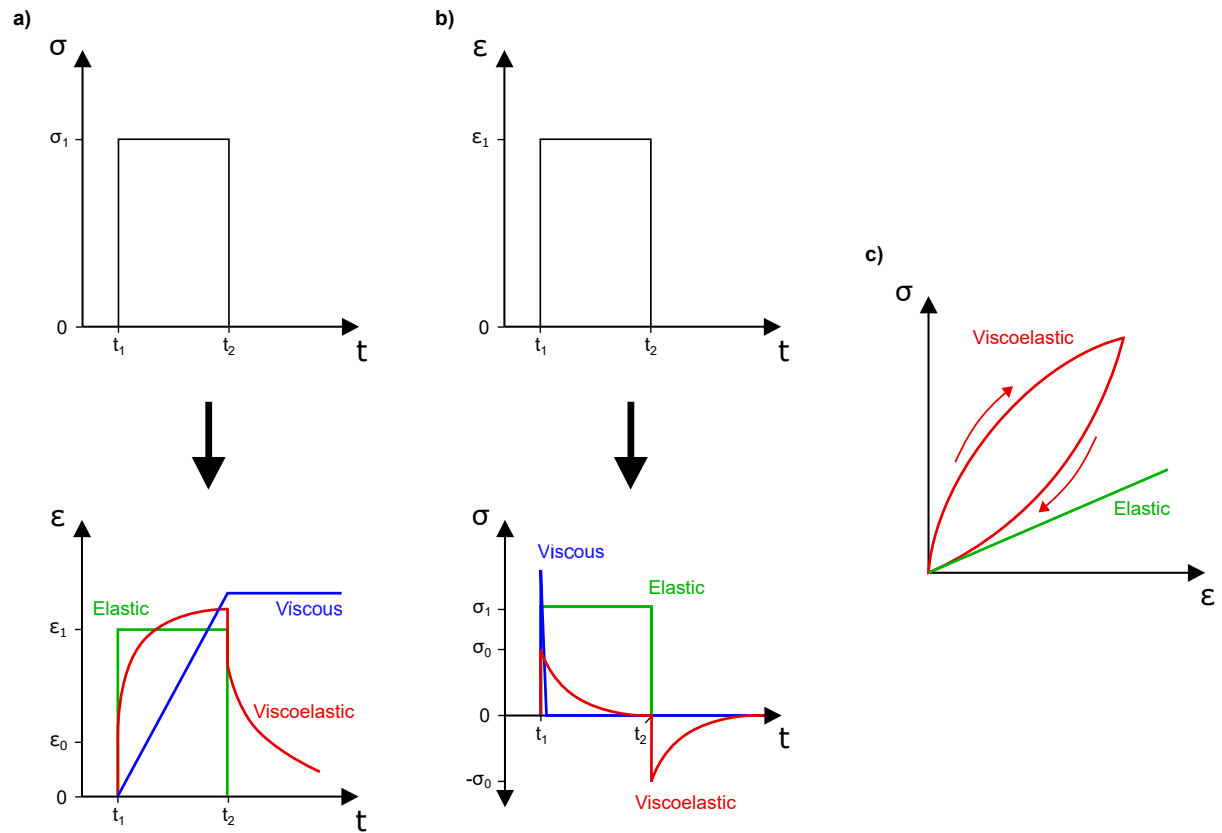


Figure 2.3: a) Upon application of a stress σ_1 to a material over a period of time, different strain responses are observed for elastic, viscoelastic, and viscous materials. b) Similarly, the application of a strain over a period of time, induces different stresses for elastic, viscoelastic, and viscous materials. c) For elastic materials, a linear relationship between stress and strain is observed, while viscoelastic materials show a hysteresis loop.

The hysteresis that is observed upon deformation of viscoelastic materials is precisely the reason why PSAs are able to resist considerable shear forces even though their mechanism of adhesion relies on relatively weak dispersive interactions. When pulling an adhesive off a substrate, a large proportion of the energy is dissipated within the bulk of the adhesive, which minimises the energy that is left to interfere with the van der Waals forces at the interface. This is in contrast to geckos, whose movements would be heavily restricted if their toes were viscoelastic and dissipated large amounts of energy.

2.2.2 Rheology: Evaluating Viscoelasticity

Rheology is the study of the flow of materials and it explores viscoelasticity under different conditions. Generally, the relationship between stress, strain, time, and temperature is evaluated using a rheometer. A common test setup for PSAs involves a parallel plate geometry in between which an adhesive sample is placed. A small oscillating shear strain, $\hat{\gamma}$, is then applied with an angular frequency, ω , and a maximum strain, $\hat{\gamma}_0$:

$$\hat{\gamma}(t) = \hat{\gamma}_0 \sin(\omega t) \quad (2.3)$$

The resulting shear stress, τ , is then recorded as a function of the imposed strain:

$$\tau(t) = \tau_0 \sin(\omega t + \delta) \quad (2.4)$$

where τ_0 is the maximum observed stress and δ is the phase shift, which characterises a potential lag period in the response. A completely elastic material does not exhibit any phase shift and creates an immediate stress when a strain is applied (see Fig. 2.4a). Contrarily, a phase shift of $\delta = \frac{\pi}{2}$ is observed for completely viscous materials, which results in a lag period between the application of a strain and a resulting stress (see Fig. 2.4b). Evidently, the response of a viscoelastic material is a combination of the purely elastic and purely viscous behaviour with a phase shift $0 > \delta > \frac{\pi}{2}$ (see Fig. 2.4c).

The complex shear modulus, G^* , is directly related to the maximum applied strain and the maximum observed stress:

$$G^* = \frac{\tau_0}{\hat{\gamma}_0} \quad (2.5)$$

The complex shear modulus consists of an elastic component as well as a viscous component (see Fig. 2.4d). The elastic component is called storage modulus, G' , and is defined as follows:

$$G' = G^* \cos(\delta) \quad (2.6)$$

The viscous component is called loss modulus, G'' , and can be calculated from:

$$G'' = G^* \sin(\delta) \quad (2.7)$$

The storage and loss modulus can then be correlated through the loss tangent, $\tan(\delta)$:

$$\tan(\delta) = \frac{G''}{G'} \quad (2.8)$$

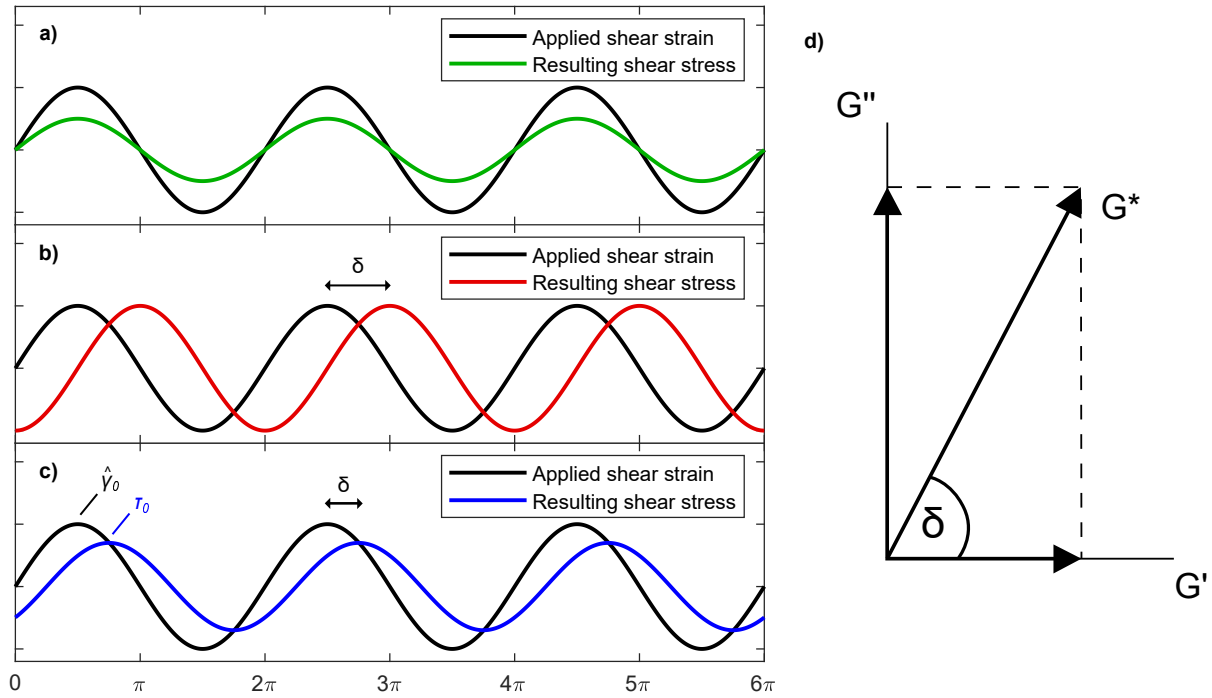


Figure 2.4: In rheological measurements, a small oscillatory shear strain is imposed on a sample. The corresponding shear stress is shown for a) an ideally elastic material, b) an ideally viscous material, and c) a viscoelastic material. d) The relationship between complex modulus, storage modulus, loss modulus, and the phase shift is shown in a vector graph.

In a typical rheological measurement, the linear viscoelastic region of the sample is determined first. Here, the shear strain is gradually increased, while the frequency of the oscillations is kept constant (see Fig.2.5a). The linear viscoelastic region is characterised by reversible deformations, such that the measurement does not perturb the structure of the sample. Therefore, the moduli remain constant in this region. Above a critical strain, however, the internal structure is irreversibly disturbed and the moduli start to decrease.

In order to determine the viscoelastic behaviour at different time scales, a frequency sweep experiment is often performed. Thereby, the frequency is gradually decreased over a range of interest, while the strain is kept constant (see Fig. 2.5b). The measurements are performed at a strain within the linear viscoelastic region to ensure that the deformations do not cause any irreversible changes to the sample. A frequency sweep experiment can then be used to correlate the viscoelastic properties of PSAs to their performance behaviour. Thereby, shear resistance and contact formation are attributed to the low frequency region (≤ 0.1 Hz), tack corresponds to a medium frequency region (approximately 1 Hz), and peel processes occur within the high frequency region (≥ 1 Hz)[39, 40].

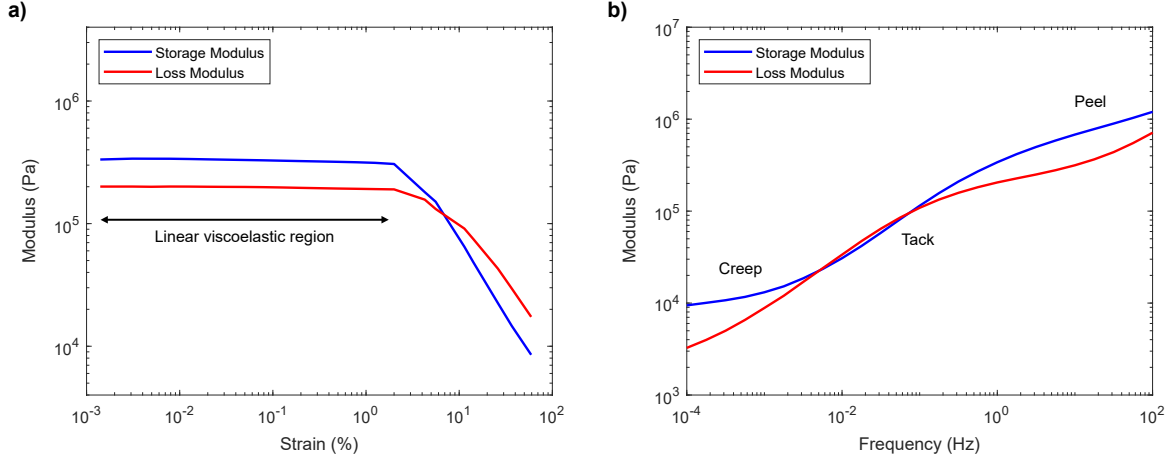


Figure 2.5: a) A typical strain sweep experiment at a constant frequency of 1 Hz. The linear viscoelastic region is characterised by stable moduli. b) A typical frequency sweep experiment in the linear viscoelastic region at a constant strain of 0.1 %. The performance parameters creep, tack, and peel can be correlated to the viscoelastic properties at different time scales.

2.2.3 Viscoelastic Properties and Adhesive Performance

Peel experiments are a common way to probe the performance of adhesives. However, the measured peel forces result from a complex interplay of different parameters[41]. When the adhesion is based on van der Waals forces, the peel force, F , is determined by the energy dissipation, Ψ , during peel and the work of adhesion[42]:

$$F = W_a \cdot (1 + \Psi) \quad (2.9)$$

Therefore, in order to achieve strong adhesion, the contact area between the PSA and the substrate should be maximised, which increases W_a . For rough substrates, such as human skin, this requires a certain flowability of the adhesive in order to fill the crevices. The Johnson-Kendall-Roberts theory can be used to estimate a critical elastic modulus, G_c , below which a material can spontaneously (under no load) flow into the crevices[43–45]:

$$G_c = \frac{\pi W_a (1 - \nu^2)}{2} \sqrt{\frac{3R}{L^3}} \quad (2.10)$$

where ν is the Poisson's ratio of the adhesive, R is the radius of the crevice, and L is the depth of the crevice (see Section 10.1 for details). PSAs typically provide a work

of adhesion of $W_a = 0.04 \text{ N/m}$ [46] and have a Poisson's ratio of $\nu = 0.5$ [47]. On a typical surface for PSA bonding with a crevice depth of $L = 1 \text{ }\mu\text{m}$ and a crevice radius of $R = 10 \text{ }\mu\text{m}$, the critical modulus becomes $G_c \approx 258 \text{ kPa}$. This is in line with the Dahlquist criterion, which states that a typical PSA should have a modulus below approximately 300 kPa in order to flow into the crevices of a surface and show measurable tack[48]. However, human skin is not a typical surface. In *Paper III*, the structure of a skin replica was analysed with a mechanical profilometer. Here, a groove depth of $L = 12 \text{ }\mu\text{m}$ and a radius of $R = 10 \text{ }\mu\text{m}$ was estimated. The increase in depth of the features as compared to a typical surface results in a reduction of the critical modulus to $G_c \approx 6 \text{ kPa}$.

The fact that human skin provides a relatively large roughness was also acknowledged by Chang, when he postulated different viscoelastic windows for PSAs[49]. The four corners of the window are determined by the storage and loss modulus at the bonding frequency as well as the debonding frequency. The combination of these parameters will then determine the peel adhesion of the adhesive (in Fig. 2.6a - d different scenarios are schematically illustrated). The author then described that skin adhesives are required to have a low storage modulus at the bonding frequency to increase the contact area and a high loss modulus at the debonding frequency to maximise energy dissipation and prevent detachment during movement. Subsequently, the peel force of PSAs has been correlated with the ratio of the loss modulus at the debonding frequency and the storage modulus at the bonding frequency. The following proportionality has been observed experimentally for different adhesives with similar surface energies[50]:

$$F \propto \frac{G''(\text{debonding frequency})}{G'(\text{bonding frequency})} \quad (2.11)$$

Noteworthy, Eq. 2.11 is only valid for adhesive that fail along the interface. Peel forces resulting from cohesive failure or large deformations otherwise may exceed the linear viscoelastic region and cannot be predicted by the model.

2.2.4 Tuning the Viscoelastic Properties

The viscoelastic properties of a polymer material are controlled by the physical properties of its chains. The chains typically exist in a coiled conformation and their molecular weight greatly influences the flow properties. With increasing chain length, an increasing resistance to flow is generally observed, which means that the viscosity increases. Chemical cross-links as well as physical entanglements between the chains cause an additional increase in viscosity. Depending on the relaxation times of the polymer chains and the testing frequency, the viscous and elastic contributions to the behaviour can vary. At high frequencies, the time scales of the deformations are typically shorter than the relaxation times of the polymer and the response may be dominated by an elastic behaviour. On the other hand, at low frequencies, the polymer chains may relax during deformation and therefore the rheological response may be dominated by a viscous behaviour instead[51].

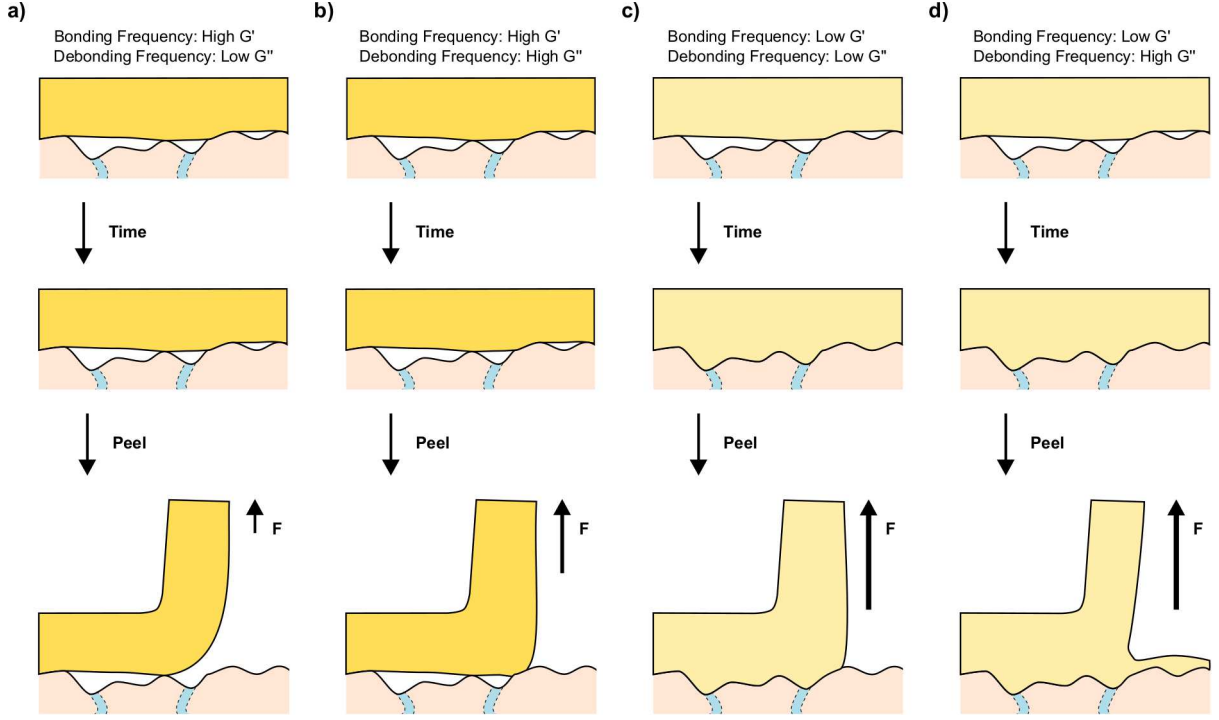


Figure 2.6: The behaviour of four hypothetical adhesives upon application on a rough substrate. a) and b) An adhesive with a high storage modulus at the bonding frequency does not flow into the crevices and therefore exhibits a limited contact area. Different peel forces may be observed depending on the energy dissipation. c) and d) An adhesive with a low storage modulus at the bonding frequency is able to flow into the crevices and therefore increases its contact area. Too much energy dissipation during peel may lead to cohesive failure.

The addition of particulate fillers to the polymer matrix also greatly affects the viscoelastic properties of the material. The effect of the particles on the viscoelastic properties strongly depends on parameters including particle loading, size, shape, and interactions with the matrix[52]. Suspensions of particles in polymer liquids are often evaluated in terms of their reduced viscosity, η_r , which is defined as the viscosity of the suspension divided by the viscosity of the pure polymer. During flow, hydrodynamic interactions between the particles often dominate the viscoelastic behaviour and cause an increase in viscosity (see illustration in Fig. 2.7a). There exist many empirical and semi-empirical equations to describe the development of the reduced viscosity as a function of particle loading[53]. Among them is the Krieger-Dougherty equation[54]:

$$\eta_r = [1 - (\phi/\phi_{max})]^{-2.5\phi_{max}} \quad (2.12)$$

where ϕ_{max} is the maximum particle loading. Deviations from such behaviour have

been reported when particulate structures occur within the composite[55]. Particulate structures may occur when the particles come into close proximity. For nanocomposites, particulate structures are often reported in the form of percolated networks, which can be inferred by a drastic increase in viscosity or storage modulus as a function of particle loading [56–59] (see illustration in Fig. 2.7b). Moreover, percolated networks manifest themselves with the occurrence of a plateau in the storage modulus at low frequencies[52, 60, 61]. This apparent yield stress occurs when a network of particles has formed and their elastic properties dominate. Importantly, rheological percolation does not require physical contact between the particles. Instead, it may be observed as soon as the interparticle distance is in the order of the polymer chain length of the matrix[56, 62, 63]. The effect of particle loading on the viscoelastic properties of skin adhesives will be discussed in detail in *Paper I*.

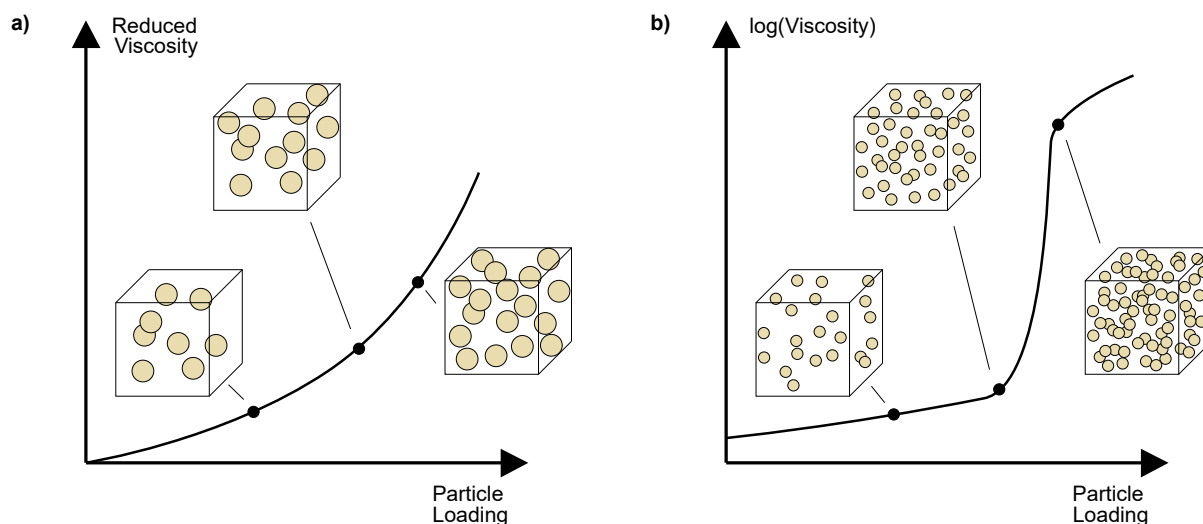


Figure 2.7: a) Illustration of the development of the reduced viscosity when hydrodynamic interactions between the particles dominate the viscoelastic behaviour. b) Rheological percolation may be observed when the interparticle distance becomes small enough to entrap individual polymer chains of the matrix.

2.3 PSAs and Water

The presence of water at the interface between a substrate and a PSA can have detrimental effects on the adhesion. Like with geckos, a film of water may prohibit contact formation of the adhesive in the first place or simply perturb the van der Waals interactions, which are responsible for the bonding. Additionally, water may penetrate into the adhesive and impair its mechanical properties. Such a loss of adhesion has been reported for structural

adhesives, where the materials were exposed to moist environments[64–69]. Similarly, skin adhesives have also been shown to lose adhesion due to the presence of moisture[70–77]. In contrast to most structural adhesives, however, moisture does not reach the interface through the skin adhesive but rather through the substrate (see Fig. 2.8a and 2.8b). Transepidermal water loss is responsible for the emergence of moisture at rest, while perspiration occurs during physical activity. In addition to the interference with contact formation, perturbation of van der Waals interactions, and weakening of the mechanical properties, water is also absorbed by skin, which causes a change in surface energy. A loss of adhesion may then be caused by a combination of these contributions.

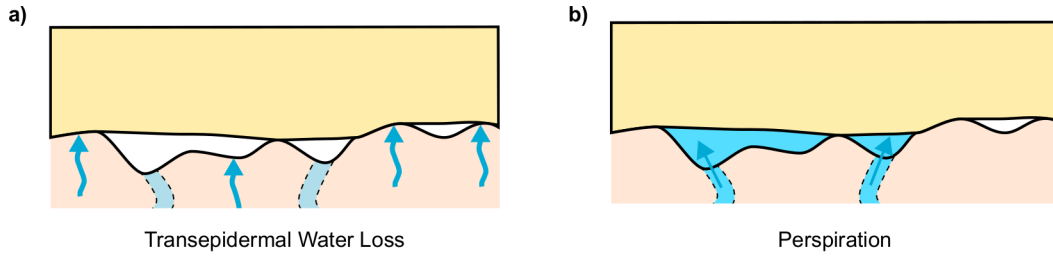


Figure 2.8: Schematic illustration of an adhesive on skin. Moisture is transported directly to the interface through the skin. a) Transepidermal water loss is responsible for the water transport at rest and b) perspiration occurs during physical activity.

2.3.1 Removal of Water from the Interface

Since the accumulation of moisture at the skin-adhesive interface not only has a detrimental effect on adhesion but also causes skin damage, the removal of water is considered necessary for adhesives during prolonged wear. The transport of water through polymeric materials is governed by diffusion processes, which can be described with Fick’s law:

$$\frac{\partial C}{\partial t} = D \frac{\partial^2 C}{\partial x^2} \quad (2.13)$$

where C is the concentration of the diffusing species, t refers to time, D is the diffusion coefficient, and x describes the position. The transport kinetics within the material are determined by the diffusion coefficient, which in turn strongly depends on the chemical nature of the polymer as well as its physical structure[78, 79]. The diffusion kinetics are often evaluated gravimetrically and described with a power-law relation[80–83]:

$$\frac{M_t}{M_\infty} = kt^n \quad (2.14)$$

where M_t is the weight of the sample at time t , M_∞ is the weight of the saturated sample, and k is a constant materials parameter. The exponent n thereby describes the diffusion kinetics within the material. When the relaxation times within the polymer are faster than the diffusion caused by a concentration gradient, Fickian kinetics with

an exponent $n = 1/2$ are observed. However, when the water uptake of the polymer is limited by the chain mobility, a linear relationship with $n = 1$ is typically observed. Since adhesive polymers typically have low water diffusivities, hydrophilic particles are often incorporated into the matrix to provide water transport[84]. In this case, the water diffusion kinetics not only depend on the chemical nature and physical structure of the particles but also their arrangement within the composite[85]. The benefit of particle incorporation can only be observed upon network formation such that the matrix no longer limits water diffusion. Therefore, a critical particle loading is necessary in order to achieve network formation and increase the water diffusion throughout the adhesive. In *Paper I*, it will be shown that the particles are isolated during dry conditions and network formation only takes place upon particle swelling when the adhesive is exposed to water (see illustration in 2.9).

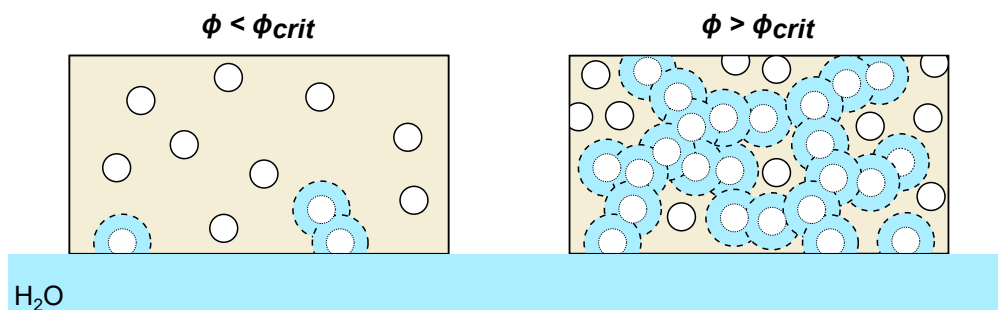


Figure 2.9: Schematic illustration of the water absorption by an adhesive composite. Below the critical particle loading, the particles remain isolated and water transport is limited by the polymer matrix. Above the critical particle loading, network formation occurs upon swelling of the particles and the water diffusivity is increased.

2.3.2 Bio-inspired Adhesives

A different attempt to maintain good adhesion in wet environments can be taken through the use of chemical adhesion. Thereby, chemical species, which allow for specific interactions with the substrate (e.g. hydrogen bonding), are integrated into the adhesives. Many of these adhesives are inspired by mussels and therefore include DOPA in the formulation[86, 87]. Recently, the development of an adhesive for wet environments has also been reported, where the adhesion mechanism relies on diffusion at the interface[88]. Water thereby enables the diffusion of the monomers and cross-linkers into the substrate before polymerisation and cross-linking is initiated.

Such chemical and diffusive adhesion results in much stronger interactions than van der Waals forces and consequently higher peel forces can be maintained after exposure to water. Crucially, however, skin health may be compromised not only by hazardous chemicals but also by too strong adhesion, which may cause mechanical trauma upon removal.

Since ostomy care adhesives are changed frequently, this thesis will focus on adhesives based on dispersive interactions to minimise skin irritations.

3 Project Definition

3.1 State of the Art

The requirements for skin adhesives are often fulfilled by antagonist properties. Therefore, formulations of skin adhesives are finely tuned to achieve the right balance for the application. Commercially available skin adhesives are often based on acrylics, silicones, or rubbers and provide adhesion due to van der Waals interactions[38, 89]. During wear conditions, these polymers are above their glass transition temperature and therefore provide the required chain mobility to establish good contact with the substrate. The necessary cohesive strength is then introduced through chemical or physical cross-linking of the polymers. Since the permeability of these polymers is typically rather low, hydrophilic components such as pectin, gelatin or carboxymethyl cellulose, which are generally referred to as hydrocolloids, are often incorporated to absorb excess moisture from the skin[84].

Although early patents of adhesives for ostomy care products include acrylic adhesives[90, 91], modern formulations are predominantly based on rubber or silicone. Thereby, rubber-based adhesives often have a matrix containing polyisobutylene (PIB) to provide adhesion and a styrene block copolymer to provide cohesion[92–97]. Carboxymethyl cellulose is a typical component of such adhesives to aid the absorption of moisture from the skin since the matrix has limited permeability to water. On the other hand, silicone adhesives exhibit higher permeabilities and can therefore be found with or without the incorporation of hydrophilic particles[98, 99]. Recently, some more exotic formulations have also been patented, where the hydrocolloids in the adhesive have been replaced by salts to reduce the swelling[100], or where honey has been incorporated in order to aid the adhesion[101].

3.2 Commercial Adhesives on Human Skin

In order to gain a better understanding of the problem formulation, I have worn several commercial adhesives on my skin. Through a gravimetric assessment of the sweat uptake of the adhesives as well as qualitative observations (such as visual changes of the adhesives or the occurrence of a loss of adhesion), the behaviour of the adhesives during wear was evaluated. A range of different commercial adhesives, which consisted of a polymer matrix and different hydrocolloids, was thereby chosen for the self-tests. Their water uptake abilities were probed through immersion tests and the results are indicated in Tab. 3.1.

Table 3.1: Sample overview for the self-tests of the commercial adhesives.

Name	Coloplast Adhesive	Water Uptake after 2 h (g/cm ²)
<i>Adhesive 1</i>	PL46	0.19
<i>Adhesive 2</i>	PL165	0.22
<i>Adhesive 3</i>	PL134	0.02
<i>Adhesive 4</i>	CP263-2	0.04
<i>Adhesive 5</i>	CP263-6	0.34

3.2.1 Commercial Adhesives on Human Skin at Rest

As a starting point, three different adhesives (*Adhesive 1*, *Adhesive 2*, and *Adhesive 3*) were worn during rest to investigate solely the effect of TEWL on the adhesive. The study included normal daily activities without any exercise and was carried out sporadically over the course of several weeks. The adhesives were weighed initially, placed on the forearm, then removed and weighed again.

For non-occluded skin, a TEWL of approximately 0.001 - 0.0015 g/cm²/h can be expected on the forearm[102, 103]. However, the adhesives only absorbed 0.0002 - 0.0004 g/cm²/h when worn on the skin (see Fig. 3.1). This indicates that some occlusion occurs during wear at rest and moisture might accumulate in the skin. Noteworthy though, no loss of adhesion was perceived over the course of the wear time and TEWL did not seem to impact the adhesive performance.

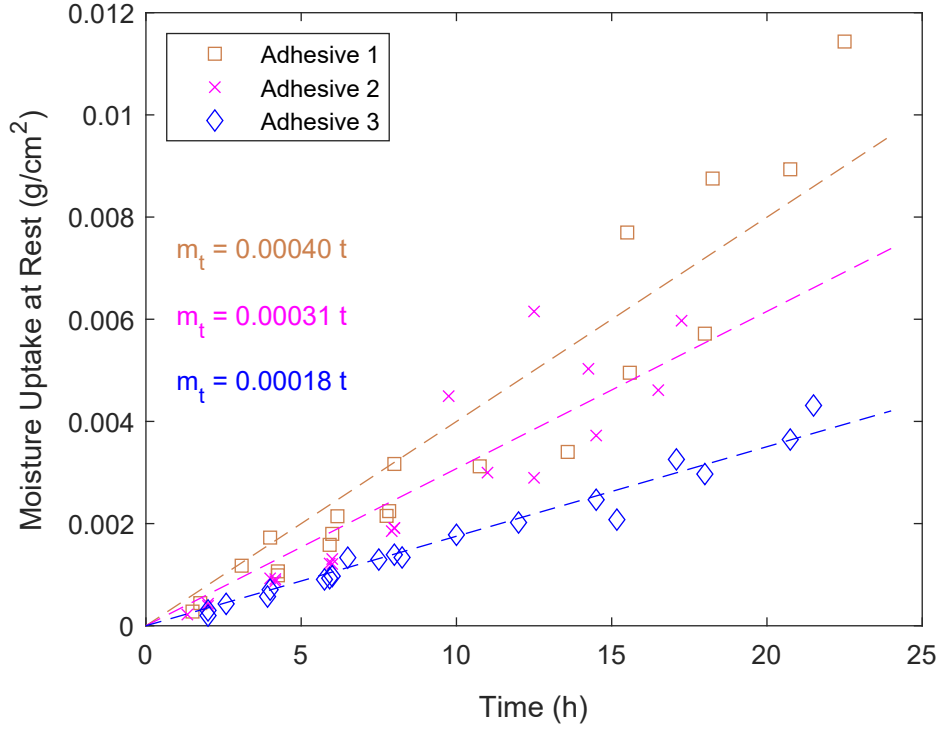


Figure 3.1: Moisture uptake of the adhesives during wear at rest.

3.2.2 Commercial Adhesives on Human Skin during Exercise

Different commercial adhesives were worn on the abdomen while biking to work in order to learn about their behaviour during exercise. An exercise time of 30 min was achieved by the route from Copenhagen to DTU, whereas biking from Copenhagen to Coloplast resulted in 90 min of exercise. The adhesives were weighed initially, then applied to the skin by hand pressure, and dwelled for approximately 10 min before the exercise protocol.

Sweat Uptake and Adhesion

The sweat uptake of the adhesives was evaluated gravimetrically after exercise. Four adhesives with different water uptake capabilities were worn simultaneously. This way, the adhesives were subject to the same sweating conditions and any differences in their sweat uptake results from the adhesive compositions. In Fig. 3.2a, the sweat uptake of the adhesives is shown over the course of several experiments. During experiments 8 and 9, a sponge was additionally placed on the skin during exercise to evaluate the sweat rate of the unoccluded skin. In Fig. 3.2b, an average of the sweat uptake over all experiments is shown. Firstly, it can be seen that the application of the adhesives hampers the sweat flow as compared to the unoccluded skin (sponge). Secondly, it was found that the sweat

uptake correlated with the water uptake abilities from Tab. 3.1, even though large variations in the sweat uptake were observed due to changes in the daily conditions.

Images of the adhesives after wear are shown in Fig. 3.2c. Especially the lower absorbing adhesives (*Adhesive 3* and *Adhesive 4*) show the presence of sweat at the interface. In contrast, the higher absorbing adhesives (*Adhesive 2* and *Adhesive 5*) appeared to limit the occurrence of free sweat at the interface.

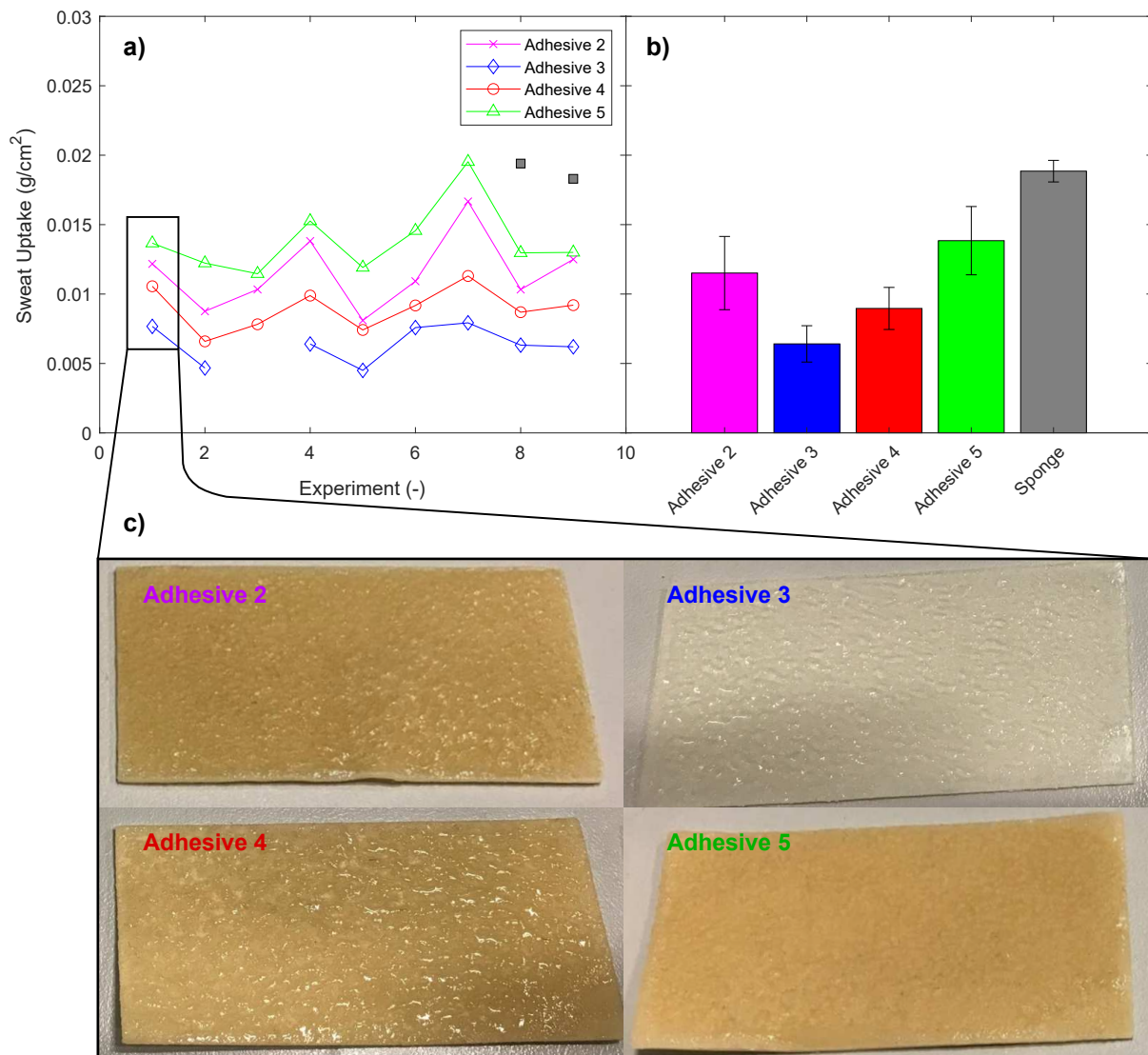


Figure 3.2: Sweat uptake of four different adhesives worn simultaneously upon biking for 30 min. a) The individual bike rides are depicted. b) The average is shown along with the standard deviation. c) Images of the adhesive surfaces after the bike ride.

During another set of experiments the sweat uptake and the perceived adhesion of *Adhesive 4* and *Adhesive 5* were evaluated. The two adhesives were worn simultaneously during two different exercise durations. Generally, *Adhesive 5* showed a higher sweat absorption than *Adhesive 4* (see Fig. 3.3), which was consistent with the water uptake capabilities of the adhesives. As expected, the sweat absorption also increased with increasing exercise duration. During short exercise times, the adhesion was only perceived as compromised in one case for the low absorption adhesive (*Adhesive 4*). However, after prolonged exercise times, a decrease in adhesion was perceived in 6/10 cases for *Adhesive 4* and in 3/10 cases for *Adhesive 5*. A complete loss of adhesion with delamination was observed during 3 and 1 instances for *Adhesive 4* and *Adhesive 5*, respectively. This implies that prolonged exercise and perspiration times indeed have a negative impact on adhesion. Thereby, the effect of perspiration on adhesives with a high absorption capability appears to be less detrimental.

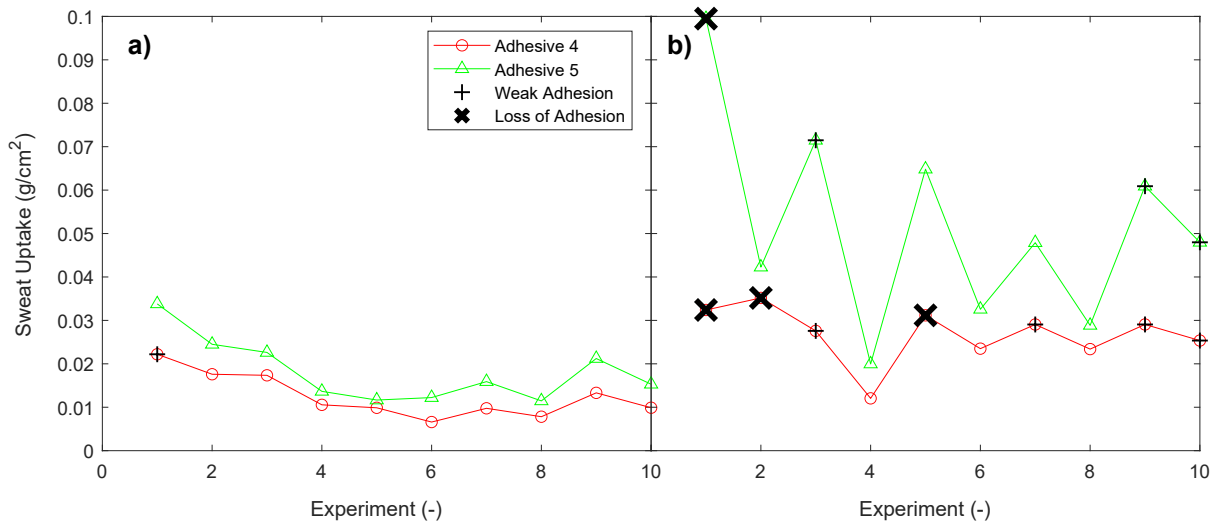


Figure 3.3: Sweat uptake of two different adhesives worn simultaneously upon biking for a) 30 min and b) 90 min. At short exercise times, adhesion was sufficient in all cases. At long exercise times, however, the low absorption adhesive completely delaminated in several cases.

Changes in the Viscoelastic Properties during Exercise

The effect of sweat absorption on the viscoelastic properties of *Adhesive 2* was briefly investigated. During exercise, approximately 0.065 g/cm^2 of sweat were taken up by the adhesive before its viscoelastic properties were evaluated using rheometry. In Fig. 3.4, the moduli of *Adhesive 2* are shown in the dry state (—) as well as after exercise (—). After exercise, the moduli decreased drastically at frequencies above approximately 10^{-2} , while an increase was observed at lower frequencies. According to Eq. 2.11, a decrease of G'' at high frequencies and an increase in G' at low frequencies would both cause a decrease in the peel force. Therefore, the change in viscoelastic properties during exercise would be expected to result in a lower peel force of *Adhesive 2* as compared to dry conditions. Noteworthy, certain hydration levels appear to exist, where the moduli of the adhesive increase as compared to dry conditions. A hydration level of 0.009 g/cm^2 of *Adhesive 2* was achieved through equilibration at 32°C and $75\% \text{ RH}$, which results in a stiffening of the adhesive (see — in Fig. 3.4). An increased G'' at high frequencies may thereby increase energy dissipation and therefore also increase the observed peel force. However, the increase may be balanced by the increased G' at low frequencies, which restricts the bonding process and may in turn decrease the peel force.

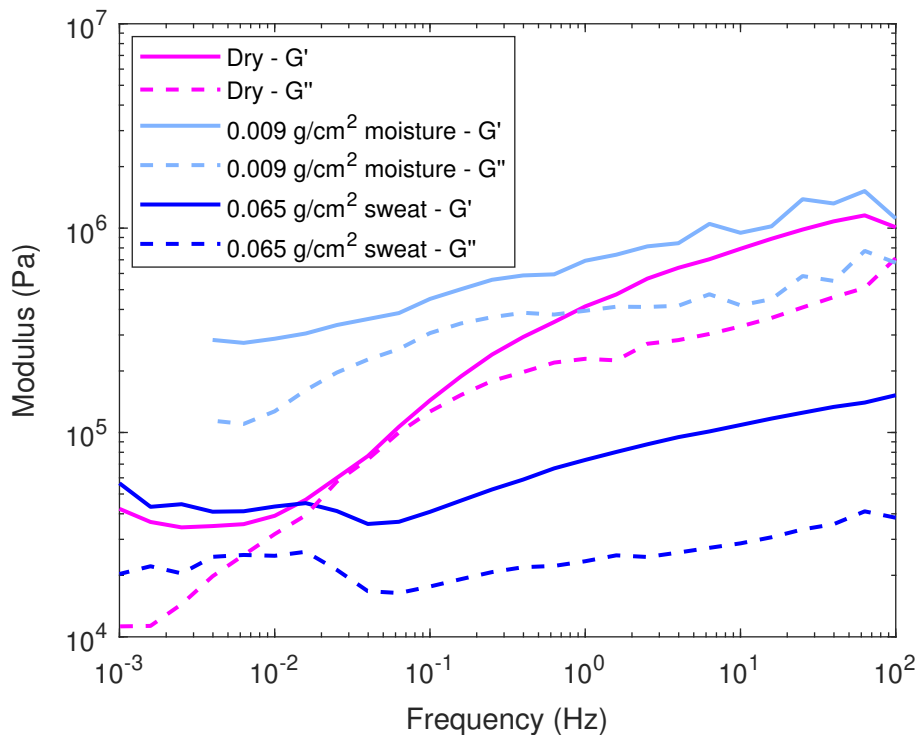


Figure 3.4: The mechanical properties of *Adhesive 2* in the dry state, after exposure to a humid environment of 32°C and $75\% \text{ RH}$, and after exercise.

3.3 Project Plan

This PhD thesis seeks to identify strategies to maintain adhesion in wet environments. This will enable the development of new skin adhesive formulations for prolonged wear situations. Since TEWL does not appear to have any detrimental effects on the adhesion, this project mainly focusses on adhesion during perspiration. In order to avoid the countless variations observed during perspiration on human skin and to ensure reproducibility, an *in vitro* perspiration simulator will be developed for the testing of skin adhesives. The results from the perspiration simulator will be compared to the behaviour of the adhesives on human skin. The perspiration simulator will then serve as a tool to develop novel formulations of skin adhesives.

Literature as well as the experiments in Section 3.2 suggest that the absorption of sweat may be beneficial for the maintenance of adhesion during wear. However, the complex interplay between the particle content, sweat absorption, viscoelastic properties, and peel adhesion of skin adhesives is not very well understood. Adjustments in the adhesive composition may thereby introduce changes in all of the above properties simultaneously.

In this PhD thesis, firstly, I aim to understand the influence of the adhesive composition on the sweat absorption properties of skin adhesives. I will investigate the water transport mechanism within heterogeneous polymer composites and evaluate the effect of particle content and the viscoelastic properties of the matrix. Secondly, I will evaluate the effect of the particle content on the viscoelastic properties of the adhesive composite and find correlations with the resulting peel adhesion under dry conditions. Thirdly, through a systematic design of experiments, I will decouple the effects of the sweat absorption capabilities from the effects of the viscoelastic properties on the peel adhesion during perspiration. Finally, I aim to implement these learnings and design new skin adhesive compositions with an improved performance during perspiration. The performance of the developed skin adhesives will then be compared to the performance of a commercial adhesive to demonstrate the development. In particular, I will focus on adhesives with the ability to readily establish good contact with the skin, even at low application pressures and short dwell times. This way, ostomates are spared one of many procedures during their pouch changing routine without compromising the performance of the adhesive.

4 Materials and Methods

This chapter describes the materials that were used during this thesis as well as their processing and characterisation. All standard procedures are described here and any deviations from these procedures will be specifically mentioned in the relevant sections of the thesis.

4.1 Raw Materials for Adhesive Composites

An overview of the raw materials that were used in this thesis can be found in Tab. 4.1.

Table 4.1: Materials used within this thesis.

Commercial Name	Supplier	Chemistry	Function
Oppanol B12 SFN	BASF	Polyisobutylene (PIB)	Matrix - Adhesion
Kraton D1161	Kraton	Styrene-Isoprene-Styrene (SIS)	Matrix - Cohesion
Potato Starch	KMC	Starch (Pot)	Filler - Viscoelastic Properties
Polysurf CS 67	Ashland	Cetyl hydroxyethyl cellulose (CHEC)	Filler - Water absorption
GR-221	Stewart Superabsorbent	Sodium poly(acrylic acid) (PAA)	Filler - Water absorption
MX5050	Dupont	Negative photoresist film (50 μm)	Substrate for peel test
G2625	Sigma-Aldrich	Gelatine from porcine skin, Type A	Substrate for peel test

4.2 Processing of Raw Materials into Adhesive Composites

All adhesive composites were mixed in a high shear mixer (Plastograph, Brabender) for 45 min at 90 °C and 30 rpm. A total of 60 g was mixed at any one time and a vacuum pump was applied to avoid the incorporation of air bubbles during mixing. In a first step, the adhesive matrix was mixed, where SIS and PIB were inserted into the mixing chamber at the desired weight fractions. In a second step, the adhesive composite was mixed by inserting the pre-mixed adhesive matrix into the mixer before inserting the particles at the desired weight fraction. Finally, the adhesive composites were pressed to a thickness of 1 mm using a hydraulic press (Stenhøj, Denmark) at 90 °C with a load of 10 t for 30 s. 20 g of adhesive were pressed at any one time and the desired sample geometry was realised through punching.

4.3 Methods for Characterisation

The characterisation techniques, which were used in this thesis are summarised in Tab. 4.2. A more detailed description will follow in the subsequent sections.

Table 4.2: Methods used for the characterisation of raw materials.

Technique	Instrument	Purpose
He-Pycnometry	Accupyc 1330 (Micromeritics)	Raw materials - density evaluation
Laser Diffraction	Mastersizer 2000 (Malvern)	Raw materials - particle size analysis
Optical microscopy	Eclipse LV100ND (Nikon)	Raw materials - particle size analysis
Particle Immersion Test	Analytical Balance XS105 (Mettler Toledo)	Raw materials - estimation of sweat absorption capacity
Adhesive Immersion Test	Analytical Balance XS204 (Mettler Toledo)	Adhesive Composites - evaluation of sweat absorption over time
Rheometry	Discovery HR-2 rheometer (TA instruments)	Adhesive composites - evaluation of the viscoelastic properties
X-ray μ CT	Xradia Versa XRM-410 (Zeiss)	Adhesive composites - microstructural analysis
Peel Test	<ul style="list-style-type: none"> • Universal Testing System 5943 (Instron) • Universal Testing System 34SC-2 (Instron) • Model GL Force Gauge (Dillon) 	Adhesive composites - evaluation of the peel adhesion
Mechanical Profilometry	<ul style="list-style-type: none"> • Dektak 3030 (Bruker) • SJ-410 (Mitutoyo) 	Adhesive composites - evaluation of surface topography Peel Substrates - evaluation of surface topography
Sessile Drop	ThetaLite 100 (Biolin Scientific)	Peel Substrates - Evaluation of water contact angles

4.3.1 Characterisation of Raw Materials

In this section, the characterisation methods for the raw materials are described along with the results. A summary of the properties of the raw materials is provided at the end of the section.

He-Pycnometry

He-Pycnometry was used to measure the true density of the particles through a gas displacement method. In He-Pycnometry, a sample is placed within a chamber of known volume and the chamber is subsequently filled with He. Thereafter, the gas is emptied into a second chamber of known volume and the resulting equilibrium pressure can be used to calculate the precise volume of the sample. Weighing the sample then allows for the determination of the density. The analysis was conducted with the default settings of the instrument at a purge pressure of 19.5 psig and an equilibration rate of 0.0050 psig/min. The average sample volume was obtained from ten determinations, which included a minimum of three purges each. The results are summarised in Tab. 4.3. The density of PIB and SIS was 0.92 g/cm^3 according to the manufacturer and any mixture of the two components was assumed to have a density of 0.92 g/cm^3 as well.

Laser Diffraction

Laser diffraction analysis was employed to evaluate the volume-weighted particle size distributions of the different particles in this thesis. The measurement principle is based on Fraunhofer diffraction, which states that the scattering angle of a laser beam depends on the particle size. The intensity profile over different scattering angles can then be converted to a particle size distribution. Typically, the particles are assumed to be spherical for such calculations and the results should be supported by optical microscopy. Compared to optical microscopy, a large number of particles is analysed to obtain the particle size distributions (in the order of 10^9 particles).

In order to measure the size of primary particles rather than agglomerates, the particles need to be dispersed. In this thesis, a dry dispersion unit (Scirocco 2000 from Malvern) was used to disperse the particles during the measurement. A brief method development was performed to determine the optimal pressure for deagglomeration of particles. Here, a pressure of 2.0 bar was found to provide good dispersion during the measurements. The resulting particle size distributions are shown in Fig. 4.1. A volume-weighted average diameter, $D[4, 3]$, was calculated over the entire range of the distribution and is summarised in Tab. 4.3.

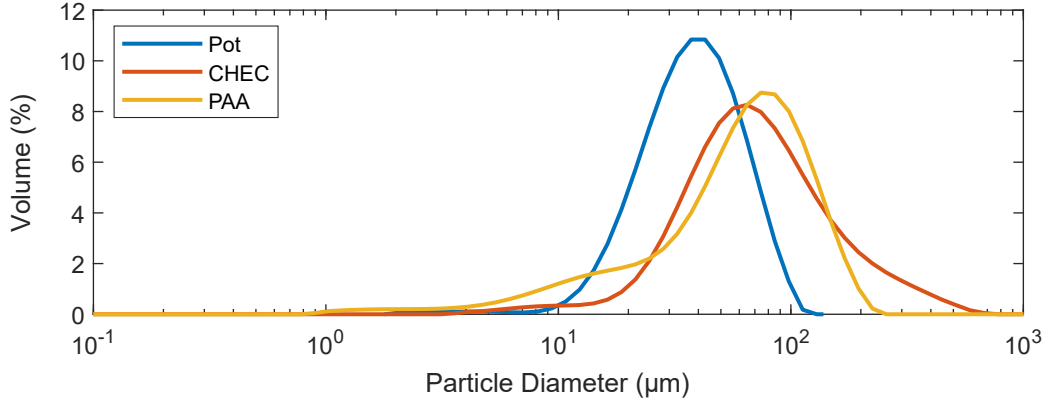


Figure 4.1: Volume-weighted particle size distributions of the particles in this study.

Optical Microscopy

Optical microscopy was used to evaluate the particle morphology of PAA and compare the obtained particle sizes with laser diffraction. Here, the particle diameters of more than 500 individual particles were determined and distributed into bins in order to obtain a particle size distribution. A number- as well as volume-weighted distribution were calculated and compared to the volume-weighted distribution from laser diffraction. Thereby, PAA exhibited a wide distribution of particle sizes, which meant that the number- and volume-weighted distribution were very different (see Fig. 4.2). This resulted in a number-weighted average diameter $d_{mic} = 18 \mu\text{m}$ in contrast to $D[4, 3] = 68 \mu\text{m}$. While a small number of large particles have a small effect on the number-weighted distribution, they have a large effect on the volume-weighted distribution. The volume-weighted distributions from microscopy and laser diffraction qualitatively showed good agreement. Noteworthy, the volume-distribution from microscopy was effectively based on only very few large particles, which may cause the observed discrepancies.

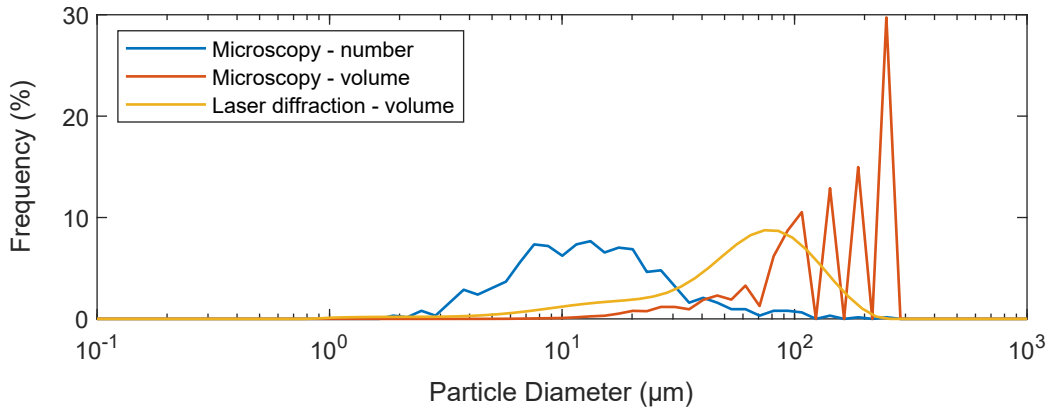


Figure 4.2: PAA particle size distributions from optical microscopy and laser diffraction.

Particle Immersion Test

In order to estimate the sweat absorption capacity of PAA, the particles were immersed in a 0.154 M NaCl solution. Here, 0.5 g of particles were weighed into a measuring cylinder, which was filled with 100 mL of the saline solution. The particles then swelled and a phase separation could be observed (see Fig. 4.3a). From the volume of the opaque phase, which constituted the swollen particles, the absorption capacity was estimated. The results are summarised in Tab. 4.3.

Furthermore, the absorption capacity of PAA was also evaluated in a 0.154 M NaCl solution, which was adjusted to pH 2 using HCl (see Fig. 4.3b) as well as in a 0.77 M CaCl_2 solution (see Fig. 4.3c). The pH of the solution as well as the presence of divalent ions thereby influence the swelling capacity of the PAA particles. The effect of such swelling restrictions within skin adhesives is investigated in Chapter 5.

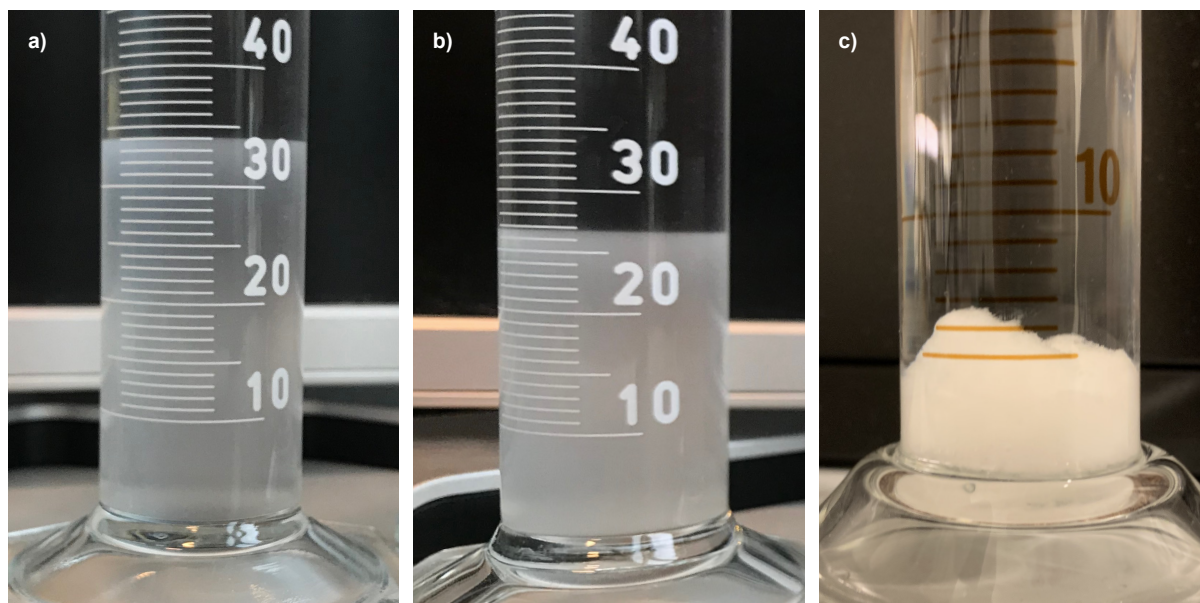


Figure 4.3: a) Immersion of 0.5 g PAA in 0.154 M NaCl solution to estimate the sweat absorption capacity. Additionally, 0.5 g PAA were immersed in b) 0.154 M NaCl at pH 2 and b) 0.77 M CaCl_2 to investigate the effect of pH and the presence of divalent ions on the swelling capacity.

Summary of the Characteristics of the Raw Materials

The relevant properties of the raw materials are summarised in Tab. 4.3.

Table 4.3: Properties of the raw materials within this study.

Commercial Name	Density (g/cm ³)	$D[4, 3]$ (μm)	d_{mic} (μm)	Absorption Capacity (g/g)
Pot	1.52	41	-	-
CHEC	1.38	93	-	-
PAA	1.65	68	18	68

4.3.2 Characterisation of Adhesive Composites

In this section, the characterisation methods for the adhesive composites are described. The results will be presented in the following chapters of the thesis.

Immersion Test

The sweat absorption capabilities of the adhesive composites were estimated through immersion in 0.154 M NaCl solution at 32 °C. Here, adhesive composites were punched out to dimensions of 25 mm x 25 mm x 1 mm and adhered to a pre-weighed polystyrene backing plate (see schematics in Fig. 4.4). The backing plate with the adhesive sample was weighed before immersion in the saline solution. After pre-determined time intervals the samples were then removed, blotted, weighed, and re-immersed. As a minimum, an average of three replicates for each adhesive was reported.

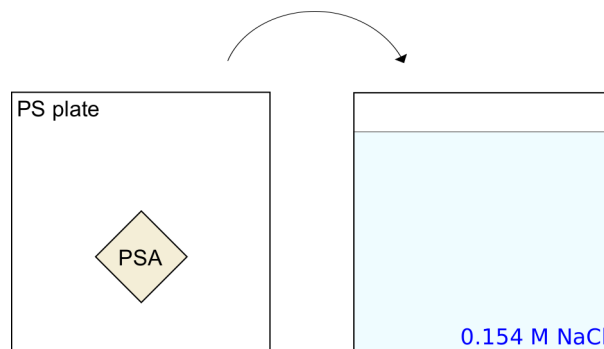


Figure 4.4: Schematic illustration of the immersion test setup to estimate the sweat absorption capabilities of the adhesives.

Rheometry

Rheometry was conducted to analyse the viscoelastic behaviour of the adhesive composites. The adhesive composites were punched in a circular shape with diameters of 20 mm or 25 mm. The experiments were conducted with a parallel plate geometry at a constant temperature of 32 °C. To ensure good contact, the rheometer gap was closed until an initial contact force of 5 N was reached. Thereafter, the gap was opened to achieve a normal force of 0 N, which was also kept during the rest of the experiment. After an equilibration time of 15 min, a frequency sweep experiment was run at a strain of 0.1 % over a range of 100 Hz - 0.0001 Hz. After an additional 5 min of equilibration time, a strain sweep experiment was performed at a frequency of 1 Hz over a range of 0.002 % - 50 %.

The strain sweep experiments were performed to ensure that the frequency sweep occurred within the linear viscoelastic region of the adhesive composites. In the linear viscoelastic region the deformations are small enough not to disturb the structure of the composite. In order to be able to perform the experiments on the same sample, frequency sweep experiments were conducted prior to the strain sweep experiments.

X-ray μ CT

X-ray μ CT measurements were performed in collaboration with Søren Bredmose Simonsen to analyse the structure within the adhesive composites. A description of the measurements details can be found in *Paper I*.

Peel Test

Peel tests were conducted as a performance indicator of the adhesive composites. For the measurements, the adhesive composites were punched to dimensions of 100 mm by 25 mm. A backing tape (4124, Tesa) was applied to the adhesive composites prior to their application to the substrate. The application to the substrate occurred with the use of a silicone pad with a pressure of 1770 Pa for 1 min in order to mimic poor application by a user. Different dwelling conditions were then introduced before finally peeling the adhesive composite from the substrate. Peeling occurred at a constant angle of 90° and a speed of 304 mm/min (corresponding to a peel frequency of approximately 5 Hz) while the forces were recorded. The peel curves were then evaluated between 20 - 80 mm displacement and an average of three replicates was reported.

The peel forces strongly depend on the substrate that was used during the experiment. To mimic the properties of human skin, a perspiration simulator was developed during this thesis and a detailed description can be found in Chapter 6. Two iterations of the simulator were made with two distinct artificial skin substrates. Both substrates included topographical features to mimic the roughness of human skin as well as a distribution of holes to enable perspiration. In the first iteration, the artificial skin consisted of a UV-curable polymer film (MX5050), where the skin topography was imprinted. In the second iteration, the simulator included a polyimide substrate, which was coated with a thin layer of gelatine to mimic the chemistry, hydration, and wettability of human skin.

4.3.3 Characterisation of Artificial Skin Substrates

Mechanical Profilometry

A mechanical profilometer was used to determine the surface topography of the artificial skin substrates for the peel test. The substrates were scanned over a length of 5 mm with a force of 0.01 mN. To calculate the average roughness a minimum of 20 scans was performed in different positions and directions of the artificial skin.

Sessile Drop

The contact angle, θ , was measured on the artificial skin substrates over a period of 10 s, with a starting point 10 s after the droplet touched the surface. An average value of 4 separate determinations was calculated for both substrates.

4.4 Adhesion to Human Skin

For a qualitative assessment of the adhesion to human skin, adhesives were applied to my left and right forearm. First, the forearms were stripped multiple times with a commercial adhesive (*Adhesive 2*) in order to remove the outermost layer of skin cells. Then the adhesive composites with dimensions of 100 mm x 25 mm x 1 mm were applied manually such that good adhesion was perceived. After 10 min of dwell time at rest, the adhesive composites were peeled (see above) to yield the peel forces from skin in dry conditions.

To investigate the effect of perspiration, a bike ride for a duration of approximately 30 min was introduced after the dwell period of the adhesive. A peel experiment was then performed within 5 min of the end of the exercise.

Part II

Results and Discussion

5 Water Transporting Networks

In this chapter, I will show how water is transported throughout the adhesive composites. Due to the heterogeneous nature of the adhesives, a network of hydrophilic particles is necessary to provide a pathway for the water molecules in order to achieve continuous and fast water transport. Otherwise, if particles are not connected, water diffusion is limited by the permeability of the polymer matrix.

5.1 Particle Networks in Skin Adhesives (*Paper I*)

In *Paper I*, the formation of particle networks in polymer composites has been investigated. Model adhesives were prepared containing PAA particles at different volume fractions within a matrix consisting of PIB (80 wt.%) and SIS (20 wt.%). X-ray micro-computed tomography (μ CT) was used to visualise the particles within the adhesive and determine the interparticle distances for adhesives with nominal volume fractions, ϕ_{nom} , of 0.09, 0.12, and 0.27. In addition to the adhesives in *Paper I*, an adhesive with $\phi_{nom} = 0.06$ has also been analysed using X-ray μ CT, which will be reported in this thesis. The following sections include a description of the analysis of the X-ray μ CT data (section 5.1.1), the results of the additional composition (section 5.1.2), and a summary of *Paper I* (section 5.1.3).

5.1.1 Analysis of X-ray μ CT Data

From the X-ray μ CT measurements, raw data was obtained, which consisted of the volume of every individual particle as well as the corresponding coordinates of its center of gravity. At first, all particles with a volume below $3 \mu\text{m}^3$ were removed (equivalent diameter of $2 \mu\text{m}$) to filter the noise. Then, the real volume fraction, ϕ_{CT} , of particles within the sample was calculated. Here, the volume fraction was calculated in a cubic cell of 0.064 mm^3 between the coordinates $x_1 = 300 \mu\text{m}$ and $x_2 = 700 \mu\text{m}$, $y_1 = 300 \mu\text{m}$ and $y_2 = 700 \mu\text{m}$, as well as $z_1 = 300 \mu\text{m}$ and $z_2 = 700 \mu\text{m}$ (see schematics in Fig. 5.1a).

Next, the particle size distribution was determined from the volume of the particles. With the approximation that the particles were spherical, the diameter of every individual particle could be determined (see schematics in Fig. 5.1b).

The interparticle distances were calculated by subtracting the particle radii from the corresponding distance between the centers of gravity of two particles. First, the distances between Particle 1 and all other particles were calculated. The smallest distance was then recorded as the interparticle distance for Particle 1 (see schematics in Fig. 5.1c). Second, the distances between Particle 2 and all other particles were calculated. The smallest distance was again recorded as the interparticle distance and the process was repeated for the remaining particles.

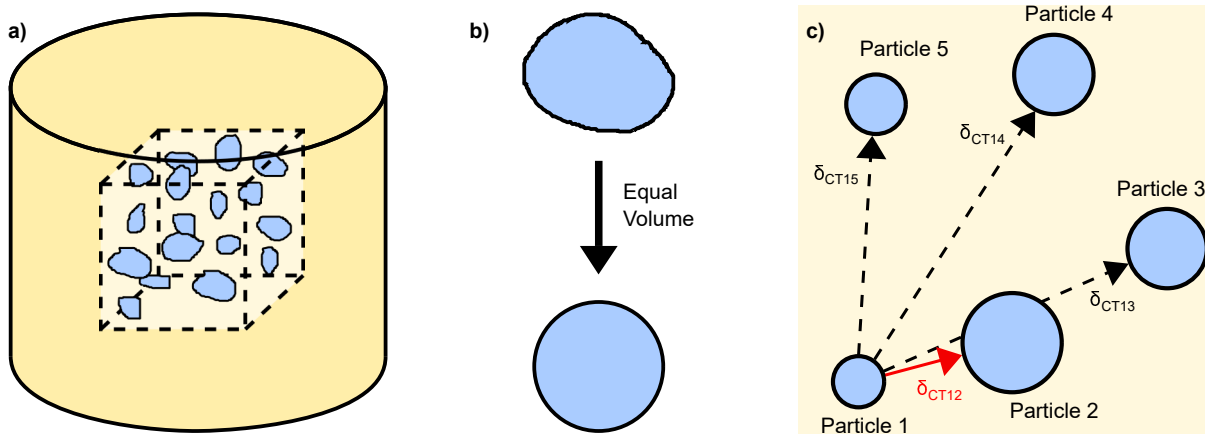


Figure 5.1: Schematic presentation of the analysis of the X-ray μ CT measurements. a) The particle volume fraction was calculated within a portion of the analysed sample. b) To calculate the particle diameters the particles were reduced to spheres with equal volume. c) The interparticle distance of every individual particle was calculated as the minimum surface-to-surface distance to all other particles.

The process finally yielded the shortest surface-to-surface distances to the nearest neighbours for all particles within the sample (see Fig. 5.2a). In order to obtain the interparticle distances in a histogram, intervals for the data were created. Since the obtained distances only spanned values over one decade from approx. $2\text{ }\mu\text{m}$ to $50\text{ }\mu\text{m}$, linear bin sizes were chosen to evaluate the data (see Fig. 5.2b). The data was then found to correspond to a normal distribution around a mean interparticle distance, δ_{CT} , with a standard deviation, σ_{CT} (see Fig. 5.2c). On the other hand, when distributing the interparticle distances into logarithmically spaced bins, a poor fit was obtained (see Fig. 5.2d and 5.2e). This also indicates that linear binning was a sensible choice and therefore all data was analysed with linear bin sizes.

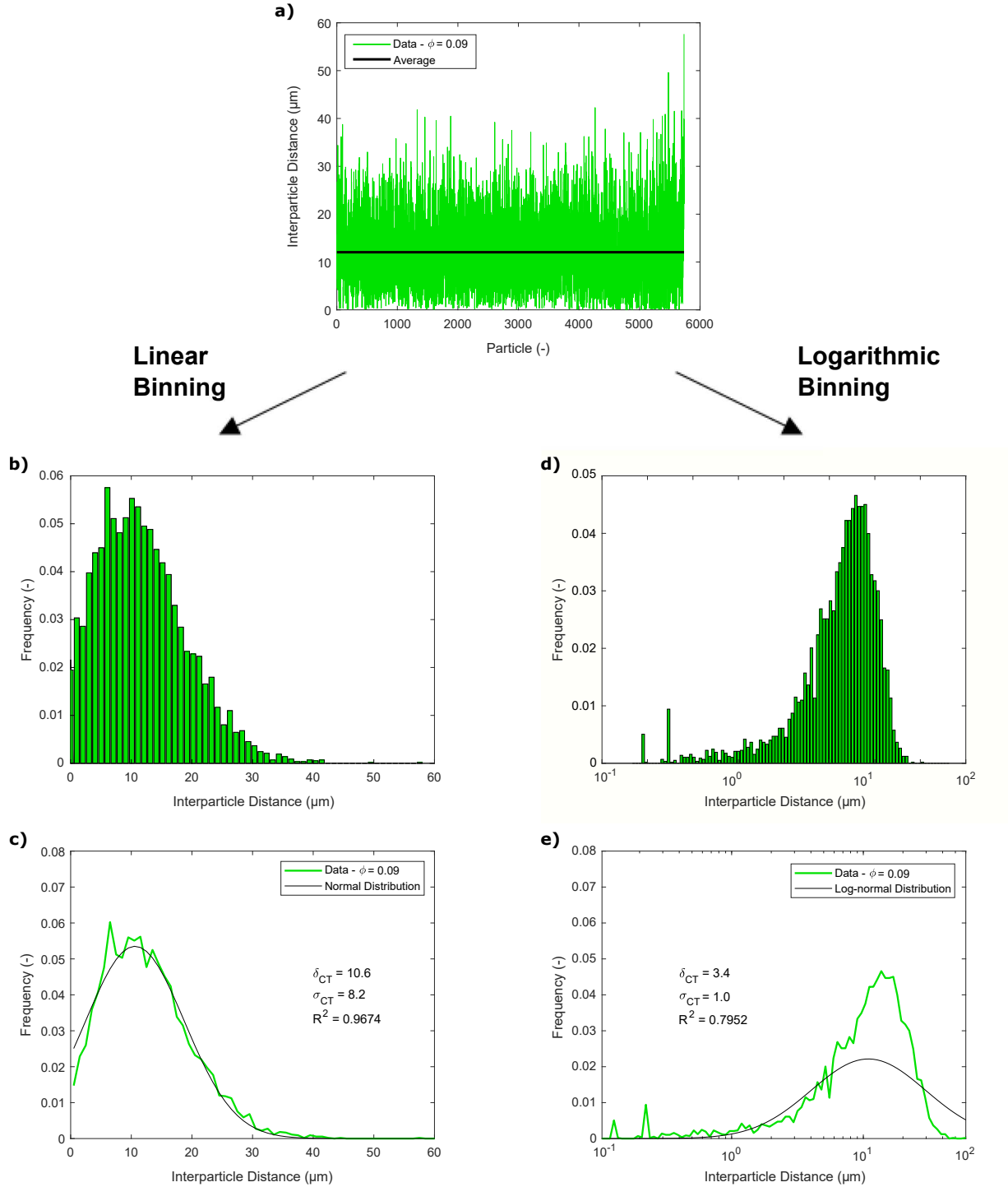


Figure 5.2: Using X-ray μCT the interparticle distances were evaluated for an adhesive containing PAA particles at a volume fraction of $\phi_{nom} = 0.09$. a) The surface-to-surface distance to the nearest neighbour is shown for all particles. b) The histogram for linear linear binning. c) The corresponding normal distribution shows a good fit. d) The histogram for logarithmic binning. e) The corresponding log-normal distribution shows a poor fit.

5.1.2 X-ray μ CT of Additional Composition

In *Paper I*, it was shown that the interparticle distances of composites with nominal volume fractions of 0.09, 0.12, and 0.27 were normally distributed. Similarly, the analysis of a composite with a nominal volume fraction of 0.06 also yielded normally distributed interparticle distances (see Fig. 5.3a). The distribution of interparticle distances of the compositions from *Paper I* are shown in Fig. 5.3b - d for comparison. Unfortunately, the additional sample had an actual volume fraction of $\phi_{CT} = 0.12$ instead of the expected $\phi_{nom} = 0.06$. Consequently, the additional sample exhibited a distribution of interparticle distances similar to the composite containing particles at $\phi_{nom} = 0.12$ (see Fig. 5.3a and 5.3c). Likely, such a discrepancy occurred due to the small sample volume ($< 1 \text{ mm}^3$) for the X-ray μ CT measurements. While being instrumental to achieving good contrast between the polymer matrix and the particles, the small sample may not be fully representative of the entire composite. The additional sample showed that the model calculations for the interparticle distances can be applied to the composites in the study but did not yield any additional data points. Therefore, the additional sample was not included in *Paper I*.

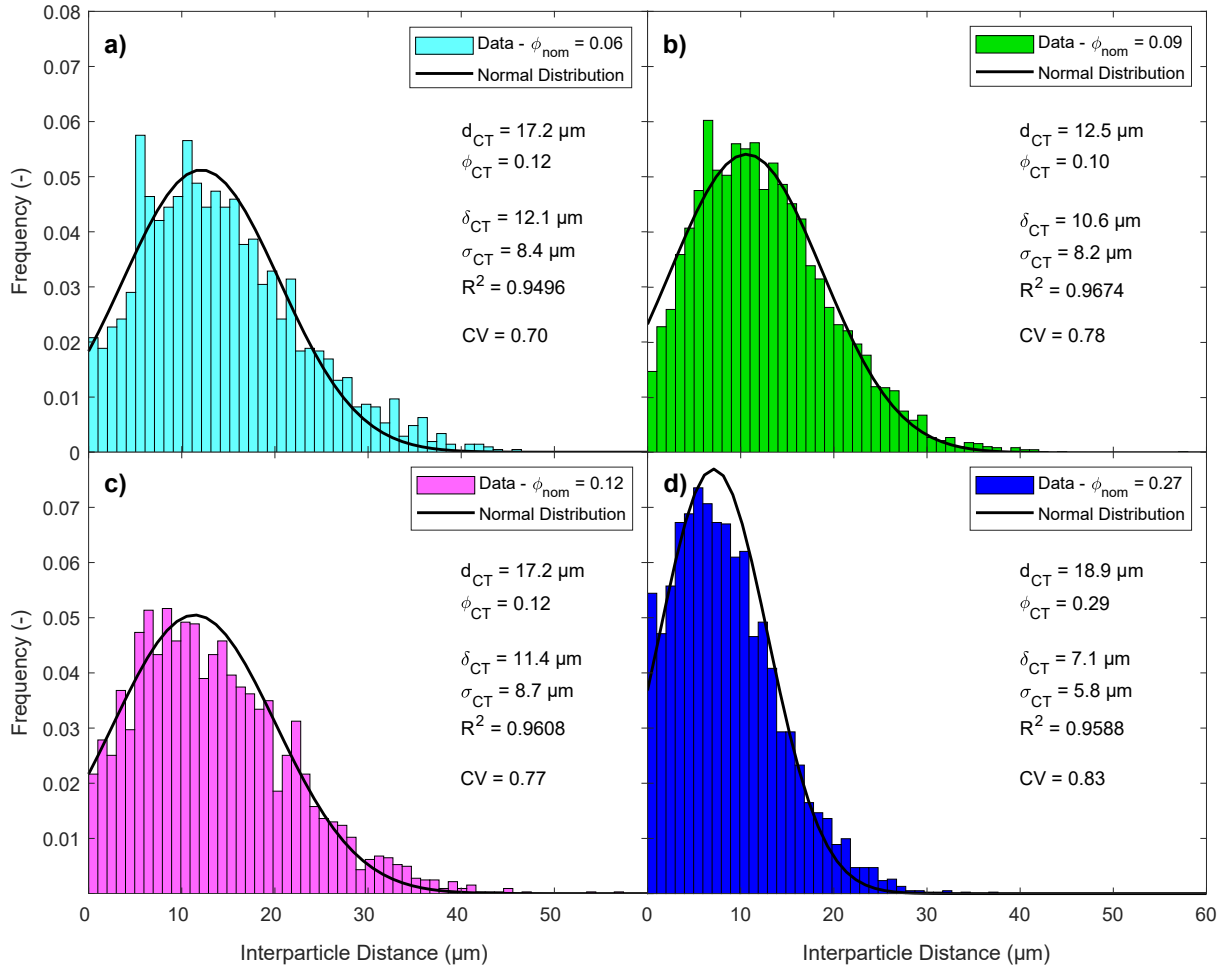


Figure 5.3: The interparticle distances from X-ray μ CT are shown with their best-fit normal distributions. The adhesives contain particles at nominal volume fractions a) $\phi_{nom} = 0.06$, b) $\phi_{nom} = 0.09$, c) $\phi_{nom} = 0.12$, d) $\phi_{nom} = 0.29$. Figure partly adapted from [104] with permission from *The Royal Society of Chemistry*.

5.1.3 Summary of *Paper I*

In *Paper I*, it was shown that particle networks for water transport formed upon swelling after exposure to water. Above a critical volume fraction, the particles were sufficiently close such that the interparticle distance could be overcome by swelling (see schematics in Fig. 5.4a). Naturally, this critical volume fraction strongly depended on the amount of swelling. When exposed to a 0.154 M NaCl solution at 32 °C, the particle diameter increased by 36.7 μm and the effects of network formation could already be observed at a nominal particle loading $\phi_{nom} = 0.09$. At this particle loading almost 90 % of particles are within 36.7 μm of their nearest neighbour according to the developed model (see Fig. 5.4b). On the other hand, particles only swelled by approx. 2.8 μm when exposed to 75

% RH and 32 °C. Here, first indications of network formation were observed at a nominal particle loading $\phi_{nom} = 0.19$. At this particle loading only approx. 10 % of particles were within 2.8 μm of their nearest neighbour. Particle irregularities or directional swelling, which were not accounted for in the model, could be responsible for the observation of particle networks at such low connectivities. In line with the model calculations, rheological percolation was not observed for any of the adhesive composites.

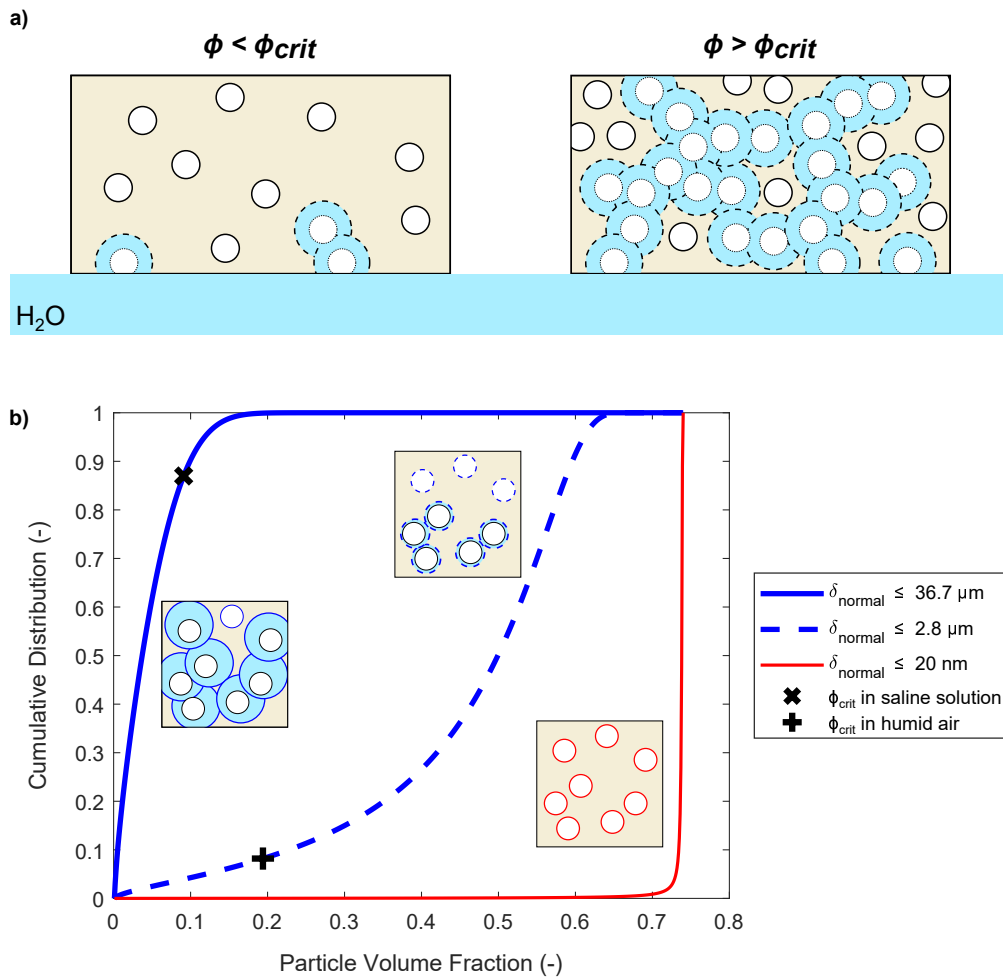


Figure 5.4: a) Schematic illustration of swelling-induced network formation and the critical volume fraction. b) The cumulative distribution at three different interparticle distances as a function of particle loading. The predictions were made using the established model in *Paper I* to represent swelling in 0.154 M NaCl solution ($\delta \leq 36.7 \mu\text{m}$), swelling at 32 °C and 75 % RH ($\delta \leq 2.80 \mu\text{m}$), and the polymer matrix chain length for rheological percolation ($\delta \leq 20 \text{ nm}$). Figure partly adapted from [104] with permission from *The Royal Society of Chemistry*.

5.2 Adhesive Design Considerations for Water Transport (*Paper II*)

In *Paper II*, the implications of swelling-induced network formation in skin adhesives containing PAA particles are discussed. Since the hydrophilic particles are isolated, the viscoelastic properties of the surrounding polymer matrix govern the swelling of the particles. The matrix influences the swelling kinetics as well as the swelling capacity and therefore also the critical particle loading necessary for swelling-induced network formation (see schematics in Fig. 5.5). Therefore, the water uptake of skin adhesives can be readily tuned through adjustments in the viscoelastic properties of the matrix. Here, the addition of SIS to the polymer matrix was found to increase the stiffness of the adhesives, limit the particle swelling and consequently increase the critical particle loading for swelling-induced network formation. At the same time, note should be taken of the environmental conditions of the adhesive. The presence of multivalent ions or changes in pH can limit the swelling of the hydrophilic particles and therefore cause an increase in the critical particle loading necessary for swelling-induced network formation (see schematics in Fig. 5.5). A composite at a loading $\phi = 0.12$ containing 20 wt.% SIS in the matrix will readily transport water in a 0.154 M NaCl solution, be on the verge of facilitating continuous transport in an acidic environment at pH 2 and act as a water barrier in a 0.077 M CaCl_2 solution.

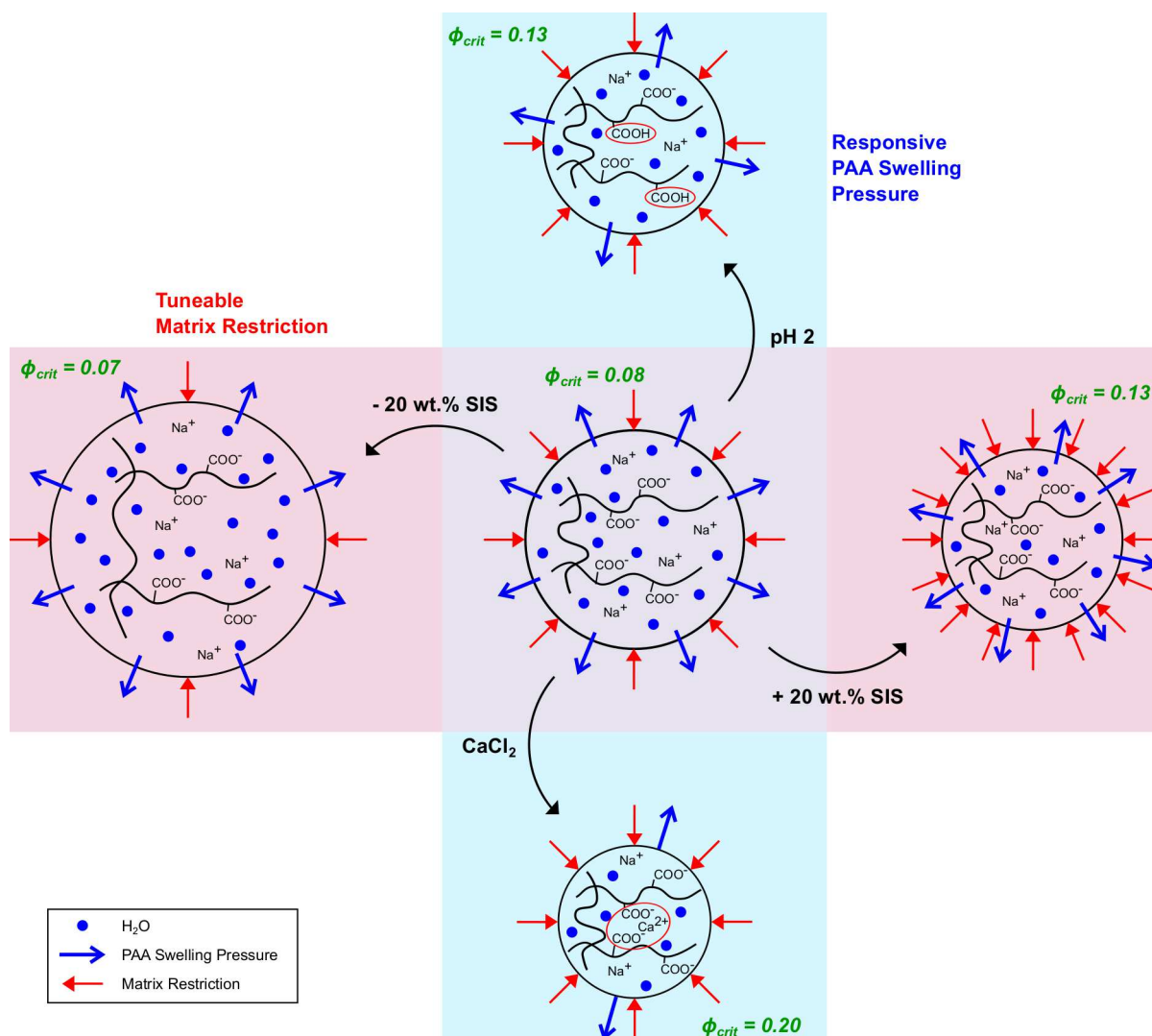


Figure 5.5: Schematic illustration of the effects of the viscoelastic properties of the matrix, a reduction in pH, and the presence of divalent ions on the swelling-induced network formation in skin adhesives.

5.3 Key Conclusions

- The particles within the skin adhesives are separated by a layer of polymer matrix
- Upon exposure to water, the particles swell and form a network, which enables the transport of water throughout the bulk of the adhesive
- For network formation, a critical concentration of particles is necessary, at which the interparticle distances can be overcome by the swelling
- The critical concentration for swelling-induced network formation strongly depends on the swelling of the particles
- The swelling of particles is greatly influenced by the polymer matrix, where a stiffer matrix not only influences the water uptake kinetics but also the capacity and therefore increases the critical concentration for swelling-induced network formation
- The swelling of particles is also greatly influenced by the environmental parameters, where exposure to divalent ions or acidic conditions can also hamper the water uptake and therefore increase the critical concentration for swelling-induced network formation

6 Adhesive Performance during Perspiration

Human skin shows many intra- and interindividual variabilities, which makes it difficult to control and reproduce the conditions during an experiment. Important properties for adhesion such as roughness and water contact angle span large intervals of values and may change upon hydration[16, 18, 105, 106]. Furthermore, when testing adhesives during perspiration, different sweat rates and sweat compositions have to be accounted for[107–109]. Therefore, the development of a perspiration simulator was of utmost importance to test the performance of skin adhesives during perspiration under well-defined conditions.

6.1 Development of a Perspiration Simulator

The perspiration simulator is designed as a simplification of the processes occurring in human skin during sweating. It should mimic human skin in the relevant parameters and enable reproducible experimental conditions. Homogeneous sweating through the sweat pores of the perspiration simulator is thereby crucial for the experiments. According to Poiseuille’s law, the resistance, R , of a liquid to flow through a pore is determined by the liquid viscosity, η , the length of the pore, L , and the diameter of the pore, d :

$$R = \frac{128\eta L}{\pi d^4} \quad (6.1)$$

The volume flow rate, Q_n , through a pore with a specific area is then determined by the pressure difference, ΔP , before and after the pore and the resistance to flow:

$$Q_n = \frac{\Delta P}{R} = \frac{\pi d^4}{128\eta L} \Delta P \quad (6.2)$$

From Eq. 6.2 it can easily be seen that the flow through a pore strongly depends on its diameter. Therefore, it is challenging to achieve homogeneous flow through a single membrane, where pores have a distribution of sizes. Large pores have a much smaller resistance to flow and will consequently also have the largest contribution to the entire flow (see illustration in Fig. 6.1a). Hou et al.[110] have solved this problem through a bilayer approach, where a second membrane with much smaller pores is used to regulate the flow in the first place. One single pore of the surface membrane thereby covers a myriad of pores of the bottom membrane, which has two important implications (see illustration in Fig. 6.1b). Firstly, the resistance to flow is much larger in the bottom membrane, which

means that the pressure drop in the surface membrane becomes insignificant. Hence, the pores of the surface membrane can be viewed as individual pores, which do not compete with other pores for flow. Secondly, the distribution of pore sizes in the bottom membrane becomes irrelevant because a large number of pores feeds into one single pore of the surface membrane. This number of pores, N , can be calculated from the pore density of the bottom membrane, α , and the pore diameter of the surface membrane, d_S :

$$N = \frac{\pi d_S^2 \alpha}{4} \quad (6.3)$$

In such a bilayer device, the membranes are placed in series and their resistances to flow can be added together. Since the resistance to flow is much larger in the bottom membrane, the resistance of the surface membrane can be neglected. Therefore, the overall flow rate is controlled by the pore diameter of the bottom membrane, d_m , and its thickness, L_m . The volume flow rate through one pore of the surface membrane then becomes:

$$Q_n = \frac{\pi^2 d_m^4 d_s^2 \alpha}{512 \eta L_m} \Delta P \quad (6.4)$$

Here, the flow simply scales with the pore size of the surface membrane as $Q_n \propto d_S^2$ and the effect of the differences in flow resistance is greatly reduced from a single-layer design, where $Q_n \propto d_S^4$. For two hypothetical pores with diameters of 80 μm and 100 μm respectively, the flow would be 2.4 times higher for the larger pore in a single membrane device, whereas a bilayer design could reduce the discrepancy to 1.6 times higher flow through the larger pore. Therefore, a more homogeneous flow can be achieved through the use of a bilayer device.

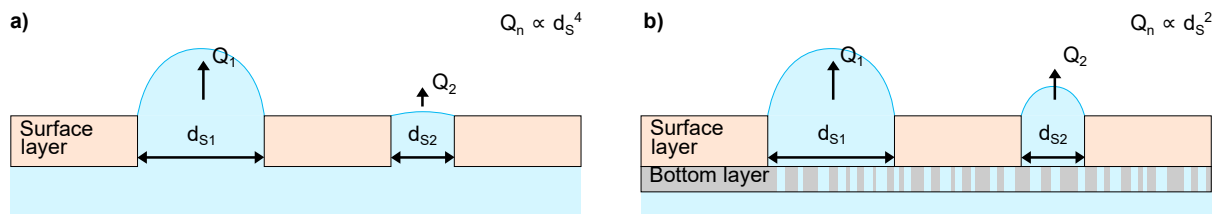


Figure 6.1: a) Flow of liquid through a single membrane with different pore sizes, d_{S1} and d_{S2} . The flow is much larger for the larger pore as $Q_n \propto d_S^4$. b) Flow of liquid through a bilayer membrane. The flow resistance is much larger in the bottom membrane and therefore the flow through the pores of the surface layer becomes less affected by the distribution of pore diameters as $Q_n \propto d_S^2$.

6.1.1 First iteration (*Paper III*)

In *Paper III*, the development of a perspiration simulator is described along with a demonstration of how adhesives can be tested on the device. Briefly, the simulator consists of a syringe pump, a sweat reservoir, and an artificial skin layer (see Fig. 6.2). The artificial skin has two components: a surface layer, which closely mimics the topography of human skin, and a track-etched membrane, which ensures homogeneous flow throughout the artificial skin even at low flow rates. The device resembles human skin in terms of roughness, sweat gland size, sweat gland density, and water contact angle. Moreover, the sweat rate and sweat composition can be adjusted according to the research needs. Human skin is soft and therefore deforms during peel, which affects the peel angle and the measured forces. A stiff substrate was therefore chosen for the model, which will minimise its energy dissipation during peel and enables to keep a constant peel angle. This way, the focus is on the adhesive and events occurring at the interface between the adhesive and the substrate. Furthermore, the substrate of choice does not hydrate significantly upon exposure to water. Therefore, the changes in surface properties during perspiration are not mimicked. Even though the simulator differs from human skin in some aspects, the setup offers well-defined and reproducible experimental conditions to test adhesives during perspiration.

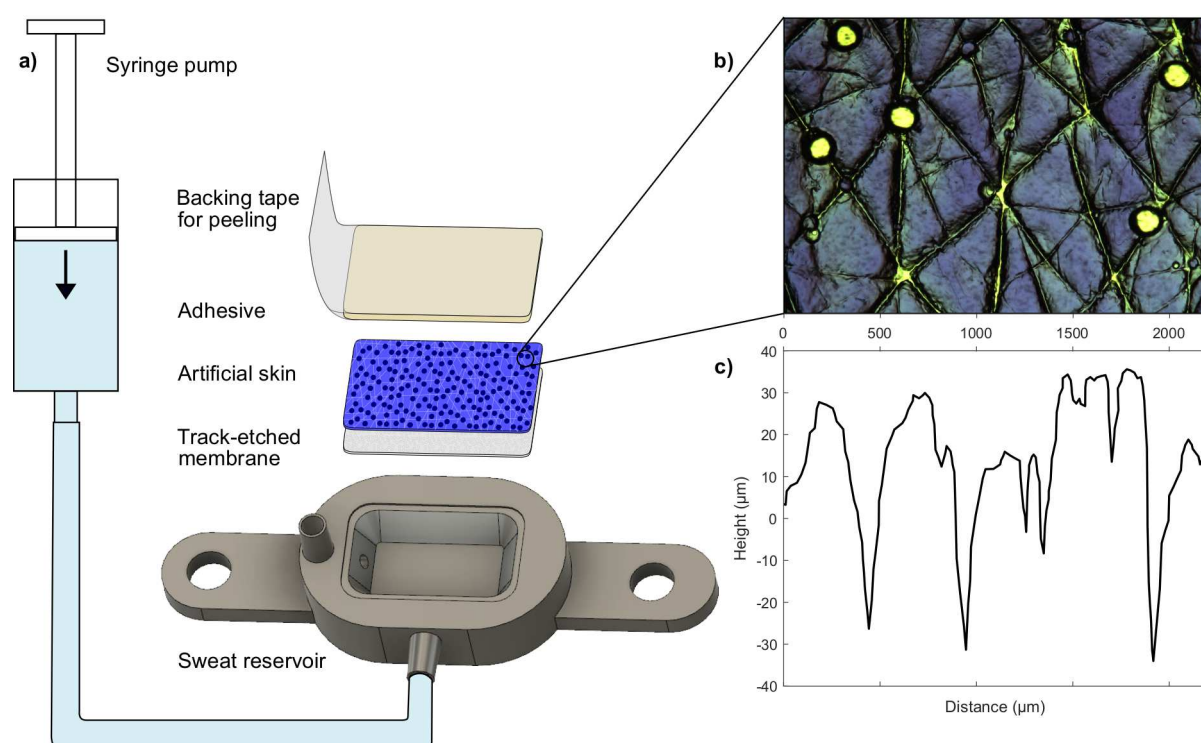


Figure 6.2: a) Schematics of the perspiration simulator: the artificial skin with dimensions of $40 \times 25 \text{ mm}^2$ is adhered to the reservoir, which is connected to the syringe pump. b) A micrograph of the artificial skin layer from the top reveals the topography of the artificial skin, which closely mimics the topography of human skin. c) A cross-section of the surface profile of the artificial skin. Figure partly adapted from [111] with permission from the *International Journal of Adhesion and Adhesives*.

Considerations for Adhesive Design

The perspiration simulator is used to evaluate the performance of skin adhesives during perspiration. At the beginning, a commercial adhesive (*Adhesive 2*) was applied to the perspiration simulator to yield an initial peel force of 0.7 N. The peel force was then found to increase over time under dry conditions because the adhesive was sufficiently soft to allow for cold flow and further contact formation after application (see Fig. 6.3). After perspiration on the simulator, however, the peel force of *Adhesive 2* increased even more than during dry conditions. From wear tests on human skin, it can be seen that a change in viscoelastic properties of the adhesives occurs upon hydration (see Fig. 3.4). Therefore, an increase in peel force after perspiration could potentially occur due to the changed viscoelastic properties of the adhesive. Here, the viscoelastic properties could have changed in a way that more contact formation is enabled over the duration of the experiment or that higher energy dissipation occurs during peel. Alternatively, specific interactions with the substrate could also cause an increase in peel force upon hydration. Naturally, the

increase in peel force after perspiration could also be the result of a combination of these phenomena (see Chapter 9 for a more detailed discussion).

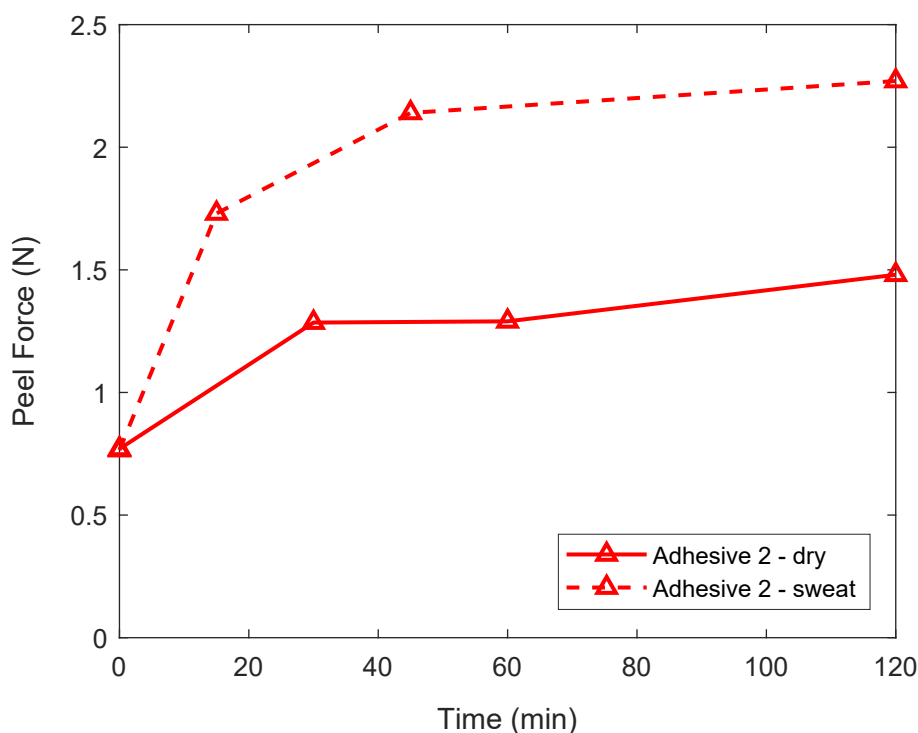


Figure 6.3: Peel force of the commercial adhesive *Adhesive 2* as a function of time in dry conditions as well as after perspiration on the perspiration simulator. The peel force of *Adhesive 2* increased after perspiration as compared to dry conditions.

Summary of *Paper III*

In *Paper III*, the competing effects of delamination and further contact formation during perspiration were decoupled through the design of the adhesives. Two model adhesives were designed to avoid cold flow under dry conditions with the addition of 40 wt.% SIS into the matrix. The role of the sweat absorption capabilities of the adhesives is then investigated. The performance of two model adhesives is determined through measurements of their peel forces after predetermined perspiration times (see Fig. 6.4a and 6.4b). Through the use of a fluorescent liquid, the movements of the liquid at the interface during perspiration are visualised and correlated with the peel forces (see schematics in Fig. 6.4c). Thereby, the peel forces are found to decrease as soon as the liquid spreads across

the interface between the artificial skin and the adhesive (see Fig. 6.4d). The spreading of liquid is prevented through the absorption of liquid into the adhesive, which allows for the maintenance of peel adhesion over a prolonged period of time.

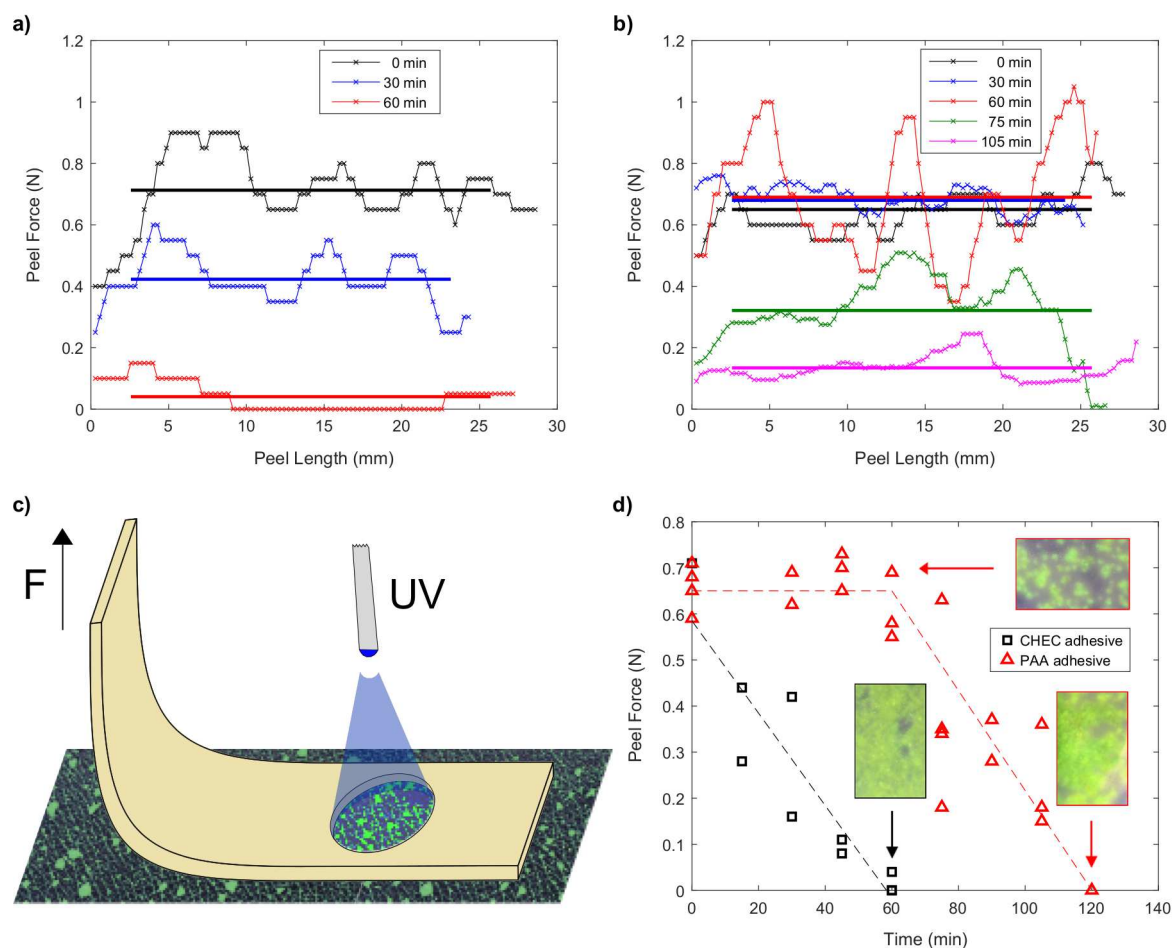


Figure 6.4: Representative peel curves after predetermined perspiration times for a) the CHEC adhesive and b) the PAA adhesive. The solid lines represent the average value of a single peel curve. c) Illustration of the experimental setup. The peel adhesion was correlated with the spreading of liquid across the interface. d) Average peel forces for the two model adhesives as a function of perspiration time. Figure partly adapted from [111] with permission from the *International Journal of Adhesion and Adhesives*.

Areas of Improvement for the Perspiration Simulator

The first iteration of the perspiration simulator brought some limitations in terms of sample size and mechanical stability. The topography of the artificial skin layer was achieved through an imprint of a skin replica. First, a two-component silicone resin was used to fabricate a mould of human skin. Then, the structure was transferred from the silicone mould to a photoresist film with a thickness of 50 μm through a lamination process. The entire process proved challenging to obtain large areas without defects in the skin structure, thus limiting the area of the artificial skin. Furthermore, the photoresist film became very brittle upon curing under UV radiation. This provided excellent stability of the skin structure, however, the stability of the thin film photoresist was impaired during peeling. At high peel forces, a delamination of the artificial skin could therefore be observed, rather than a delamination of the adhesive.

Furthermore, when sweat is supplied through a syringe pump at a controlled flow rate, a large pressure build-up may occur for occlusive adhesives. If the supplied liquid exceeds the absorption capabilities of the adhesives, the pressure inside the reservoir increases until delamination occurs. This may lead to unrealistic pressures and induce new failure modes. This is exemplified through the application of some commercial adhesives in Fig. 6.5. Here, *Adhesive 4* has lower absorption capabilities than *Adhesive 5*, which causes an increased pressure. When the bonding of *Adhesive 4* was increased by dwelling for 16 h at 75 °C, the pressure build-up in the reservoir was even higher.

6.1.2 Second iteration

In order to improve the perspiration simulator, a completely new device was developed (see illustration in Fig. 6.6a). Though, a similar approach was taken, where the artificial skin layer consisted of two components: a track-etched membrane to regulate the flow and a top membrane to mimic human skin. The dimensions of the artificial skin were increased to an area of 100 x 25 mm². To ensure good mechanical stability, a polyimide support with a thickness of approximately 400 μm was chosen for the top layer. A regular pattern of holes with a diameter of 253.1 ± 5.1 μm at a density of 100 holes/cm² was incorporated to represent the sweat glands. However, due to the enhanced mechanical stability, the human skin structure could not be imprinted. Instead, ridges with a height of 14.9 ± 0.6 μm and a width of 84.5 ± 7.3 μm were introduced on the surface between every second row of holes in order to yield a well-defined roughness pattern (see Fig. 6.6b and 6.6c). The arithmetic roughness, R_a , was calculated from the line scans, which do not include the holes. Since the holes are infinitely deep, the measured depths depend on the stylus size of the profilometer as well as its speed and therefore would yield arbitrary roughness parameters.

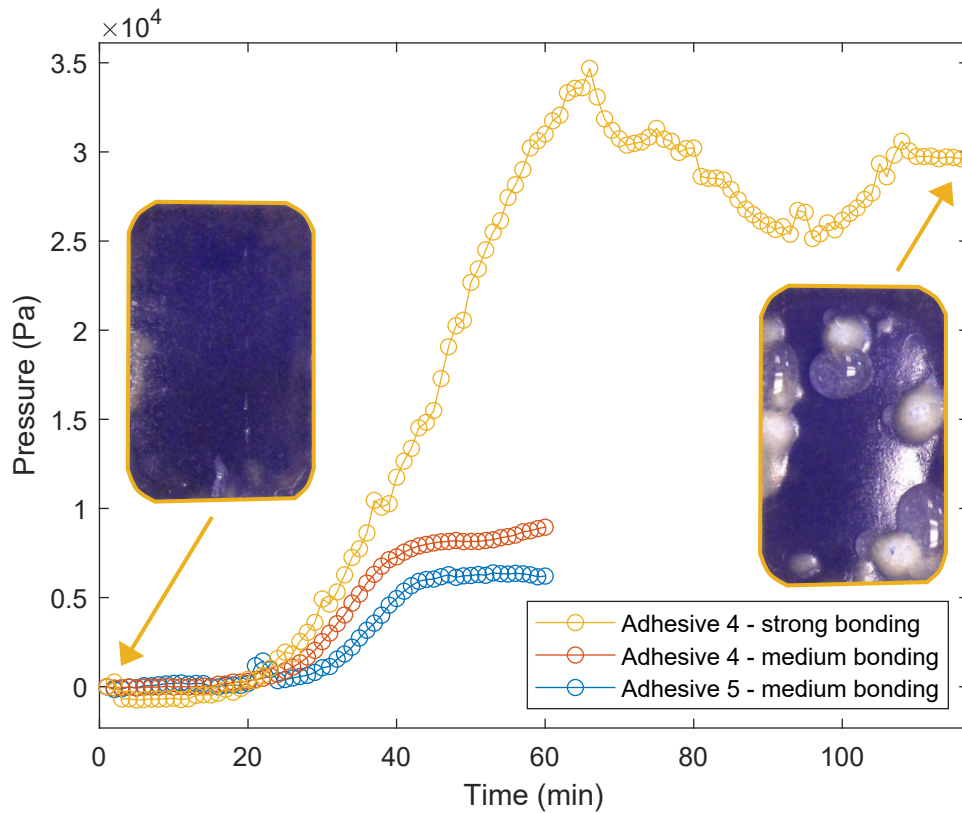


Figure 6.5: Pressure as a function of perspiration time in a flow-controlled perspiration simulator. As soon as the sweat rate exceeds the sweat uptake capabilities of the adhesives, an increase in pressure is observed until delamination occurs. Strong bonding enables higher pressure, while the absorption of liquid reduces the pressure. For strongly bonded adhesives, bubble formation and burst can be observed.

Furthermore, to resemble human skin in terms of chemistry, hydration, and wettability, the polyimide support was coated with a layer of gelatine. Here, a gelatine solution was prepared, where 25 g gelatine were dissolved in 500 mL ultrapure water under constant stirring at approximately 55 °C. After cleaning the polyimide support with ethanol and drying with compressed air, it was placed in a plasma cleaner (PDC-32G, Harrick Plasma) and treated for 10 min at 500 mTorr at high power. This process enabled the creation of radicals and ensured subsequent adhesion of the gelatine layer. Therefore, the treated polyimide support was immediately dipped into the gelatine solution with a holding time of approximately 3 s. After removal, excess solution was drained from the polyimide support by vertical hanging (20 s) and subsequent application of vacuum. This enabled further removal of excess solution and ensured that the holes in the polyimide support were not blocked by gelatine. Thereafter, the gelatine-coated substrate was dried

at room temperature before it was exposed to formaldehyde vapour for 48 h in order to cross-link the gelatine layer. Cross-linking thereby improved the mechanical stability of gelatine and minimised its solubility in water. Finally, the gelatine-coated substrates were placed in the fume hood for 24 h to allow for evaporation of remaining formaldehyde from the substrates. The coating process did not alter the roughness profile of the substrate significantly (see Fig. 6.6d and 6.6e). The height of the ridges remained at 15.9 ± 0.8 μm , while their width remained at 77.9 ± 12.8 μm . Additionally, the presence of holes was confirmed by the line scans and shows that gelatine blockage was avoided.

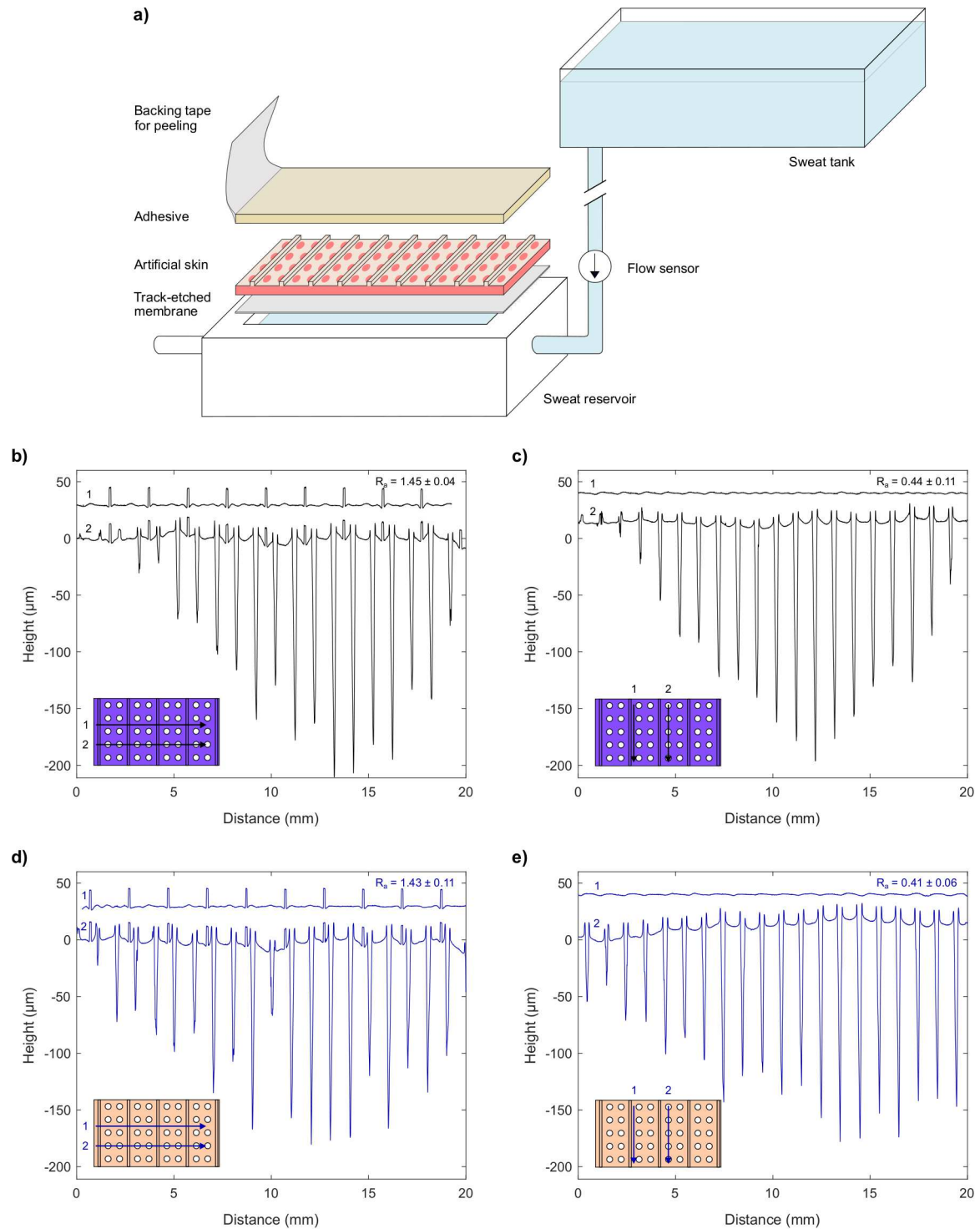


Figure 6.6: a) Schematic depiction of the perspiration simulator. b) - e) Surface profiles of the substrates for the artificial skin in two directions. Different line scans were performed to either avoid the measurement of the holes or include them. b) Surface profile of the polyimide support in an orthogonal direction to the ridges and c) parallel to the ridges. d) Surface profile of the gelatine-coated polyimide support in an orthogonal direction to the ridges and e) parallel to the ridges.

Moreover, the new version of the perspiration simulator was operated with a pressure-controlled flow. The flow rate through the artificial skin layer was regulated through the track-etched membrane such that realistic sweating pressures and rates were obtained. The flow through the artificial skin can be monitored continuously through a flow sensor (MFS3D from Elveflow). Any subsequently described experiments on the perspiration simulator were conducted on the second iteration of the device. A detailed description and further characterisation of the entire setup has been published[112]. A comparison between the characteristics of the models and human skin can be found in Tab. 6.1.

Table 6.1: Summary of perspiration simulator characteristics.

Property	Human skin	Perspiration simulator - Iteration 1	Perspiration Simulator - Iteration 2
Mechanical stability	Limited stability of human skin (stripping of cells)	Limited stability of the artificial skin	Good stability
Sample size	$\approx 2 \text{ m}^2$ [113]	40 mm x 25 mm	100 mm x 25 mm
Topography	Skin topography	Imprint of human skin	Controlled roughness
Roughness R_a	12 - 28 μm [18, 105, 106]	$12.1 \pm 1.3 \text{ }\mu\text{m}$	$1.4 \pm 0.1 \text{ }\mu\text{m}$
Water contact angle	58 - 139 $^\circ$ [16]	$69.2 \pm 3.6 \text{ }^\circ$	$97.8 \pm 0.6 \text{ }^\circ$
Sweat gland diameter	90 - 100 μm [114]	$86.8 \pm 17.5 \text{ }\mu\text{m}$	$253.1 \pm 5.1 \text{ }\mu\text{m}$
Sweat gland density	100 - 550 cm^{-2} [115]	100 cm^{-2}	100 cm^{-2}
Sweat rate	$< 1 - 20 \text{ nL/gland/min}$ [107, 108]	Can be tuned according to research needs	Can be tuned according to research needs
Sweat pressure	1.8 - 5.6 kPa [116]		
Sweat composition	Variable electrolyte compositions [109]		

In order to illustrate the working principles of the bilayer setup, an experiment has been performed on the perspiration simulator (iteration 2), where parts of the sweat pores were blocked by an occlusive tape. For a given sweating pressure of 3.8 kPa, the flow rates were then monitored as a function of sweat pore coverage (see Fig. 6.7a). While 75 % of the area were covered by the occlusive tape, a flow rate of 7.3 $\mu\text{L}/\text{min}$ was observed. Removing parts of the occlusive tape, such that only approx. 50 % of the area were covered, resulted in an increase of the flow rate to approx. 13.4 $\mu\text{L}/\text{min}$. Upon entire removal of the tape, the flow rate increased to approx. 23.1 $\mu\text{L}/\text{min}$. This shows that the total flow rate through the perspiration simulator is proportional to the area of unoccluded sweat pores (see Fig. 6.7b). As explained in section 6.1, the pressure drop within the bottom membrane is much higher than the pressure drop within the surface layer, which means that the flow through the individual sweat pores is unaffected by the flow through the rest of the sweat pores.

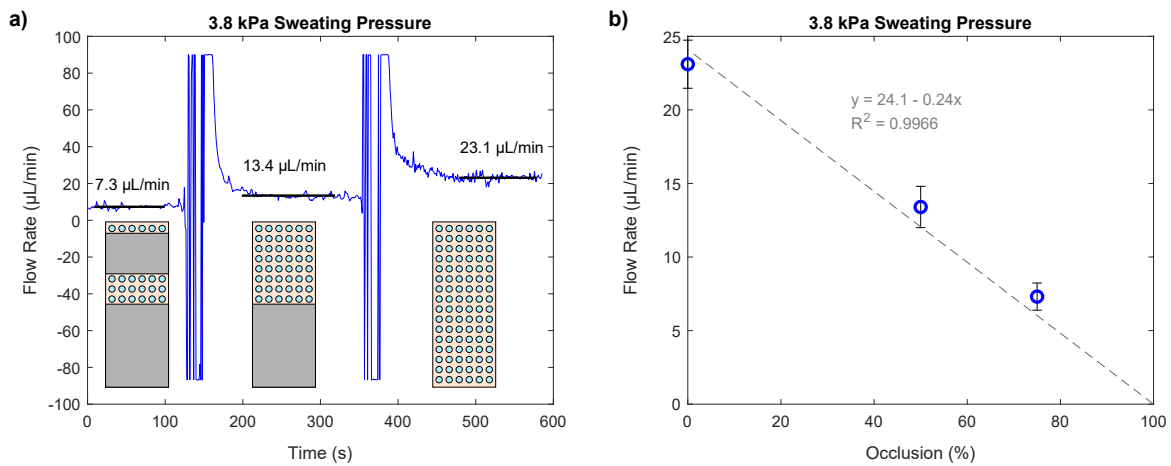


Figure 6.7: a) The flow rate through the perspiration simulator was monitored while 75, 50, and 0 % of the sweat pores were occluded. b) The flow rate was found to scale with the area of unoccluded sweat pores, which illustrates the working principle of the track-etched membrane.

6.2 Adhesive Performance Testing

6.2.1 The Impact of the Viscoelastic Properties and Sweat Absorption Capabilities (*Paper IV*)

In *Paper IV* the performance of four different adhesive compositions is reported during perspiration on the perspiration simulator. The compositions were designed such that the role of the viscoelastic properties and sweat absorption capabilities of the adhesives could be decoupled. The adhesive matrix consisted of a blend containing 80 wt.% and 20 wt.% SIS in all cases. The viscoelastic properties of the adhesives were controlled through the total volume fractions of particles, while the sweat absorption capabilities were limited by the weight fraction of absorbing particles. Particles based on poly(acrylic acid) were used as the absorbing species, while non-absorbing potato starch particles were added to adjust the viscoelastic properties. Non-absorbing adhesives were found to readily lose adhesion after perspiration on the perspiration simulator (see Fig. 6.8a). The failure mode shifted from a cohesively dominated break in the dry conditions to a complete adhesive break after perspiration. Different failure mechanisms were observed depending on the combination of the viscoelastic properties of the adhesive and the applied sweating pressure. Viscoelastic flow was observed in soft adhesives (Pot-12) upon perspiration, which resulted in cavity formation and growth thereby reducing the interfacial contact area of the adhesive (see schematics in Fig. 6.8a). On the other hand, an elastic detachment without the formation of cavities occurred for sufficiently stiff adhesives (Pot-27). Viscoelastic flow provides a means for energy dissipation within the adhesives, thusly relieving parts of the pressure from the interface. In *Paper IV*, indications were discussed that the occurrence of viscoelastic flow may enable prolonged adhesion during perspiration.

The introduction of absorbing fillers into the adhesives (PAA-12 and PAAPot-27) led to a maintenance of peel forces over a prolonged period of time during perspiration (see Fig. 6.8b). Here, the absorption of sweat into the bulk of the adhesives appeared to have relieved some of the pressure from the interface and therefore enabled to retain adhesion. However, in contrast to the non-absorbing adhesives, the failure mode of the absorbing adhesives was cohesively dominated after perspiration. Particle swelling within the adhesives thereby weakened the material and caused a loss in cohesive strength (see schematics in Fig. 6.8b). These findings demonstrate the important considerations for the design of adhesive formulations to withstand perspiration over a prolonged period of time.

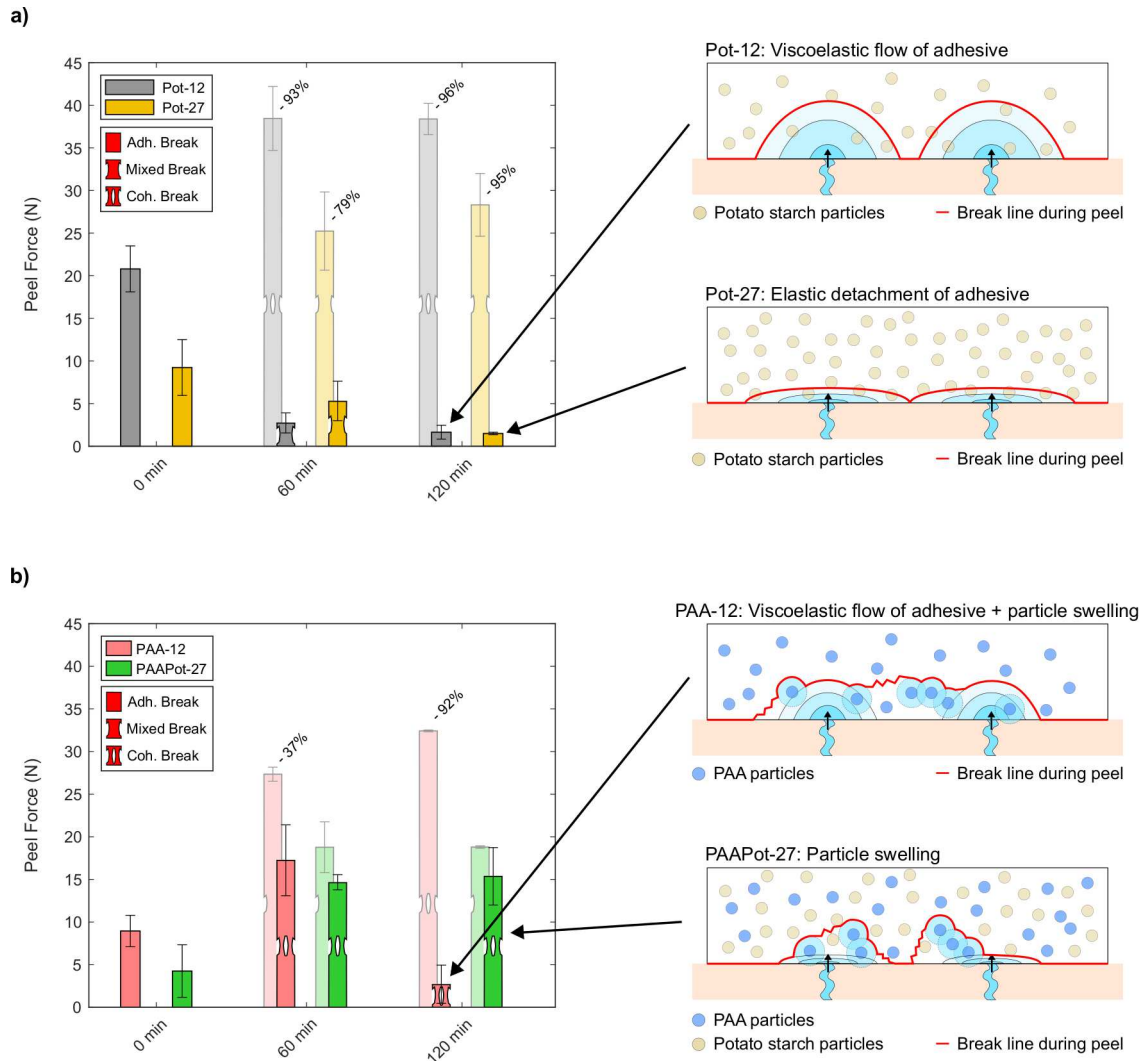


Figure 6.8: a) The peel forces for non-absorbing adhesives decrease readily upon perspiration at a pressure of 3 kPa on the perspiration simulator. Viscoelastic flow of the soft adhesive (Pot-12) led to cavity formation and growth, which resulted in a reduced contact area and a loss of adhesion. On the other hand, the stiff adhesive (Pot-27) detached elastically without the formation of cavities. b) The peel forces of absorbing adhesives (PAA-12 and PAAPot-27) remain moderately high during perspiration. Sweat absorption acts as a pressure relief from the interface and therefore promotes adhesion. However, the swelling of particles leads to a weakening of the bulk properties, which results in cohesive failure after perspiration.

6.2.2 Excessive Absorption of Sweat

In addition to the adhesives tested in *Paper IV*, another formulation was evaluated on the perspiration simulator. The same procedures were employed throughout the perspiration

experiments in order to ensure that the results could be directly compared. Since the ability to absorb sweat was found to benefit the maintenance of adhesion during perspiration, an adhesive with even higher absorption capabilities was designed. In order to achieve similar viscoelastic properties to the adhesives in *Paper IV*, an adhesive with PAA particles at a volume fraction of $\phi = 0.27$ was fabricated (PAA-27). The design of the adhesives is illustrated schematically in Fig. 6.9 and a summary of the formulations can be found in Tab. 6.2.

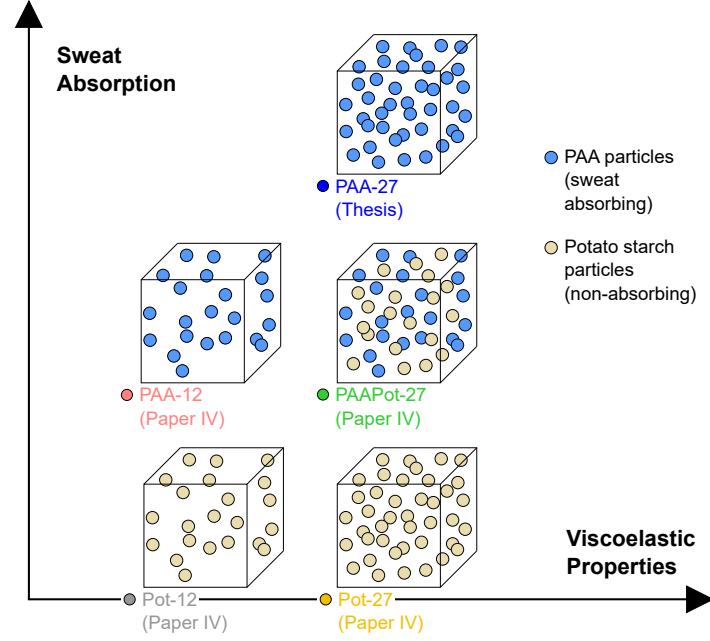


Figure 6.9: Schematic illustration of the design of adhesives to be tested on the perspiration simulator. To isolate the role of viscoelastic properties and sweat absorption capabilities during perspiration, adhesives were designed to vary in only one parameter at a time.

Table 6.2: Summary of the adhesive compositions tested on the perspiration simulator.

Composite name	Particles	Weight fraction w (-)	Total volume fraction ϕ (-)	Publication
Pot-12	Pot	0.19	0.12	<i>Paper IV</i>
PAA-12	PAA	0.20	0.12	<i>Paper IV</i>
PAAPot-27	PAA + Pot	0.20 + 0.19	0.27	<i>Paper IV</i>
Pot-27	Pot	0.38	0.27	<i>Paper IV</i>
PAA-27	PAA	0.40	0.27	Thesis

The new adhesive formulation PAA-27 was compared to PAAPot-27 and Pot-27 from *Paper IV* under the same experimental conditions. PAAPot-27 and Pot-27 were chosen as reference adhesives due to the similar viscoelastic properties. In the immersion test, PAA-27 showed higher uptake of artificial sweat than the reference adhesives as the loading of absorbing PAA particles was higher (see Fig. 6.10a). However, the viscoelastic properties of the three adhesives were almost indistinguishable, which also led to similar peel forces in dry conditions (see Fig. 6.10b - d).

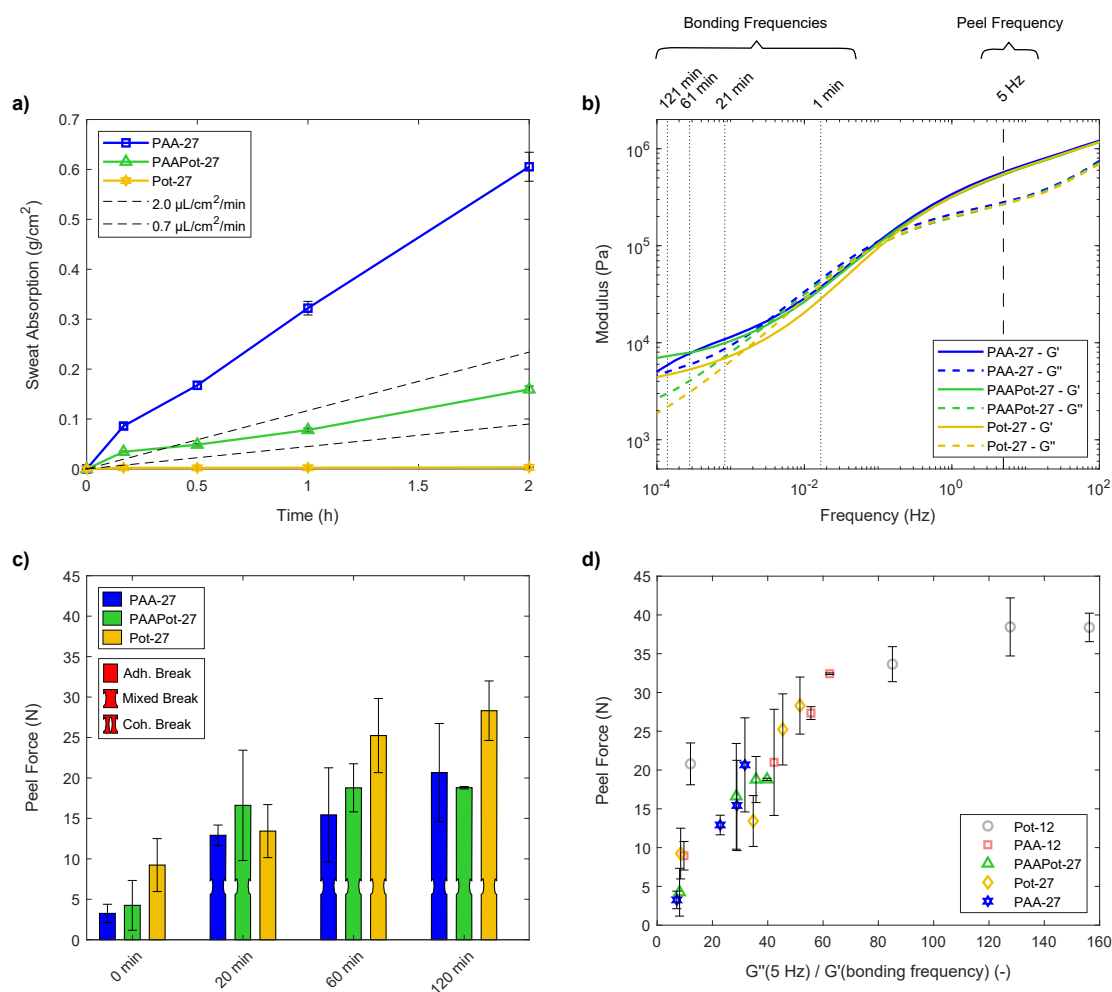


Figure 6.10: Characterisation of the adhesive formulations. a) Weight uptake upon full immersion in artificial sweat (0.154 M NaCl solution). PAA-27 showed the highest sweat uptake due to high loading of PAA particles. b) Rheological frequency sweep experiments revealed similar viscoelastic properties for PAA-27, PAAPot-27, and Pot-27. c) Peel forces from the artificial skin under dry conditions. In line with the expectation from rheology, similar peel forces were observed for PAA-27, PAAPot-27, and Pot-27. d) Correlation of the measured peel forces with the viscoelastic properties of the adhesives.

To evaluate the performance of PAA-27 during perspiration, the adhesive was tested on the perspiration simulator at two distinct sweating pressures of 3 kPa and 6 kPa. PAA-27 showed similar mechanical strength as Pot-27, which means that viscoelastic flow is unlikely to occur at a sweating pressure of 3 kPa. During perspiration at 3 kPa, PAA-27 experienced higher sweat flow rates than PAAPot-27 and Pot-27, likely because of its higher sweat absorption capabilities (see Fig. 6.11a). While the peel forces of PAA-27 were higher than the peel forces of Pot-27, no significant deviations were observed between PAA-27 and PAAPot-27 (see Fig. 6.11b). However, compared to the dry peel forces after 120 min, a larger reduction was observed for PAA-27 than for PAAPot-27 (reduction of 45 % and 18 %, respectively). Possibly, this could have been caused by an increased absorption of sweat, which weakened the adhesive to a larger extent. Both absorbing adhesives exhibited a cohesively dominated failure mode as the swelling of particles weakened the adhesives. Altogether, at a low sweating pressure of 3 kPa, higher sweat absorption capabilities did not improve the performance of the adhesive. Instead, higher absorption of sweat may have adverse effects on the integrity of the adhesive.

At an increased sweating pressure of 6 kPa, all adhesives exhibited the same sweat flow rate (see Fig. 6.11c) even though their sweat absorption capabilities were different. The peel forces of PAA-27, PAAPot-27, and Pot-27 were similar after 20 min and 60 min, respectively, and remained moderately high (see Fig. 6.11d). Compared to the dry peel forces after 60 min, however, a larger reduction was observed for Pot-27 than for PAAPot-27 and PAA-27 (reduction of 54 %, 36 %, and 36 %, respectively). This further demonstrates the benefits of sweat absorption during perspiration to maintain the peel adhesion of skin adhesives. On the other hand, the absorption of sweat into the adhesive was found to weaken its integrity as indicated by the cohesively dominated failure upon hydration.

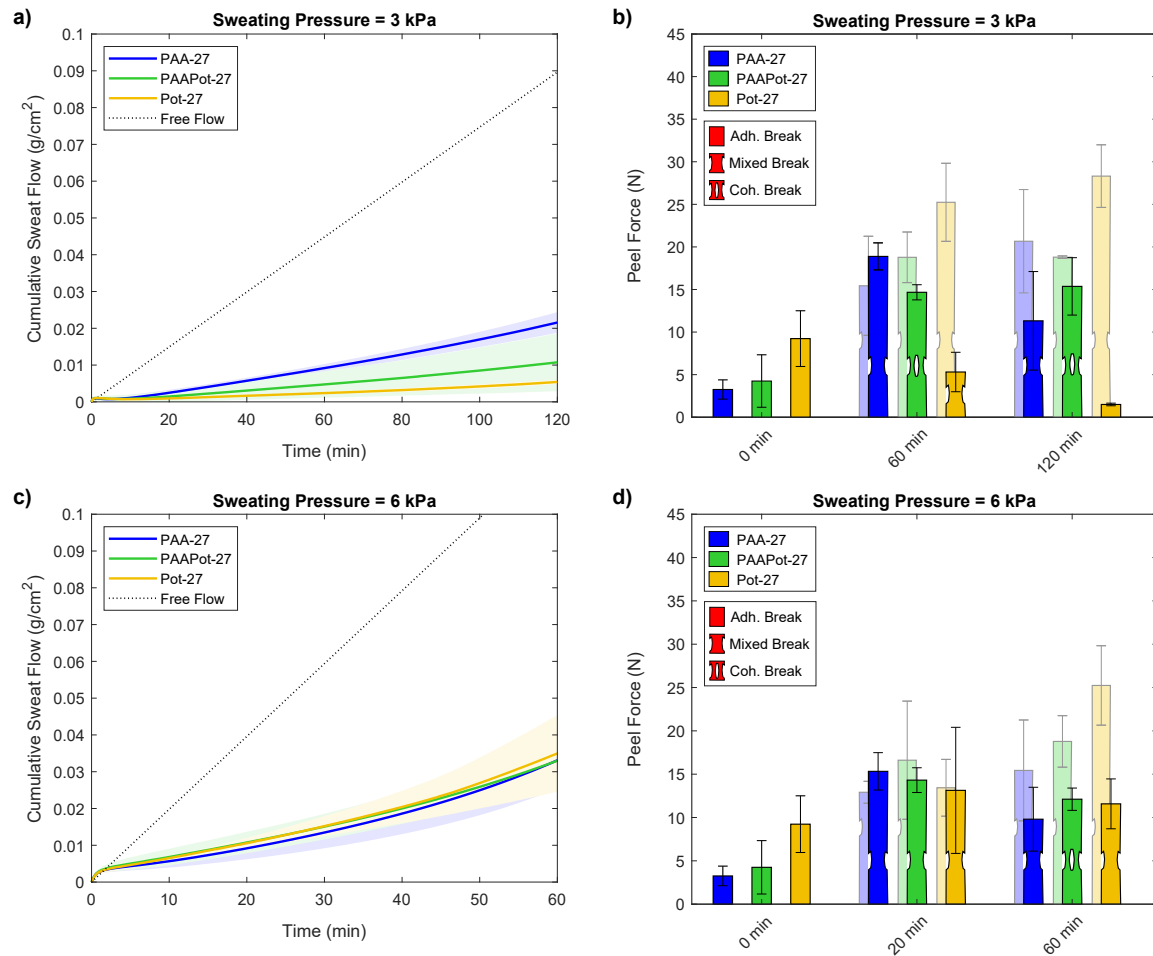


Figure 6.11: a) The cumulative sweat flow at a perspiration pressure of 3 kPa increases with increasing sweat absorption capabilities. b) The peel forces after perspiration at a pressure of 3 kPa remain higher for the absorbing adhesives PAA-27 and PAAPot-27. c) The cumulative sweat flow at a perspiration pressure of 6 kPa was indistinguishable for all adhesives, regardless of their sweat absorption capabilities. d) The peel forces after perspiration at a pressure of 6 kPa show a smaller decrease for the absorbing adhesives PAA-27 and PAAPot-27.

6.3 Comparison with Adhesive Behaviour on Human Skin

I have worn the adhesives in Fig. 6.9 on my forearm in order to make a qualitative comparison with the results obtained on the perspiration simulator. The study was carried out sporadically over a period of 3 months, where adhesives were peeled from my left and right forearm in dry conditions as well as after exercise (approximately 30 min bike ride). The average peel forces of 3 measurements and their standard deviation are shown in Fig.

6.12a. The large error bars indicate the difficulty of peel experiments from human skin, even on one individual subject. Thereby, changes in the skin conditions (e.g. hydration, mechanical properties, or roughness), sweating intensity, physical movements, environmental conditions, and adhesive homogeneity are among the factors that are responsible for the deviations.

Nevertheless, some qualitative statements and comparisons can be extracted. In the dry state, all adhesives exhibited high peel forces and stripped the skin (skin structure was found on the adhesives after peel and their tack was lost). This implies that the dry peel forces (shaded bars in Fig. 6.12a) are a measure of the cohesive strength of the skin rather than the adhesion of the adhesives.

6.3.1 Non-Absorbing Adhesives

The non-absorbing adhesives (Pot-12 and Pot-27) exhibited a drastic decrease in their peel forces after exercise, which is consistent with the observations on the perspiration simulator. The decrease in peel forces can be readily observed during peeling (see Fig. 6.12b and 6.12c) and is associated with the occurrence of sweat at the interface between the skin and the adhesive.

Micrographs of Pot-12 after peeling reveal the transfer of a skin layer to the adhesive due to strong adhesion in the dry state (see Fig. 6.12d). After exercise, circular features appeared on the adhesive among the previously observed skin structures (see Fig. 6.12e). A topographical line scan of the surface showed that the circular features extended into the adhesive (see Fig. 6.12f). Consistent with the findings from the perspiration simulator, viscoelastic flow and cavity formation have occurred and adhesive failure was observed around the sweat pores (see Fig. 6.12g).

The adhesion of Pot-27 was also sufficiently high to cause a stripping of the skin in the dry state (see Fig. 6.12h). While circular features also occurred after exercise, the topography of the surface was comparatively flat (see Fig. 6.12i and 6.12j). In this case, the adhesive failed without any notable occurrence of viscoelastic flow and cavity formation (see Fig. 6.12k). Instead, adhesive failure occurred due to elastic detachment, which has also been observed on the perspiration simulator.

6.3.2 Absorbing Adhesives

The absorbing adhesives (PAA-12, PAAPot-27, and PAA-27) showed considerably higher peel forces after exercise than the non-absorbing adhesives (see Fig. 6.12a). A cohesively dominated failure of the absorbing adhesives was observed after perspiration on human

skin as well as on the perspiration simulator. On the perspiration simulator, PAAPot-27 and PAA-27 showed similar performance, which was better than PAA-12. However, among the absorbing adhesives, PAAPot-27 showed the poorest performance during the *in vivo* study. Due to the large error bars, no significant differences could be observed between the absorbing adhesives after exercise. The discrepancies may simply have occurred due to the lack of control over sweat rate and exercise intensity during exercise. Nevertheless, an attempt is made to explain the adhesive-specific performance in the following paragraphs.

The discrepancy between PAA-12 and PAAPot-27 may have occurred due to the viscoelastic properties of the adhesives. During the *in vivo* study, physical movements may have constantly interrupted the skin-adhesive interface. Since soft adhesives are able to re-fill the crevices of the skin at a faster rate than stiff adhesives, the loss in peel force may be smaller for PAA-12 than PAAPot-27. In line with the hypothesis, a minutely higher peel force after exercise was also observed for Pot-12 than Pot-27 (see Fig. 6.12a).

The discrepancy between PAA-27 and PAAPot-27 may have occurred due to the sweat absorption capabilities of the adhesives. If the premise is accepted that local delamination of the adhesives may occur due to physical movements during exercise, the stiff adhesives would behave less occlusive than expected from the perspiration simulator. Areas of the skin, where the adhesives have locally delaminated may fill with sweat. A highly absorbing adhesive (such as PAA-27) would then be able to remove excess sweat faster and re-establish the contact area[112].

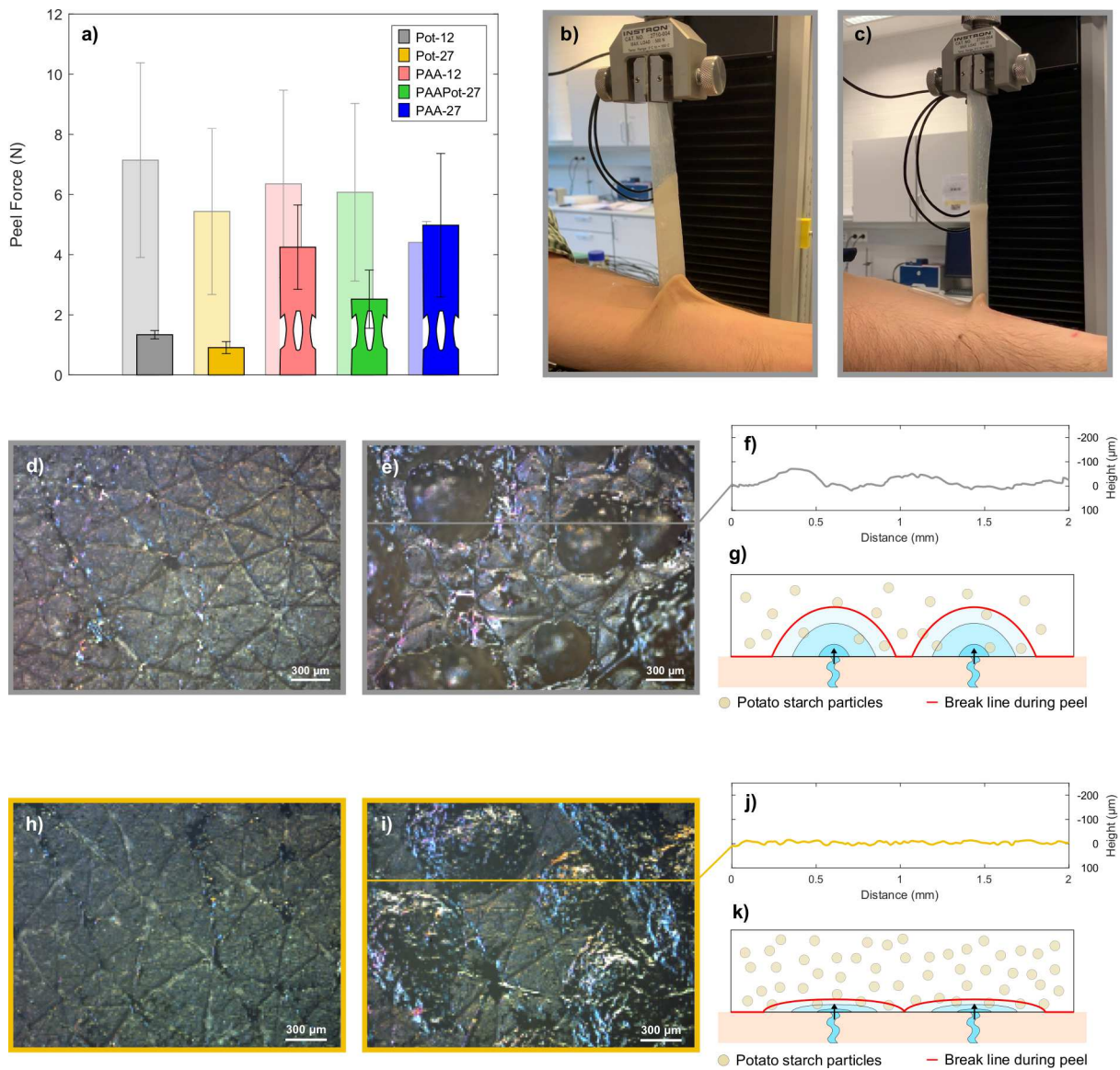


Figure 6.12: Results of the *in vivo* study. a) Peel forces of the adhesives under dry conditions (shaded bars) as well as after exercise (full bars). b) Image of Pot-12 during peel from dry skin. c) Image of Pot-12 during peel after exercise. d) Micrograph of Pot-12 after peel from dry skin. e) Micrograph of Pot-12 after peel from sweating skin. f) Topographical line scan of Pot-12 after peel from sweating skin. g) Schematic illustration of the failure mechanism of Pot-12. h) Micrograph of Pot-27 after peel from dry skin. i) Micrograph of Pot-27 after peel from sweating skin. j) Topographical line scan of Pot-27 after peel from sweating skin. k) Schematic illustration of the failure mechanism of Pot-27.

6.4 Key Conclusions

- The perspiration simulator is a simplification of human perspiration and mimics human skin in some key properties
- The perspiration simulator presents a well-defined and reproducible experimental setup for testing adhesives during perspiration
- Depending on the combination of the viscoelastic properties of the adhesive and the pressure exerted by the sweat glands during perspiration, different failure mechanisms may be observed.
 - If the perspiration pressure overcomes the mechanical strength of the adhesive, viscoelastic may occur, which can lead to cavity formation and growth.
 - If the mechanical strength of the adhesive exceeds the perspiration pressure, no notable viscoelastic flow occurs.
- Absorption of sweat may relieve the pressure from the interface and thus enable adhesion over a prolonged period
- Absorption of sweat into the adhesive weakens its integrity, which may lead to cohesive failure during peel
- A balance between the absorption capabilities and the viscoelastic properties is required

7 New Skin Adhesive Formulations with Prolonged Resistance to Perspiration

From the evaluation of skin adhesives on the perspiration simulator, it became evident that the absorption of sweat is beneficial for adhesion but detrimental for cohesion. Especially after the absorption of sweat, cohesive failure was dominant during the peel experiments. Therefore, new adhesive formulations are designed with the aim to maintain peel forces as well as their integrity during perspiration. Thereby, the peel adhesion will be maximised for one formulation, while another formulation is designed to avoid skin damage through a moderation of its peel adhesion. The new formulations will be realised through an increase in SIS content in the matrix, which will limit the swelling of the individual particles as well as the resulting peel forces. The performance of the new adhesive formulations will be compared to PAAPot-27, which was the best performing adhesive in Chapter 6, as well as a commercial adhesive (*Adhesive 2*).

7.1 Design of New Skin Adhesive Formulations

7.1.1 Tuning the Polymer Matrix

The addition of SIS to PIB changes the viscoelastic properties of the matrix and increases the mechanical strength. Matrices containing 20 wt.% SIS and 40 wt.% SIS respectively had been analysed through rheological frequency sweep experiments in *Paper II*. With the increase in SIS content, the storage modulus as well as the loss modulus increase at frequencies below approximately 1 Hz (— and — in Fig. 7.1). Since the elastic component has a larger increase than the viscous component, the loss tangent decreases and the matrix behaves more elastically. However, the addition of 40 wt.% SIS to the matrix will have dramatic effects on the bonding of the adhesive and peel forces will be strongly compromised. Therefore, the addition of 25 wt.% SIS and 30 wt.% SIS was considered instead for the new adhesive formulations. Here, only a moderate increase in the moduli was observed at frequencies below approximately 1 Hz (see — and — in Fig. 7.1).

In Chapter 5, the mechanism of sweat absorption and transport within skin adhesives was investigated and in the following the learnings from *Paper II* will be implemented.

Upon exposure to artificial sweat (0.154 M NaCl solution), the PAA particles were found to exert an average swelling pressure of approximately 4.5 kPa. This constant stress then caused different swelling rates of the particles depending on the viscoelastic properties of the matrix. More specifically, the magnitude of the loss modulus determined the swelling rates. Accordingly, the frequencies of the polymer matrices in Fig. 7.1 were extracted when the loss modulus corresponded to 4.5 kPa ($f(G'' = 4.5 \text{ kPa})$). These frequencies are summarised in Tab. 7.1 and converted into the swelling rates.

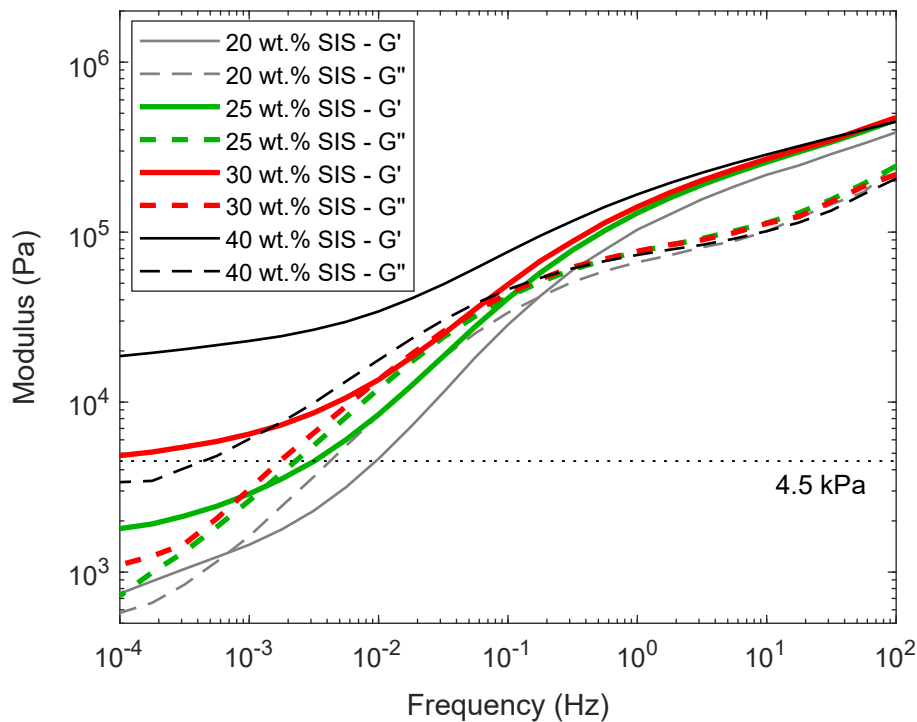


Figure 7.1: Viscoelastic properties of the polymer matrices with different SIS content. The swelling pressure of the PAA particles is indicated at 4.5 kPa.

A critical particle loading is necessary in order to observe absorption of sweat (and no absorption is observed below this loading). The critical particle loading therefore represents the intersect with the x-axis of the particle swelling rate (determined from the viscoelastic properties of the polymer matrices). In *Paper II*, the critical weight fractions for matrices containing 20 wt.% SIS and 40 wt.% SIS were determined as 0.13 and 0.21 respectively. Through linear interpolation, the critical weight fractions for the matrices containing 25 wt.% SIS and 30 wt.% were estimated and summarised in Tab. 7.1. This way, the sweat absorption capabilities of the new adhesive formulations could be estimated (see Fig. 7.2).

Table 7.1: Summary of the parameters used to estimate the sweat absorption capabilities of the new adhesive formulations.

SIS content in matrix (wt.%)	$f(G'' = 4.5 \text{ kPa})$ (s^{-1})	Swelling rate (h^{-1})	Critical particle weight fraction (-)
20	0.0035	12.5	0.13
25	0.0026	9.2	0.15 (interpolated)
30	0.0018	6.5	0.17 (interpolated)
40	0.0012	4.2	0.21

7.1.2 Tuning the Particle Loading

In Chapter 6, it was concluded that moderate sweat absorption capabilities are sufficient for stiff adhesives to enable prolonged adhesion during perspiration. Here, the adhesives PAAPot-27 and PAA-27 did not show any significant differences in terms of their performance during perspiration (see Fig. 6.11). However, both adhesives performed significantly better than the non-absorbing adhesive Pot-27. For the design of new skin adhesive formulations, the swelling rates within the adhesive PAAPot-27 were therefore deemed sufficient (\circ in Fig. 7.2). To achieve a similar swelling rate in the matrix containing 25 wt.% SIS, the addition of PAA particles at a weight fraction $w = 0.27$ is necessary ($+$ in Fig. 7.2). On the other hand, particles were added at a weight fraction $w = 0.37$ to the polymer matrix containing 30 wt.% SIS ($+$ in Fig. 7.2) in order to achieve sweat absorption comparable to *Adhesive 2*. A summary of the new formulations can be found in Tab. 7.2.

Table 7.2: Summary of the new skin adhesive formulations for prolonged resistance to perspiration.

Composite name	SIS content in matrix (wt.%)	Particles	Weight fraction w (-)	Volume fraction ϕ (-)
SIS-25PAA-17	25	PAA	0.27	0.17
SIS-30PAA-24	30	PAA	0.37	0.24

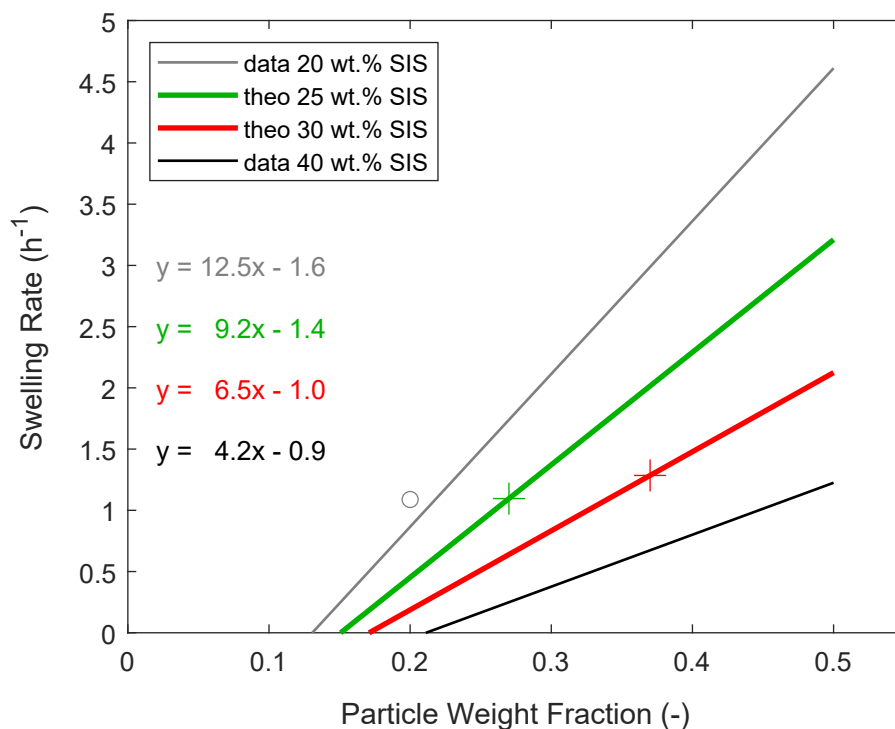


Figure 7.2: Swelling rates in 0.154 M NaCl solution as a function of the particle weight fraction in polymer matrices with different SIS content. Data for the matrices containing 20 wt.% SIS and 40 wt.% SIS was obtained experimentally. The curves for matrices containing 25 wt.% SIS and 30 wt.% SIS were deduced from their viscoelastic properties. \circ , $+$, and $+$ indicate the particle weight fractions, which yield the desired swelling rates within the respective matrices.

7.2 Performance of New Skin Adhesive Formulations

7.2.1 Characterisation of New Skin Adhesive Formulations

The new skin adhesive formulations were characterised in terms of their sweat absorption capabilities, viscoelastic properties, and peel forces in dry conditions. Upon immersion in 0.154 M NaCl solution, SIS25-PAA17 exhibited similar sweat absorption capabilities as PAAPot-27 (see Fig. 7.3a). Here, the restricted swelling and the increase in the concentration of absorbing particles were balanced successfully to obtain an adhesive formulation with comparable sweat absorption properties. On the other hand, SIS30-PAA24 showed an increased sweat absorption during immersion, which was comparable to *Adhesive 2*.

In terms of their viscoelastic properties, SIS25-PAA17 and PAAPot-27 were also very

similar (see Fig. 7.3b). The increase in the stiffness of the matrix was balanced with a decrease in the total particle loading. As expected, SIS30-PAA24 showed an increase in the moduli at low frequencies (< 0.01 Hz) due to the increased SIS content and the comparable total particle content. However, unexpectedly a decrease in moduli at higher frequencies (> 0.1 Hz) was observed for SIS30-PAA24.

The decreased loss modulus at the peel frequency and increased storage modulus at the bonding frequency of SIS30-PAA24 also notably affected its peel forces in dry conditions (see Fig. 7.3c and 7.3d). Only *Adhesive 2* had even lower peel forces due to its increased storage modulus. Since SIS25-PAA17 and PAAPot-27 exhibited similar viscoelastic properties, their peel forces are indistinguishable in dry conditions. Noteworthy, SIS25-PAA17 and SIS30-PAA24 exhibited adhesive failure in all cases.

7.2.2 Peel Adhesion of New Skin Adhesive Formulations on Perspiration Simulator

The performance of the new skin adhesive formulations was evaluated through the use of the perspiration simulator. The experiments were performed in a similar manner as described in Chapter 6 such that the results can be directly compared.

Formulation with Maximised Adhesion

The new skin adhesive formulation with maximised adhesion (SIS25-PAA17) was evaluated on the perspiration simulator at sweating pressures of 3 kPa and 6 kPa. Two-sample t-tests were performed with a significance level of 0.05 in order to evaluate changes in the peel forces in dry conditions and after perspiration. Since the viscoelastic properties as well as sweat absorption capabilities of SIS25-PAA17 were similar to PAAPot-27, a similar performance was observed for both adhesives during perspiration (see Fig. 7.4a - d). Only after 60 min of perspiration at 6 kPa, the difference in peel forces between the adhesives was statistically significant. At this point, a reduction of the peel force as compared to dry conditions of 61 % was found for SIS25-PAA17, while PAAPot-27 only exhibited a reduction of 36 %. Even though a large reduction was observed for SIS25-PAA17, its peel force was still considered high (8.5 N) after 60 min of perspiration at 6 kPa (representing extreme sweating in humans[116]).

Importantly, the failure mode of SIS25-PAA17 was adhesive in all cases, also after perspiration. Therefore, the swelling of the particles was restricted sufficiently through the increase in SIS content such that cohesive failure was avoided during perspiration.

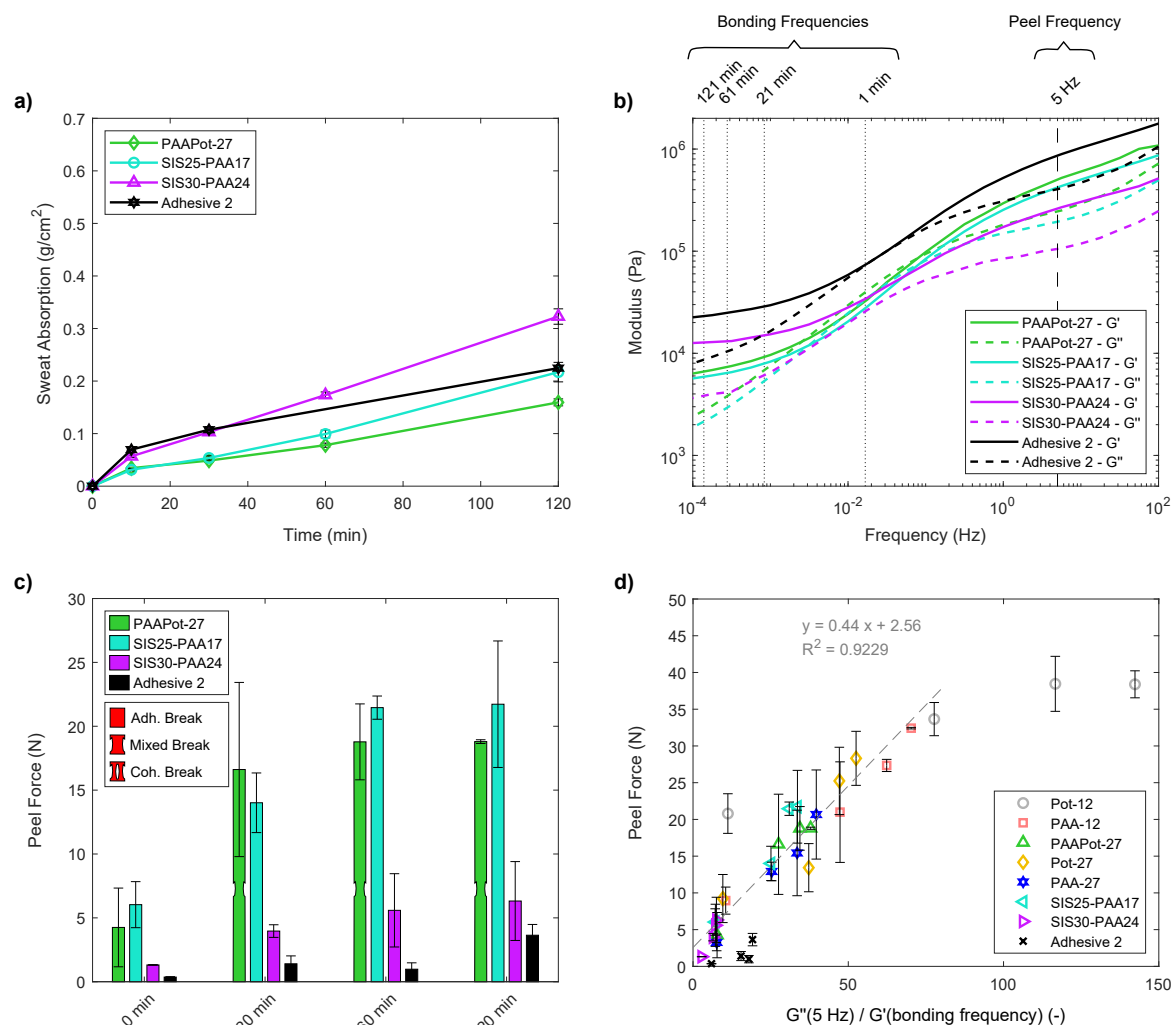


Figure 7.3: Characterisation of the new skin adhesive formulations. a) In the immersion test, similar uptake of artificial sweat is observed for SIS25-PAA17 and PAAPot-27, while SIS30-PAA24 and *Adhesive 2* show an increased uptake. b) Rheological frequency sweep experiments show that similar viscoelastic properties are observed for SIS25-PAA17 and PAAPot-27. While SIS30-PAA24 showed higher moduli at high frequencies, a decrease in moduli occurred at high frequencies. *Adhesive 2* showed the highest moduli at all frequencies. c) The peel forces on the artificial skin under dry conditions increased over time as more contact area was established during dwell. SIS25-PAA17 and PAAPot-27 showed similar peel forces at all times, while SIS30-PAA24 and *Adhesive 2* showed lower peel forces. d) Correlation of the peel forces with the viscoelastic properties of the adhesives at the respective bonding times.

7.2. Performance of New Skin Adhesive Formulations

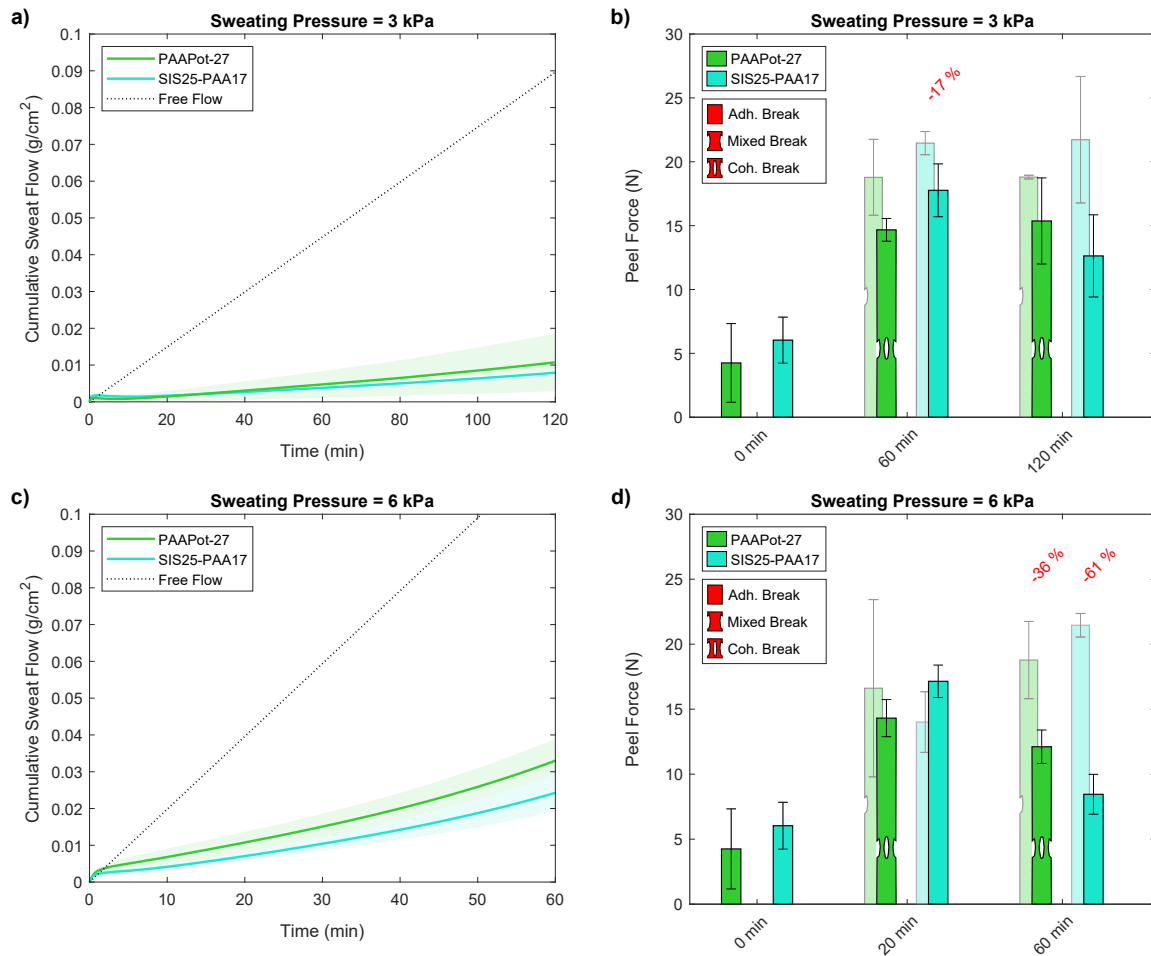


Figure 7.4: a) The cumulative sweat flow at a perspiration pressure of 3 kPa. b) The peel forces after perspiration at a pressure of 3 kPa. Dry peel forces are presented as the shaded bars and a reduction in peel force is indicated when the difference is statistically significant. c) The cumulative sweat flow at a perspiration pressure of 6 kPa. d) The peel forces after perspiration at a pressure of 6 kPa. Dry peel forces are presented as the shaded bars and a reduction in peel force is indicated when the difference is statistically significant.

Formulation with Moderate Adhesion (Skin-Friendly)

SIS30-PAA24 was designed as a more skin-friendly adhesive with moderate peel forces. Therefore, its performance was compared to a commercial adhesive (*Adhesive 2*) under the same experimental conditions as the previous studies on the perspiration simulator. The cumulative sweat flow during perspiration and the peel forces after perspiration are shown in Fig. 7.5a - d. Since the initial adhesion of *Adhesive 2* was very low (approximately 0.4 N peel force), sweat was readily able to penetrate the interface and the sweat flow rate was close to the free flow rate in all cases. Therefore, *Adhesive 2* also showed a poor peel performance after perspiration with peel forces below 2 N in all cases.

On the other hand, SIS30-PAA24 had a slightly higher initial peel adhesion (approximately 1.3 N) and is able to limit sweat flow at 3 kPa as well as 6 kPa (see Fig. 7.5a and 7.5c). The resulting peel forces after perspiration are not significantly reduced as compared to the dry peel forces (see Fig. 7.5b and 7.5d). On the contrary, the peel force even showed a significant increase after 20 min of perspiration at 6 kPa. A small but not significant increase in peel forces was also observed after 120 min of perspiration at 3 kPa. The cumulative sweat flows at the respective perspiration conditions were approximately 0.010 g/cm² and 0.009 g/cm². Such a limited amount of sweat at the interface or within the adhesive may have caused an increase in peel force due to a change in the viscoelastic properties or the occurrence of specific interactions with the substrate (see Chapter 9 for a more detailed discussion).

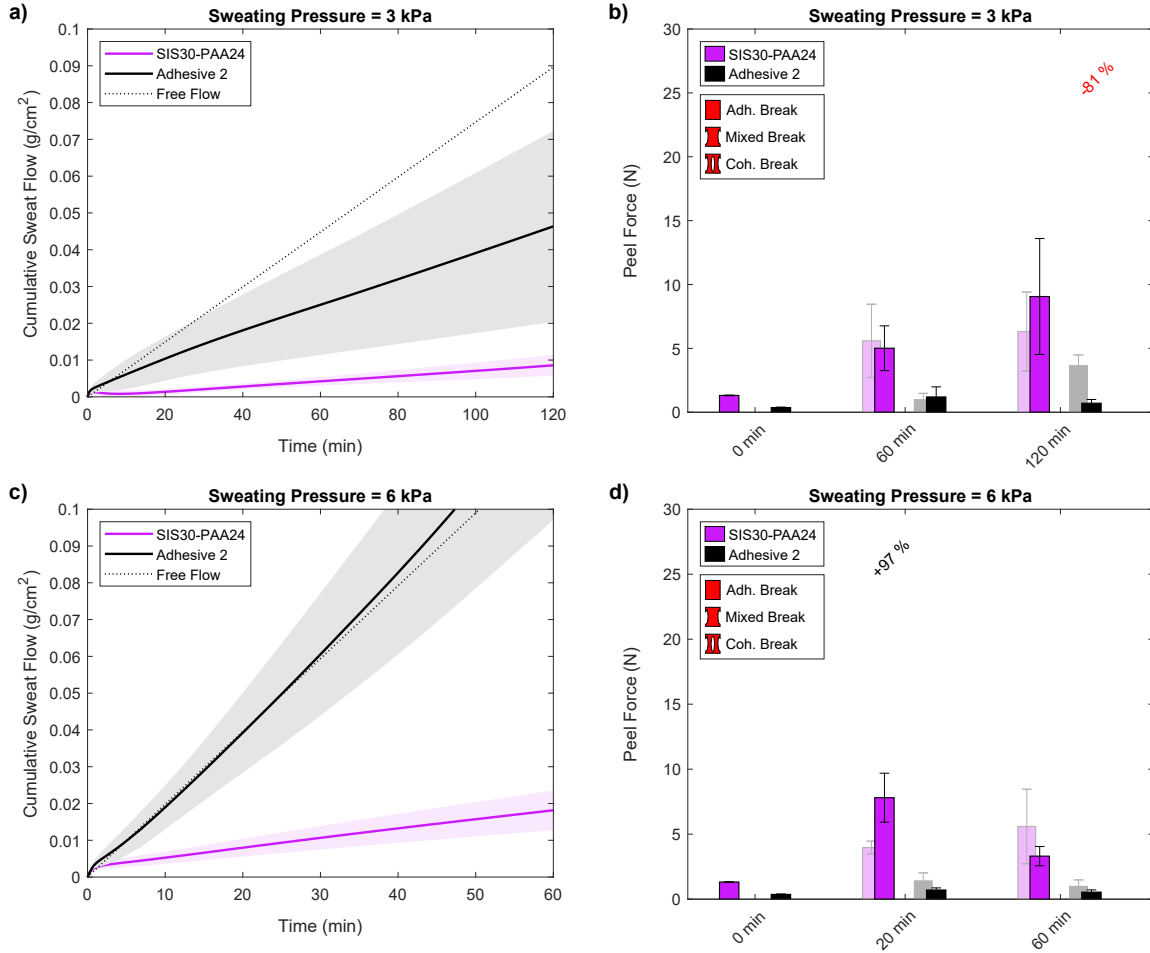


Figure 7.5: a) The cumulative sweat flow at a perspiration pressure of 3 kPa. b) The peel forces after perspiration at a pressure of 3 kPa. Dry peel forces are presented as the shaded bars and a reduction in peel force is indicated for statistically significant differences. c) The cumulative sweat flow at a perspiration pressure of 6 kPa. d) The peel forces after perspiration at a pressure of 6 kPa. Dry peel forces are presented as the shaded bars and a change in peel force is indicated for statistically significant differences.

Importantly, as stated in the beginning of this thesis, the aim was to develop skin adhesives with improved performance during perspiration even if the adhesive is applied in a poor manner. Therefore, the adhesives have been applied to the artificial skin with a pressure of 1770 Pa for 1 min to simulate poor application by a user. Crucially, better bonding conditions may result in more contact formation and subsequently improve the performance of the adhesive. In Section 10.2, I will show that *Adhesive 2* indeed performs well during perspiration when applied with a larger pressure (7848 Pa for 1 min). However, the new formulations even show good performance during perspiration without careful application of the adhesive.

7.2.3 Comparison with Adhesive Performance on Human Skin

The new formulations as well as the commercial adhesive have also been tested on human skin during perspiration. In Fig. 7.6a the performance of all adhesives is shown on human skin (extension of Fig. 6.12). Noteworthy, the peel adhesion of SIS25-PAA17 decreased by approximately 74 % after perspiration as compared to dry conditions. However, its performance was similar to PAAPot-27 on the perspiration simulator as well as on human skin (apart from the different failure mechanism). On the other hand, SIS30-PAA24 exhibited good performance during perspiration on human skin, without a statistically significant decrease in peel adhesion. Furthermore, its peel forces exceeded the corresponding peel forces of *Adhesive 2* on human skin.

Finally, the peel adhesion of all adhesives on human skin can be compared to the their peel adhesion on the perspiration simulator. Since the study on the perspiration simulator was not performed with 30 min of perspiration, I have chosen to compare the data with 20 min perspiration at 6 kPa (see 7.6b) and 60 min of perspiration at 3 kPa (see 7.6c). Here, the peel adhesion to human skin shows good coincidence with the peel adhesion to the perspiration simulator after 60 min of perspiration at 3 kPa. Similar trends were observed, which indicates the validity of the perspiration simulator.

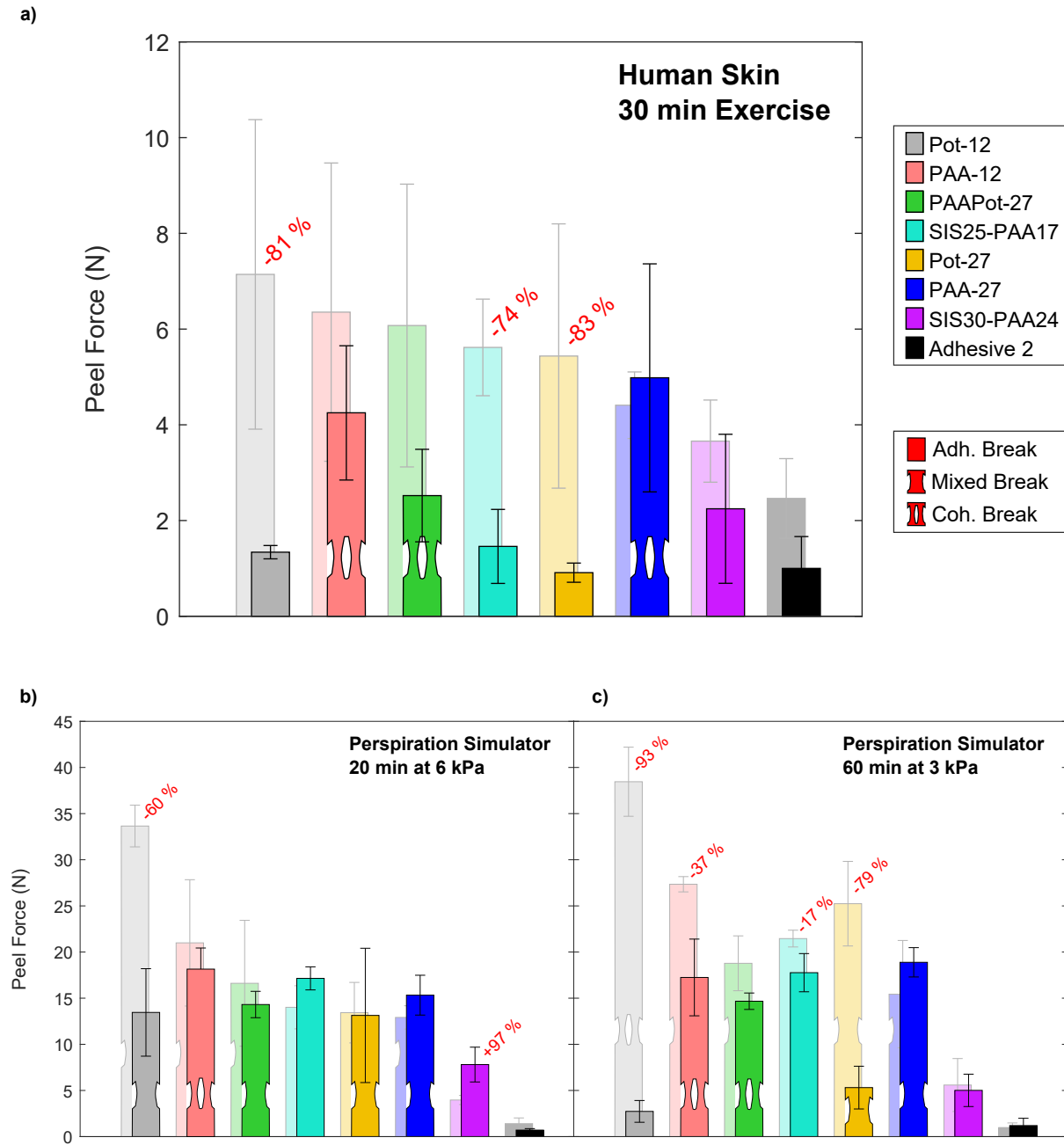


Figure 7.6: Performance of all skin adhesives during perspiration. The average peel adhesion of three individual replicates is shown under dry conditions (shaded bars) and after perspiration (full bars). Peel adhesion a) on human skin after 30 min of exercise, b) on the perspiration simulator after 20 min of perspiration at 6 kPa, and c) on the perspiration simulator after 60 min of perspiration at 3 kPa.

7.3 Key Conclusions

- The learnings from Chapter 5 and Chapter 6 were implemented to develop two new skin adhesive formulations with improved performance during perspiration.
- SIS25-PAA17 is a formulation with maximised adhesion. High peel adhesion was observed in all cases.
- SIS30-PAA24 is a skin-friendly formulation with moderate adhesion. No significant decrease in peel force was observed after perspiration as compared to dry conditions.
- Both new formulations exhibited strong enough cohesion such that the failure mode remained adhesive
- Both new formulations outperformed a commercial adhesive (*Adhesive 2*) during perspiration under the given test conditions

Part III

Concluding Remarks

8 Conclusions

This thesis aimed to gain a fundamental understanding of the processes leading to a loss of adhesion on human skin and subsequently identify strategies to maintain adhesion. Wet conditions have proven especially challenging for skin adhesives and may cause undesired detachment. Even though novel bio-inspired adhesives have been reported with exceptionally strong adhesion in wet environments, this study was limited to skin adhesives with an adhesion mechanism based on van der Waals interactions to ensure easy removal.

To investigate the behaviour of skin adhesives during wet conditions, a perspiration simulator was developed, which mimics human skin in some key characteristics. This eliminated the countless variations associated with human skin and instead enabled well-defined and reproducible perspiration conditions. Through a systematic design of adhesives, the impact of their viscoelastic properties and sweat absorption capabilities during perspiration were decoupled. The addition of hydrophilic particles was shown to promote adhesion over prolonged periods during perspiration. Sweat is thereby absorbed by the particles, relieving the pressure created by the sweat glands from the interface. However, particle swelling may lead to a rupture of the adhesive matrix and cause cohesive failure during peel. Therefore, it is paramount to balance the viscoelastic properties of the matrix with the swelling of the particles upon absorption of sweat.

The absorption of sweat into the bulk of the adhesives was shown to occur through networks of hydrophilic particles above a critical particle loading. Crucially, such networks first form during swelling of the particles upon exposure to moisture. The fact that swelling is required for network formation implies that the absorption kinetics and the critical particle loading for water absorption strongly depend on the viscoelastic properties of the matrix. Besides the particle chemistry and particle loading, the viscoelastic properties of the polymer matrix therefore become an important parameter to tune the sweat absorption properties of the adhesive.

On the basis of these learnings, two new skin adhesive formulations were designed with improved performance during perspiration. Briefly, the adhesives provided sufficient sweat absorption, while their cohesion was increased through adjustments in the viscoelastic properties of the polymer matrix. As a consequence, the adhesives showed remarkable resistance against perspiration and outperformed a commercial adhesive within this experimental setup.

9 Outlook

This study solely focussed on the performance of skin adhesives during perspiration and further studies will be necessary to improve the overall adhesive performance. While answering a few question, the PhD study has also led to many new questions. In the following, I will try to summarise one of the most intriguing questions.

Increased Adhesion in Wet Environments

Several experiments have indicated that the peel adhesion of skin adhesives may increase upon moderate hydration (see Fig. 6.3 and Fig. 7.5). On one hand, hydrocolloids are known to develop specific interactions with certain substrates upon hydration[117, 118], which is based on a similar adhesion mechanism as the underwater adhesion of mussels. Thereby, water acts as a plasticiser and enables the polymer chains of the hydrocolloids to re-arrange such that hydrogen bonds can be formed with the respective sites on the substrate. Importantly, an optimum hydration of the hydrocolloids exists, where low hydration levels may not provide sufficient mobility, while excessive hydration may lead to dissolution of the polymer chains. This implies that specific hydration levels may enable the particles within the adhesives to form hydrogen bonds in addition to the van der Waals interactions by the polymer matrix. This may lead to an increase in the peel adhesion upon hydration.

On the other hand, the viscoelastic properties of skin adhesives may change upon hydration. The plasticising effect of water is generally found to cause a softening of the adhesives[72, 119] and excessive hydration may even disintegrate the adhesive[77]. According to Eq. 2.11, changes in the viscoelastic properties of the adhesives may lead to increased peel adhesion in two different ways. Firstly, through an increase in the loss modulus at high frequencies, energy dissipation is increased and in turn the peel force appears higher. Secondly, a decrease in the storage modulus at low frequencies may enable the adhesive to establish larger contact areas and therefore increase its peel adhesion.

A systematic design of experiments would be required to determine the contributions of specific interactions and changes in the viscoelastic properties upon hydration to the performance of the adhesive. I will conclude this thesis with a brief exploratory study, where I attempt to probe the changes of the viscoelastic properties of skin adhesives in wet environments.

Exploratory Study of Changes of the Viscoelastic Properties of Adhesives in Wet Environments

The new adhesive formulation SIS30-PAA24 (see Chapter 7) showed an increase in peel adhesion after 20 min of perspiration at a pressure of 6 kPa as compared to dry conditions (see Fig. 7.5d). In order to evaluate the viscoelastic properties of the adhesives at the time of peel, a rheological analysis was performed of the adhesive after perspiration. Thereby, the artificial skin with the adhesive attached was removed from the perspiration simulator after 20 min of perspiration at a pressure of 6 kPa. Then, a rheological analysis was performed on the adhesive while still being attached to the artificial skin. Crucially, the gap was set to zero between the artificial skin and the top plate of the rheometer before the experiment. Else, the rheological measurements were performed in a similar manner as described in Chapter 4, with the only difference being that the frequency sweeps were only conducted between 100 Hz - 0.001 Hz. Since the distribution of water could not be controlled during the measurement, I limited the frequency range to decrease the measurement time to approximately 2 h. During the perspiration experiment, a cumulative sweat flow of approximately 0.01 g/cm² occurred, which evidently led to a slight decrease in moduli as well as a decrease in the loss tangent (see Fig. 9.1a and 9.1b). A decrease in the moduli would lead to a decrease in the energy dissipation as well as an increase in contact formation, which would have opposite effects on the peel adhesion according to Eq. 2.11. In order to estimate the effect of the changes in the viscoelastic behaviour on the observed peel adhesion, the loss modulus and storage modulus were evaluated at the relevant frequencies (5 Hz and 0.001 Hz, respectively). Since the loss modulus shows a larger decrease than the storage modulus, the peel adhesion would be expected to decrease by approximately 20 %.

Importantly, since sweat is supplied through sweat pores in finite areas, the liquid is not distributed evenly throughout the surface of the adhesive. There exist areas of the adhesive with large quantities of absorbed sweat but also areas that are dry after perspiration. An image of SIS30-PAA24 after peeling from the perspiration simulator is shown in Fig. 9.2a. The white spots thereby correspond to the areas where sweat has been absorbed. With the assumption that the diffusion of sweat into the adhesive is isotropic, sweat would be distributed in a half sphere around the sweat pores (see Fig. 9.2b).

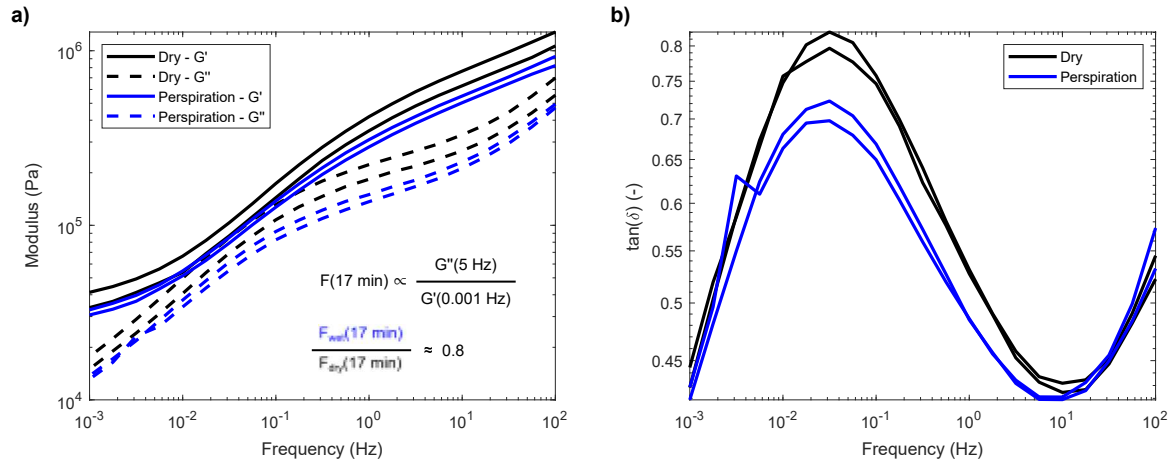


Figure 9.1: The viscoelastic behaviour of SIS30-PAA24 on the artificial skin after perspiration for 20 min at a pressure of 6 kPa. A cumulative sweat flow of approximately 0.01 g/cm^2 during perspiration led to a) a slight decrease in moduli and b) a decrease in the loss tangent.

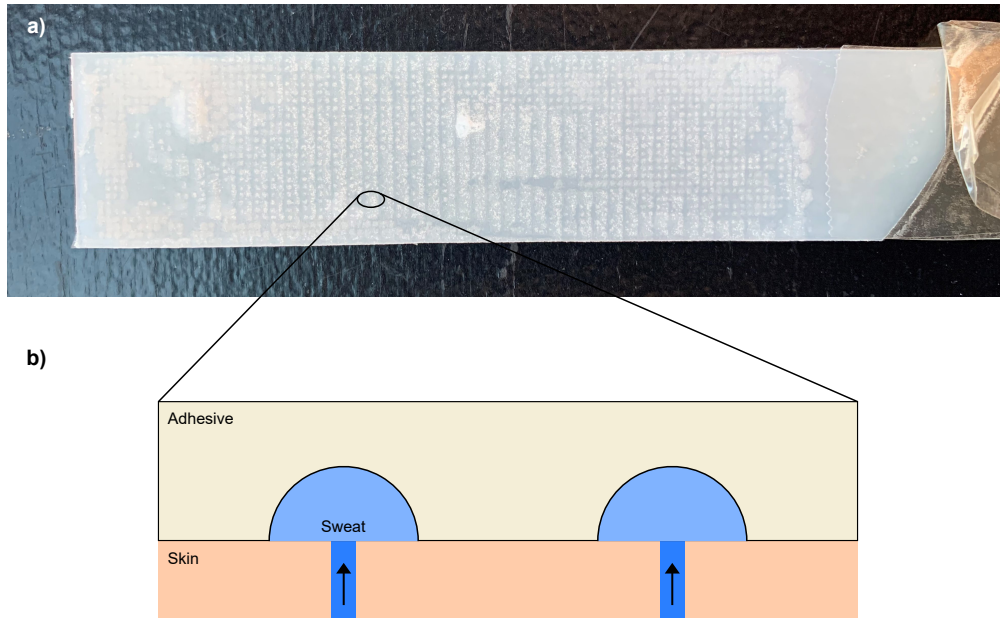


Figure 9.2: a) Image of SIS30-PAA24 after 20 min of perspiration at a pressure of 6 kPa. b) Schematic illustration of the expected distribution of absorbed sweat within the adhesive.

In order to estimate the changes in the viscoelastic properties of the wet portion of the adhesive only, adhesives were exposed to environments with controlled humidities. Here, the entire adhesive reached an equilibrium state of hydration with homogeneously distributed water. Two adhesives (SIS30-PAA24 and *Adhesive 2*) were evaluated through rheometry after being exposed to both 75 % RH and 100 % RH. SIS30-PAA24 showed a decrease in moduli as well as a decrease in the loss tangent with increasing hydration (see Fig. 9.3a and 9.3b). On the other hand, an increase in the storage modulus at low frequencies as compared to dry conditions was observed for *Adhesive 2* when equilibrated at 75 % RH (see Fig. 9.3c). With increasing hydration, however, also the storage modulus decreased. At both hydration levels a decrease in the loss tangent occurred (see Fig 9.3d). Noteworthy, different states of hydration were achieved for the two adhesives due to the nature of the different hydrocolloids.

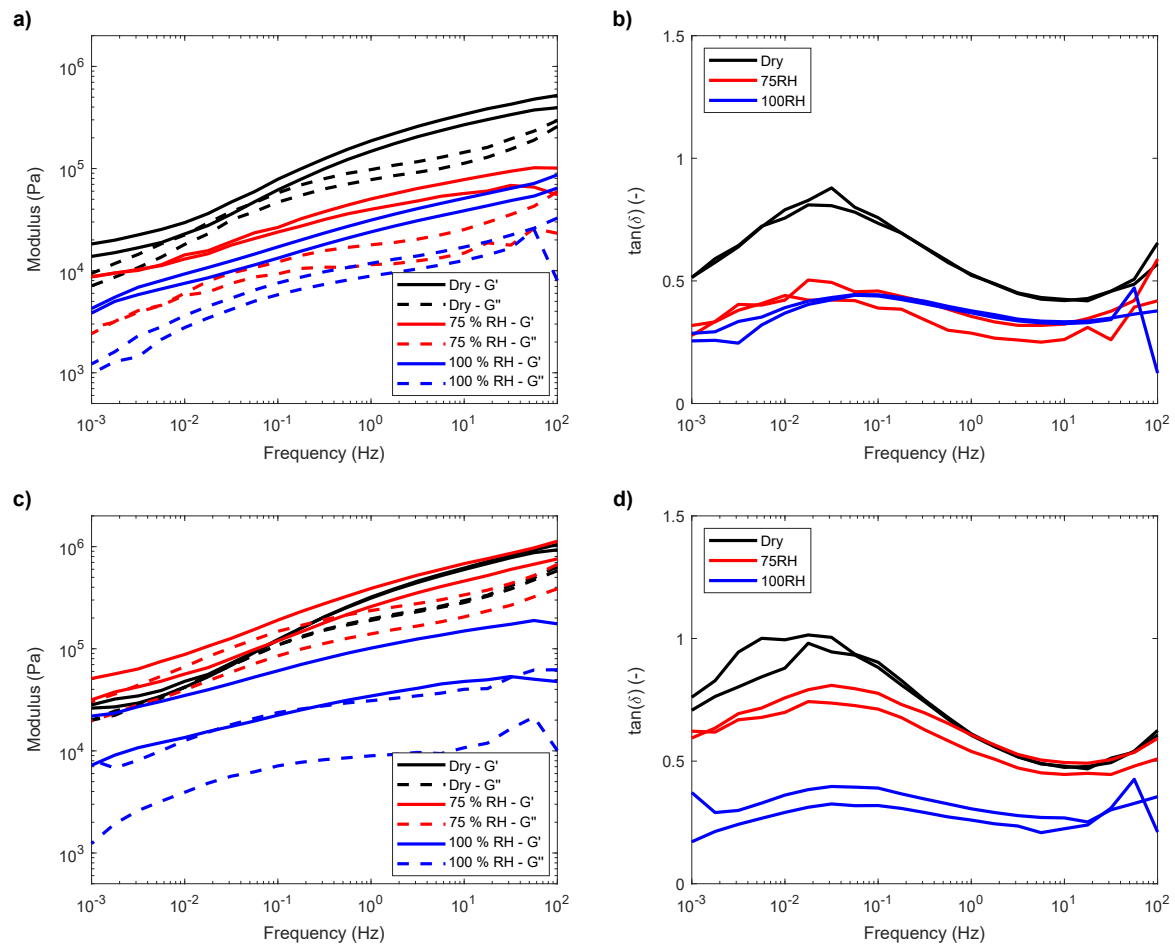


Figure 9.3: The viscoelastic behaviour of adhesives after equilibration at 75 % RH and 100 % RH. a) The moduli and b) the loss tangent of SIS30-PAA24 as a function of frequency. c) The moduli and d) the loss tangent of *Adhesive 2* as a function of frequency.

The effect of the changes in the viscoelastic properties upon hydration was again estimated using Eq. 2.11. In Fig. 9.4 the development of the estimated peel forces is shown as a function of the particle hydration when exposed to environments at 75 % RH and 100 % RH. It appears that the decrease in energy dissipation (loss modulus at 5 Hz) outweighs the increase in contact formation (decrease in the storage modulus at 0.001 Hz) and an overall decrease in the peel adhesion is expected for both adhesives.

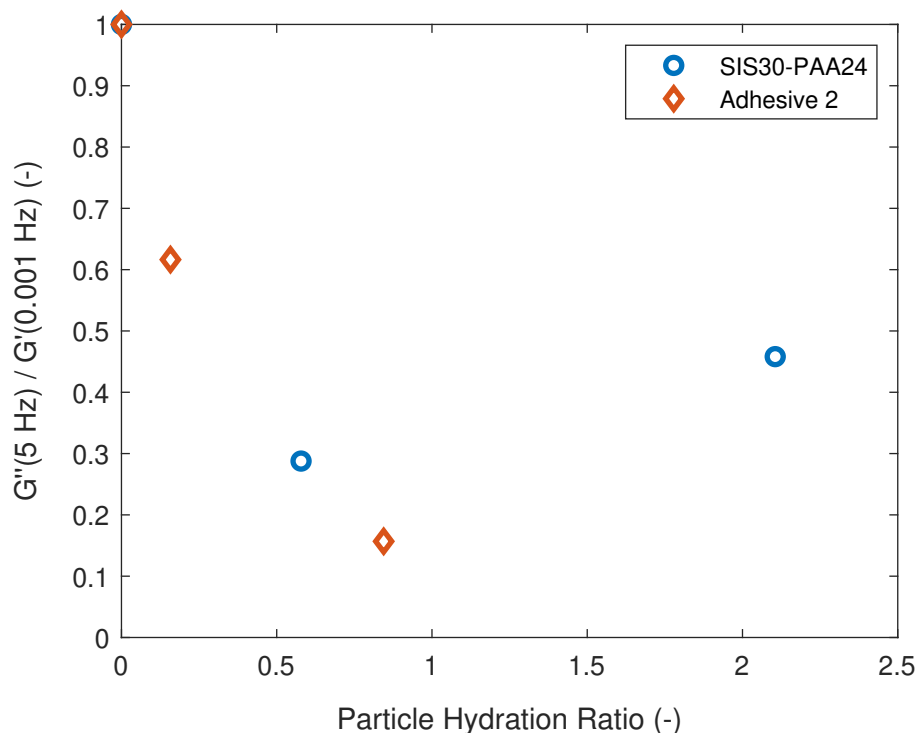


Figure 9.4: The peel adhesion is estimated from the viscoelastic properties of the hydrated adhesives using Eq. 2.11.

Summary of the Exploratory Study

Under specific perspiration conditions, increased peel adhesion had been observed for both *Adhesive 2* and SIS30-PAA24 (see Fig. 6.3 and Fig. 7.5, respectively). However, the viscoelastic properties of both adhesives appear to change such that a decrease in the peel adhesion would be expected. This points towards the occurrence of specific interactions in the form of hydrogen bonds between the particles and the artificial skin, causing an increase in peel adhesion.

10 Appendix

10.1 Calculation of the Critical Modulus for Cold Flow of Viscoelastic Materials

According to Hertz[120], the contact area between two elastic spheres can be calculated after bringing them together through an external pressure. The JKR theory[43] extends the Hertzian contact area through the incorporation of adhesive forces (i.e. the interfacial energy). This implies that a finite contact area exists even in the absence of an external pressure. Such a contact radius, a , can then be calculated as a function of the work of adhesion, W_a , the radii of the spheres, and their mechanical properties:

$$a^3 = \frac{6W_a\pi R^2}{K} \quad (10.1)$$

The materials constant K is then defined through the Poisson's ratio, ν , and the elastic modulus, E , of the two different materials:

$$K = \frac{4}{3\pi} \frac{1}{k_1 + k_2} \quad \text{with} \quad k_1 = \frac{1 - \nu_1^2}{\pi E_1} \quad \text{and} \quad k_2 = \frac{1 - \nu_2^2}{\pi E_2} \quad (10.2)$$

The constant, R , is defined through the radii, r , of the two spheres:

$$\frac{1}{R} = \frac{1}{r_1} + \frac{1}{r_2} \quad (10.3)$$

The JKR theory is also routinely used to calculate the contact areas between a hard sphere and a soft, flat substrate. Thereby, the radius of one of the materials becomes infinitely large to resemble a flat surface:

$$r_1 \rightarrow \infty \quad \text{and therefore} \quad R = r_2 \quad (10.4)$$

Assuming that the sphere is completely rigid and all deformation occurs within the substrate, the following holds:

$$E_2 \rightarrow \infty \quad \text{and therefore} \quad k_2 \rightarrow 0 \quad \text{and} \quad K = \frac{4 E_1}{3 (1 - \nu_1^2)} \quad (10.5)$$

Consequently, the contact radius between the two materials in the absence of any external pressure can be calculated as:

$$a^3 = \frac{9W_a\pi(1 - \nu_1^2)R^2}{2E_1} \quad (10.6)$$

The deformation of the substrate is a consequence of the adhesive forces between the two materials and an indentation, L , occurs (see illustration in Fig. 10.1). The indentation is then given as follows[121, 122]:

$$L = \left(\frac{\sqrt{3}W_a\pi(1 - \nu_1^2)}{2E_1} \right)^{\frac{2}{3}} R^{\frac{1}{3}} \quad (10.7)$$

It can easily be seen that the penetration depth is limited by the magnitude of the elastic modulus. Through the transformation of Eq. 10.7, the elastic modulus for a given indentation and sphere radius can be calculated:

$$E_1 = \frac{\pi W_a(1 - \nu_1^2)}{2} \sqrt{\frac{3R}{L^3}} \quad (10.8)$$

An inverse setup of the illustration in Fig. 10.1, may be interpreted as an adhesive on human skin. The indentation depth, L , may be exchanged with the skin groove depth and the sphere radius, r , may be exchanged with the radius of the skin asperities. With an estimation of the work of adhesion and the Poisson's ratio of the adhesive, a critical modulus can be estimated, above which the adhesive is not able to flow into the crevices. Importantly, the analysis is restricted to elastic materials and does not account for viscoelastic flow.

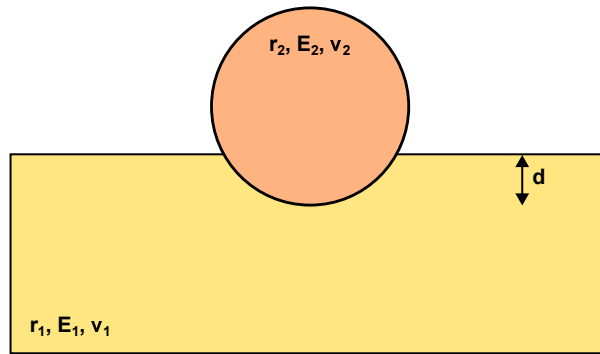


Figure 10.1: Illustration of a rigid sphere, which is in contact with a soft, flat surface. Even in the absence of an external load an indentation occurs as a consequence of the adhesive forces between the materials.

10.2 The Impact of the Bonding Conditions on the Performance of Skin Adhesives during Perspiration

In order to evaluate the effect of the bonding conditions on the performance of skin adhesives during perspiration, experiments were conducted using a commercial adhesive (*Adhesive 2*). The experiments were conducted on the perspiration simulator (iteration 2) as described in Chapter 6. In Chapter 7, the performance of *Adhesive 2* during perspiration was evaluated after the adhesive had been applied to the artificial skin with a light pressure of 1770 Pa for 1 min. As a result, the initial peel force was below 1 N (see Fig. 10.2 a), indicating little contact formation of the adhesive. Consequently, sweat could readily penetrate the interface and the sweat flow below the adhesive corresponded to the free flow rate (see Fig. 10.2 b).

On the other hand, when *Adhesive 2* is applied with a higher pressure (7848 Pa for 1 min), the initial peel force is approximately 8 N on the artificial skin (see Fig. 10.2 a). The relatively good bonding conditions result in an occlusion of the sweat pores as indicated by the limited sweat flow rate (see Fig. 10.2 b). Therefore, perspiration does not lead to a decrease in peel force after 60 min of perspiration at a pressure of 6 kPa.

This shows that the initial bonding conditions are crucial for the results obtained after perspiration. *Adhesive 2* shows great performance during perspiration when applied with a high pressure. However, at low application pressures, the performance of the adhesive during perspiration is poor and may result in undesired detachment.

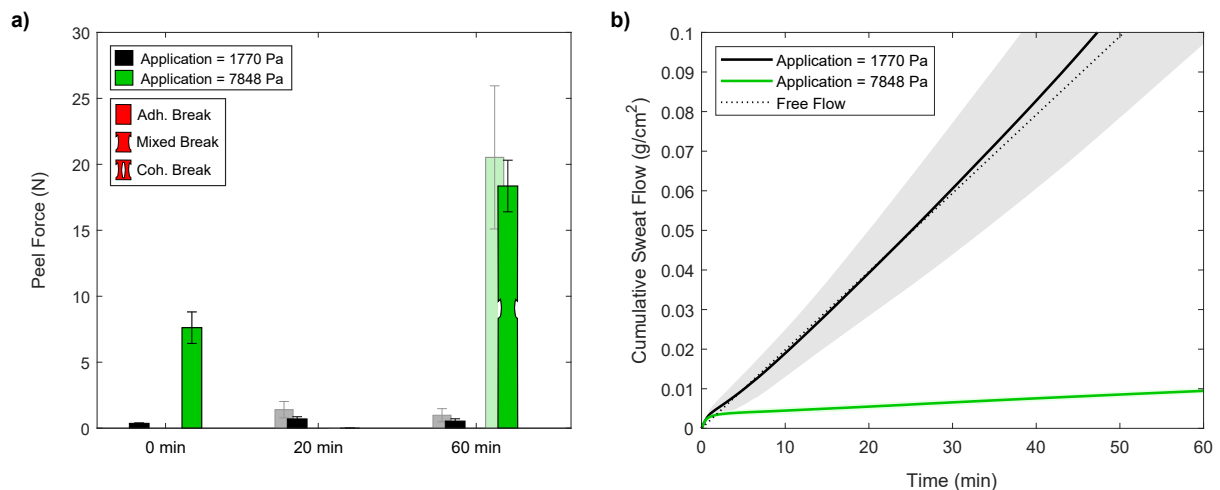


Figure 10.2: The influence of the application pressure on the performance of *Adhesive 2* during perspiration at a sweating pressure of 6 kPa. a) The cumulative sweat flow and b) the peel adhesion over a period of 60 min.

Bibliography

- (1) Claessens, I.; Probert, R.; Tielemans, C.; Steen, A.; Nilsson, C.; Andersen, B. D.; Størling, Z. M. The Ostomy Life Study: the everyday challenges faced by people living with a stoma in a snapshot. *Gastrointestinal Nursing* **2015**, *13*, 18–25.
- (2) Tafreshi, M. Z.; Rassouli, M.; Dabirian, A.; Yaghmaie, F. Quality of life in ostomy patients: a qualitative study. *Patient Preference and Adherence* **2010**, *5*, 1.
- (3) Popek, S.; Grant, M.; Gemmill, R.; Wendel, C. S.; Mohler, M. J.; Rawl, S. M.; Baldwin, C. M.; Ko, C. Y.; Schmidt, C. M.; Krouse, R. S. Overcoming challenges: life with an ostomy. *The American Journal of Surgery* **2010**, *200*, 640–645.
- (4) Danielsen, A. K.; Christensen, B. M.; Mortensen, J.; Voergaard, L. L.; Herlufsen, P.; Balleby, L. Establishment of a regional Danish database for patients with a stoma. *Colorectal Disease* **2015**, *17*, O27–O33.
- (5) Andersen, B. D.; Schmidt, D. S.; Christensen, B. M.; Balleby, L. *Stomidatabasen i Region Hovedstaden - Årsrapport 2010*; tech. rep.; Styregruppen for Kirurgisk Sygepleje (SKS) i Region Hovedstaden, 2010.
- (6) Andersen, B. D.; Schmidt, D. S.; Voergaard, L. L.; Herlufsen, P.; Christensen, B. M.; Balleby, L. *Stomidatabasen i Region Hovedstaden - Årsrapport 2011*; tech. rep.; Styregruppen for Kirurgisk Sygepleje (SKS) i Region Hovedstaden, 2011.
- (7) Andersen, B. D.; Frandsen, A. M.; Voergaard, L. L.; Herlufsen, P.; Krosgaard, M.; Christensen, B. M. *Stomidatabasen i Region Hovedstaden - Årsrapport 2012*; tech. rep.; Styregruppen for Kirurgisk Sygepleje (SKS) i Region Hovedstaden, 2012.
- (8) Andersen, B. D.; Frandsen, A. M.; Voergaard, L. L.; Herlufsen, P.; Krosgaard, M.; Christensen, B. M. *Stomidatabasen i Region Hovedstaden - Årsrapport 2013*; tech. rep.; Styregruppen for Kirurgisk Sygepleje (SKS) i Region Hovedstaden, 2013.
- (9) Andersen, B. D.; Frandsen, A. M.; Voergaard, L. L.; Herlufsen, P.; Krosgaard, M.; Christensen, B. M. *Stomidatabasen i Region Hovedstaden - Årsrapport 2014*; tech. rep.; Styregruppen for Kirurgisk Sygepleje (SKS) i Region Hovedstaden, 2014.
- (10) Andersen, B. D.; Frandsen, A. M.; Voergaard, L. L.; Herlufsen, P.; Krosgaard, M.; Christensen, B. M. *Stomidatabasen i Region Hovedstaden - Årsrapport 2015*; tech. rep.; Styregruppen for Kirurgisk Sygepleje (SKS) i Region Hovedstaden, 2015.

- (11) Herlufsen, P.; Olsen, A. G.; Carlsen, B.; Nybaek, H.; Jemec, G. B.; Karlsmark, T.; Laursen, T. N. Study of peristomal skin disorders in patients with permanent stomas. *British Journal of Nursing* **2006**, *15*, 854–862.
- (12) Honari, G.; Maibach, H. In *Applied Dermatotoxicology*; Elsevier: 2014, pp 1–10.
- (13) Holbrook, K. A.; Odland, G. F. Regional Differences in the Thickness (Cell Layers) of the Human Stratum Corneum: An Ultrastructural Analysis. *Journal of Investigative Dermatology* **1974**, *62*, 415–422.
- (14) Warner, R. R.; Stone, K. J.; Boissy, Y. L. Hydration Disrupts Human Stratum Corneum Ultrastructure. *Journal of Investigative Dermatology* **2003**, *120*, 275–284.
- (15) Egawa, M.; Hirao, T.; Takahashi, M. In vivo Estimation of Stratum Corneum Thickness from Water Concentration Profiles Obtained with Raman Spectroscopy. *Acta Dermato-Venereologica* **2007**, *87*, 4–8.
- (16) Ginn, M. E.; Noyes, C. M.; Jungermann, E. The contact angle of water on viable human skin. *Journal of Colloid And Interface Science* **1968**, *26*, 146–151.
- (17) Christensen, M.; Hargens, C.; Nacht, S.; Gans, E. Viscoelastic Properties of Intact Human Skin: Instrumentation, Hydration Effects, and the Contribution of the Stratum Corneum. *Journal of Investigative Dermatology* **1977**, *69*, 282–286.
- (18) Egawa, M.; Oguri, M.; Kuwahara, T.; Takahashi, M. Effect of exposure of human skin to a dry environment. *Skin Research and Technology* **2002**, *8*, 212–218.
- (19) Dąbrowska, A. K.; Adlhart, C.; Spano, F.; Rotaru, G.-M.; Derler, S.; Zhai, L.; Spencer, N. D.; Rossi, R. M. In vivo confirmation of hydration-induced changes in human-skin thickness, roughness and interaction with the environment. *Biointerphases* **2016**, *11*, 031015.
- (20) Blank, I. H. Factors which influence the water content of the stratum corneum. *The Journal of investigative dermatology* **1952**, *18*, 433–440.
- (21) Kasting, G. B.; Barai, N. D. Equilibrium water sorption in human stratum corneum. *Journal of Pharmaceutical Sciences* **2003**, *92*, 1624–1631.
- (22) Sparr, E.; Millemcamps, D.; Isoir, M.; Burnier, V.; Larsson, Å.; Cabane, B. Controlling the hydration of the skin through the application of occluding barrier creams. *Journal of the Royal Society, Interface* **2013**, *10*, 20120788.
- (23) Zhai, H.; Maibach, H. I. Occlusion vs. skin barrier function. *Skin Research and Technology* **2002**, *8*, 1–6.
- (24) Gray, M.; Black, J. M.; Baharestani, M. M.; Bliss, D. Z.; Colwell, J. C.; Goldberg, M.; Kennedy-Evans, K. L.; Logan, S.; Ratliff, C. R. Moisture-associated skin damage: Overview and pathophysiology. *Journal of Wound, Ostomy and Continence Nursing* **2011**, *38*, 233–241.

-
- (25) Adams, M. Water and adhesion. *International Journal of Adhesion and Adhesives* **1983**, *3*, 68–69.
- (26) Akdogan, Y.; Wei, W.; Huang, K.-Y.; Kageyama, Y.; Danner, E. W.; Miller, D. R.; Rodriguez, N. R. M.; Waite, J. H.; Han, S. Intrinsic Surface-Drying Properties of Bioadhesive Proteins. *Angewandte Chemie - international edition* **2014**, *53*, 11253–11256.
- (27) Prahlad, H.; Pelrine, R.; Stanford, S.; Marlow, J.; Kornbluh, R. In *2008 IEEE International Conference on Robotics and Automation*, IEEE: 2008, pp 3028–3033.
- (28) Leung, B. C.; Goeser, N. R.; Miller, L. A.; Gonzalez, S. In *2015 IEEE Aerospace Conference*, IEEE: 2015; Vol. 2015, pp 1–8.
- (29) Messner, K.; Gao, J. The menisci of the knee joint. Anatomical and functional characteristics, and a rationale for clinical treatment. *Journal of Anatomy* **1998**, *193*, 161–178.
- (30) Autumn, K.; Liang, Y. A.; Hsieh, S. T.; Zesch, W.; Chan, W. P.; Kenny, T. W.; Fearing, R.; Full, R. J. Adhesive force of a single gecko foot-hair. *Nature* **2000**, *405*, 681–685.
- (31) Autumn, K.; Sitti, M.; Liang, Y. A.; Peattie, A. M.; Hansen, W. R.; Sponberg, S.; Kenny, T. W.; Fearing, R.; Israelachvili, J. N.; Full, R. J. Evidence for van der Waals adhesion in gecko setae. *Proceedings of the National Academy of Sciences* **2002**, *99*, 12252–12256.
- (32) Ruibal, R.; Ernst, V. The structure of the digital setae of lizards. *Journal of Morphology* **1965**, *117*, 271–293.
- (33) Autumn, K.; Liang, Y. A.; Hsieh, S. T.; Zesch, W.; Chan, W. P.; Kenny, T. W.; Fearing, R.; Full, R. J. Adhesive force of a single gecko foot-hair. *Nature* **2000**, *405*, 681–685.
- (34) Stark, A. Y.; Sullivan, T. W.; Niewiarowski, P. H. The effect of surface water and wetting on gecko adhesion. *Journal of Experimental Biology* **2012**, *215*, 3080–3086.
- (35) Marcellini, D. L. Activity Patterns of the Gecko *Hemidactylus frenatus*. *Copeia* **1971**, *1971*, 631.
- (36) Parker, W. S. Aspects of the Ecology of a Sonoran Desert Population of the Western Banded Gecko, *Coleonyx variegatus* (Sauria, Eublepharinae). *American Midland Naturalist* **1972**, *88*, 209.
- (37) Waite, J. Nature's underwater adhesive specialist. *International Journal of Adhesion and Adhesives* **1987**, *7*, 9–14.
- (38) Creton, C. Pressure-Sensitive Adhesives : An Introductory Course. *MRS bulletin* **2003**, *28*, 434–439.
- (39) Yarusso, D. J. In *Adhesion Science and Engineering*, Dillard, D. A., Pocius, A. V., Eds.; Elsevier: 2002, pp 499–533.
-

- (40) Sun, S.; Li, M.; Liu, A. A review on mechanical properties of pressure sensitive adhesives. *International Journal of Adhesion and Adhesives* **2013**, *41*, 98–106.
- (41) Gu, Z.; Li, S.; Zhang, F.; Wang, S. Understanding Surface Adhesion in Nature: A Peeling Model. *Advanced Science* **2016**, *3*, 1500327.
- (42) Du, J.; Lindeman, D. D.; Yarusso, D. J. Modeling the Peel Performance of Pressure Sensitive Adhesives. *The Journal of Adhesion* **2004**, *80*, 601–612.
- (43) Johnson, K. L.; Kendall, K.; Roberts, A. D. Surface Energy and the Contact of Elastic Solids. *Proceedings of the Royal Society A: Mathematical, Physical and Engineering Sciences* **1971**, *324*, 301–313.
- (44) Creton, C.; Leibler, L. How does tack depend on time of contact and contact pressure? *Journal of Polymer Science Part B: Polymer Physics* **1996**, *34*, 545–554.
- (45) Xu, X.; Jagota, A.; Hui, C.-Y. Effects of surface tension on the adhesive contact of a rigid sphere to a compliant substrate. *Soft Matter* **2014**, *10*, 4625–4632.
- (46) Kinning, D. J.; Schneider, H. M. In *Adhesion Science and Engineering*, Dillard, D. A., Pocius, A. V., Chaudhury, M., Eds., 2002, pp 535–571.
- (47) Anderson, M. L.; Mott, P. H.; Roland, C. M. The Compression of Bonded Rubber Disks. *Rubber Chemistry and Technology* **2004**, *77*, 293–302.
- (48) Dahlquist, C. A. In *Treatise on adhesion and adhesives*, Patrick, R. L., Ed., 1969; Vol. 2, p 219.
- (49) Chang, E. P. Viscoelastic Windows of Pressure-Sensitive Adhesives. *The Journal of Adhesion* **1991**, *34*, 189–200.
- (50) Yang, H. W. H. Water-based polymers as pressure-sensitive adhesives—viscoelastic guidelines. *Journal of Applied Polymer Science* **1995**, *55*, 645–652.
- (51) Klompen, E. T. J. Mechanical properties of solid polymers: Constitutive modelling of long and short term behaviour, Ph.D. Thesis, Technical University of Eindhoven, 2005.
- (52) Shenoy, A. V., *Rheology of Filled Polymer Systems*; Springer Netherlands: Dordrecht, 1999.
- (53) Metzner, A. B. Rheology of Suspensions in Polymeric Liquids. *Journal of Rheology* **2002**, *29*, 739–775.
- (54) Krieger, I. M. A Dimensional Approach to Colloid Rheology. *Transactions of the Society of Rheology* **1963**, *7*, 101–109.
- (55) Le Meins, J.-F.; Moldenaers, P.; Mewis, J. Suspensions of monodisperse spheres in polymer melts: particle size effects in extensional flow. *Rheologica Acta* **2003**, *42*, 184–190.

-
- (56) Du, F.; Scogna, R.; Zhou, W.; Brand, S.; Fischer, J.; Winey, K. Nanotube Networks in Polymer Nanocomposites: Rheology and Electrical Conductivity. *Macromolecules* **2004**, *37*, 9048–9055.
- (57) Hu, G.; Zhao, C.; Zhang, S.; Yang, M.; Wang, Z. Low percolation thresholds of electrical conductivity and rheology in poly(ethylene terephthalate) through the networks of multi-walled carbon nanotubes. *Polymer* **2006**, *47*, 480–488.
- (58) Kota, A. K.; Cipriano, B. H.; Duesterberg, M. K.; Gershon, A. L.; Powell, D.; Raghavan, S. R.; Bruck, H. A. Electrical and rheological percolation in polystyrene/MWCNT nanocomposites. *Macromolecules* **2007**, *40*, 7400–7406.
- (59) Abbasi, S.; Carreau, P. J.; Derdouri, A.; Moan, M. Rheological properties and percolation in suspensions of multiwalled carbon nanotubes in polycarbonate. *Rheologica Acta* **2009**, *48*, 943–959.
- (60) Utracki, L. A. Flow and flow orientation of composites containing anisometric particles. *Polymer Composites* **1986**, *7*, 274–282.
- (61) Pötschke, P.; Fornes, T. D.; Paul, D. R. Rheological behavior of multiwalled carbon nanotube/polycarbonate composites. *Polymer* **2002**, *43*, 3247–3255.
- (62) Hao, X.; Kaschta, J.; Schubert, D. W. Viscous and elastic properties of polylactide melts filled with silica particles: Effect of particle size and concentration. *Composites Part B: Engineering* **2016**, *89*, 44–53.
- (63) Huang, X.; Kim, C.; Ma, Z.; Jiang, P.; Yin, Y.; Li, Z. Correlation Between Rheological, Electrical, and Microstructure Characteristics in Polyethylene/Aluminum Nanocomposites. *Journal of Polymer Science; Part B: Polymer physics* **2008**, *46*, 2143–2154.
- (64) Bowditch, M. The durability of adhesive joints in the presence of water. *International Journal of Adhesion and Adhesives* **1996**, *16*, 73–79.
- (65) Zanni-Deffarges, M.; Shanahan, M. Diffusion of water into an epoxy adhesive: comparison between bulk behaviour and adhesive joints. *International Journal of Adhesion and Adhesives* **1995**, *15*, 137–142.
- (66) Armstrong, K. Long-term durability in water of aluminium alloy adhesive joints bonded with epoxy adhesives. *International Journal of Adhesion and Adhesives* **1997**, *17*, 89–105.
- (67) Moidu, A. K.; Sinclair, A. N.; Spelt, J. K. Adhesive Joint Durability Assessed Using Open-faced Peel Specimens. *The Journal of Adhesion* **1998**, *65*, 239–257.
- (68) Frigione, M.; Aiello, M.; Naddeo, C. Water effects on the bond strength of concrete/concrete adhesive joints. *Construction and Building Materials* **2006**, *20*, 957–970.
- (69) Popineau, S.; Shanahan, M. E. Simple model to estimate adhesion of structural bonding during humid ageing. *International Journal of Adhesion and Adhesives* **2006**, *26*, 363–370.
-

- (70) Spencer, T. S.; Smith, S. E.; Conjeevaram, S. Adhesive interactions between polymers and skin in transdermal delivery systems. *Polymeric Materials Science and Engineering, Proceedings of the Acs Division of Polymeric Materials Science and Engineering* **1990**, *63*, 337.
- (71) Kenney, J. F.; Haddock, T. H.; Sun, R. L.; Parreira, H. C. Medical-grade acrylic adhesives for skin contact. *Journal of Applied Polymer Science* **1992**, *45*, 355–361.
- (72) Ferrari, F.; Bertoni, M.; Rossi, S.; Bonferoni, M. C.; Caramella, C.; Waring, M. J.; Aulton, M. E. Comparative Rheomechanical and Adhesive Properties of Two Hydrocolloid Dressings: Dependence on the Degree of Hydration. *Drug Development and Industrial Pharmacy* **1996**, *22*, 1223–1230.
- (73) Chalykh, A. A.; Chalykh, A. E.; Novikov, M. B.; Feldstein, M. M. Pressure-sensitive adhesion in the blends of poly(N-vinyl pyrrolidone) and poly(ethylene glycol) of disparate chain lengths. *The Journal of Adhesion* **2002**, *78*, 667–694.
- (74) Cunningham, D. D.; Lowery, M. G. Moisture Vapor Transport Channels for the Improved Attachment of a Medical Device to the Human Body. *Biomedical Microdevices* **2004**, *6*, 149–154.
- (75) Tokumura, F.; Yoshiura, Y.; Homma, T.; Nukatsuka, H. Regional differences in adhesive tape stripping of human skin. *Skin Research and Technology* **2006**, *12*, 178–182.
- (76) Roy, S. H.; De Luca, G.; Cheng, M. S.; Johansson, A.; Gilmore, L. D.; De Luca, C. J. Electro-mechanical stability of surface EMG sensors. *Medical & Biological Engineering & Computing* **2007**, *45*, 447–457.
- (77) Kong, D.; Zhang, Q.; You, J.; Cheng, Y.; Hong, C.; Chen, Z.; Jiang, T.; Hao, T. Adhesion loss mechanism based on carboxymethyl cellulose-filled hydrocolloid dressings in physiological wounds environment. *Carbohydrate Polymers* **2020**, *235*, 115953.
- (78) Crank, J, *The Mathematics of Diffusion*, Second; Oxford university press: 1975.
- (79) Van Der Wel, G. K.; Adan, O. C. Moisture in organic coatings - a review. *Progress in Organic Coatings* **1999**, *37*, 1–14.
- (80) Frisch, H. Sorption and Transport in Glassy Polymers - A Review. *Polymer Engineering & Science* **1980**, *20*, 2–13.
- (81) Peppas, N. A.; Brannon-Peppas, L. Water diffusion and sorption in amorphous macromolecular systems and foods. *Journal of Food Engineering* **1994**, *22*, 189–210.
- (82) Liu, M.; Wu, P.; Ding, Y.; Li, S. Study on diffusion behavior of water in epoxy resins cured by active ester. *Physical Chemistry Chemical Physics* **2003**, *5*, 1848–1852.

-
- (83) De Kee, D.; Liu, Q.; Hinestroza, J. Viscoelastic (Non-Fickian) Diffusion. *The Canadian Journal of Chemical Engineering* **2008**, *83*, 913–929.
- (84) Ferrari, F.; Bertoni, M.; Bonferoni, M. C.; Rossi, S.; Caramella, C.; Waring, M. J. Comparative evaluation of hydrocolloid dressings by means of water uptake and swelling force measurements: I. *International Journal of Pharmaceutics* **1994**, *112*, 29–36.
- (85) Wang, W.; Sain, M.; Cooper, P. A. Study of moisture absorption in natural fiber plastic composites. *Composites Science and Technology* **2006**, *66*, 379–386.
- (86) Lee, H.; Lee, B. P.; Messersmith, P. B. A reversible wet/dry adhesive inspired by mussels and geckos. *Nature* **2007**, *448*, 338–341.
- (87) Zhao, Y.; Wu, Y.; Wang, L.; Zhang, M.; Chen, X.; Liu, M.; Fan, J.; Liu, J.; Zhou, F.; Wang, Z. Bio-inspired reversible underwater adhesive. *Nature Communications* **2017**, *8*, 1–8.
- (88) Yang, S.; Xu, W.; Tu, M.; Jiang, L. Diffusive Adhesives for Water-Rich Materials: Strong and Tunable Adhesion Beyond the Interface. *Chemistry – A European Journal* **2019**, *25*, 8085–8091.
- (89) Venkatraman, S.; Gale, R. Skin adhesives and skin adhesion. *Biomaterials* **1998**, *19*, 1119–1136.
- (90) Kross, R. D. Ostomy Gasket, 1976.
- (91) Doehnert, D. F.; Hill, A. S. Stoma Seal Adhesive, 1985.
- (92) Osburn, F. G. Skin Barrier Composition, 1985.
- (93) Doyle, A.; Freeman, F. M. Adhesive Composition Resistant to Biological Fluids, 1985.
- (94) Stempel, E. Adhesive Skin Barrier Composition for Ostomy Appliance, 1996.
- (95) Chen, F.; Ciok, D. Pressure Sensitive Adhesive Composition, 2002.
- (96) Chen, F. Pressure Sensitive Adhesive Composition, 2002.
- (97) Fattman, G. F. Hydrocolloid Adhesive Compositions, 2004.
- (98) Fattman, G. F.; Sambasivam, M. Ostomy Appliance With Recovery Resistant Moldable Adhesive, 2007.
- (99) Sambasivam, M.; Fattman, G. F. Hot-Melt Silicone Based Ostomy and Wound Care Skin Attachment Adhesive, 2007.
- (100) Kwok Hing Lam, P.; Bach, A.; Lykke, M.; Toftkær, A.; Buus, H.; Kongebo, T. Pressure Sensitive Adhesive Composition Comprising Salt, 2014.
- (101) Moavenian, A. Flange Extender Comprising Honey, 2017.
- (102) Kleesz, P.; Darlenski, R.; Fluhr, J. W. Full-body skin mapping for six biophysical parameters: Baseline values at 16 anatomical sites in 125 human subjects. *Skin Pharmacology and Physiology* **2011**, *25*, 25–33.
-

- (103) Firooz, A.; Sadr, B.; Babakoochi, S.; Sarraf-Yazdy, M.; Fanian, F.; Kazerouni-Timsar, A.; Nassiri-Kashani, M.; Naghizadeh, M. M.; Dowlati, Y. Variation of Biophysical Parameters of the Skin with Age, Gender, and Body Region. *The Scientific World Journal* **2012**, *2012*, 1–5.
- (104) Eiler, J.; Simonsen, S. B.; Hansen, D.; Bingöl, B.; Hansen, K.; Thormann, E. Water Transport in Polymer Composites through Swelling-Induced Networks of Hydrogel Particles. *Soft Matter* **2020**.
- (105) Lagarde, J.; Rouvrais, C.; Black, D. Topography and anisotropy of the skin surface with ageing. *Skin Research and Technology* **2005**, *11*, 110–119.
- (106) Li, L.; Mac-Mary, S.; Marsaut, D.; Sainthillier, J. M.; Nouveau, S.; Gharbi, T.; de Lacharriere, O.; Humbert, P. Age-related changes in skin topography and microcirculation. *Archives of Dermatological Research* **2006**, *297*, 412–416.
- (107) Sato, K.; Sato, F. Individual variations in structure and function of human eccrine sweat gland. *American Journal of Physiology-Regulatory, Integrative and Comparative Physiology* **1983**, *245*, R203–R208.
- (108) Sonner, Z.; Wilder, E.; Heikenfeld, J.; Kasting, G.; Beyette, F.; Swaile, D.; Sherman, F.; Joyce, J.; Hagen, J.; Kelley-Loughnane, N.; Naik, R. The microfluidics of the eccrine sweat gland , including biomarker partitioning , transport , and biosensing implications. *Biomicrofluidics* **2015**, *9*.
- (109) Lara, B.; Gallo-Salazar, C.; Puente, C.; Areces, F.; Salinero, J. J.; Del Coso, J. Interindividual variability in sweat electrolyte concentration in marathoners. *Journal of the International Society of Sports Nutrition* **2016**, *13*, 1–8.
- (110) Hou, L.; Hagen, J.; Wang, X.; Papautsky, I.; Naik, R.; Kelley-Loughnane, N.; Heikenfeld, J. Artificial microfluidic skin for in vitro perspiration simulation and testing. *Lab on a Chip* **2013**, *13*, 1868–1875.
- (111) Eiler, J.; Hansen, D.; Bingöl, B.; Hansen, K.; Heikenfeld, J.; Thormann, E. In Vitro Evaluation of Skin Adhesives during Perspiration. *International Journal of Adhesion and Adhesives* **2020**, *99*, 102574.
- (112) Hansen, D.; Zajforoushan Moghaddam, S.; Eiler, J.; Hansen, K.; Thormann, E. Performance of Polymeric Skin Adhesives during Perspiration. *ACS Applied Polymer Materials* **2020**, *2*, 1535–1542.
- (113) Mosteller, R. Simplified Calculation of Body-Surface Area. *New England Journal of Medicine* **1987**, *317*, 1098.
- (114) Tripathi, S. R.; Miyata, E.; Ishai, P. B.; Kawase, K. Morphology of human sweat ducts observed by optical coherence tomography and their frequency of resonance in the terahertz frequency region. *Scientific Reports* **2015**, *5*, 9071.
- (115) Taylor, N. A.; Machado-Moreira, C. A. Regional variations in transepidermal water loss, eccrine sweat gland density, sweat secretion rates and electrolyte composition in resting and exercising humans. *Extreme Physiology & Medicine* **2013**, *2*, 4.

- (116) Choi, J.; Xue, Y.; Xia, W.; Ray, T. R.; Reeder, J. T.; Bandodkar, A. J.; Kang, D.; Xu, S.; Huang, Y.; Rogers, J. A. Soft, skin-mounted microfluidic systems for measuring secretory fluidic pressures generated at the surface of the skin by eccrine sweat glands. *Lab Chip* **2017**, *17*, 2572–2580.
- (117) Chen, J. L.; Cyr, G. N. In *Adhesion in biological systems*; Academic Press: 1970, pp 163–181.
- (118) Ben-Zion, O.; Nussinovitch, A. Physical properties of hydrocolloid wet glues. *Food Hydrocolloids* **1997**, *11*, 429–442.
- (119) Roos, A.; Creton, C.; Novikov, M. B.; Feldstein, M. M. Viscoelasticity and tack of poly(vinyl pyrrolidone)-poly(ethylene glycol) blends. *Journal of Polymer Science, Part B: Polymer Physics* **2002**, *40*, 2395–2409.
- (120) Hertz, H. Ueber die Berührung fester elastischer Körper. *Journal für die reine und angewandte Mathematik* **1882**, *1882*, 156–171.
- (121) Piétrement, O.; Troyon, M. General Equations Describing Elastic Indentation Depth and Normal Contact Stiffness versus Load. *Journal of Colloid and Interface Science* **2000**, *226*, 166–171.
- (122) Efremov, Y.; Bagrov, D.; Kirpichnikov, M.; Shaitan, K. Application of the Johnson–Kendall–Roberts model in AFM-based mechanical measurements on cells and gel. *Colloids and Surfaces B: Biointerfaces* **2015**, *134*, 131–139.

Manuscripts

Paper I - Water Transport in Polymer Composites through Swelling-Induced Networks of Hydrogel Particles



Cite this: DOI: 10.1039/d0sm01103g

Water transport in polymer composites through swelling-induced networks of hydrogel particles†

Johannes Eiler,^{a,b} Søren Bredmose Simonsen,^c Daniel Hansen,^{a,b}
Bahar Bingöl,^b Kristoffer Hansen^b and Esben Thormann^{a,*}

Water diffusion in polymer composites is not only affected by the chemical nature of the materials but also by their internal structures. To enable the design of polymer composites with controlled diffusion kinetics, we investigate the effect of hydrogel particle networks on the water transport. The composites in this study comprise hydrogel particles based on sodium poly(acrylic acid), which are incorporated at different concentrations into a soft and sticky polymer matrix. Through the use of X-ray micro computed tomography, the internal structure of the polymer composites is examined and the interparticle distances are calculated. The structure of the composites is then related to the water diffusion kinetics upon exposure to saline solution as well as humid air. Even though the hydrogel particles are isolated and the interparticle distances are in the order of several micrometers, a sudden increase in the water diffusion kinetics is observed above a critical concentration. Due to the low water permeability of the matrix, such a change in the water diffusion kinetics is indicative of network formation. During hydration, swelling enables the hydrogels to overcome the interparticle distances and form a network for water transport.

Received 15th June 2020,
Accepted 7th August 2020

DOI: 10.1039/d0sm01103g

rsc.li/soft-matter-journal

1 Introduction

Polymer composites are used in a wide variety of applications because they combine desirable properties of polymers with functional properties of the fillers. Skin adhesives are one such type of composites, where the polymer matrix is used to provide adhesion and fillers are introduced to adjust the viscoelastic behaviour, release active ingredients, or allow for water transport.^{1–6} The latter is important to avoid moisture accumulation below the adhesive due to transepidermal water loss or perspiration. Water at the skin-adhesive interface can have adverse effects on adhesion and causes hyperhydration of the skin. Therefore, removal of water is crucial to promote skin health as well as retain adhesion during perspiration.^{7–13}

Since the polymer matrices in such composites often have low permeabilities, the water transport behaviour is tuned through the addition of hydrogel particles.^{14–17} The relationship between mass uptake and time is indicative of the type of diffusion. Fickian diffusion scales with the square root of time and is characterised by random movement of the diffusant.^{18–20}

In that case, the uptake kinetics of polymer composites can be described with an effective diffusion coefficient, D_{eff} :

$$D_{\text{eff}} = \frac{\pi L^2}{16 M_{\infty}^2} \cdot \frac{M_t^2}{t} \quad (1)$$

where L is the thickness of the composite, M_t the water uptake at time t , and M_{∞} the uptake capacity.^{21–24} The effective diffusion coefficient describes the water transport kinetics of the composite as a homogeneous material and holds contributions of the diffusion within the polymer matrix as well as within the particles. For heterogeneous systems, where the individual components show different water transport properties, the effective diffusion coefficient strongly depends on the respective concentrations. Maxwell–Garnett has postulated an equation which can be used to predict the concentration dependence for composites with a continuous matrix phase and isolated particles:^{25,26}

$$D_{\text{eff}} = D_m \cdot \left(1 + \frac{3 \cdot (D_f - D_m) \cdot \phi}{D_f + 2D_m - (D_f - D_m) \cdot \phi} \right) \quad (2)$$

where D_f and D_m are the diffusion coefficients of the particles and the matrix respectively and ϕ is the particle volume fraction. However, as soon as the particles form a network, two continuous phases exist and the diffusion kinetics deviate from the predictions by Maxwell–Garnett. For particles that exhibit a higher diffusion coefficient than the matrix, the diffusion is no longer limited by the permeability of the matrix

^a Department of Chemistry, Technical University of Denmark, 2800 Kgs. Lyngby, Denmark. E-mail: esth@kemi.dtu.dk

^b Coloplast A/S, 3050 Humlebæk, Denmark

^c Department of Energy Conversion and Storage, Technical University of Denmark, 2800 Kgs. Lyngby, Denmark

† Electronic supplementary information (ESI) available. See DOI: 10.1039/d0sm01103g

but rather the connectivity of the particles. Consequently, a change in the water diffusion kinetics or saturation of polymer composites can be observed above a critical concentration, where the particles have formed a continuous network.^{27,28}

The interparticle distance of particles in a polymer composite can be calculated as a function of the particle volume fraction, geometry, and arrangement. Typically, particles in polymer composites are characterised by a distribution of sizes and irregular shapes. Depending also on the dispersion of the particles, a variety of interparticle distances can be observed. However, in order to approximate the structure in polymer composites, a model interparticle distance, δ_{model} , can be calculated based on a hexagonally close-packed structure (see ESI†) of spherical particles with a diameter, d , and a volume fraction, ϕ :

$$\delta_{\text{model}} = \left(\left(\frac{\sqrt{2}}{\phi} \cdot \frac{4\pi}{3} \right)^{\frac{1}{3}} - 2 \right) \cdot \frac{d}{2} \quad (3)$$

In this study, we use a model system for skin adhesives to investigate the relationship between the distribution of particles within the composite and the resulting water transport properties. A model for the distribution of interparticle distances in polymer composites at different volume fractions is established and evaluated with X-ray micro computed tomography (μCT). The internal structure is then correlated with the water diffusion kinetics of the composites. Here, we choose to immerse the composites in saline solution and expose them to a humid environment to simulate transepidermal water loss and perspiration respectively (see schematics in Fig. 1). This enables a better understanding of the effect of particle networks on the water diffusion kinetics in polymer composites.

2 Materials and methods

Rubber-based composite systems with different particle loadings were investigated. For skin adhesives, polyisobutene (PIB) is

typically used to provide adhesion and styrene-isoprene-styrene (SIS) is added to improve the mechanical properties. In our composites, the polymer matrix consisted of 80 wt% PIB (BASF, Germany) and 20 wt% SIS (Kraton, USA). The polymers were mixed in a Brabender Plastograph (Brabender, Germany) at 90 °C and 30 rpm for 45 min in batches of 60 g. Since the density of both polymers was 0.92 g cm⁻³, the blend was also expected to have the same density. Cross-linked sodium poly(acrylic acid) hydrogel particles (PAA, Stewart Superabsorbent, USA) were used as a hydrophilic filler. The particle size distribution had been characterised by optical microscopy and an average diameter, $d_{\text{mic}} = 18.2 \mu\text{m}$, was determined. The hydrogel particles with a density of 1.65 g cm⁻³ were added to the matrix to yield nominal volume fractions, ϕ_{nom} , of 0.06, 0.09, 0.12, 0.19, 0.27, 0.35, 0.46, and 0.57 respectively. The composites were mixed in batches of 60 g for another 45 min under vacuum at 90 °C and 30 rpm. The samples were then pressed to a thickness of 1 mm in between two release liners (siliconised paper). A hydraulic press (Stenhøj, Denmark) at 90 °C was used at a load of 10 t with a holding time of 30 s.

2.1 X-ray micro computed tomography

X-ray μCT was performed to assess the distribution of particles within the polymer matrix in the dry state. Composites with nominal volume fractions of 0.09, 0.12, and 0.27 were chosen to represent the composite system. The contrast between the materials in our study originates from the differences in their density and it has been shown that even small density differences can give sufficient contrast for the analysis.^{29–32} X-ray μCT scans were conducted using a lab-based Xradia Versa XRM-410 instrument using a W reflection target and a CCD with 2000 × 2000 pixels. Scans were performed at a voltage of 40 kV, a power of 10 W, no filter, 10× optical magnification, camera binning 2, an exposure time of 20 s and a total of 3201 projections over a 360° rotation, resulting in a pixel resolution of 1.1 μm . Samples with approximate dimension of 1 mm × 1 mm × 1 mm were mounted on plastic sticks with a diameter of ca. 1 mm.

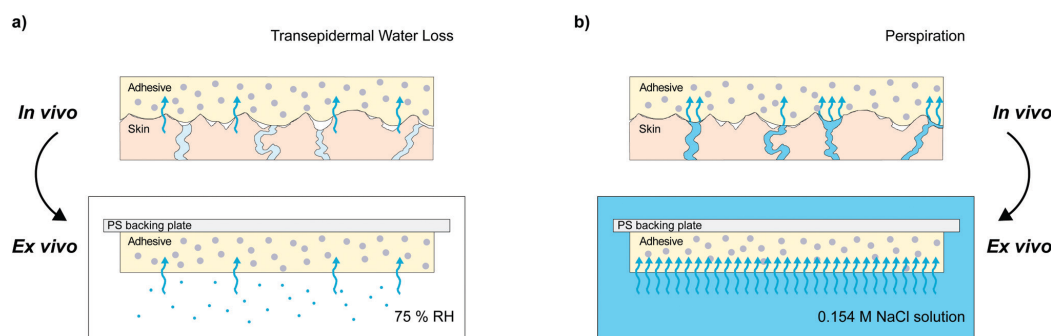


Fig. 1 Illustration of an adhesive on human skin. In order to maintain skin health as well as adhesion, moisture should be removed from the skin-adhesive interface (blue arrows). (a) To simulate transepidermal water loss, the polymer composites are exposed to a humid environment at 75% RH and 32 °C. (b) Perspiration is simulated by the immersion of the polymer composites in 0.154 M NaCl solution at 32 °C.

The recorded data was reconstructed using Feldkamp–Davis–Kress reconstruction algorithm with recon filter = sharp and beam hardening constant = 0.05. The reconstructed 3D data was processed and analyzed by using the commercial software Avizo in the following way: filtering with a Symmetric Nearest Neighbor (SNN) filter with size = 7 in 3D. The filler particles were segmented by a global threshold and labels were smoothed in 3D with size = 3. To analyze individual particles, Separate Objects algorithm was applied with method = Chamfer, 3D, neighborhood = 6 and marker extent = 3. The data analysis was carried out with a cutoff for particle diameters below 2 μm .

2.2 Rheology

The viscoelastic properties of the composites were assessed in duplicate with a Discovery HR-2 rheometer (TA instruments, USA) with a parallel plate geometry at 32 °C. The samples had a diameter of 20 mm and a thickness of 1 mm. Amplitude sweep experiments at a frequency of 1 Hz were conducted to identify the linear viscoelastic region of the polymer composites. Frequency sweeps between 0.0001 and 100 Hz were then measured at a strain within the viscoelastic region (0.1%). One representative frequency sweep curve is reported for each composition (see ESI† for all curves).

2.3 Vapour uptake

To simulate conditions for transepidermal water loss, the polymer composites were exposed to a humid environment of 75% RH and 32 °C. The composites of 1 mm thickness and 50 mm in diameter were adhered to a polystyrene backing plate and placed in a climate chamber (Binder, Germany). The mass uptake of three replicates of each composite was monitored gravimetrically using an analytical balance. From the uptake capacity of the pure particles, the normalised vapour swelling of the composites and the effective diffusion coefficient were calculated.

2.4 Liquid immersion

An immersion test in saline solution (0.154 M NaCl) at 32 °C was conducted to evaluate the response of the polymer composites upon exposure to sweat. Here, the sample dimensions were 25 mm by 25 mm with a thickness of 1 mm. To measure the mass uptake, the composites were periodically removed from the liquid, weighed and re-immersed. In all cases, the mass increase was the sum of particle swelling within the composite and particle elution from the matrix. Therefore, the data was not used to extract diffusion kinetics. After the occurrence of significant disintegration, the samples were discarded. An average of six replicates for each composite was reported.

3 Results and discussion

3.1 Structural analysis

X-ray μCT measurements were conducted to evaluate the internal structure of the polymer composites at nominal particle loadings of 0.09, 0.12, and 0.27. The individual hydrogel particles were segmented out and visualised within the polymer

matrix and compared to the morphology of the hydrogel particles before incorporation into the polymer matrix (see video rendering and images in ESI†). In addition to the visualisation of particles, quantitative data was also extracted from the X-ray μCT measurements. Firstly, the effective particle volume fraction within the composite, ϕ_{eff} , was calculated from the volume of the particles. This yielded values of 0.10, 0.12, and 0.29 for the respective composites, thusly showing close agreement with the nominal particle loadings.

Secondly, the particle size was estimated from the volume of the individual particles. Even though the particles appeared irregular in shape, only minimal elongation was observed. Hence, the particle morphology was reduced to spheres in order to determine a particle size distribution and estimate their average diameter, d_{CT} . The results coincided well with the particle size distributions and average diameter obtained by optical microscopy, d_{mic} (see Fig. 2). Noteworthy, the composite with a nominal particle volume fraction of $\phi_{\text{nom}} = 0.09$ contained a larger amount of fine particles. This resulted in a decreased average particle diameter of $d_{\text{CT}} = 12.5 \mu\text{m}$ as compared to $d_{\text{mic}} = 18.2 \mu\text{m}$.

Thirdly, the center of gravity of every individual particle was determined. In combination with the associated particle diameters, the interparticle distances could be calculated as the shortest surface-to-surface distances. Consequently, a myriad of interparticle distances was obtained for all three composites. Their distributions could be approximated with normal distributions around an average, δ_{CT} , with a standard deviation σ_{CT} (see Fig. 3a–c). The occurrence of a normal distribution thereby stems from a random distribution of particles within the composite. Here, the coefficient of variation, $\text{CV} = \frac{\sigma_{\text{CT}}}{\delta_{\text{CT}}}$, is an indicator of the degree of dispersion.³³ For all three composites a coefficient of variation of $\text{CV} \approx 0.8$ was observed. The fact that a constant coefficient of variation was observed indicates

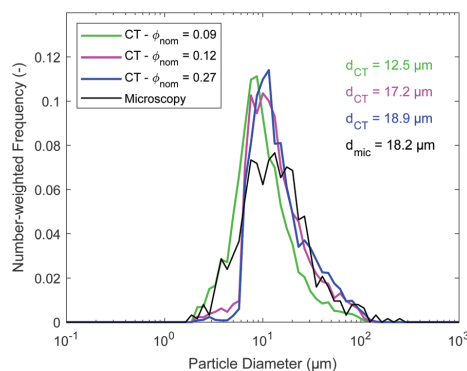


Fig. 2 Particle size distribution of the hydrogel particles in the polymer matrix at three different volume fractions, $\phi_{\text{nom}} = 0.09$ (green), $\phi_{\text{nom}} = 0.12$ (purple) and $\phi_{\text{nom}} = 0.27$ (blue) as well as before incorporation (black). The particle sizes were obtained from X-ray μCT data for the polymer composites and from optical light microscopy for the particles before incorporation into the polymer matrix.

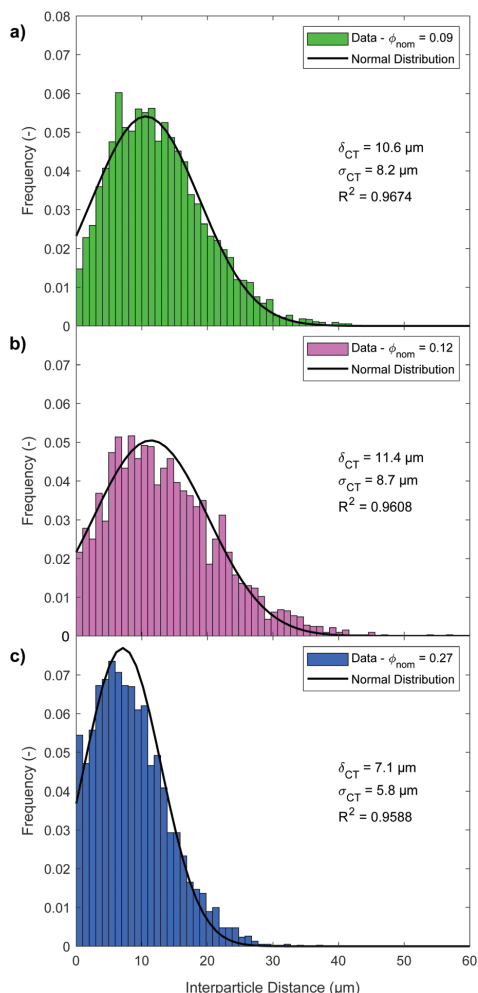


Fig. 3 The observed interparticle distances of the hydrogel particles in the polymer matrix are shown for composites with nominal particle volume fractions of (a) $\phi_{\text{nom}} = 0.09$, (b) $\phi_{\text{nom}} = 0.12$, and (c) $\phi_{\text{nom}} = 0.27$. The experimental data was approximated with a normal distribution and a mean as well as a standard deviation were determined.

that the same degree of dispersion was achieved at all particle loadings.

3.2 Model for the distribution of interparticle distances

The volume fraction, particle size distribution, and normal distribution of interparticle distances all imply good dispersion of the hydrogel particles within the composite. Therefore, the experimentally obtained interparticle distances were compared with the model calculations. Inserting ϕ_{eff} and d_{CT} into eqn (3) yields the model interparticle distances for the respective composites, which are summarised in Table 1 and show good

Table 1 Summary of results from the X-ray μ CT measurements

$\phi_{\text{nom}} (-)$	$\phi_{\text{CT}} (-)$	$d_{\text{CT}} (\mu\text{m})$	$\delta_{\text{model}} (\mu\text{m})$	$\delta_{\text{CT}} (\mu\text{m})$	$\sigma_{\text{CT}} (\mu\text{m})$	CV (-)
0.09	0.10	12.5	11.7	10.6	8.2	0.78
0.12	0.12	17.2	14.3	11.4	8.7	0.77
0.27	0.29	18.9	6.9	7.1	5.9	0.83

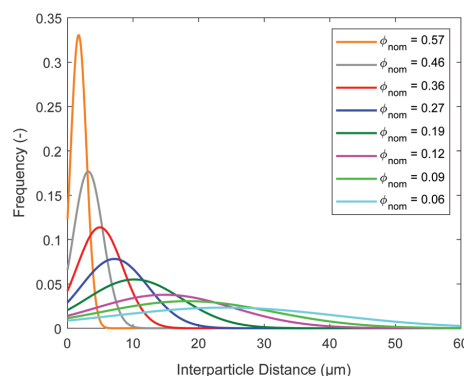


Fig. 4 Model distributions of interparticle distances are depicted for polymer composites containing different volume fractions of hydrogel particles. Inserting a particle diameter of $18 \mu\text{m}$ and the relevant volume fractions into eqn (4), the interparticle distances within the composites in this study could be estimated.

agreement with the experimental values. Even though the model is based on a hexagonally close-packed structure, it describes the average interparticle distance adequately.

In order to also account for the random distribution of particles and the variety of interparticle distances, a normal distribution is then imposed on the model calculations:

$$\delta_{\text{normal}} = \frac{1}{\sqrt{2\pi\sigma^2}} \cdot e^{-\frac{(x-\delta_{\text{model}})^2}{2\sigma^2}} \quad (4)$$

This enables us to estimate the entire distribution of interparticle distances for the remaining composites (see Fig. 4). Thereby, an average particle diameter of $d = 18 \mu\text{m}$ was used along with a standard deviation of $\sigma = 0.8 \cdot \delta_{\text{model}}$, which was determined from the constant coefficient of variation. Due to the size of the particles, the interparticle distances remain in the order of micrometers. Even at the highest particle loading $\phi_{\text{nom}} = 0.57$ in this study, the average interparticle distance is $\delta_{\text{model}} \approx 1.6 \mu\text{m}$.

3.3 Absence of rheological percolation

Particle-particle interactions greatly influence the viscoelastic properties of polymer composites. While colloidal interactions such as van der Waals, steric, electrostatic, and depletion forces only occur at distances up to several nanometers, hydrodynamic interactions have much larger length scales.³⁴ Studies on nanocomposite systems suggest that the occurrence of particle networks can be inferred by the onset of a power-law dependence of the viscosity or storage modulus on the particle

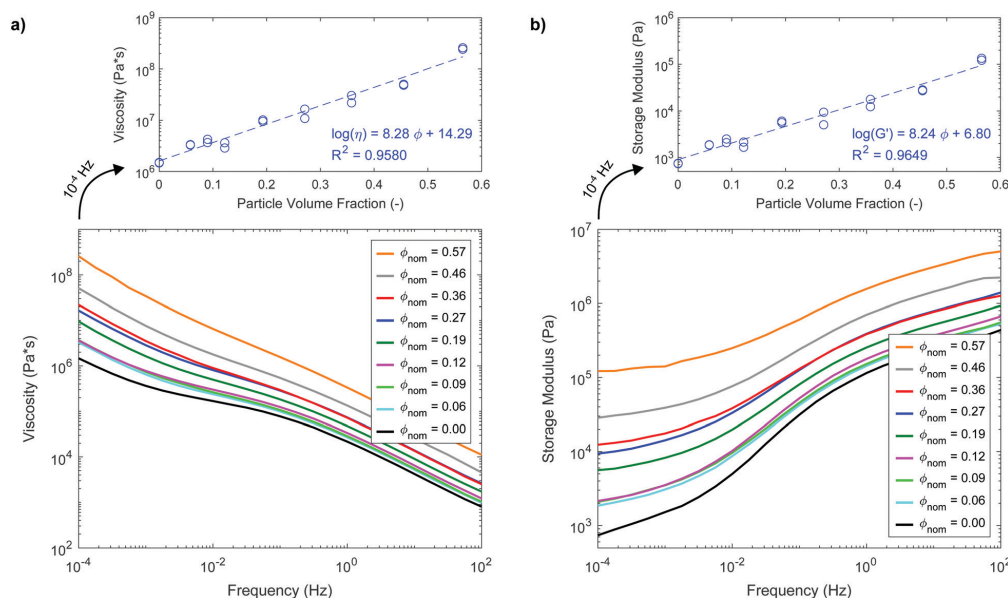


Fig. 5 The rheological measurements were carried out within the linear viscoelastic region at an amplitude of 0.1%. (a) The viscosity and (b) the storage modulus as a function of frequency for different particle volume fractions. At a frequency of 0.0001 Hz, both properties increased with particle loading.

volume fraction.³⁵ A drastic increase in the rheological property, which can span several orders of magnitude, can be observed around the percolation threshold.^{36–38} Moreover, percolated networks manifest themselves with the occurrence of a plateau in the storage modulus at low frequencies, where polymer chains are able to relax during deformation.^{39–41} This apparent yield stress occurs when a network of particles has formed and their elastic properties dominate the mechanical response of the polymer composite. It has been shown that the observation of rheological percolation strongly depends on the particle size. As the interparticle distance increases with increasing particle diameter (see eqn (3)), the particle–particle interactions become less pronounced and rheological percolation may not be observed.^{42–44} Since the interparticle distances in the composites of this study were in the order of several micrometers, the onset of a power-law behaviour was not observed during rheological measurements in either the viscosity or the storage modulus (see Fig. 5a and b). Instead, both rheological properties exhibited a smooth exponential increase with increasing particle loading. This was consistent with an increasing proportion of stiff particles in a soft polymer matrix and a stiffening through their hydrodynamic interactions⁴⁵ (see also ESI†). However, an additional stiffening effect due to the formation of percolated networks did not seem to occur.

3.4 Particle networks in humid conditions

To mimic transepidermal water loss from skin, the polymer composites were exposed to a humid environment of 75% RH and 32 °C. The polymer matrix exhibited low water permeability

(see ESI†) and also did not contribute to the increase in mass during these conditions. However, the hydrogel particles reached an equilibrium swelling of $54.5 \pm 0.1\%$ by weight within the polymer matrix when exposed to 75% RH and 32 °C. Due to such opposing behaviour, the water diffusion kinetics of the composites therefore strongly depend on the particle loading and connectivity. As expected, the composites in this study showed increasing water vapour uptake with increasing particle loading (see Fig. 6). The uptake scaled with the square-root of time in all cases and was therefore associated with Fickian diffusion.

Evidently, the distance between the hydrogel particles decreases with increasing particle loading. Therefore, the polymer matrix, which separates the particles, becomes thinner and its permeance increases and allows for faster water transport. At particle volume fractions $\phi_{nom} \leq 0.12$, the increase in permeance may have sufficed to explain the increase in the water vapour uptake rate, $\frac{M_t}{\sqrt{t}}$ (see Fig. 7a). However, a dramatic increase in the water vapour uptake rate occurred at particle loadings $\phi_{nom} \geq 0.19$. This implies that the diffusion of water is not strictly limited by the permeability of the matrix anymore and suggests that water is transported directly between the particles. The sharp increase in the water vapour uptake rate is therefore indicative of network formation within the polymer composites to enhance the transport kinetics.

Furthermore, the effective diffusion coefficient of the composites was calculated from eqn (1) and plotted against the particle volume fraction (see Fig. 7b). At low volume fractions

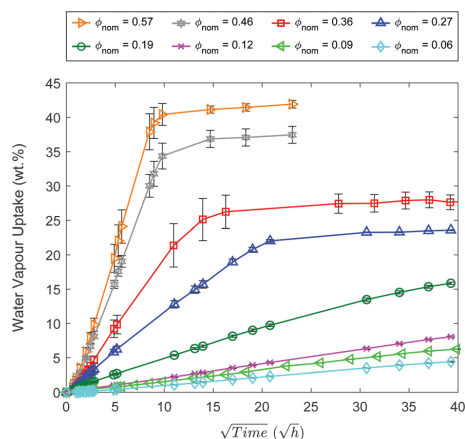


Fig. 6 Water vapour uptake of composites with different particle volume fractions at 32 °C and 75% RH. The uptake scaled with the square root of time until a saturation occurred, which indicates that the kinetics were Fickian.

$\phi_{\text{nom}} \leq 0.12$, the diffusion coefficient was independent of the particle loading, while at volume fractions $\phi_{\text{nom}} \geq 0.19$, an increase in the diffusion coefficient was observed until a plateau finally occurred at $\phi_{\text{nom}} \geq 0.46$. The development of D_{eff} with particle loading deviated notably from the predictions by Maxwell–Garnett (eqn (2)). Since the Maxwell–Garnett equation is based on isolated particles, the deviation of the experimental results also implies that particles are not completely isolated but networks have formed at particle loadings $\phi_{\text{nom}} \geq 0.19$.

3.5 Particle networks in wet conditions

To simulate exposure to sweat, the polymer composites were submersed into saline solution. Also here, the polymer matrix showed low permeability and also did not contribute to the mass uptake of the composites. On the other hand, the hydrogel particles within the polymer matrix swelled by approximately $2640 \pm 200\%$ by weight during exposure to 0.154 M NaCl solution. Due to this discrepancy, the diffusion kinetics of the composites strongly depend on the particle loading and structure. At $\phi_{\text{nom}} = 0.06$, only an initial uptake but no further increase in weight was observed (see Fig. 8). This indicates that the hydrogel particles were isolated and therefore no continuous transport occurred after some uptake by particles at the surface. Here, the interparticle distances were too large to allow for water transport between the isolated hydrogel particles at the given time scales.

At $\phi_{\text{nom}} = 0.09$, an initial absorption, likely to be caused by hydrogel particles at the surface, was followed by a plateau. During the plateau, particle swelling and elution were balanced until a further weight increase of the composite was observed. This implies that water was absorbed beyond the first layer of hydrogel particles at the surface and a network has formed. A continuous water transport was observed at nominal particle

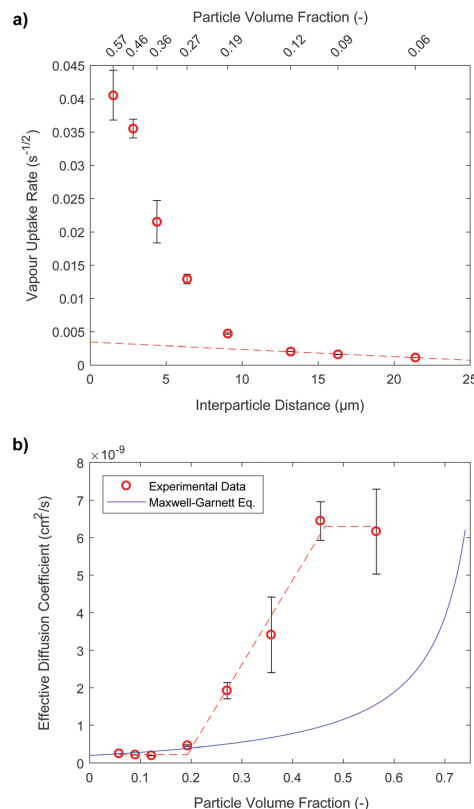


Fig. 7 (a) The vapour uptake rate of the polymer composites as a function of their average interparticle distance. As the hydrogel particles come closer, the thickness of the polymer film in between decreases and thus the permeance increases. However, at loadings $\phi \geq 0.19$ the effect of an increased permeance does not suffice to explain the uptake kinetics any more. (b) The effective diffusion coefficient at 75% RH and 32 °C as a function of particle loading. The discrepancy between the experimental data and the predictions through the Maxwell–Garnett equation implies that the hydrogel particles were not isolated at loadings $\phi \geq 0.19$.

volume fractions $\phi_{\text{nom}} \geq 0.12$, which indicates that particle networks exist.

3.6 Swelling-induced network formation

The observation of network phenomena strongly depends on the experimental technique. Rheological percolation requires mechanical interactions of the particles in a three-dimensional network. It has been associated with the entrapment of polymer chains, and therefore interparticle distances in the order of the length of the polymer chains of the matrix.^{36,43,46} For the polymer composites in this study, SIS is expected to have the longest chains and its radius of gyration was estimated to 20 nm.^{47,48} The amount of hydrogel particles within that distance can be calculated from the model distributions of interparticle distances in Fig. 4. Here, the cumulative

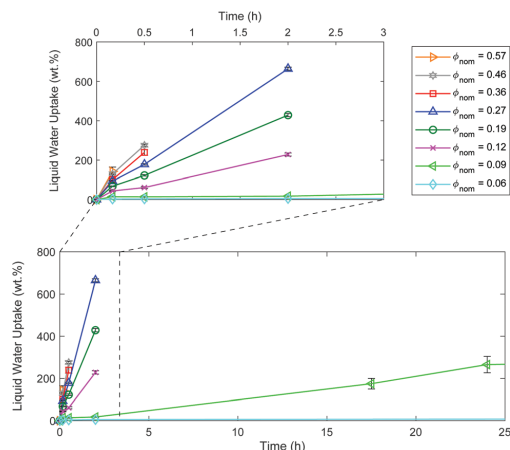


Fig. 8 The liquid water uptake of the polymer composites upon immersion in saline solution as a function of time. At a particle loading $\phi_{\text{nom}} = 0.06$, only minimal water uptake was observed. Here, the uptake of liquid water was limited to hydrogel particles at the surface without further transport into the bulk. Though, considerable water uptake was observed at particle volume fractions $\phi_{\text{nom}} \geq 0.09$. This implies that particle networks facilitated a continuous transport of water.

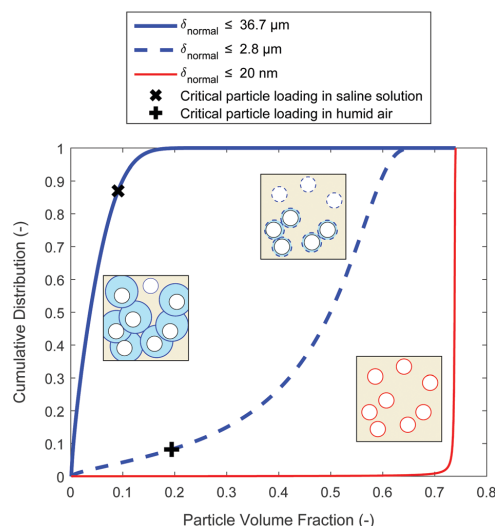


Fig. 9 The total amount of hydrogel particles within three specific inter-particle distances as a function of particle loading. The predictions were made from the cumulative distributions of the established model (eqn (4)) to represent swelling in 0.154 M NaCl solution ($\delta \leq 36.7 \mu\text{m}$), swelling at 32 °C and 75% RH ($\delta \leq 2.80 \mu\text{m}$), and the polymer matrix chain length for rheological percolation ($\delta \leq 20 \text{ nm}$).

distribution reveals the amount of particles with an interparticle distance below 20 nm. Taking into account the distributions at different particle loadings, a curve can be constructed, which shows the amount of particles with $\delta_{\text{normal}} \leq 20 \text{ nm}$ as a function of particle loading (see Fig. 9). Consequently, the cumulative distributions reveal that only a negligible fraction of hydrogel particles was within 20 nm of their nearest neighbours. First in the vicinity of the maximum packing fraction, a steep increase would be observed. Therefore, the polymer composites in this study are not expected to show effects of rheological percolation, which is in line with the experimental observations.

Conversely, network effects can be observed upon exposure to water vapour or liquid water even though the particles were initially separated by a layer of polymer matrix as seen with X-ray μCT and indicated by the absence of rheological percolation. We have monitored the polymer composites during the absorption of water through time-resolved chemical imaging in a previous study, where the swelling of the hydrogel particles caused a rupture of the surrounding polymer matrix.¹⁷ During exposure to water vapour at 32 °C and 75% RH in this study, the hydrogel particles swell by 54.5%, which corresponds to an increase of 2.8 μm in diameter. We speculate that the expansion of the particles causes a rupture of the polymer matrix and enables a swelling-induced network formation if the interparticle distances are sufficiently small. Experimentally, this leads to the observation of enhanced transport kinetics above a critical particle loading $\phi_{\text{nom}} = 0.19$. A further increase in particle loading results in a smooth increase in D_{eff} until a plateau occurs at $\phi_{\text{nom}} = 0.46$. A smooth increase in particle connectivity is also observed in the model calculations (see Fig. 9). However, here, the plateau only

occurs at particle loadings $\phi \geq 0.63$. Particle irregularities or directional swelling, which were not accounted for in the model, could be responsible for the observed discrepancies.

During exposure to saline solution, the hydrogel particles even swell by 2640% and their diameter increases by 36.7 μm . Experimentally, only composites above a critical particle loading of $\phi_{\text{nom}} = 0.09$ show a continuous absorption of liquid water beyond the surface of the composite. At this particle loading, approx. 87% of the hydrogel particles are within the swelling distance of their nearest neighbour according to the model (see Fig. 9). The increased swelling of the hydrogel particles therefore leads to a decrease in the critical loading for swelling-induced network formation as compared to the exposure to water vapour.

4 Conclusions

We explored the relationship between water diffusion and particle concentration in polymer composites with hydrogel particles as a model system for skin adhesives. A critical particle loading for continuous water transport was established and correlated with rheological percolation. It was found that water uptake can lead to swelling-induced network formation and effects of particle networks are therefore observed at loadings far below the rheological percolation threshold. This enables the design of skin adhesives with desired water diffusion kinetics at low particle loadings, while minimising the impact on the viscoelastic properties. Naturally, network formation based on water uptake highly depends on the degree

of swelling, which was exemplified by exposing the polymer composites to environments with different water activities. Thereby, increasing the amount of swelling brought a decrease in the critical loading for network formation. Therefore, it is of paramount importance to test the polymer composites within the relevant environment for the final application.

Conflicts of interest

There are no conflicts to declare.

Acknowledgements

Innovation Fund Denmark is gratefully acknowledged for financial support through the Grand Solutions Project #6151-00007B. The 3D Imaging Centre at the Technical University of Denmark is further acknowledged for conducting the X-ray μ CT experiments and segmentation of the data.

Notes and references

- 1 I. Webster, *Int. J. Adhes. Adhes.*, 1997, **17**, 69–73.
- 2 L. G. Ovington, *Clin. Dermatol.*, 2007, **25**, 33–38.
- 3 Z. Czech and A. Kowalczyk, *Wide Spectra of Quality Control*, 2011, pp. 309–332.
- 4 A. M. Wokovich, S. Prodduturi, W. H. Doub, A. S. Hussain and L. F. Buhse, *Eur. J. Pharm. Biopharm.*, 2006, **64**, 1–8.
- 5 B. Tighe and A. Mann, in *Advanced Wound Repair Therapies*, ed. D. Farrar, Elsevier, 2011, pp. 247–283.
- 6 N. Bait, B. Grassl, C. Deraill and A. Benaboura, *Soft Matter*, 2011, **7**, 2025–2032.
- 7 H. Matsumura, K. Oka, K. Umekage, H. Akita, J. Kawai, Y. Kitazawa, S. Suda, K. Tsubota, Y. Ninomiya, H. Hirai, K. Miyata, K. Morikubo, M. Nakagawa, T. Okada and K. Kawai, *J. Dermatol. Treat.*, 1997, **8**, 139–142.
- 8 H. Zhai and H. I. Maibach, *Skin Res. Technol.*, 2002, **8**, 1–6.
- 9 M. Gray, J. M. Black, M. M. Baharestani, D. Z. Bliss, J. C. Colwell, M. Goldberg, K. L. Kennedy-Evans, S. Logan and C. R. Ratliff, *J. Wound Ostomy Cont. Nurs.*, 2011, **38**, 233–241.
- 10 J. Eiler, D. Hansen, B. Bingöl, K. Hansen, J. Heikenfeld and E. Thormann, *Int. J. Adhes. Adhes.*, 2020, **99**, 102574.
- 11 D. Hansen, S. Zafjoroushan Moghaddam, J. Eiler, K. Hansen and E. Thormann, *ACS Appl. Polym. Mater.*, 2020, **2**, 1535–1542.
- 12 T. S. Spencer, S. E. Smith and S. Conjeevaram, *Polym. Mater.: Sci. Eng.*, 1990, **63**, 337.
- 13 D. D. Cunningham and M. G. Lowery, *Biomed. Microdevices*, 2004, **6**, 149–154.
- 14 F. Ferrari, M. Bertoni, M. C. Bonferoni, S. Rossi, C. Caramella and M. J. Waring, *Int. J. Pharm.*, 1994, **112**, 29–36.
- 15 R. Lipman, Hydrocolloid PSAs: New Formulation Strategies, *Medical Device & Diagnostic Industry Magazine*, 1999, vol. 21, pp. 132–148.
- 16 P. A. Edwardson, M. Walker, R. S. Gardner and E. Jacques, *J. Pharm. Biomed. Anal.*, 1991, **9**, 1089–1094.
- 17 D. Hansen, J. R. Brewer, J. Eiler, N. M. Komjani, K. Hansen and E. Thormann, *ACS Appl. Polym. Mater.*, 2020, **2**, 837–845.
- 18 A. Kishimoto, *Prog. Org. Coat.*, 1972, **1**, 91–112.
- 19 J. Crank, *The Mathematics of Diffusion*, 2nd edn, 1975.
- 20 G. K. Van Der Wel and O. C. Adan, *Prog. Org. Coat.*, 1999, **37**, 1–14.
- 21 C.-H. Shen and G. S. Springer, *J. Compos. Mater.*, 1976, **10**, 2–20.
- 22 H. Alamri and I. M. Low, *Polym. Test.*, 2012, **31**, 620–628.
- 23 M. R. Vanlandingham, R. F. Eduljee and J. W. Gillespie, *J. Appl. Polym. Sci.*, 1999, **71**, 787–798.
- 24 A. Espert, F. Vilaplana and S. Karlsson, *Composites, Part A*, 2004, **35**, 1267–1276.
- 25 J. C. Maxwell Garnett, *Proc. R. Soc. London*, 1904, **203**, 385–420.
- 26 J. R. Kalnin, E. A. Kotomin and J. Maier, *J. Phys. Chem. Solids*, 2002, **63**, 449–456.
- 27 A. Lekatou, S. Faïdi, D. Ghidaoui, S. Lyon and R. Newman, *Composites, Part A*, 1997, **28**, 223–236.
- 28 W. Wang, M. Sain and P. A. Cooper, *Compos. Sci. Technol.*, 2006, **66**, 379–386.
- 29 T. Centea and P. Hubert, *Compos. Sci. Technol.*, 2011, **71**, 593–599.
- 30 M. J. Emerson, K. M. Jespersen, A. B. Dahl, K. Conradsen and L. P. Mikkelsen, *Composites, Part A*, 2017, **97**, 83–92.
- 31 M. W. Czabaj, M. L. Riccio and W. W. Whitacre, *Compos. Sci. Technol.*, 2014, **105**, 174–182.
- 32 M. Ueda, K. Mimura and T.-K. Jeong, *Adv. Compos. Mater.*, 2016, **25**, 31–43.
- 33 Z. P. Luo and J. H. Koo, *J. Microsc.*, 2007, **225**, 118–125.
- 34 M. M. Rueda, M.-C. Auscher, R. Fulchiron, T. Périé, G. Martin, P. Sonntag and P. Cassagnau, *Prog. Polym. Sci.*, 2017, **66**, 22–53.
- 35 A. K. Kota, B. H. Cipriano, M. K. Duesterberg, A. L. Gershon, D. Powell, S. R. Raghavan and H. A. Bruck, *Macromolecules*, 2007, **40**, 7400–7406.
- 36 F. Du, R. Scogna, W. Zhou, S. Brand, J. Fischer and K. Winey, *Macromolecules*, 2004, **37**, 9048–9055.
- 37 G. Hu, C. Zhao, S. Zhang, M. Yang and Z. Wang, *Polymer*, 2006, **47**, 480–488.
- 38 S. Abbasi, P. J. Carreau, A. Derdouri and M. Moan, *Rheol. Acta*, 2009, **48**, 943–959.
- 39 L. A. Utracki, *Polym. Compos.*, 1986, **7**, 274–282.
- 40 A. V. Shenoy, *Rheology of Filled Polymer Systems*, Springer, Netherlands, Dordrecht, 1999.
- 41 P. Pötschke, T. D. Fornes and D. R. Paul, *Polymer*, 2002, **43**, 3247–3255.
- 42 A. Dorigato, A. Pegoretti and A. Penati, *EXPRESS Polym. Lett.*, 2010, **4**, 115–129.
- 43 X. Hao, J. Kaschta and D. W. Schubert, *Composites, Part B*, 2016, **89**, 44–53.
- 44 G. Havet and A. I. Isayev, *Polym. Sci., Ser. A*, 2012, **54**, 476–492.
- 45 G. Huber and T. A. Vilgis, *Macromolecules*, 2002, **35**, 9204–9210.
- 46 X. Huang, C. Kim, Z. Ma, P. Jiang, Y. Yin and Z. Li, *J. Polym. Sci., Part B: Polym. Phys.*, 2008, **46**, 2143–2154.
- 47 N. Dixit, A. Pape, L. Rong, E. Joseph and S. M. Martin, *Macromolecules*, 2015, **48**, 1144–1151.
- 48 R. W. Richards, *Eur. Polym. J.*, 1995, **31**, 1197–1206.

Supplementary Information

Water Transport in Polymer Composites through Swelling-Induced Networks of Hydrogel Particles

Johannes Eiler^{1,2}, Søren Bredmose Simonsen³, Daniel Hansen^{1,2}, Bahar Bingöl², Kristoffer Hansen², and Esben Thormann^{*1}

¹Department of Chemistry, Technical University of Denmark, 2800 Kgs. Lyngby, Denmark

²Coloplast A/S, 3050 Humlebæk, Denmark

³Department of Energy Conversion and Storage, Technical University of Denmark, 2800 Kgs. Lyngby, Denmark

^{*}Corresponding author: esth@kemi.dtu.dk

1 Model Calculations for the Interparticle Distance

To estimate the spacing between the particles within the composite, a simple model with spheres in a hexagonal close-packed (hcp) structure was established. The unit cell is a hexagonal prism, which contains six complete spheres (see Fig. S1 a). Its volume, V_{hcp} , can therefore be expressed as a function of the radius of the particle, r , and the particle volume fraction, ϕ :

$$V_{hcp} = \frac{6}{\phi} \cdot \frac{4}{3\pi} \cdot r^3 \quad (1)$$

The unit cell has a basal side length, a , and a height, h , which corresponds to the height of two tetrahedra with side length a :

$$h = 2 \cdot \frac{\sqrt{6}}{3} \cdot a \quad (2)$$

The volume of the unit cell can therefore also be written as:

$$V_{hcp} = \frac{3\sqrt{3}}{2} \cdot a^2 \cdot h = \frac{6}{\sqrt{2}} \cdot a^3 \quad (3)$$

Through Eq. 1 and 3, the basal side length can be expressed as:

$$a = \left(\frac{\sqrt{2}}{\phi} \cdot \frac{4\pi}{3} \right)^{\frac{1}{3}} \cdot r \quad (4)$$

In the model, the interparticle distance, δ_{model} , is calculated as the distance between the surfaces of two neighbouring spheres:

$$\delta_{model} = a - 2r = \left(\left(\frac{\sqrt{2}}{\phi} \cdot \frac{4\pi}{3} \right)^{\frac{1}{3}} - 2 \right) \cdot r \quad (5)$$

The resulting interparticle distances are shown as a function of particle loading and particle size in Fig. S1 b.

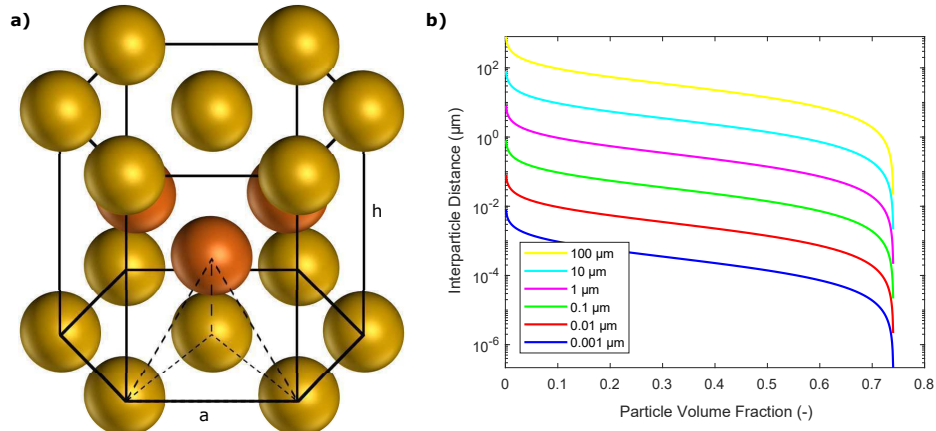


Figure S1: a) In the theoretical model, spherical particles were arranged in a hexagonally close-packed structure. The size of the spheres and the unit cell were determined by the particle size and their volume fraction respectively. b) The resulting interparticle distance, δ_{hcp} , as a function of particle volume fraction, ϕ , for different particle diameters.

2 Structural Analysis

X-ray μ CT measurements were conducted to evaluate the internal structure of the polymer composites at nominal particle loadings, ϕ_{nom} , of 0.09, 0.12, and 0.27. An example of the data obtained from the measurements is shown in Fig. S2 a and b. The individual hydrogel particles were segmented out and visualised within the polymer matrix and compared to the morphology of the hydrogel particles before incorporation into the polymer matrix (see Fig. S3 a and b).

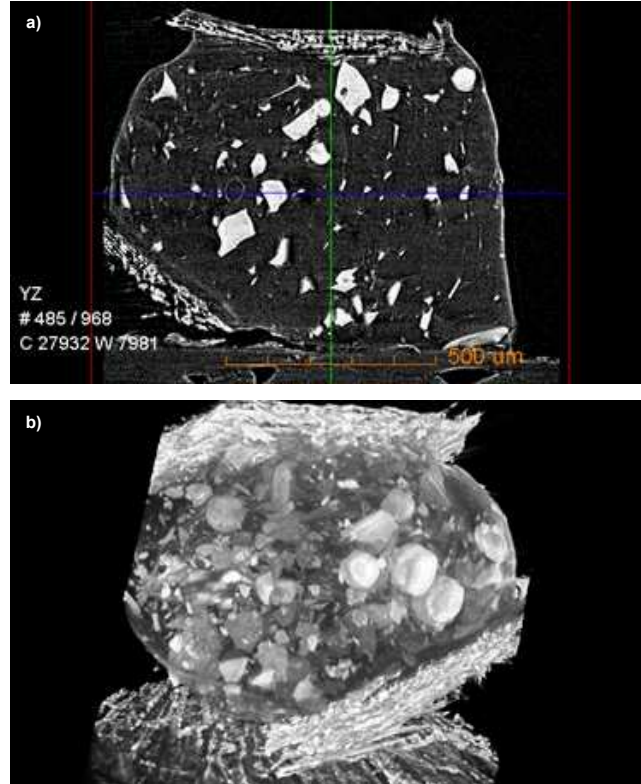


Figure S2: a) 2D slice in the reconstructed 3D volume from the x-ray μ CT scan of the composite containing particles at a volume fraction of $\phi_{nom} = 0.09$. The image is presented as given by the scanner software. b) 3D volume rendering of the reconstructed data from the x-ray μ CT scan of the composite containing particles at a volume fraction of $\phi_{nom} = 0.09$. The image is presented as given by the scanner software.

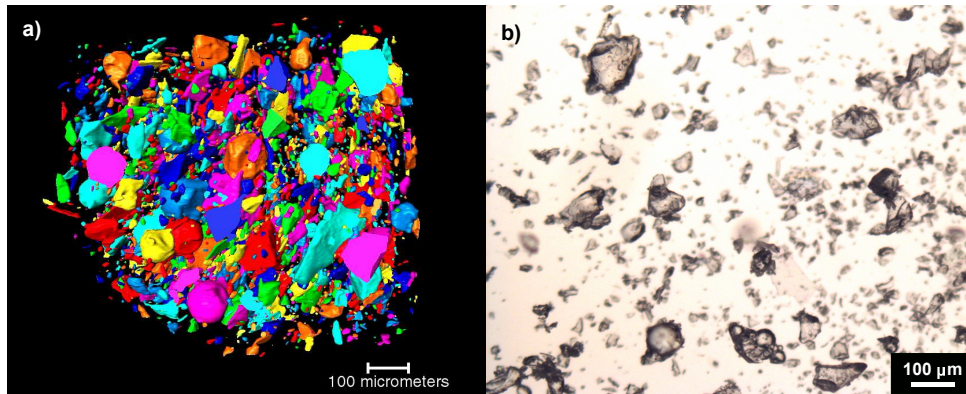


Figure S3: a) Hydrogel particles at $\phi_{nom} = 0.09$ in a soft and sticky matrix presented as a surface rendering of a segmentation of the x-ray μ CT data. b) Hydrogel particles before incorporation into the polymer matrix presented by a micrograph from optical light microscopy.

3 Rheological Measurements

Rheological measurements were carried out to evaluate the viscoelastic properties of the composites and gain information about the occurrence of particle networks. Amplitude sweeps were carried out at a frequency of 1 Hz over an amplitude range of 0.002 - 50 %. All measurements are shown in Fig. S4 a - i.

Frequency sweeps were carried out at an amplitude of 0.1 % over a frequency range of 0.0001 - 100 Hz. All measurements are shown in Fig. S4 j - r.

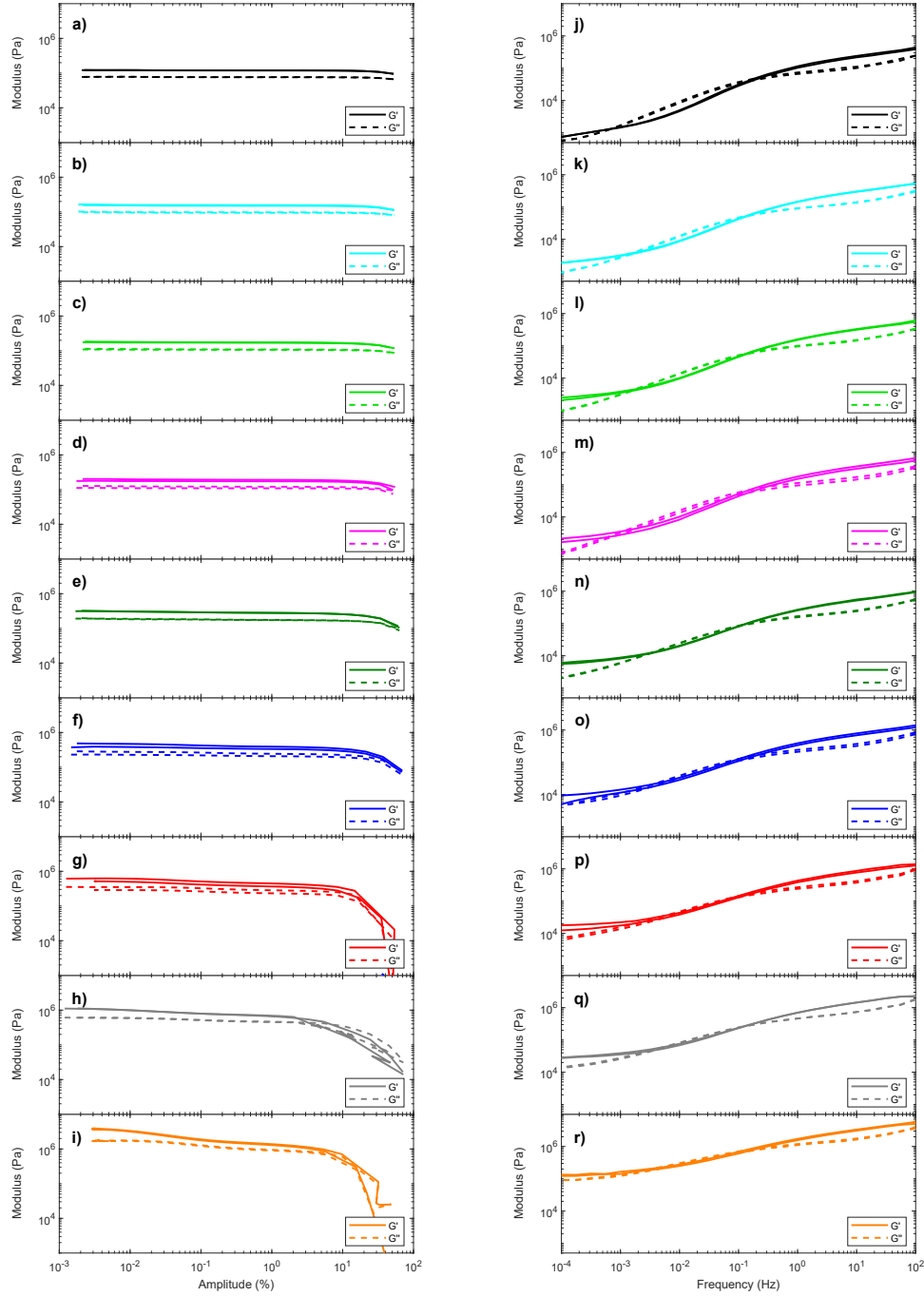


Figure S4: Amplitude sweep experiments at a frequency of 1 Hz at loadings of a) $\phi_{nom} = 0.00$, b) $\phi_{nom} = 0.06$, c) $\phi_{nom} = 0.09$, d) $\phi_{nom} = 0.12$, e) $\phi_{nom} = 0.19$, f) $\phi_{nom} = 0.27$, g) $\phi_{nom} = 0.36$, h) $\phi_{nom} = 0.46$, and i) $\phi_{nom} = 0.57$. Frequency sweep experiments at an amplitude of 0.1 % at loadings of j) $\phi_{nom} = 0.00$, k) $\phi_{nom} = 0.06$, l) $\phi_{nom} = 0.09$, m) $\phi_{nom} = 0.12$, n) $\phi_{nom} = 0.19$, o) $\phi_{nom} = 0.27$, p) $\phi_{nom} = 0.36$, q) $\phi_{nom} = 0.46$, and r) $\phi_{nom} = 0.57$.

4 Reduced Viscosity

Suspensions of particles in polymer liquids are dominated by hydrodynamic interactions and are often evaluated in terms of their reduced viscosity, which is defined as the viscosity of the suspension divided by the viscosity of the pure polymer. There exist many empirical and semi-empirical equations to describe the development of the reduced viscosity as a function of particle loading[1]. Thereby, Le Meins et al.[2] have used the Krieger-Dougherty equation to evaluate their suspensions:

$$\eta_r = \left(1 - \frac{\phi}{\phi_{max}}\right)^{-2.5\phi_{max}} \quad (6)$$

where η_r is the reduced viscosity, ϕ is the particle loading, and ϕ_{max} is the maximum particle loading. These empirical equations are typically evaluated at moderate strain rates around 0.1 s^{-1} . In Fig. S5, the development of the reduced viscosity is shown for the composites in our study along with the predictions according to the Krieger-Dougherty equation. The data show good coincidence with the predictions, implying that the hydrodynamic interactions between the particles are responsible for the increase in the reduced viscosity.

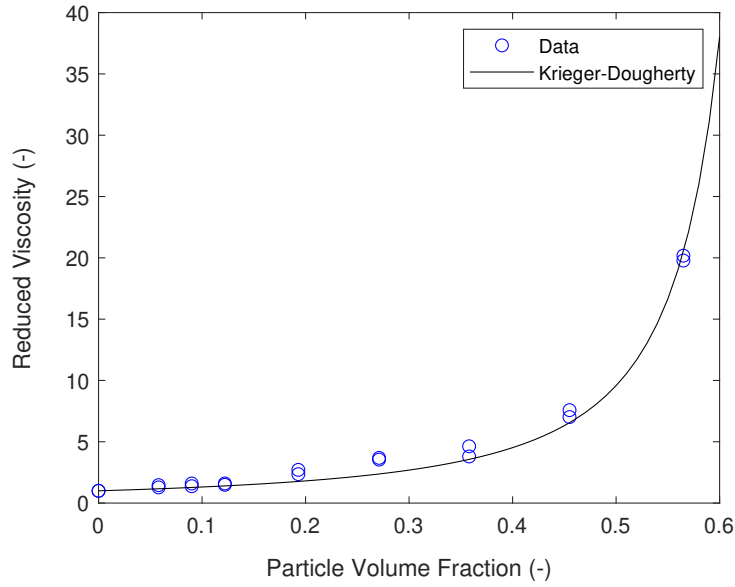


Figure S5: Development of the reduced viscosity at different particle volume fractions. The reduced viscosity has been calculated from the viscosity curves in Fig. 5 a in the manuscript at a frequency of 0.1 Hz.

5 Vapour Permeability of the Matrix

The water vapour transmission rate of the unfilled polymer matrix with a thickness of 1 mm was measured over a saturated NaCl solution (approx. 75 % RH) at 32 °C. After a lag period, during which the film was saturated, a water vapour transmission rate of 1.1×10^{-5} g/cm²/h was observed. In our experiments, if we assume that the polymer matrix is saturated instantaneously, there will be a water vapour transmission of 1.1×10^{-5} g/cm²/h (this can be regarded as the maximum rate of transmission). In Fig. S6, the cumulative transmission of water vapour through the matrix is shown along with the moisture uptake data for all composites in our study. At low particle concentrations, $\phi_{nom} = 0.06$ and $\phi_{nom} = 0.09$, the transmission through the matrix is in the order of the vapour uptake of the composites. Here, the particles are isolated and the diffusion within the particles only plays a minor role for the total diffusion. Increasing the particle loading, means that the transmission through the matrix becomes less important and diffusion through the particles is dominant.

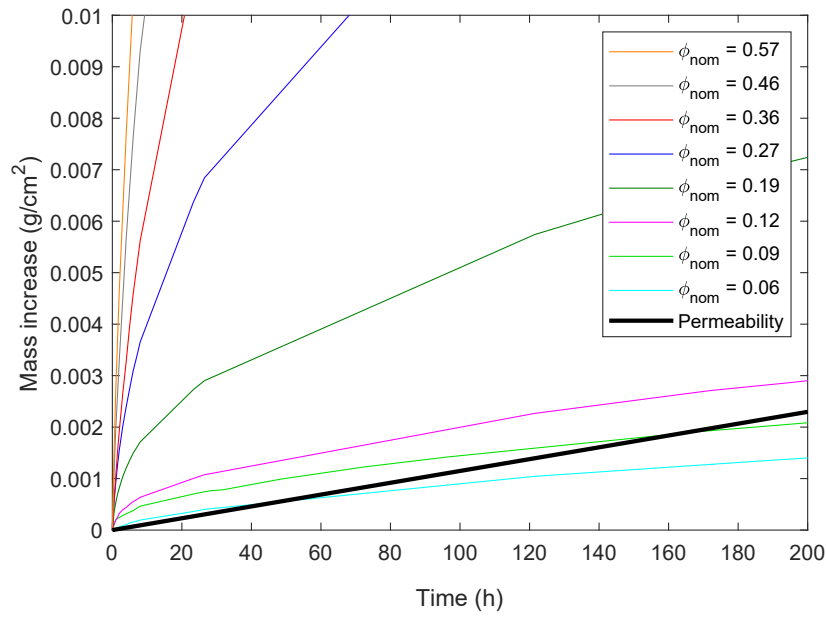


Figure S6: Water vapour uptake of the composites at 75 % RH and 32 °C. The water vapour transmission of the polymer matrix is indicated as the permeability for comparison.

References

- [1] A. B. Metzner, "Rheology of Suspensions in Polymeric Liquids," *Journal of Rheology*, vol. 29, no. 6, pp. 739–775, 2002.
- [2] J.-F. Le Meins, P. Moldenaers, and J. Mewis, "Suspensions of monodisperse spheres in polymer melts: particle size effects in extensional flow," *Rheologica Acta*, vol. 42, pp. 184–190, jan 2003.

Paper II - Tuneable and Responsive Formation of Swelling-Induced Hydrogel Networks for Water Transport in Polymer Composites

Tuneable and Responsive Formation of Swelling-Induced Hydrogel Networks for Water Transport in Polymer Composites

Johannes Eiler,^{†,‡} Daniel Hansen,^{†,‡} Bahar Bingöl,[‡] Kristoffer Hansen,[‡] and Esben
Thormann^{*,†}

[†]*Department of Chemistry, Technical University of Denmark, 2800 Kgs. Lyngby, Denmark*

[‡]*Coloplast A/S, 3050 Humlebæk, Denmark*

E-mail: esth@kemi.dtu.dk

Abstract

We investigate the tuneability and responsiveness of swelling-induced network formation of sodium poly(acrylic acid) hydrogel particles within a viscoelastic, hydrophobic polymer matrix. Efficient water transport throughout the polymer composite is only observed when networks of hydrogel particles exist, which form above a critical concentration of particles upon swelling. This critical concentration is adjusted through changes in the viscoelastic properties of the matrix where a stiffening hampers the swelling of the hydrogels and therefore increases the critical concentration. Network formation and water transport kinetics further respond to environmental stimuli like changes in pH or ionic composition. An acidic environment or the presence of divalent ions are shown to greatly reduce the swelling of the hydrogels and therefore increase the critical concentration needed for swelling-induced network formation.

Keywords

Polymer composites, Poly(acrylic acid), Water diffusion, Viscoelasticity, Network formation

1 Introduction

Smart materials, which can change their functionality based on environmental stimuli, have become ever more sought-after over the past decades. Polymers to be used as biosensors have been developed, which can e.g. change colour, shape, or wettability upon changes in salt concentration, temperature, or pH.¹⁻⁵ Similarly, research on membranes has been conducted to switch their permeabilities based on stimuli such as light, ionic strength, or electrical fields.⁶⁻⁸

Poly(acrylic acid) (PAA) is one of these polymers to show such stimulus-responsive behaviour. The polymer chains extend and swell dramatically upon hydration due to their hydrophilicity after deprotonation. When cross-linked and formulated into particles, a network of PAA can absorb up to 1000 g/g water and thus also finds applications as a superabsorbent polymer.^{9,10} Naturally, the water uptake behaviour of such materials also strongly depends on the pH of the solution. At low pH, the deprotonation of acid groups is limited, which leads to a coiled, hydrophobic structure of the polymer chains and hampers the water uptake.^{11,12} A maximum water uptake is often observed at neutral pH and above, where the polymer chains are charged.¹³

In order to further enhance the water uptake kinetics, PAA is often neutralised by substituting the hydrogen atom of the acid group with a sodium ion (see schematics in Fig. 1a and 1b). Upon hydration, the salt readily dissociates and creates an osmotic pressure within the polymer network.¹⁴ Here, the increased water uptake kinetics are no longer limited by Fickian diffusion but rather the relaxation times of the polymer chains.^{15,16} Consequently, the presence of ions in water can reduce the water uptake kinetics of neutralised PAA due to

a decrease in the driving force presented by the osmotic pressure. The presence of multivalent ions, though, not only decreases the osmotic pressure but also creates physical cross-links between the acid groups and therefore further reduces the swelling.^{11,12,17,18}

When incorporated into hydrophobic matrices, a network of such hydrogel particles is essential for the transport of water throughout the material (see schematics in Fig. 1c). Similar to electrical conductivity or mechanical stiffening, the composites do not exhibit the functional properties of the particles below a critical filler volume fraction, ϕ_{crit} .^{19–21} We have previously shown with X-ray micro-computed tomography that the interparticle distances decrease with increasing filler volume fraction, ϕ , and that network formation only occurs upon swelling of the hydrogel particles.²² Moreover, using chemical imaging, we have visualised the expansion of hydrogels within the polymer composite upon hydration, which leads to the formation of a network.²³ Consequently, any changes in the swelling behaviour of the hydrogel particles will also affect the network formation within the composites.

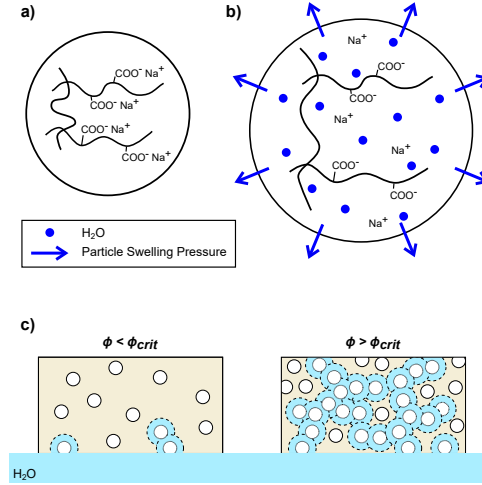


Figure 1: Schematic of a PAA-based hydrogel particle in a) the dry state and b) the hydrated state. c) Schematic illustration of polymer composites containing PAA hydrogel particles when exposed to water. Below the critical concentration for swelling-induced network formation, the particles remain isolated and water uptake is limited. Above the critical concentration, a network of particles forms upon swelling and enables continuous water uptake.

In this study, we explore the effect of different swelling restrictions on the network formation within water transporting composites. Firstly, hydrogel swelling is restricted by the matrix. Here, an increased stiffness is expected to limit the swelling of hydrogel particles and thus change the kinetics of water uptake as well as the associated critical concentration for network formation. Secondly, hydrogel swelling is restricted by a reduction in pH and the introduction of divalent ions, respectively. Both stimuli are expected to reduce the hydrogel particle swelling and therefore increase the critical concentration for swelling-induced network formation.

2 Material and Methods

Polymer composites based on a matrix of 80 wt.% polyisobutylene (PIB) and 20 wt.% styrene-isoprene-styrene (SIS) were used as a standard composition. In addition to this standard composition, polymer matrices containing 0 and 40 wt.% SIS, respectively, were also fabricated. The mixer (Brabender, Germany) was heated to 90 °C before SIS (Kraton, USA) and PIB (BASF, Germany) were inserted and mixed at 30 rpm for 45 min. The density of both polymers was 0.92 g/cm³ and therefore the density of the blends was also expected to be 0.92 g/cm³. Particles based on sodium poly(acrylic acid) (Stewart Superabsorbent, USA) with a density of 1.65 g/cm³ were then added at volume fractions of 0.06, 0.09, 0.12, 0.19, 0.27, and 0.36 respectively and mixed for another 45 min. To achieve a controlled geometry of the samples, the composites were pressed to a uniform thickness of 1 mm using a hydraulic press (Stenhøj, Denmark).

2.1 Rheology

The mechanical properties of the three different polymer matrices were evaluated in duplicate using a Discovery HR-2 rheometer (TA instruments, USA) with a parallel plate geometry at 32 °C. A circular punch was used to obtain samples with a diameter of 20 mm. First, amplitude sweep experiments at a frequency of 1 Hz were conducted to determine the linear viscoelastic region. Then, frequency sweep measurements were carried out between 100 Hz and 0.0001 Hz at an amplitude of 0.1 %, which was within the linear viscoelastic region for all polymer matrices.

2.2 Immersion Test

Liquid immersion tests in a 0.154 M NaCl solution were conducted at 32 °C to assess the swelling ratio of the polymer composites over time. The composites with dimensions of 25 x 25 x 1 mm³ were thereby inserted into the liquid, removed after predetermined time intervals to measure the weight gain and hereafter re-immersed. The swelling ratio of all 18 different compositions was determined gravimetrically as follows:

$$Swelling\ Ratio = \frac{m_t - m_d}{m_d} \quad (1)$$

where m_t is the weight of the composite after immersion for a given time, t , and m_d is the dry weight of the composite. In case of notable disintegration, the samples were discarded. Additionally, the standard composites containing 20 wt.% SIS were also tested in a solution with 0.154 M NaCl, which was adjusted to pH 2 using HCl as well as a solution, where the 0.154 M NaCl was exchanged with 0.077 M CaCl₂.

3 Results and Discussion

3.1 Tuneable Network Formation

The critical concentration for swelling-induced network formation and the water uptake kinetics were tuned by adjustments in the mechanical properties of the matrix through the addition of 0, 20 and 40 wt.% SIS. With increasing SIS content, the matrix was stiffened as indicated by an increased complex modulus, G^* , and a decreased loss tangent, $\tan \delta$ (see Fig. 2).

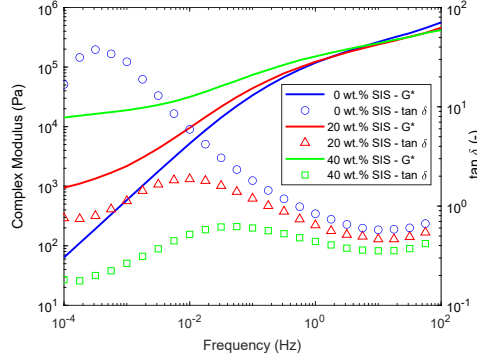


Figure 2: Rheological frequency sweep of polymer matrices with 0, 20, and 40 wt.% SIS respectively. Increasing the SIS content resulted in an increased complex modulus as well as a decreased loss tangent, thus stiffening the matrix.

The swelling ratio of the composites in a 0.154 M NaCl solution was then monitored gravimetrically. Only at a particle concentration of $\phi = 0.06$, no notable water uptake occurred within the softest matrix, containing no SIS (see Fig. 3a). Here, the swelling of the hydrogel particles was restricted to an extent, where the interparticle distances could not be bridged. Water was not transported into the bulk of the composite as network formation has not occurred. An increase in particle loading meant that particles came closer to their neighbouring particles. At loadings $\phi \geq 0.09$, the hydrogel particles were sufficiently close such that the swelling could induce network formation as indicated by continuous swelling of the composites. Hence, the critical concentration for swelling-induced network formation was $0.06 < \phi_{crit} < 0.09$ in a pure PIB matrix.

The addition of 20 wt.% SIS to the matrix generally resulted in a reduction of the swelling kinetics as compared to the composites without SIS (see Fig. 3b). Also here, no notable swelling was observed at a particle loading of $\phi = 0.06$ because the interparticle distances were too large. A lag period in the water uptake occurred at $\phi = 0.09$ where substantial swelling was necessary to overcome the interparticle distance. Therefore, the critical concen-

tration for swelling-induced network formation is expected to be close to this volume fraction for a matrix containing 20 wt.% SIS. Then, at particle loadings $\phi \geq 0.12$, continuous swelling was observed, which is indicative of hydrogel networks.

The swelling kinetics of the composites were further decreased when the matrix contained 40 wt.% SIS (see Fig. 3c). The swelling was completely restricted for particle loadings $\phi \leq 0.09$ while a lag period occurred at $\phi = 0.12$. At higher particle loadings $\phi \geq 0.19$ network formation occurred readily and continuous water uptake was observed.

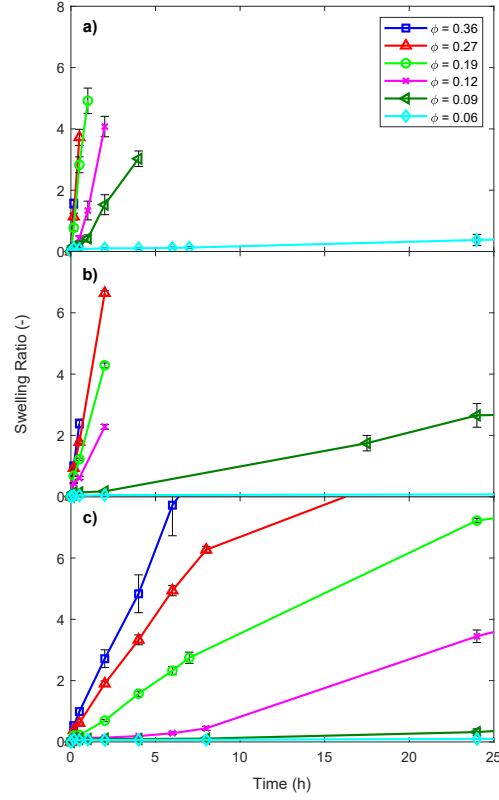


Figure 3: The swelling ratios of composites in a 0.154 M NaCl solution at 32 °C. By varying the stiffness of the matrix through the addition of SIS, different uptake kinetics are observed at: a) 0 wt.% SIS, b) 20 wt.% SIS, and c) 40 wt.% SIS.

To evaluate the change in water transport kinetics, the swelling ratio of the composites over time in Fig. 3a - c was approximated with a linear fit. This yielded swelling rates for all particle loadings in three different matrices. Here, the rates increased linearly with the particle weight fraction above a certain concentration (see Fig. 4a). The intercept with the x-axis was therefore interpreted as the critical concentration for swelling-induced network formation. Converting the intercepts to volume fractions, this yields $\phi_{crit} = 0.07$, $\phi_{crit} = 0.08$, and $\phi_{crit} = 0.13$ for matrices containing 0, 20, and 40 wt.% SIS, respectively. Evidently, the critical concentration for swelling-induced network formation is greatly influenced by

the mechanical properties of the matrix. An increase in the rigidity thereby reduces the swelling of the hydrogels such that higher particle loadings are necessary to achieve network formation (see schematics in Fig. 4b).

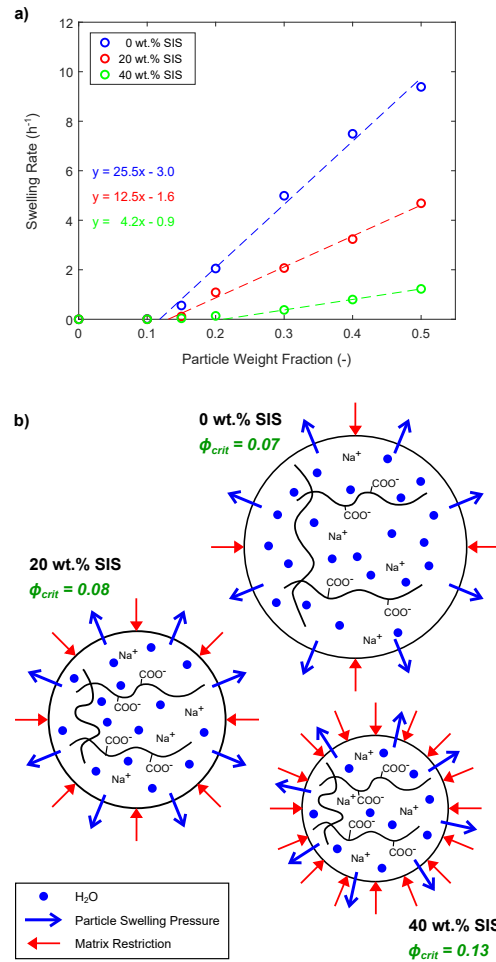


Figure 4: a) Swelling rates as a function of particle weight fraction. The swelling rates increased linearly with particle content above the critical concentration for swelling-induced network formation. The resulting slopes decreased with increasing mechanical stiffness. b) Schematic representation of the restrictions posed by the matrices.

The addition of hydrogel particles leads to higher swelling capacities of the composites and therefore also higher swelling rates. The slopes of this concentration dependency in Fig. 4a can be interpreted as the particle swelling rate within the respective matrices. Above the critical concentration, the addition of hydrogel particles into a matrix containing no SIS in-

creases the total swelling rate by 25.5 h^{-1} . While the particle swelling rate decreases to 12.5 h^{-1} in a matrix with 20 wt.% SIS, it decreases even further to 4.2 h^{-1} in a matrix containing 40 wt.% SIS. Since the hydrogel particles are isolated and surrounded by the polymer matrix in the dry state, the swelling is associated with an exertion of pressure on the matrix. This in turn causes a time-dependent deformation of the viscoelastic polymer matrix. For similar composite systems, it has previously been suggested that such low strain rates are associated with a viscous deformation of the polymer composites.²⁴

We speculate that the limits of elastic deformation are reached within the matrix after short times already and its viscous component therefore governs the swelling rates. Hence, the rheological response of the matrix was split into the elastic and viscous components with the storage modulus, G' , and the loss modulus, G'' . Since the particle swelling is influenced by the matrix (see Fig. 4a), the particle swelling rates were correlated with the viscoelastic properties of the polymers. Therefore, the particle swelling rates of 25.5 , 12.5 , and 4.2 h^{-1} were converted to frequencies of 0.0071 , 0.0035 , and 0.0012 Hz for the respective matrices. At these frequencies, the respective loss modulus of the matrix is approximately 4.5 kPa for each of the three cases (see Fig. 5). This implies that the hydrogel particles exert a pressure $P \approx 4.5 \text{ kPa}$ during swelling in a 0.154 M NaCl solution. This lies in the range of swelling pressures reported in literature, where hydrogel particles were exposed to liquids with known osmotic pressure or where a force apparatus was used to measure the swelling pressure directly.^{11,25} There, it has been shown that the osmotic pressure of such particles changes from $> 100 \text{ kPa}$ to $< 1 \text{ kPa}$ as a function of hydration. With increasing water content, the osmotic pressure decreases and therefore the determined swelling pressure of 4.5 kPa should be regarded as an average pressure during hydration of the hydrogel particles. This swelling pressure of the particles then causes variable swelling rates of the composites because of the different viscoelastic properties of the matrices.

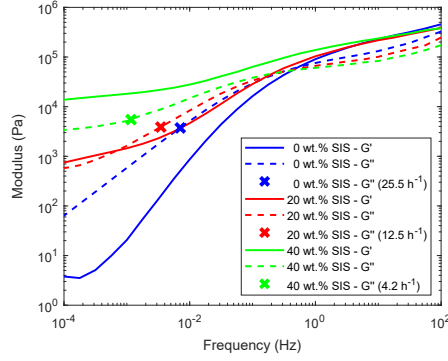


Figure 5: Frequency sweep of polymer matrices with 0, 20, and 40 wt.% SIS. The frequencies, which correspond to the particle swelling rates are marked. The magnitude of the loss modulus at these frequencies corresponds to the swelling pressure of the hydrogel particles.

3.2 Responsive Network Formation

Besides mechanical restrictions, which limit hydrogel swelling, the water transport also heavily depends on environmental stimuli such as pH and the presence of specific ions. The swelling ratio of composites with a matrix containing 20 wt.% SIS was therefore also investigated in a 0.154 NaCl solution, which was adjusted to pH 2. Acidic conditions were found to hamper the swelling of all composites and no notable swelling was observed for composites with loadings of $\phi \leq 0.09$ (see Fig. 6a). The protonation of acid groups likely limited the swelling to an extent, where network formation was not possible at these particle loadings. A lag period in the swelling ratio occurred at $\phi = 0.12$ and continuous water uptake was observed at $\phi \geq 0.19$.

Finally, the swelling ratio of composites with a matrix containing 20 wt.% SIS was also investigated in a 0.077 M CaCl_2 solution. Even though the ionic strength of the solution was kept the same as in the NaCl solution, the swelling was greatly reduced in the presence

of Ca^{2+} (see Fig. 6b). The divalent Calcium ions were thereby expected to act as cross-linkers for the negatively charged acid groups of the hydrogel particles, thusly restricting the swelling. As a result, the swelling kinetics decreased and the water uptake did not scale linearly with time anymore. Instead, the water uptake scaled with the square root of time, which is indicative of Fickian diffusion and means that the kinetics are no longer restricted by chain relaxations of the polymer.²⁶ Continuous swelling of the composites was first observed at particle loadings $\phi \geq 0.27$. A lag period in the water uptake was observed at $\phi = 0.19$ and no notable swelling occurred at loadings $\phi \leq 0.12$.

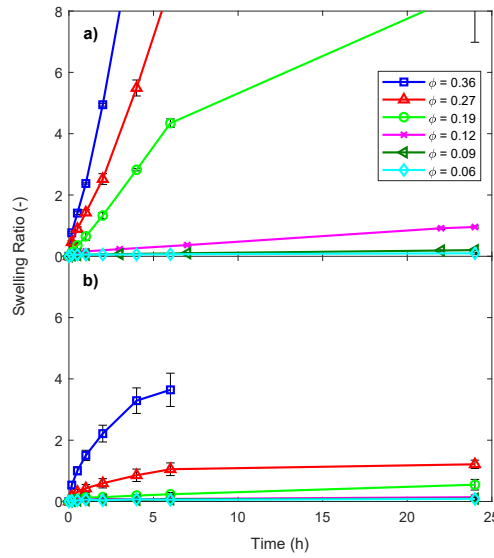


Figure 6: a) Swelling ratio of composites with a polymer matrix containing 20 wt.% SIS in a 0.154 M NaCl solution at pH 2 and 32 °C. Swelling was hampered by the protonation of acid groups. b) Swelling ratio of composites with a polymer matrix containing 20 wt.% SIS in a 0.77 M CaCl_2 solution at 32 °C. Swelling was heavily restricted by the presence of divalent ions due to the creation of physical cross-links within the hydrogel particles.

To determine the critical concentration for swelling-induced network formation, the water uptake kinetics from Fig. 6a and 6b were estimated with a linear fit. Even though the

uptake kinetics followed Fickian diffusion in a 0.077 M CaCl_2 solution, a linear fit between 0 and 2 h was chosen to estimate the maximum swelling rate under these conditions. The resulting swelling rates then increased linearly with the particle weight fraction above the critical concentration (see Fig. 7a). The intercept with the x-axis was again interpreted as the critical concentration for swelling-induced network formation, yielding volume fractions $\phi_{crit} = 0.13$ at pH 2 and $\phi_{crit} = 0.20$ when exposed to 0.077 M CaCl_2 (see schematics in Fig. 7b).

Moreover, the particle swelling rates of 8.7 h^{-1} and 4.8 h^{-1} were converted to frequencies of 0.0024 and 0.0013 Hz, respectively. The loss modulus of the polymer matrix containing 20 wt.% SIS corresponds to approximately 3.1 kPa and 2.0 kPa at these frequencies (see Fig. 5). Hence, we estimate the average swelling pressure of the hydrogels to decrease from 4.5 kPa to 3.1 kPa when the pH of a 0.154 NaCl solution is lowered to 2. Upon exchange of NaCl with CaCl_2 in the solution, the average swelling pressure was even further decreased to 2.0 kPa. These findings are in line with previous findings, where decreases in the osmotic pressure were reported under similar conditions.^{11,27,28} The changes in swelling pressure and kinetics clearly demonstrate the effect of environmental stimuli on swelling-induced network formation.

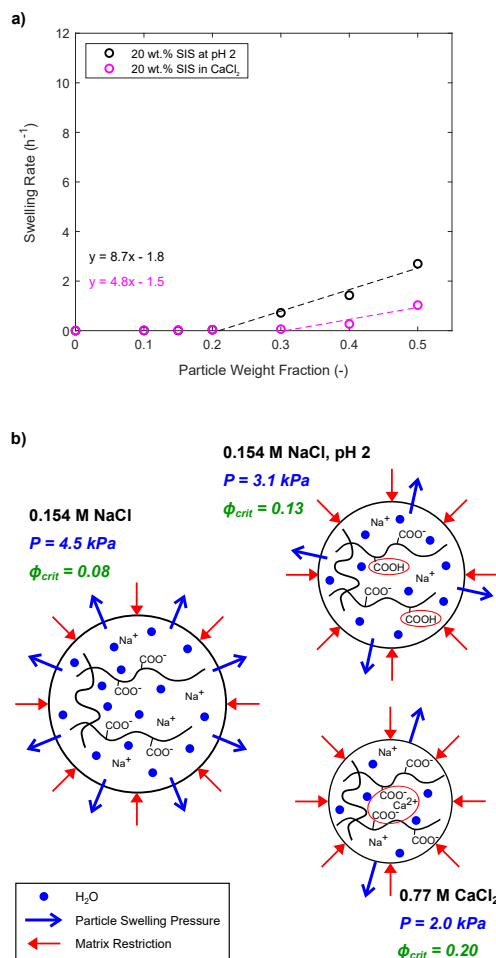


Figure 7: a) Swelling rates in a 0.154 M NaCl solution at pH 2 and in a 0.077 M $CaCl_2$ solution as a function of particle weight fraction. The swelling rates increased linearly with particle content above the critical concentration for swelling-induced network formation. The resulting slopes decreased as compared to the swelling rates in a 0.154 M NaCl solution. b) Schematic representation of the protonation of acid groups at pH 2 and the creation of physical cross-links when exposed to Ca^{2+} resulting in a lower swelling pressure.

4 Conclusions

We investigated the effect of swelling restrictions on the network formation in polymer composites containing PAA-based hydrogel particles. Here, connected networks of particles for efficient water transport only form upon swelling. Below a critical concentration, water transport into the bulk of the composite does not occur. Accordingly, we showed that the critical concentration for swelling-induced network formation can be tuned through physical restrictions. Since the swelling of hydrogel particles induces deformations within the matrix, its viscoelastic properties govern the swelling kinetics and can suppress bulk swelling altogether. Moreover, the swelling was restricted by exposure to divalent ions as well as a salt solution with reduced pH, respectively. In both cases, the swelling restrictions led to an increase in the critical concentration for swelling-induced network formation. Compositions can therefore be tuned to selectively facilitate water transport depending on the environment. A composite at a loading $\phi = 0.12$ containing 20 wt.% SIS in the matrix will readily transport water in a 0.154 M NaCl solution, be on the verge of facilitating efficient transport in an acidic environment at pH 2 and act as a water barrier in a 0.077 M CaCl_2 solution.

Acknowledgement

Innovation Fund Denmark is gratefully acknowledged for financial support through the Grand Solutions Project #6151-00007B.

References

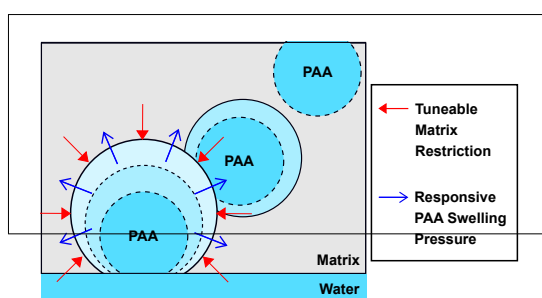
- (1) Maji, S.; Cesur, B.; Zhang, Z.; De Geest, B. G.; Hoogenboom, R. Poly(N-isopropylacrylamide) coated gold nanoparticles as colourimetric temperature and salt sensors. *Polymer Chemistry* **2016**, 7, 1705–1710.

- (2) Chiappelli, M. C.; Hayward, R. C. Photonic Multilayer Sensors from Photo-Crosslinkable Polymer Films. *Advanced Materials* **2012**, *24*, 6100–6104.
- (3) Paek, K.; Yang, H.; Lee, J.; Park, J.; Kim, B. J. Efficient Colorimetric pH Sensor Based on Responsive Polymer–Quantum Dot Integrated Graphene Oxide. *ACS Nano* **2014**, *8*, 2848–2856.
- (4) Wei, M.; Gao, Y.; Li, X.; Serpe, M. J. Stimuli-responsive polymers and their applications. *Polymer Chemistry* **2017**, *8*, 127–143.
- (5) Xing, B.; Hao, J. Reversibly Switchable Wettability. *Chemical Society Reviews* **2009**, *39*, 769–782.
- (6) Wang, X.; Hu, J.; Liu, G.; Tian, J.; Wang, H.; Gong, M.; Liu, S. Reversibly Switching Bilayer Permeability and Release Modules of Photochromic Polymersomes Stabilized by Cooperative Noncovalent Interactions. *Journal of the American Chemical Society* **2015**, *137*, 15262–15275.
- (7) Zhai, G.; Toh, S. C.; Tan, W. L.; Kang, E. T.; Neoh, K. G.; Huang, C. C.; Liaw, D. J. Poly(vinylidene fluoride) with Grafted Zwitterionic Polymer Side Chains for Electrolyte-Responsive Microfiltration Membranes. *Langmuir* **2003**, *19*, 7030–7037.
- (8) Yamauchi, T.; Kokufuta, E.; Osada, Y. Electrically controlled protein permeation through a poly(vinyl alcohol)/poly(acrylic acid) composite membrane. *Polymer Gels and Networks* **1993**, *1*, 247–255.
- (9) Zohuriaan-Mehr, M. J.; Kabiri, K. Superabsorbent Polymer Materials: A Review. *Iranian Polymer Journal* **2008**, *17*, 451–477.
- (10) Zohuriaan-Mehr, M. J.; Omidian, H.; Doroudiani, S.; Kabiri, K. Advances in non-hygienic applications of superabsorbent hydrogel materials. *Journal of Materials Science* **2010**, *45*, 5711–5735.

- (11) Horkay, F.; Basser, P. J. Ionic and pH effects on the osmotic properties and structure of polyelectrolyte gels. *Journal of Polymer Science Part B: Polymer Physics* **2008**, *46*, 2803–2810.
- (12) Parvathy, P. C.; Jyothi, A. N. Water sorption kinetics of superabsorbent hydrogels of saponified cassava starch- graft -poly(acrylamide). *Starch - Stärke* **2012**, *64*, 803–812.
- (13) Ehtiati, K.; Moghaddam, S. Z.; Daugaard, A. E.; Thormann, E. How Dissociation of Carboxylic Acid Groups in a Weak Polyelectrolyte Brush Depend on Their Distance from the Substrate. *Langmuir* **2020**, *36*, 2339–2348.
- (14) Elliott, M. Superabsorbent Polymers. *BASF Aktiengesellschaft* **2004**, 1–13.
- (15) Bajpai, S. K.; Johnson, S. Superabsorbent hydrogels for removal of divalent toxic ions. Part I: Synthesis and swelling characterization. *Reactive and Functional Polymers* **2005**, *62*, 271–283.
- (16) Witono, J. R.; Noordergraaf, I. W.; Heeres, H. J.; Janssen, L. P. Water absorption, retention and the swelling characteristics of cassava starch grafted with polyacrylic acid. *Carbohydrate Polymers* **2014**, *103*, 325–332.
- (17) Dunér, G.; Thormann, E.; Ramström, O.; Dédinaïté, A. Letter to the Editor: Friction between Surfaces—Polyacrylic Acid Brush and Silica—Mediated by Calcium Ions. *Journal of Dispersion Science and Technology* **2010**, *31*, 1285–1287.
- (18) Huang, J.; Zajforoushan Moghaddam, S.; Thormann, E. Structural Investigation of a Self-Cross-Linked Chitosan/Alginate Dialdehyde Multilayered Film with in Situ QCM-D and Spectroscopic Ellipsometry. *ACS Omega* **2019**, *4*, 2019–2029.
- (19) McClory, C.; McNally, T.; Baxendale, M.; Pötschke, P.; Blau, W.; Ruether, M. Electrical and rheological percolation of PMMA/MWCNT nanocomposites as a function of CNT geometry and functionality. *European Polymer Journal* **2010**, *46*, 854–868.

- (20) Huang, X.; Kim, C.; Ma, Z.; Jiang, P.; Yin, Y.; Li, Z. Correlation Between Rheological, Electrical, and Microstructure Characteristics in Polyethylene/Aluminum Nanocomposites. *Journal of Polymer Science; Part B: Polymer physics* **2008**, *46*, 2143–2154.
- (21) Wang, W.; Sain, M.; Cooper, P. A. Study of moisture absorption in natural fiber plastic composites. *Composites Science and Technology* **2006**, *66*, 379–386.
- (22) Eiler, J.; Simonsen, S. B.; Hansen, D.; Bingöl, B.; Hansen, K.; Thormann, E. Water Transport in Polymer Composites through Swelling-Induced Networks of Hydrogel Particles. *Soft Matter* **2020**,
- (23) Hansen, D.; Brewer, J. R.; Eiler, J.; Komjani, N. M.; Hansen, K.; Thormann, E. Water Diffusion in Polymer Composites Probed by Impedance Spectroscopy and Time-Resolved Chemical Imaging. *ACS Applied Polymer Materials* **2020**, *2*, 837–845.
- (24) Goutay, N. Adhésion stable en milieu humide de pansements dits "hydrocolloïdes". Ph.D. thesis, 2016.
- (25) Dubrovskii, S.; Lagutina, M.; Kazanskii, K. Method of measuring the swelling pressure of superabsorbent gels. *Polymer Gels and Networks* **1994**, *2*, 49–58.
- (26) Frisch, H. Sorption and Transport in Glassy Polymers - A Review. *Polymer Engineering & Science* **1980**, *20*, 2–13.
- (27) Horkay, F.; Bassar, P. J.; Hecht, A.-M.; Geissler, E. Calcium-induced volume transition in polyacrylate hydrogels swollen in physiological salt solutions. *Macromolecular Bioscience* **2002**, *2*, 207.
- (28) Horkay, F.; Bassar, P. J.; Hecht, A.-M.; Geissler, E. Osmotic and SANS Observations on Sodium Polyacrylate Hydrogels in Physiological Salt Solutions. *Macromolecules* **2000**, *33*, 8329–8333.

Graphical TOC Entry



Paper III - In Vitro Evaluation of Skin Adhesives during Perspiration



In vitro evaluation of skin adhesives during perspiration

Johannes Eiler^{a,b}, Daniel Hansen^{a,b}, Bahar Bingöl^b, Kristoffer Hansen^b, Jason Heikenfeld^c, Esben Thormann^{a,*}

^a Department of Chemistry, Technical University of Denmark, 2800 Kgs. Lyngby, Denmark

^b Coloplast A/S, 3050, Humlebæk, Denmark

^c School of Electronic and Computing Systems, University of Cincinnati, OH, 45221, USA

ARTICLE INFO

Keywords:

Artificial skin
Perspiration
Peel
Adhesion
Interfaces

ABSTRACT

To bridge the gap between current in vitro and in vivo testing, we present the use of a perspiration simulator to evaluate the performance of skin adhesives during sweating. The perspiration simulator mimics human skin in key aspects such as roughness, water contact angle, sweat pore size, sweat pore density, and can be operated at different perspiration rates. In contrast to in vivo testing, a well-defined experimental setup with minimal variation is therefore successfully achieved. To demonstrate the capabilities of the reported perspiration simulator, two model adhesives with different water absorption capabilities are assessed. The peel forces as a function of time are thereby measured during perspiration of a 0.154 M NaCl solution. The peel force decreases immediately when the perspiration rate exceeds the water uptake as determined by an immersion test. However, when the water absorption capabilities are sufficiently high, a delay in the decrease in peel force is observed. Through the use of a fluorescent dye, we can further correlate the loss of adhesion with a spreading of liquid at the skin-adhesive interface.

1. Introduction

Pressure-sensitive adhesives (PSAs) are polymeric materials that bond to surfaces solely due to van der Waals interactions generated by a mild pressure. Since they do not rely on any chemical reaction, irradiation, or heat and due to the possibility to design strong and yet removable adhesives they have widespread applications. In this work, we focus on medical adhesives, which are worn directly on the skin to aid wound healing, introduce pharmaceutically active ingredients, or attach devices [1–9].

Maintaining adhesion during prolonged wear is thereby crucial to ensure patient safety and therapeutical efficacy. However, some studies have shown that the peel strength of skin adhesives decreases upon perspiration. This loss of adhesion was speculated to be caused by moisture at the interface, where the presence of free water could perturb the skin-adhesive interactions or cause a change in skin surface energy through hydration [10–12]. Regardless of the failure mechanism, it has become widely accepted that the removal of moisture from the skin-adhesive interface is vital for retaining adhesion during perspiration [10–15].

To allow moisture transport away from the skin, hydrocolloids are therefore often added to the polymer matrix of the PSA, resulting in better skin health [16–18] and stronger adhesion during perspiration [19,20]. The performance of the adhesive formulations is then typically evaluated through clinical trials. However, in vivo studies are expensive, time-consuming, and suffer from large variabilities. This is problematic when the variations in adhesion to human skin outweigh the effects of formulation adjustments. Parameters like skin roughness, surface energy, sweat rate, as well as sweat composition not only differ between individuals but also depend on the environmental conditions and it is thus difficult to evaluate the effect of perspiration on the adhesive performance [11,21–28]. This might be the reason Roy et al. failed to reach statistical significance when comparing adhesion before and after exercise, even though the individual test samples showed up to a 65% decrease in peel force [29].

Ex vivo, the performance of medical PSAs is currently assessed in a multi-step approach, where the ability to absorb moisture and the adhesive strength are evaluated separately. The moisture handling capabilities are often determined gravimetrically via immersion in saline solution [30]. The entire surface of the adhesive is thereby exposed to

* Corresponding author.

E-mail addresses: joel@kemi.dtu.dk (J. Eiler), danha@kemi.dtu.dk (D. Hansen), dkbbi@coloplast.com (B. Bingöl), dkkrh@coloplast.com (K. Hansen), heikenjc@ucmail.uc.edu (J. Heikenfeld), esth@kemi.dtu.dk (E. Thormann).

<https://doi.org/10.1016/j.ijadhadh.2020.102574>

Received 5 October 2019; Accepted 7 February 2020

Available online 14 February 2020

0143-7496/© 2020 Elsevier Ltd. All rights reserved.

the aqueous environment and the weight increase is monitored periodically. This does not directly translate into a wear situation because sweat glands only make up approx. 0.5% of the abdominal skin area (with an average of 100 sweat glands/cm² and a diameter of 50–80 µm) [27]. Additionally, the distance between sweat glands equates to approx. 1 mm and therefore a large portion of the PSA initially remains dry during perspiration on human skin (see illustration in Fig. 1). Moreover, sweat is supplied in finite volumes and rates on human skin, whereas an excess of liquid is constantly present during an immersion test. Consequently, an immersion test grossly overestimates the moisture handling capabilities of PSAs on human skin.

Adhesion is typically evaluated through peel or tack tests on substrates like steel or glass [31,32]. Repeatable peel force measurements can be achieved, however, these substrates do not mimic the surface energy, topography, or mechanical properties of human skin. Furthermore, measurements are routinely performed under dry conditions, limiting the predictability of adhesion during prolonged wear. Though, some experimental studies of adhesion under wet conditions are reported in literature. As an example, Bowditch discussed the effects on adhesion when a bonded structure was immersed in water or exposed to a humid environment [33]. Moisture thereby reached the interface via diffusion through the adhesives and caused a reduction in bond strength. In a different approach, Karnal et al. first immersed a PSA in water before contact with a tack probe was established [34]. A reduction in adhesive strength was also observed in this case as compared to dry conditions. Even though these studies give insights into the complex interactions between a PSA, the substrate, and water, none of these experiments mimic perspiration below an adhesive, where a PSA is applied under dry conditions and sweat is subsequently transported to the interface in a liquid state.

It becomes evident that a repeatable test protocol is needed to understand adhesion phenomena during perspiration and to develop new adhesives. This study introduces a perspiration simulator that is able to evaluate the performance of skin adhesives during perspiration. With the simulator, it is possible to replicate typical values of skin roughness, sweat gland size, sweat gland density, sweat composition, as well as sweat rates. In contrast to human skin, where these parameters change during perspiration, the experimental setup remains constant with the perspiration simulator. This reproducibility is a distinct advantage when compared to in vivo studies and allows for precise control of the test conditions, enabling an understanding of the effects of changes in material compositions on the adhesive performance. Moreover, with the perspiration simulator it is also possible to adjust the liquid composition as desired. This permits us to introduce a fluorescent dye in order to follow the movement of the liquid at the interface between the PSA and the substrate.

2. Materials and methods

2.1. Perspiration simulator

In order to solely probe the effect of perspiration, the perspiration simulator is a simplification of the conditions on human skin. A rigid substrate is chosen for the simulator in order to minimize energy dissipation in the substrate and keep a constant angle during peel. This is in contrast to human skin, where deformations in the skin during peel can

greatly affect the measured forces. Additionally, unlike human skin, the selected substrate is not able to hydrate upon exposure to water. Though this does not perfectly represent the conditions during sweating on human skin, the surface and mechanical properties are kept constant. In this study, we apply a modified version of the perspiration simulator previously described by Hou et al. which was later used to develop sweat sensing technology [35–37]. Briefly, the simulator consisted of a sophisticated artificial skin membrane which was glued to an acrylic holder, enabling a homogeneous flow of liquid even at very low rates. Also in this study, in order to create the surface pattern on the artificial skin, a replica of a human forearm was created with a two-component silicone resin (Repliflo, CuDerm, USA). The pattern was then imprinted onto a 50 µm thick negative photoresist film (MX5050, Dupont, USA) at 95 °C and approx. 100 kPa. The film was cured through exposure to UV light with a wavelength of 365 nm for 30 s at 4 mW cm^{−2}. Once the skin topography was established, the polymer film was cured under UV exposure. A second layer of the UV-curable polymer film was attached to the back side of the patterned, cured film to give mechanical stability for adhesion testing. The sweat pores with a density of 100 cm^{−2} were then created with a VLS3.50 CO₂ laser (Univerval Laser Systems, USA) before a track-etched membrane (hydrophilic Polycarbonate with pore diameter: 5 µm, pore density: 4e5 cm^{−2}, thickness: 21 µm, it4ip, Belgium) was adhered to the artificial skin (see Fig. 2). The topography of the artificial skin was evaluated using a Dektak 3030 mechanical profilometer (Bruker, USA). The static water contact angle of the smooth artificial skin was assessed using a ThetaLite 100 optical tensiometer (Biolin Scientific, Sweden). A water droplet with a volume of approx. 10 µL was placed on the surface for 30 s before the contact angle was monitored over a period of 10 s.

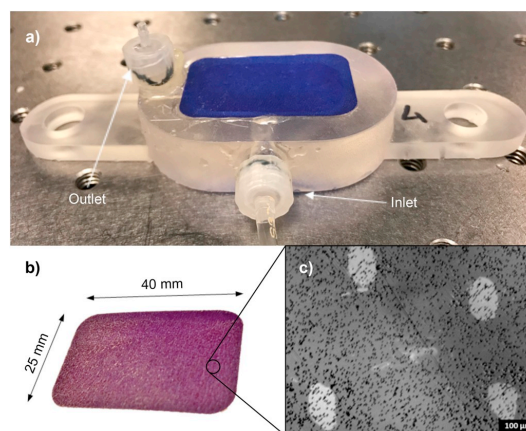


Fig. 2. a) The perspiration simulator with an inlet and outlet valve in the reservoir. b) The artificial skin membrane. c) Microscopy image of the artificial skin: The dark spots are the holes of the track-etched membrane with an average diameter of 5 µm, whereas the large bright spots are the holes in the top membrane.

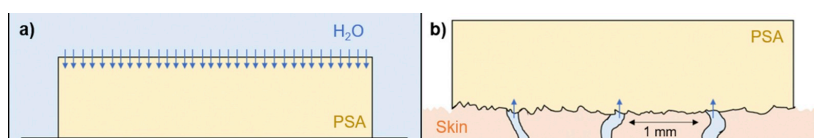


Fig. 1. Schematic representation of the adhesive exposure to liquid during a) an industry-typical immersion test and b) the adhesive on the skin, where sweat glands cover approx. 0.5% of the abdominal skin area.

Paper II - Tuneable and Responsive Formation of Swelling-Induced Hydrogel Networks for Water Transport in Polymer Composites

J. Eiler et al.

International Journal of Adhesion and Adhesives 99 (2020) 102574

A larger area with a rectangular geometry was necessary to evaluate adhesion through peel experiments. Therefore, to further optimize the simulator for adhesive testing, a water reservoir was designed to fit a piece of artificial skin with a length of 40 mm and a width of 25 mm. Additionally, to allow for dwelling of the adhesives under dry conditions, it was necessary to fill the reservoir with liquid after the application of the PSA. Hence, an outlet valve was included which could be opened during filling to avoid bubble formation in the reservoir (see Fig. 2).

2.2. Adhesives

Two rubber-based composite systems were investigated in this study. In both cases, a mixture of polyisobutene (PIB, BASF, Germany) and styrene-isoprene-styrene (SIS, Kraton, USA) was used as the polymer matrix. PIB is typically used in PSAs to provide adhesion and SIS is added to improve the mechanical properties. With a SIS content of the polymer matrix of 40 wt%, the PSAs in this study were designed to be mechanically stiff, in order to avoid cohesive failure during peel as well as cold-flow after application. To achieve different water absorption profiles, 19.3 vol% of either sodium polyacrylic acid (PAA, Stewart Superabsorbent, USA) or cetyl hydroxyethyl cellulose particles (CHEC, Ashland, USA) were mixed into the polymer matrix. A Brabender Plastograph (Brabender, Germany) was used to mix the particles into the matrix at 30 rpm at 90 °C for 45 min under vacuum. The samples were then pressed to a thickness of 1 mm in between two release liners (siliconized paper). A hydraulic press (Stenhøj, Denmark) at 90 °C was used at a load of 10 t with a holding time of 30 s.

The rheological properties of the PSAs were evaluated with a Mars 40 rheometer with a parallel plate geometry (Haake, Germany). The measurements were performed in duplicate and an average of the measured values is reported. Amplitude sweeps at a frequency of 1 Hz were performed to determine the linear viscoelastic region. Subsequently, frequency sweeps in the linear viscoelastic region were run from 100 Hz to 0.01 Hz to characterize the PSAs. The dry peel force of the PSAs on the artificial skin was assessed with a force gauge (Dillon, USA and Instron, USA) at a peel rate of 3.5 mm/s with a constant peel angle of 90°. To apply the adhesives to the artificial skin in a reproducible manner, weights were placed on a soft silicone pad with an area of 40 mm by 25 mm to evenly distribute the load. To test the water absorption capabilities, the samples were immersed into 0.154 M NaCl solution and their water uptake was assessed gravimetrically (6 replicates were tested simultaneously). The PSAs were removed periodically from the saline solution, weighed and re-immersed.

2.3. Perspiration experiments

The PSAs were applied to the artificial skin using soft silicone pads under well-defined pressures for a constant time interval of 1 min (7 kPa for the PAA adhesive and 14 kPa for the CHEC adhesive). The adhesives were applied with different pressures to yield the same initial peel force (approx. 0.7 N) which allowed for a direct comparison of the PSAs with respect to their water absorption capabilities rather than the effect of the different rheological properties. After application, the reservoir was filled with liquid, the outlet valve of the reservoir was closed, and the perspiration experiment was started. To determine the effect of perspiration on adhesion, a saline solution of 0.154 M NaCl was pumped with a syringe pump (kd Scientific, USA and KF Technology, Italy) to mimic human sweat. Two distinct rates of 0.5 $\mu\text{L}/\text{cm}^2/\text{min}$ and 2.0 $\mu\text{L}/\text{cm}^2/\text{min}$ were applied, which corresponded to medium and high perspiration rates in the abdominal area, respectively [25]. After predetermined exposure times, the pump was stopped and the PSAs were peeled off the artificial skin with a force gauge (Dillon, USA and Instron, USA) and discarded thereafter.

In a separate experiment, the saline solution was substituted with an aqueous solution containing 0.5 mM fluorescent dye (disodium

fluorescein from Exciton, USA) which was pumped at a medium perspiration rate of 0.5 $\mu\text{L}/\text{cm}^2/\text{min}$. Images were taken periodically during the experiment under UV irradiation to monitor the movement of the liquid. The experiments were conducted to monitor the skin-adhesive interface for 60 min (CHEC adhesive) and 120 min (PAA adhesive), respectively, without any peel force measurements.

3. Results and discussion

3.1. Perspiration simulator characterization

To illustrate the similarities between the perspiration simulator and human skin, several different characterizations were undertaken. As the artificial skin was created by imprinting a mold of human skin into a polymer membrane, a remarkable topographical resemblance was achieved (see Fig. 3). The skin structure with all grooves and crevices was replicated and typical values for the arithmetic mean roughness of $12.1 \pm 1.3 \mu\text{m}$ were achieved. In comparison, arithmetic mean skin roughness values of the volar forearm between 12 and 29 μm are reported in literature [21–23]. Besides age and gender, skin roughness also greatly depends on skin hydration. This implies that skin roughness can change during perspiration in human skin and potentially affect the contact area between the skin and the PSA [38,39]. As the artificial skin in our simulator consists of a UV-cured polymer film, skin hydration is avoided

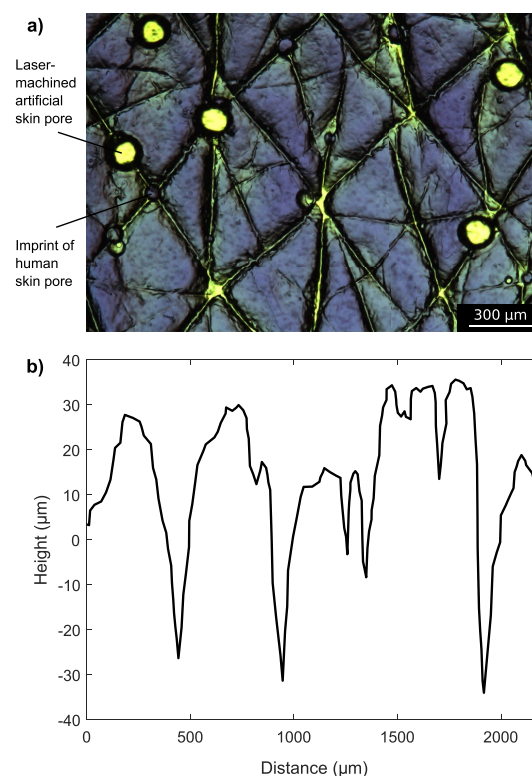


Fig. 3. Topology of the artificial skin: a) Microscopy image of the surface of the artificial skin with laser-machined sweat pores (bright circles) as well as original sweat pores from human skin (blue circles). b) Roughness profile as determined with a mechanical profilometer. (For interpretation of the references to colour in this figure legend, the reader is referred to the Web version of this article.)

and a constant roughness during perspiration can be assumed.

The images also show the laser-machined pores in the artificial skin with an average diameter of approx. $86.8 \pm 17.5 \mu\text{m}$. In comparison, the diameter of human skin pores could be estimated to approx. $58.8 \pm 20.0 \mu\text{m}$ from the imprint on the artificial skin. The artificial sweat pores were therefore confirmed to have similar sizes to human skin pores.

The static water contact angle was measured on the UV-cured artificial skin without any topographical imprint and was found to be $69.2 \pm 3.6^\circ$. On human skin, the water contact angle shows large variations and greatly depends on the pre-treatment. Ginn et al. showed that the contact angle can vary between 58° without any treatment and 139° after a solvent-wash [24]. Additionally, they found that the contact angle decreases with increasing temperature as well as increasing relative humidity. During perspiration, human skin can hydrate which induces a change in skin surface energy. Contrarily, the surface energy of the artificial skin remains constant due to its lack of hydration.

Two pump rates of 0.5 and $2.0 \mu\text{L}/\text{cm}^2/\text{min}$ were applied with a syringe pump and the corresponding perspiration rates from the perspiration simulator were measured gravimetrically. A good agreement between the pump and perspiration rate with a steady flow of liquid was observed. In vivo, a large variability in perspiration rates is seen depending on the individual, the amount of exercise, the environmental conditions, and the body part [26,27,40]. Furthermore, not only the perspiration rates are different but also the electrolyte concentrations in the sweat [28]. Constant perspiration rates with a constant electrolyte concentration can be realized with our perspiration simulator in order to exclude some of the variations from in vivo testing.

3.2. Adhesive characterization

The rheological properties of the adhesives were evaluated in frequency sweep experiments. The addition of particles to the matrix yielded an increase in storage and loss moduli, G' and G'' , as compared to the polymer matrix (see Fig. 4). A greater increase was observed for the addition of CHEC particles, possibly owing to its elongated particle morphology. The increased moduli of the CHEC adhesive resulted in a higher resistance to flow, which manifested itself in the peel force. When the adhesives were applied to the artificial skin with the same pressure (14 kPa), a lower initial peel force was observed for the CHEC adhesive (0.7 N and 1.1 N respectively) as the flow into the grooves was restricted. Subsequently, the PAA adhesive was applied with a smaller pressure of 7 kPa in order to yield the same initial peel force of 0.7 N.

A critical modulus, G_c , above which the flow of the PSA is restricted

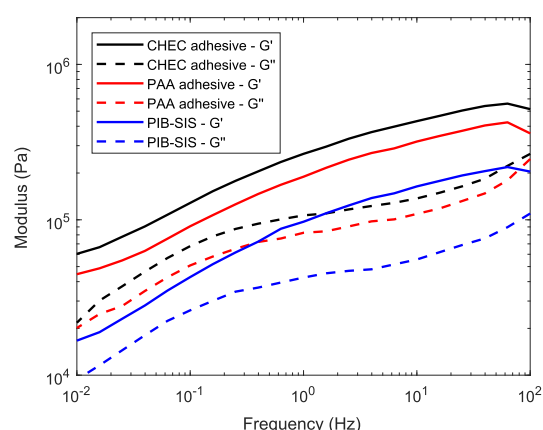


Fig. 4. Storage and loss moduli of the adhesives as a function of frequency. An increase in stiffness was observed for the addition of particles.

under no load, was estimated using the Johnson-Kendall-Roberts theory [41,42]:

$$G_c = \frac{\pi W (1 - \nu^2)}{2} \sqrt{\frac{3R}{d^3}}$$

with a typical work of adhesion, $W = 0.04 \text{ N/m}$ [43], the Poisson ratio of rubber, $\nu = 0.5$ [44], a skin asperity radius, $R = 10 \mu\text{m}$, and a skin groove depth, $d = 12 \mu\text{m}$, the critical modulus becomes $G_c = 6.2 \text{ kPa}$. The moduli of the CHEC as well as the PAA adhesive exceed this value at all tested frequencies. No further flow after the application is therefore expected for the PSAs and the peel force is assumed to remain constant under dry conditions.

Prior to evaluation on the perspiration simulator, the adhesives were also tested in a standard immersion experiment, where the samples were fully submerged in a 0.154 M NaCl solution and their weight uptake was monitored gravimetrically. While the PAA adhesive showed a higher water absorption than the CHEC adhesive, both PSAs exhibited a monotonic weight increase with time. A high initial uptake was observed for the PAA adhesive, possibly caused by particles at the surface whose swelling was not restricted by the matrix. The results are depicted in Fig. 5 along with the intended perspiration rates on the perspiration simulator.

If the applied perspiration rate exceeds the water uptake capabilities of the PSA, a pressure build-up is expected as the adhesive will effectively block the pores. If the pressure then exceeds the adhesive strength, a flooding of the interface is expected to occur, resulting in a reduction of adhesion. Due to the low peel forces of 0.7 N in our study, pressure buildup is minimized and flooding will occur readily. On the other hand, if the water uptake capabilities of the PSA exceed the perspiration rate, parts of the interface will remain dry and adhesion will be retained. To test the hypothesis, a medium perspiration rate of $0.5 \mu\text{L}/\text{cm}^2/\text{min}$ is chosen which exceeds the uptake capabilities of the CHEC adhesive but not the PAA adhesive. A decrease in peel force over time is therefore expected for the CHEC adhesive, whereas the PAA adhesive is thought to remove the supplied liquid adequately and therefore maintain adhesion during perspiration. Finally, a high rate of $2.0 \mu\text{L}/\text{cm}^2/\text{min}$ is applied at which both PSAs are expected to lose adhesion readily.

3.3. Perspiration experiments

To visualize the flow of sweat at the skin-adhesive interface, a

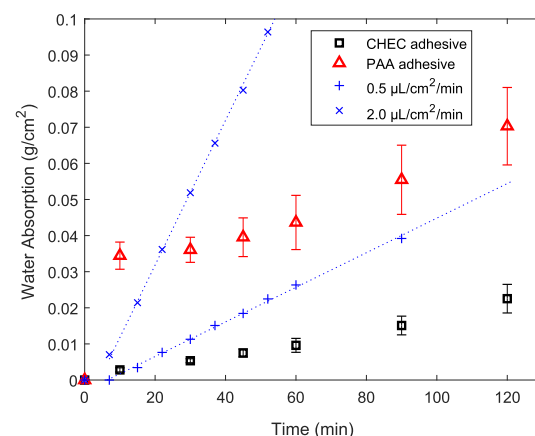


Fig. 5. Immersion test data for the two adhesives during an immersion test in 0.154 M NaCl solution. The applied pump rates on the perspiration simulator are depicted as dashed lines.

Paper II - Tuneable and Responsive Formation of Swelling-Induced Hydrogel Networks for Water Transport in Polymer Composites

J. Eiler et al.

International Journal of Adhesion and Adhesives 99 (2020) 102574

solution containing a fluorescent dye was pumped with the perspiration simulator at a rate of $0.5 \mu\text{L}/\text{cm}^2/\text{min}$. While the artificial skin was covered by the PSA, it was possible to trace the fluorescent liquid through the adhesive under UV irradiation. This way, different spreading behaviors of the liquid could be identified depending on the adhesive that was used. The portion of the dry interface during perspiration was calculated using the image analysis software Fiji [45]. In line with the expectations, the dry contact area between the substrate and the CHEC adhesive decayed rapidly within 60 min (see Fig. 6). The perspiration rate exceeded the uptake rate and caused the liquid to spread uncontrollably until the entire interface was flooded. In contrast, a spreading of the liquid was delayed below the PAA adhesive. Within the first 60 min, the liquid was confined to multiple separate areas across the interface. These areas likely corresponded to the sweat pores, where the liquid was absorbed directly into the PSA. Eventually, the liquid also spread beneath the confined areas and flooded the entire interface even though the water uptake capacity exceeded the amount of perspiration. This demonstrates that the immersion test indeed overestimates the water-handling abilities of the PSA.

To determine the effect of perspiration on adhesion, a saline solution of 0.154 M NaCl was pumped at the same rate of $0.5 \mu\text{L}/\text{cm}^2/\text{min}$. At specific time points, the adhesives were peeled off the perspiration simulator and force curves were recorded. After an initial increase in peel force, an average was determined in the steady-state region for each curve. The average peel forces were then evaluated as a function of perspiration time and related to the spreading behavior as determined with the fluorescent liquid. Due to the fact that each data point corresponds to a separate experiment on a rough substrate with a new piece of adhesive, some variation was observed. Nonetheless, an overall trend

towards a reduction in adhesion with perspiration time became apparent. The CHEC adhesive showed a monotonic decrease in peel force as a function of perspiration time and a drop from an initial value of 0.7 N–0.0 N after approx. 60 min (Fig. 7). Contrarily, the PAA adhesive exhibited a plateau region up to 60 min, where the peel force stayed relatively constant. Thereafter, the peel force also started to decrease monotonically. This loss of adhesion occurred simultaneously with a spreading of liquid at the interface as seen with the fluorescent marker and coincided with these findings.

At a high perspiration rate of $2.0 \mu\text{L}/\text{cm}^2/\text{min}$, however, the absorption capabilities of both adhesives were exceeded. At such high perspiration rates, the peel forces of the CHEC adhesive and the PAA adhesive decreased similarly as a function of perspiration time (see Fig. 8). Neither of the adhesives was able to retain adhesion during this condition and both adhesives appeared to behave equally poor. Therefore, in order to distinguish the performance of different PSA formulations during perspiration, the test conditions have to be controlled carefully.

4. Conclusions

The perspiration simulator presents a new in vitro method to evaluate the performance of medical adhesives during sweating. In contrast to current screening methods, where the adhesion and moisture handling capabilities of PSAs are evaluated separately, the perspiration simulator allows for a simultaneous assessment of these parameters. An adhesive is thereby applied to an artificial skin under dry conditions before a liquid is pumped directly to the skin-adhesive interface. The artificial skin mimics key characteristics of human skin including

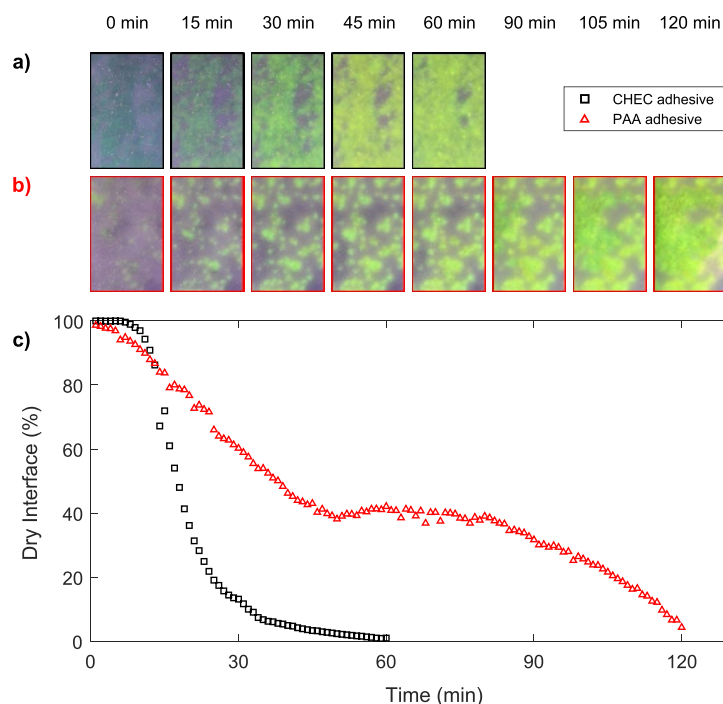


Fig. 6. Images of the adhesives on the perspiration simulator during UV exposure while pumping a fluorescent liquid. a) Below the CHEC adhesive, a rapid spreading of the liquid was observed. b) Below the PAA adhesive, the liquid was confined to the areas of the sweat glands during the first 60 min, a spreading was observed thereafter. c) The dry contact area between the adhesives and the artificial skin was determined from the images.

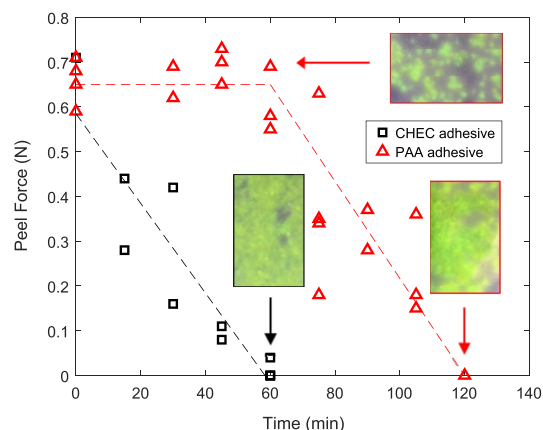


Fig. 7. Peel forces at different time points after pumping 0.154 M NaCl solution at a rate of 0.5 $\mu\text{L}/\text{cm}^2/\text{min}$. The CHEC adhesive showed a monotonic decrease in peel force from the beginning. A decreasing peel force was first observed at a later time point for the PAA adhesive. The dashed lines represent a guide for the eyes.

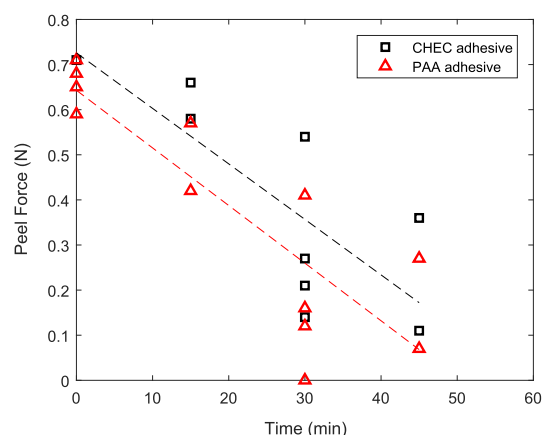


Fig. 8. Peel forces at different time points after pumping 0.154 M NaCl solution. At a pump rate of 2.0 $\mu\text{L}/\text{cm}^2/\text{min}$ the peel forces of the CHEC adhesive and the PAA adhesive decreased in a similar fashion and the samples could not be distinguished. The dashed lines represent a guide for the eyes.

roughness, water contact angle, sweat pore size and sweat pore density. In contrast to human skin, however, these parameters remain constant during perspiration on our simulator and therefore present a well-defined experimental setup. Additionally, the composition of the liquid as well as the perspiration rate can be precisely controlled and adjusted to the research needs. This makes the perspiration simulator a powerful tool to test new adhesive formulations and presents an alternative for current *in vitro* and *in vivo* testing of medical adhesives.

Two adhesives with different moisture uptake abilities were designed for evaluation on the perspiration simulator. We hypothesized that adhesion could only be maintained if the absorption capabilities of the PSA exceeded the pump rate. Based on the absorption capabilities from the immersion test, perspiration rates were chosen to distinguish between the adhesives. With the use of a fluorescent dye, we could show that pump rates which exceeded the moisture uptake abilities of the

PSAs led to a spreading of the liquid at the interface. This spreading was then associated with an immediate reduction in peel strength. On the other hand, when the pump rate was lower than the absorption rate, the liquid was prohibited from spreading and the loss of adhesion was delayed. Even though the immersion test overestimated the water handling capabilities of the PSAs on skin, it was able to predict whether immediate or delayed failure occurred.

Acknowledgements

We would like to thank the Innovation Fund Denmark for financial support through the Grand Solutions Project #6151-00007B.

References

- [1] Kannon GA, Garrett AB. Moist wound healing under occlusive dressing: a Clinical Review. *Dermatol Surg* 1995;21:583–90.
- [2] Thomas S. Hydrocolloid dressings in the management of acute wounds: a review of the literature. *Int Wound J* 2008;5:602–13. <https://doi.org/10.1111/j.1742-481X.2008.00541.x>.
- [3] Venkatraman S, Gale R. Skin adhesives and skin adhesion. *Biomaterials* 1998;19:1119–36.
- [4] Wokovich AM, Prodduturi S, Doub WH, Hussain AS, Buhse LF. Transdermal drug delivery system (TDDS) adhesion as a critical safety, efficacy and quality attribute. *Eur J Pharm Biopharm* 2006;64:1–8. <https://doi.org/10.1016/j.ejpb.2006.03.009>.
- [5] Felix J, Bishay JM, Bardy GH. Extended wear electrocardiography patch using interlaced wire electrodes. 2017. US 9,717,432 B2.
- [6] Hung M-W, Wu C-L, Chiu Y-Y. Long term physiological signal sensing patch. 2017. US 2017/0164860 A1.
- [7] Hwang I, Kim HN, Seong M, Lee S-H, Kang M, Yi H, et al. Multifunctional smart skin adhesive patches for advanced health care. *Adv Healthc Mater* 2018;7:1800275. <https://doi.org/10.1002/adhm.201800275>.
- [8] Tighe BJ, Mann A. Adhesives and interfacial phenomena in wound healing. In: Farrar D, editor. *Adv. Wound repair ther*. Elsevier; 2011. p. 247–83. <https://doi.org/10.1533/9780857093301.2.247>.
- [9] Lipani L, Dupont BGR, Doungmene F, Marken F, Tyrrell RM, Guy RH, et al. Non-invasive, transdermal, path-selective and specific glucose monitoring via a graphene-based platform. *Nat Nanotechnol* 2018;13:504–11. <https://doi.org/10.1038/s41565-018-0112-4>.
- [10] Spencer TS, Smith SE, Conjeevaram S. Adhesive interactions between polymers and skin in transdermal delivery systems. *Polym Mater Sci Eng Proc ACS Div Polym Mater Sci Eng* 1990;63:337.
- [11] Kenney JF, Haddock TH, Sun RL, Parreira HC. Medical-grade acrylic adhesives for skin contact. *J Appl Polym Sci* 1992;45:355–61. <https://doi.org/10.1002/app.1992.070450218>.
- [12] Renvoise J, Burlot D, Marin G, Deraill C. Peeling of PSAs on viscoelastic substrates: a failure criterion. *J Adhes* 2007;83:403–16. <https://doi.org/10.1080/00218460701282554>.
- [13] Horstmann M, Müller W, Asmussen B. Principles of skin adhesion and methods for measuring adhesion of transdermal systems. In: Mathiowitz E, Chickering III DE, Lehr C-M, editors. *Bioadhesive drug deliv. Syst. - fundam. Nov. Approaches dev.*; 1999. p. 175–96.
- [14] Renvoise J, Burlot D, Marin G, Deraill C. Adherence performances of pressure sensitive adhesives on a model viscoelastic synthetic film: a tool for the understanding of adhesion on the human skin. *Int J Pharm* 2009;368:83–8. <https://doi.org/10.1016/j.ijpharm.2008.09.056>.
- [15] Cunningham DD, Lowery MG. Moisture vapor transport channels for the improved attachment of a medical device to the human body. *Biomed Microdevices* 2004;6:149–54. <https://doi.org/10.1023/B:BMMD.0000031752.63215.61>.
- [16] Matsumura H, Oka K, Umekage K, Akita H, Kawai J, Kitazawa Y, et al. Effect of occlusion on skin. *J Dermatol Treat* 1997;8:139–42. <https://doi.org/10.3109/09546639709160288>.
- [17] Zhai H, Maibach HI. Occlusion vs. skin barrier function. *Skin Res Technol* 2002;8:1–6. <https://doi.org/10.1046/j.0909-752x.2001.10311.x>.
- [18] Gray M, Black JM, Baharestani MM, Bliss DZ, Colwell JC, Goldberg M, et al. Moisture-associated skin damage: overview and pathophysiology. *J Wound, Ostomy Cont Nurs* 2011;38:233–41. <https://doi.org/10.1097/WON.0b013e3182157798>.
- [19] Ferrari F, Bertoni M, Bonferoni MC, Rossi S, Caramella C, Waring MJ. Comparative evaluation of hydrocolloid dressings by means of water uptake and swelling force measurements. I. *Int J Pharm* 1994;112:29–36. [https://doi.org/10.1016/0378-5173\(94\)00301-X](https://doi.org/10.1016/0378-5173(94)00301-X).
- [20] Lipman R. Hydrocolloid PSAs: new formulation strategies. *Med Device Diagnostic Ind Mag* 1999;134.
- [21] Lagarde JM, Rouvrais C, Black D. Topography and anisotropy of the skin surface with ageing. *Skin Res Technol* 2005;11:110–9. <https://doi.org/10.1111/j.1600-0846.2005.00096.x>.
- [22] Li L, Mac-Mary S, Marsaut D, Sainthillier JM, Nouveau S, Gharbi T, et al. Age-related changes in skin topography and microcirculation. *Arch Dermatol Res* 2006;297:412–6. <https://doi.org/10.1007/s00403-005-0628-y>.

Paper II - Tuneable and Responsive Formation of Swelling-Induced Hydrogel Networks for Water Transport in Polymer Composites

J. Eiler et al.

International Journal of Adhesion and Adhesives 99 (2020) 102574

- [23] Egawa M, Oguri M, Kuwahara T, Takahashi M. Effect of exposure of human skin to a dry environment. *Skin Res Technol* 2002;8:212–8. <https://doi.org/10.1034/j.1600-0846.2002.00351.x>.
- [24] Ginn ME, Noyes CM, Jungermann E. The contact angle of water on viable human skin. *J Colloid Interface Sci* 1968;26:146–51. [https://doi.org/10.1016/0021-9797\(68\)90306-8](https://doi.org/10.1016/0021-9797(68)90306-8).
- [25] Sato K, Sato F. Individual variations in structure and function of human eccrine sweat gland. *Am J Physiol Integr Comp Physiol* 1983;245:R203–8. <https://doi.org/10.1152/ajpregu.1983.245.2.R203>.
- [26] Henkin SD, Sehl PL, Meyer F. Sweat rate and electrolyte concentration in swimmers, runners, and nonathletes. *Int J Sports Physiol Perform* 2010;5:359–66. <https://doi.org/10.1123/ijspp.5.3.359>.
- [27] Taylor NA, Machado-Moreira CA. Regional variations in transepidermal water loss, eccrine sweat gland density, sweat secretion rates and electrolyte composition in resting and exercising humans. *Extreme Physiol Med* 2013;2:4. <https://doi.org/10.1186/2046-7648-2-4>.
- [28] Lara B, Gallo-Salazar C, Puente C, Areces F, Salinero JJ, Del Coso J. Interindividual variability in sweat electrolyte concentration in marathoners. *J Int Soc Sports Nutr* 2016;13:1–8. <https://doi.org/10.1186/s12970-016-0141-z>.
- [29] Roy SH, De Luca G, Cheng MS, Johansson A, Gilmore LD, De Luca CJ. Electro-mechanical stability of surface EMG sensors. *Med Biol Eng Comput* 2007;45:447–57. <https://doi.org/10.1007/s11517-007-0168-z>.
- [30] ASTM D570-98(2018) standard test method for water absorption of plastics. West Conshohocken, PA: ASTM International; 2018. <https://doi.org/10.1520/D0570-98R18>. n.d.
- [31] Nussinovitch A, Gal A, Padula C, Santi P. Physical characterization of a new skin bioadhesive film. *AAPS PharmSciTech* 2008;9:458–63. <https://doi.org/10.1208/s12249-008-9061-9>.
- [32] Chivers RA. Easy removal of pressure sensitive adhesives for skin applications. *Int J Adhesion Adhes* 2001;21:381–8. [https://doi.org/10.1016/S0143-7496\(01\)00015-X](https://doi.org/10.1016/S0143-7496(01)00015-X).
- [33] Bowditch MR. The durability of adhesive joints in the presence of water. *Int J Adhesion Adhes* 1996;16:73–9. [https://doi.org/10.1016/0143-7496\(96\)00001-2](https://doi.org/10.1016/0143-7496(96)00001-2).
- [34] Karnal P, Roberts P, Gryska S, King C, Barrios C, Frechette J. Importance of substrate functionality on the adhesion and debonding of a pressure-sensitive adhesive under water. *ACS Appl Mater Interfaces* 2017;9:42344–53. <https://doi.org/10.1021/acsami.7b13984>.
- [35] Hou L, Hagen J, Wang X, Papautsky I, Naik R, Kelley-Loughnane N, et al. Artificial microfluidic skin for in vitro perspiration simulation and testing. *Lab Chip* 2013;13:1868–75. <https://doi.org/10.1039/c3lc41231>.
- [36] Peng R, Sonner Z, Hauke A, Wilder E, Kasting J, Gaillard T, et al. A new oil/membrane approach for integrated sweat sampling and sensing: sample volumes reduced from μL 's to nL's and reduction of analyte contamination from skin. *Lab Chip* 2016;16:4415–23. <https://doi.org/10.1039/C6LC01013J>.
- [37] Twine NB, Norton RM, Brothers MC, Hauke A, Gomez EF, Heikenfeld J. Open nanofluidic films with rapid transport and no analyte exchange for ultra-low sample volumes. *Lab Chip* 2018;18:2816–25. <https://doi.org/10.1039/C8LC00186C>.
- [38] Gerhardt L-C, Strassle V, Lenz A, Spencer N, Derler S. Influence of epidermal hydration on the friction of human skin against textiles. *J R Soc Interface* 2008;5:1317–28. <https://doi.org/10.1098/rsif.2008.0034>.
- [39] Adams MJ, Briscoe BJ, Johnson SA. Friction and lubrication of human skin. *Tribol Lett* 2007;26:239–53. <https://doi.org/10.1007/s11249-007-9206-0>.
- [40] Candas V, Brandenberger G, Lutz-Bucher B, Follenius M, Libert JP. Endocrine concomitants of sweating and sweat depression. *Eur J Appl Physiol Occup Physiol* 1984;52:225–9. <https://doi.org/10.1007/BF00433397>.
- [41] Johnson KL, Kendall K, Roberts AD. Surface energy and the contact of elastic solids. *Proc R Soc A Math Phys Eng Sci* 1971;324:301–13. <https://doi.org/10.1098/rspa.1971.0141>.
- [42] Creton C, Leibler L. How does tack depend on time of contact and contact pressure? *J Polym Sci, Part B: Polym Phys* 1996;34:545–54. [https://doi.org/10.1002/\(SICI\)1099-0488\(199602\)34:3<545::AID-POLB13>3.0.CO;2-I](https://doi.org/10.1002/(SICI)1099-0488(199602)34:3<545::AID-POLB13>3.0.CO;2-I).
- [43] Kinning DJ, Schneider HM. Release coatings for pressure sensitive adhesives. In: Dillard DA, Pocius AV, Chaudhury M, editors. *Adhes. Sci. Eng.*; 2002. p. 535–71.
- [44] Anderson ML, Mott PH, Roland CM. The compression of bonded rubber disks. *Rubber Chem Technol* 2004;77:293–302. <https://doi.org/10.5254/1.3547824>.
- [45] Schindelin J, Arganda-Carreras I, Frise E, Kaynig V, Longair M, Pietzsch T, et al. Fiji: an open-source platform for biological-image analysis. *Nat Methods* 2012;9:676–82. <https://doi.org/10.1038/nmeth.2019>.

Paper IV - How the Viscoelastic and Sweat Absorbing Properties of Skin Adhesives Affect their Performance during Perspiration

How the Viscoelastic and Sweat Absorbing Properties of Skin Adhesives Affect their Performance during Perspiration

Johannes Eiler,^{†,‡} Daniel Hansen,^{†,‡} Bahar Bingöl,[‡] Kristoffer Hansen,[‡] and Esben

Thormann^{*,†}

[†]*Department of Chemistry, Technical University of Denmark, 2800 Kgs. Lyngby, Denmark*

[‡]*Coloplast A/S, 3050 Humlebæk, Denmark*

E-mail: esth@kemi.dtu.dk

Abstract

Maintaining adhesion on human skin during perspiration is challenging and may result in undesired detachment. Improvements in the performance are generally made by adjustments in the adhesive composition, which simultaneously changes the viscoelastic properties, sweat absorption capabilities, and peel adhesion. To aid the design of skin adhesives for prolonged wear, we systematically investigate the impact of the viscoelastic properties and the sweat absorption capabilities during perspiration. Therefore, four skin adhesives are designed with a stepwise variation in one of the properties at a time to decouple the different effects. A perspiration simulator is used during the study to ensure well-defined and reproducible perspiration conditions. Depending on the sweating pressure and the adhesive formulation, different failure mechanisms are observed. The sweating pressure delaminates the non-absorbing adhesives and causes adhesive failure. Thereby, viscoelastic flow and subsequent cavity growth occur if the

sweating pressure overcomes the mechanical strength of the adhesive, while elastic detachment is observed otherwise. The addition of absorbing components results in a pressure relief and thus enables the maintenance of adhesion over prolonged periods. However, the absorption of sweat weakens the mechanical integrity of the adhesive and causes cohesively dominated failure during peel. These findings are also supported by the behaviour of the adhesives on human skin before and after perspiration. This shows that the design of skin adhesives requires an intricate balance between viscoelasticity and sweat absorption in order to maintain adhesion during perspiration.

Keywords

Skin Adhesives, Perspiration Simulator, Peel Adhesion, Viscoelastic Properties, Sweat Absorption

1 Introduction

Skin adhesives are a type of pressure-sensitive adhesive that is used to attach and maintain medical devices such as biosensors, wound dressings, and ostomy care products on the skin.¹⁻⁴ The adhesion is thereby balanced in a way that it is strong enough to support the attached device during wear yet does not cause any skin damage upon removal of the adhesive.^{5,6} Skin roughness, perspiration, and movements pose great challenges for the adhesion to skin and different approaches have been taken to solve the problem. Traditional skin adhesives are based on rubber, acrylics, or silicones to provide adhesion through van der Waals interactions with the skin.⁷⁻⁹ Some recent developments of adhesives also include bio-inspired materials, which can form hydrogen bonds with the substrate in order to provide strong adhesion, especially in wet environments.¹⁰⁻¹³

Good contact with the skin is a prerequisite to achieve strong adhesion during wear. Thus, the development of a skin adhesive has been reported recently, where the adhesion was controlled through adjustments in the chain mobility of the polymers.¹⁴ Due to the relatively large roughness of human skin, the viscoelastic properties of the adhesives need to be precisely controlled to enable flow into the crevices.¹⁵ Since the elastic component of the viscoelastic properties constitutes a resistance to flow, it presents a limitation for contact formation. On the other hand, the viscous component is responsible for energy dissipation during peel. Therefore, it has been proposed that the peel force is proportional to the loss modulus at the peel frequency and inversely proportional to the storage modulus at the bonding frequency:¹⁶

$$F_{peel} \propto \frac{G''(peel\ frequency)}{G'(bonding\ frequency)} \quad (1)$$

where F_{peel} is the peel force, G'' is the loss modulus, and G' is the storage modulus. The relationship in Eq. 1 is valid for adhesives with similar surface energies as long as the failure is mainly adhesive (i.e. not dominated by cohesive rupture). In practice, the molecular weight of the polymers, the cross-linking density, and the concentration of fillers are among the properties that can be tuned to regulate the viscoelastic behaviour of the adhesives.^{17–20}

In addition to the roughness of human skin, perspiration also greatly affects adhesion during wear. Thereby, the appearance of moisture at the skin-adhesive interface can have detrimental effects on the peel force and it has been generally accepted that the removal of sweat results in better adhesion over a prolonged period of time.^{21–24} Therefore, a mix of fillers such as gelatine, pectin, and carboxymethyl cellulose are typically incorporated into the hydrophobic polymer matrix in order to facilitate water transport.^{25–27} However, it has also been shown recently that excessive absorption of liquid can lead to a loss of adhesion.²⁸

In a previous study, we have used an in vitro perspiration simulator inspired by Hou et al.²⁹ to show that adhesion may indeed be maintained through the incorporation of hydrophilic particles into an adhesive matrix.³⁰ The peel forces of the investigated adhesives were found to decrease as soon as the absorption capabilities were exceeded and the artificial sweat spread across the interface. In a different study, we have shown that absorbing adhesives are able to remove such excess sweat from the interface after perspiration, subsequently establish larger contact areas, and increase their peel adhesion.³¹ In both studies, the adhesives were applied with only light pressure such that non-perfect contact with the substrate was obtained. This means that sweat could readily penetrate the skin-adhesive interface and interfere with further contact formation. A strategy to achieve improved performance during perspiration could therefore be the softening of skin adhesives such that larger contact areas are achieved under the same application procedure. Thereby, the adhesives may readily flow into the crevices and minimise the empty volume between the skin and the adhesive. This would occlude the sweat pores and therefore greatly reduce the penetration of the interface by sweat.

In this study, we aim to understand the effect of changes in the viscoelastic properties as well as the crucial role of sweat absorption during perspiration. The performance of adhesives is evaluated through peel tests after exposure to artificial sweat on a perspiration simulator. Four model adhesives are designed with a step-wise variation in either viscoelastic properties or sweat absorption capabilities, enabling a comparison of pairs of adhesives. This way, the different effects of changing the viscoelastic properties and sweat absorption capabilities can be systematically investigated. Finally, the findings from the study on the perspiration simulator are qualitatively compared to the adhesive performance on human skin before and after perspiration.

2 Material and Methods

2.1 Adhesives

The model adhesives were based on a polymer matrix containing 80 wt.% polyisobutylene (PIB - BASF, Germany) to provide adhesion and 20 wt.% styrene-isoprene-styrene (SIS - Kraton, USA) to provide mechanical strength. The viscoelastic properties were further controlled by the total volume fraction, ϕ , of particles within the adhesive, while the sweat absorption capabilities were limited by the weight fraction, w , of absorbing particles. Particles based on sodium poly(acrylic acid) (PAA - Stewart Superabsorbent, USA) were then introduced to enable sweat absorption of the adhesives, while non-absorbing potato starch particles (Pot - KMC, Denmark) were added to adjust the viscoelastic properties. Four compositions were then designed to yield pairs of samples with similar viscoelastic properties and sweat absorption capabilities, respectively.

2.2 Adhesive Processing

PIB and SIS were mixed in a high shear mixer (Brabender, Germany) for 45 min at 90 °C and 30 rpm. Since the densities of both polymers are 0.92 g/cm³, the blend was also expected to have the same density. PAA with a density of 1.65 g/cm³ and Pot with a density of 1.52 g/cm³ were then added to the polymer matrix to yield volume fractions according to Tab. 1. The adhesives were mixed for another 45 min at 90 °C and 30 rpm. Finally, the adhesives were pressed to a thickness of 1 mm using a hydraulic press (Stenhøj, Denmark) at 90 °C with a load of 10 t for 30 s.

Table 1: Overview of sample compositions

Composite name	Particles	Weight fraction (-)	Total volume fraction (-)
Pot-12	Pot	0.19	0.12
PAA-12	PAA	0.20	0.12
PAAPot-27	PAA + Pot	0.20 + 0.19	0.27
Pot-27	Pot	0.38	0.27

2.3 Immersion Test

The sweat absorption capabilities of the adhesives were assessed gravimetrically during immersion in artificial sweat (0.154 M NaCl solution) at 32 °C. After predetermined time intervals, the samples with an area of 25 by 25 mm² were removed, blotted, weighed, and re-immersed. An average of six replicates for each adhesive is reported.

2.4 Rheology

A Discovery HR-2 rheometer (TA instruments, USA) with a parallel plate geometry was used to determine the viscoelastic properties of the adhesives with a diameter of 20 mm at 32 °C. At first, amplitude sweep experiments at a frequency of 1 Hz were conducted to determine the linear viscoelastic region. Then, a strain of 0.1 %, which was within the viscoelastic region for all adhesives, was chosen to characterise the viscoelastic properties over a frequency range of 100 - 0.0001 Hz. One representative frequency sweep curve is reported for each composition (see ESI for all curves).

2.5 Peel Experiments

Peel experiments were conducted on the artificial skin in dry conditions as well as under perspiration conditions. A backing tape (Tesa, Germany) was applied to the adhesive prior to the application of the adhesive on the substrate. Here, the adhesives with dimensions of 100 mm by 25 mm were applied to the artificial skin using a silicone pad with a pressure of 1770 Pa for 1 min. In dry conditions, the adhesives were left to dwell for an additional 0, 60, and 120 min after application to achieve corresponding contact times as with the perspiration experiments. A 5943 Universal Testing System (Instron, USA) was used at a constant peel angle of 90° with a peel speed of 304 mm/min, which corresponds to a peel frequency of approximately 5 Hz. The peel curves were evaluated between 20 - 80 mm displacement and an average of three replicates was reported.

2.6 Perspiration Simulator

To evaluate the performance of the adhesives during perspiration, an in vitro perspiration simulator was used. As we have described in a previous study,³¹ the perspiration simulator included a tank with artificial sweat, a flow sensor (MFS 3, Elveflow, France), a sweat reservoir, a track-etched membrane, and an artificial skin layer (see schematics in Fig. 1). The artificial skin consisted of a gelatine layer, which was coated onto a polyimide support with controlled roughness. The artificial skin had holes with a diameter of approximately 250 μm to represent the sweat glands in human skin. The track-etched membrane between the sweat reservoir and the artificial skin was used to ensure homogeneous flow through the holes of the artificial skin. By adjusting the height of the tank, the pressure and flow rate through the holes could be controlled precisely.

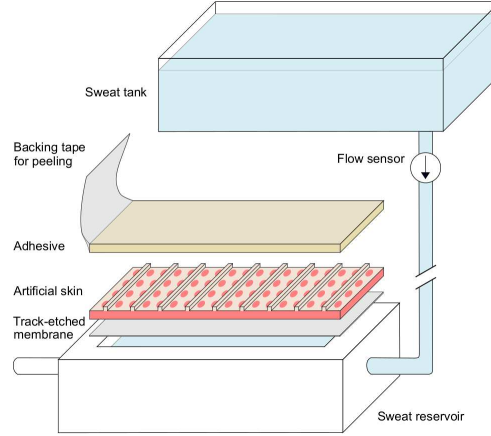


Figure 1: Schematic illustration of the perspiration simulator. A tank filled with artificial sweat was used to supply the liquid during the experiment. The flow was measured by a flow sensor and the pressure was adjusted by the tank height. The track-etched membrane ensured homogeneous flow throughout the artificial skin layer. The artificial skin featured a well-defined topography and a surface energy similar to human skin.

The perspiration experiments were conducted at a constant temperature of 32 °C and a constant pressure of 3 kPa, which corresponds to moderate sweating on human skin.³² Experiments with extreme sweating at a perspiration pressure of 6 kPa were also performed and the data is available in the ESI. A 0.154 M NaCl solution was used as an artificial sweat composition. To ensure reproducible test conditions, the flow rate through the unoccluded perspiration simulator was measured over a period of 200 s prior to application of the adhesive. Thereby, the perspiration pressure of 3 kPa resulted in a free flow rate of 0.7 ± 0.2 $\mu\text{L}/\text{cm}^2/\text{min}$. After drying the device, an adhesive with dimensions of 100 mm by 25 mm was applied to the artificial skin using a silicone pad with a pressure of 1770 Pa for 1 min. Thereafter, the flow was activated and the flow rate was monitored over the tested period (60 min and 120 min) until the experiment was finished with the measurement of the peel force of the adhesive. Triplicate analysis was performed for all experiments and an average with the corresponding standard deviation is reported. Two-sample T-tests with a significance level of 0.05 were performed to indicate differences between peel forces in dry conditions and

after perspiration.

2.7 Surface Topography Analysis

The surface topography of the adhesives was assessed after the perspiration and peel experiments with an optical microscope (Eclipse LV100ND from Nikon, Japan) as well as a mechanical profilometer (SJ-410 from Mitutoyo, Japan). With the profilometer, five line scans were performed for each sample at a speed of 0.5 mm/s over a length of 20 mm and one representative measurement is reported (see ESI for all measurements).

2.8 Adhesion to Human Skin

In order to correlate the results from the perspiration simulator to the behaviour on human skin during perspiration a qualitative study was performed. Here, peel adhesion tests were performed on the left and right inner forearm of one of the authors. The skin was stripped prior to the application of the adhesives in this study. The adhesives with a backing tape for a peel experiment were manually applied to the skin and thereafter left to dwell for 10 min. A peel test was then conducted to evaluate the peel adhesion under dry conditions. To evaluate the peel adhesion after perspiration, a bike ride (approximately 30 min) was introduced after application and dwelling. The peel forces of the adhesives were then measured within 5 min after the bike ride was finished. Two replicates of each adhesive were measured simultaneously (left and right forearm) under dry conditions as well as after perspiration and their peel forces are reported.

3 Results and Discussion

3.1 Adhesive Characterisation

The adhesives with different compositions were evaluated in terms of their sweat absorption capabilities, viscoelastic properties, and peel adhesion. Upon immersion in artificial sweat, the adhesives which contained only potato starch (Pot-12 and Pot-27), showed no notable weight increase over the course of 120 min (see Fig. 2 a). On the other hand, the adhesives which both contained PAA at a weight fraction $w = 0.2$ (PAA-12 and PAAPot-27), showed an increasing uptake of artificial sweat over time. During the immersion test, the entire surface area of the adhesives is exposed to artificial sweat, which is in contrast to the perspiration experiments, where the adhesives are exposed to artificial sweat only around the sweat pores. Since the sweat pores only make up approximately 5 % of the surface area of the artificial skin, it is expected that the immersion test overestimates the sweat uptake capabilities of the adhesives during perspiration. Therefore, the adhesives are expected to behave occlusive during perspiration and hamper the sweat flow while contact is maintained.

The viscoelastic properties of the adhesives affect the contact area with the artificial skin as well as the energy dissipation during peel. Therefore, rheological frequency sweep experiments were performed to characterise the adhesives. In our study, the bonding times consisted of application under load for 1 min and dwelling without load for an additional 0, 60, and 120 min. These bonding times were then converted to yield the corresponding bonding frequencies, which are indicated in Fig. 2 b. According to Eq. 1, a decreasing storage modulus at the bonding frequencies will increase the peel adhesion due to increasing contact formation. Contrarily, a decreasing loss modulus at a peel frequency of 5 Hz will decrease the peel adhesion since energy dissipation is limited.

Pot-12 and PAA-12, which both contained a total particle volume fraction $\phi = 0.12$, thereby showed similar magnitudes of the storage modulus, G' , and the loss modulus, G'' , throughout

the investigated frequency range (see Fig. 2 b). Only at low frequencies below approximately 10^{-3} Hz, differences in G' were observed, possibly owing to different interactions between the matrix and the particles. PAAPot-27 and Pot-27, which both contained a higher total volume fraction of particles, exhibited increased moduli as compared to Pot-12 and PAA-12 across all frequencies. Consistent with previous observations, Pot-27, which contained more potato starch than PAAPot-27, also showed a lower G' at frequencies below approximately 10^{-3} Hz.

Due to viscoelastic flow, all adhesives in this study increased their contact area on the substrate as a function of time, which resulted in increased peel forces over the course of 120 min (see Fig. 2 c). The softer adhesives (Pot-12 and PAA-12) generally showed higher peel forces and a greater tendency to cohesive break than the stiffer adhesives (PAAPot-27 and Pot-27). The soft adhesives exhibited a lower G'' at the peel frequency than the stiff adhesives (see Fig. 2 b). Therefore, less energy dissipation occurs within the soft adhesives and the increased peel forces are a result of the decreased G' according to Eq. 1. This implies that the soft adhesives formed larger contact areas with the substrate than the stiff adhesives.

Since G'' of Pot-12 and PAA-12 was indistinguishable at the peel frequency, the slightly higher peel forces of Pot-12 are also a consequence of a decreased G' and better contact formation. Similarly, Pot-27 exhibited a lower G' than PAAPot-27 at the bonding frequencies and also showed increased peel forces. Even though the adhesives showed elements of cohesive failure at bonding times of 60 min and 120 min, Eq. 1 shows good coincidence with the peel data (see Fig. 2 d).

Altogether, four adhesive compositions were realised, where sweat uptake capabilities and viscoelastic properties were changed independently. This enables us to decouple these prop-

erties and evaluate their impact on the peel adhesion.

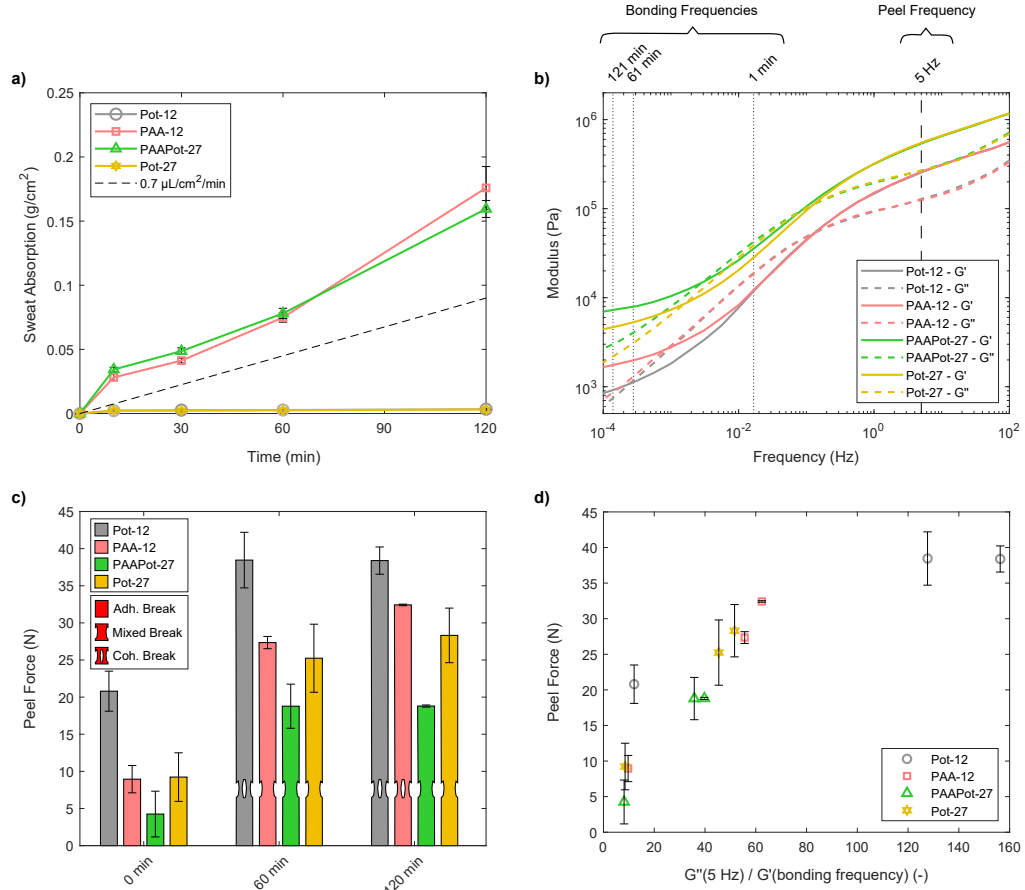


Figure 2: Characterisation of the four adhesives. a) In the immersion test, similar uptake of artificial sweat is observed for Pot-12 and Pot-27 as well as PAA-12 and PAAPot-27 respectively. The absorption capabilities were increased only through the addition of PAA to the adhesive. b) Rheological frequency sweep experiments show that similar viscoelastic properties are observed for Pot-12 and PAA-12 as well as PAAPot-27 and Pot-27. Increasing the total volume fraction of particles leads to an increase in the moduli. c) The peel forces on the artificial skin under dry conditions increased over time as more contact area was established during dwell. The stiff adhesives (PAAPot-27 and Pot-27) experienced similar peel forces at all dwell times, while the soft adhesives (Pot-12 and PAA-12) showed increased peel forces. d) Correlation of the viscoelastic properties and the resulting peel forces according to Eq. 1.

3.2 Impact of Viscoelastic Properties during Perspiration

The role of the viscoelastic properties of the adhesives during perspiration was investigated with the pair of non-absorbing adhesives (Pot-12 and Pot-27). Here, we can assume constant viscoelastic properties during perspiration as the adhesives do not hydrate. Following the application with a pressure of 1770 Pa for 1 min, the soft adhesive Pot-12 experienced higher peel forces than the stiff adhesive Pot-27 (see Fig. 3 a), presumably due to a larger contact area. After perspiration for 60 min as well as 120 min, the peel forces of both adhesives decreased dramatically. A reduction of 96 % and 95 % in peel adhesion as compared to dry conditions was observed after 120 min for Pot-12 and Pot-27, respectively. Noteworthy, while the failure was cohesively dominated in dry conditions, an adhesive failure mode was observed after perspiration with the occurrence of sweat at the interface. It appears that the pressure from the sweat pores has delaminated the adhesives during perspiration.

The sweat flow curves during perspiration give an insight into the failure mechanisms of the adhesives. A large contact area was established for the soft adhesive (Pot-12) after application, which resulted in complete occlusion of the sweat pores within the first 20 min of perspiration (see Fig. 3 b). Thereafter, the cumulative flow increased non-linearly due to an increasing sweat flow rate. Micrographs of the adhesive after perspiration for 60 min and 120 min showed the formation and growth of circular features (see Fig. 3 c and d). Topographical surface analysis confirmed that the features extended into the adhesive and cavities formed during perspiration (see Fig. 3 e). With an average cavity diameter of 750 μm and a depth of 200 μm after 120 min, the volume of one single cavity is approximately $6 \cdot 10^{-5} \text{ cm}^3$. With a pore density of 100 cm^{-2} , the cavities are able to incorporate approximately 0.006 g/cm^2 of artificial sweat. Since the cumulative sweat flow was much larger (approximately 0.028 g/cm^2) than the volume of the cavities, the artificial sweat has also penetrated the interface.

Also for the stiff adhesive (Pot-27), a large contact area was established after application, resulting in occlusion of the sweat pores (see Fig. 3 b). However, in contrast to Pot-12, the occlusive nature of Pot-27 was maintained over the entire duration of the experiment (120 min) with only minimal increase in the cumulative sweat flow. Here, the micrographs also showed the appearance of circular features (see Fig. 3 f and g). Though, these features did not grow during perspiration and neither showed any notable extension into the adhesive (see Fig. 3 h). These shallow cavities with an average cavity diameter of 426 μm and a depth of 50 μm would be able to incorporate approximately 0.0005 g/cm^2 of artificial sweat after 120 min. As the cumulative sweat flow was much larger (approximately 0.005 g/cm^2), sweat was also expected to be present at the interface.

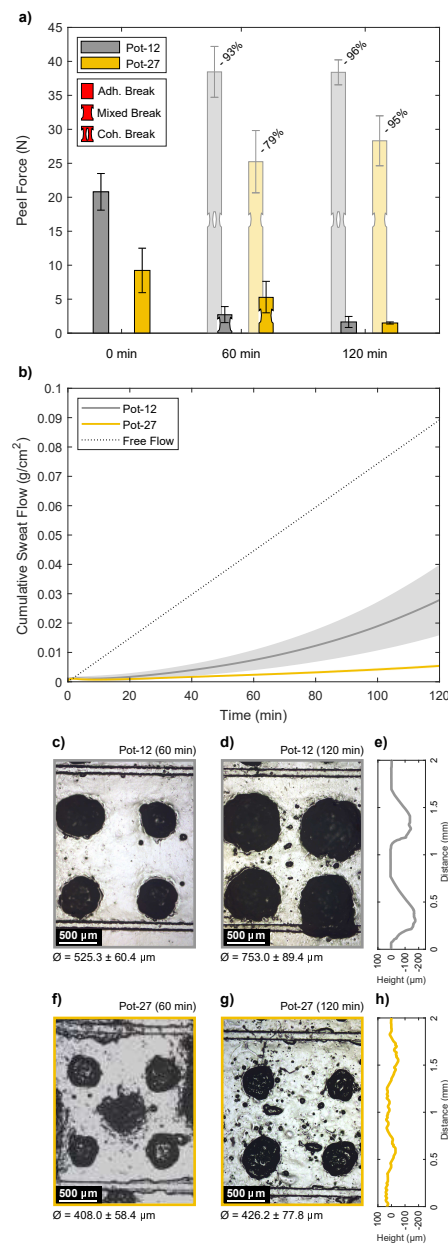


Figure 3: The effect of perspiration on the non-absorbing adhesives. a) The development of the peel forces during perspiration (full bars) and the corresponding peel forces under dry conditions (shaded bars). Statistically significant differences are indicated. b) The average cumulative sweat flow as a function of time with the standard deviation in the shaded area. c), d), and e) Micrographs and surface profile of Pot-12 after perspiration, showing the growth of cavities. f), g), and h) Micrographs and surface profile of Pot-27 after perspiration showing the cavities without notable growth.

The pressure during perspiration was sufficiently high to induce viscoelastic flow within the soft adhesive and cause the growth of cavities. Thereby, the contact area between the artificial skin and the adhesive decreased and the peel adhesion diminished (see schematics in Fig. 4 a). On the other hand, the mechanical strength of the stiff adhesive was sufficiently high in order to avoid notable viscoelastic flow at a perspiration pressure of 3 kPa. Instead, the adhesive delaminated elastically due to the pressure from the sweat pores (see schematics in Fig. 4 b). Noteworthy, a higher perspiration pressure of 6 kPa was shown to induce viscoelastic flow also in the stiff adhesive (see ESI).

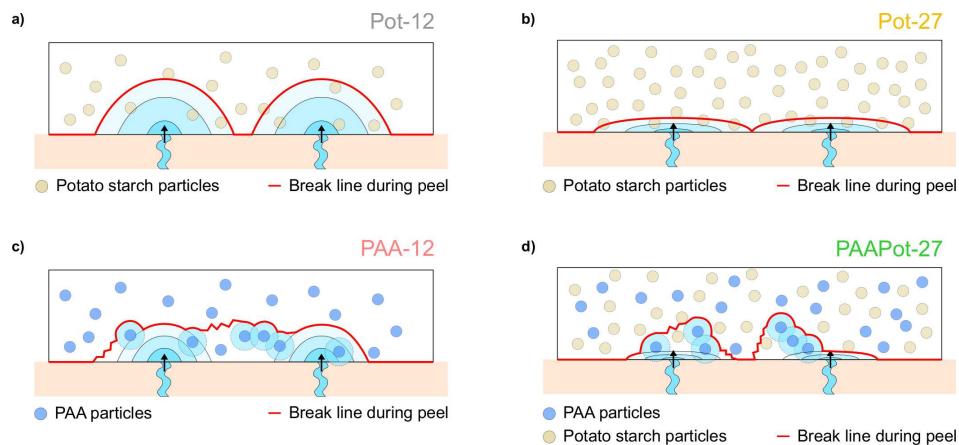


Figure 4: Schematic depiction of the failure mechanism of all adhesives after perspiration. a) Cavity formation and growth led to reduced contact area for Pot-12. b) Elastic detachment without notable growth of cavities was observed for Pot-27. c) Cavity formation and growth in combination with the absorption of sweat led to cohesive failure for PAA-12. d) While the absence of noticeable cavity formation limits the absorption of sweat, cohesive failure is still observed for PAAPot-27.

3.3 Impact of Sweat Absorption during Perspiration

In order to remove sweat from the interface between the artificial skin and the adhesive, PAA particles were incorporated into the adhesives. While keeping similar absorption capabilities,

PAA-12 and PAAPot-27 only differ in terms of their viscoelastic properties. The soft adhesive (PAA-12) experienced a moderate decrease in peel force of 37 % after perspiration for 60 min and a large decrease of 92 % after 120 min (see Fig. 5 a). On the other hand, the stiff adhesive (PAAPot-27) showed no significant reduction in peel force after perspiration over a period of 120 min. Importantly, while keeping the interface visually dry, both absorbing adhesives failed cohesively after perspiration. In comparison with the non-absorbing, soft adhesive (Pot-12), the peel adhesion of PAA-12 remained higher after 60 min of perspiration (17.3 N as compared to 2.7 N). PAAPot-27 showed drastically higher peel forces than the non-absorbing, stiff adhesive (Pot-27) not only after 60 min but also after 120 min (14.7 N and 15.4 N as compared to 5.3 N and 1.5 N). The absorption of sweat appeared to have weakened the cohesion of the adhesives rather than the interfacial adhesion to the artificial skin.

During perspiration, high flow rates were observed for the soft adhesive PAA-12, while the stiff adhesive PAAPot-27 strongly hampered the sweat flow (see Fig. 5 b). Since perspiration induces viscoelastic flow within the non-absorbing, soft adhesive (Pot-12), PAA-12 is also expected to undergo cavity formation. The increased sweat flow for PAA-12 is therefore a result of cavity formation as well as the absorption of artificial sweat by the PAA particles in the adhesive. Conversely, cavity formation was strongly limited for the non-absorbing, stiff adhesive (Pot-27) and hence, the majority of the sweat flow for PAAPot-27 was expected to be absorbed by the PAA particles. Due to the cohesively dominated failure mechanism after perspiration, micrographs and topographical scans of the absorbing adhesives were not obtained.

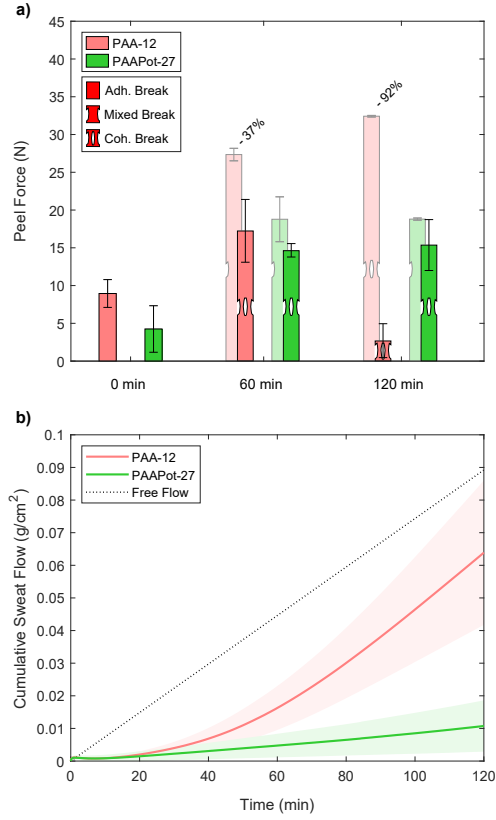


Figure 5: The effect of perspiration on the non-absorbing adhesives. a) The development of the peel forces during perspiration (full bars) and the corresponding peel forces under dry conditions (shaded bars). Statistically significant differences are indicated. b) The average cumulative sweat flow as a function of time with the standard deviation in the shaded area.

The increased peel adhesion of the absorbing adhesives indicates that the absorption of sweat aids the maintenance of adhesion during perspiration. Absorption may thereby partially relieve pressure from the interface which could limit cavity formation and growth. On the other hand, excessive swelling as observed previously³³ can lead to rupture of the polymer matrix between the cavities and cause cohesive failure of the adhesives. This is especially detrimental for the soft adhesive (PAA-12), where swelling occurs in addition to cavity formation (see schematics in Fig. 4 c). However, the swelling of the particles had a

less detrimental effect on the stiff adhesive (PAAPot-27). Here, cavity formation was limited and swelling did not rupture the polymer matrix in the same manner (see schematics in Fig. 4 d).

3.4 Adhesives during Perspiration on Human Skin

In order to ensure that the effects observed on the perspiration simulator correlate to the behaviour of skin adhesives on human skin during perspiration, a qualitative comparison was made. The peel forces of the adhesives on the dry forearm were 7.9 N on average for all adhesives in this study (see Fig. 6 a). Micrographs of the adhesives after peel revealed that the skin from the forearm was stripped and remained on the surface of the adhesives (see Fig. 6 b and c). This implies that the peel forces correspond to the cohesive strength of the skin rather than the peel adhesion of the adhesives on the skin. The peel adhesion is expected to be larger than the measured peel forces, which agrees qualitatively with the peel forces on the artificial skin during dry conditions. Certainly, this shows that further adjustments may be necessary to also optimise the adhesives for skin health.

After perspiration, the peel forces of the non-absorbing adhesives (Pot-12 and Pot-27) decreased to approximately 1.2 N (see Fig. 6 d) and sweat droplets were observed on the skin as well as the adhesives. The surface of both adhesives showed areas with the topography of the skin as well as circular features without any skin structure indicating a mixed failure mode (see Fig. 6 e and f). In the soft adhesive Pot-12, these circular features extended notably into the adhesive and formed cavities (see Fig. 6 g). Contrarily, as the line scans indicate, such cavity formation did not occur within the stiff adhesive Pot-27. This shows that viscoelastic flow of Pot-12 occurred as a consequence of the pressure from the sweat glands during perspiration, while the mechanical strength of Pot-27 was sufficiently high to

avoid notable viscoelastic flow.

Moreover, both absorbing adhesives maintained peel forces of approximately 3.3 N after perspiration (see Fig. 6 d). Here, cohesive failure was observed and a thin layer of adhesive remained on the skin after peeling, while the interface remained dry. Altogether, these findings greatly coincide with the results from the perspiration simulator.

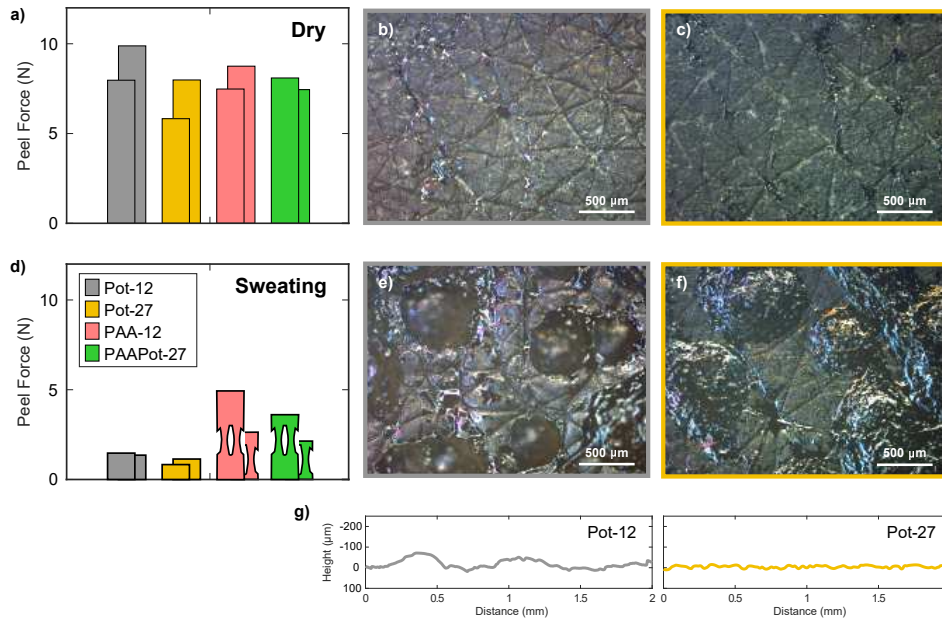


Figure 6: a) Peel forces of all adhesives on dry skin after light application and 10 min dwell time (left and right forearm). Micrographs of the adhesives after peel from the dry arm show that skin stripping has occurred for b) Pot-12 and c) Pot-27. d) Peel forces of all adhesives after light application, 10 min dry dwell time and subsequent sweating for approximately 30 min (left and right forearm). Micrographs of the adhesives after peel from sweating skin show the occurrence of circular features. e) The features appeared to be three-dimensional for Pot-12, indicating that viscoelastic flow of the adhesive has occurred. f) For Pot-27, the circular features were in focus simultaneously with the rest of the adhesive, implying that the features were two-dimensional and that notable viscoelastic flow did not occur. g) Line scans of the surface profile of Pot-12 and Pot-27 respectively after exercise.

4 Conclusions

The performance of skin adhesives during perspiration was evaluated on the basis of their peel adhesion. Here, the adhesive compositions were varied such that the impact of the viscoelastic properties and sweat absorption capabilities could be decoupled and evaluated independently. Even though soft adhesives exhibited better contact formation and high peel forces during dry conditions, their performance after perspiration was inferior to the stiff adhesives in this study. Viscoelastic flow with subsequent cavity formation and growth was observed when the sweating pressure overcame the mechanical strength of the adhesives. Naturally, soft adhesives exhibited a greater tendency for such viscoelastic flow, which constitutes a limitation for adhesive softness. Through the incorporation of hydrophilic particles into the adhesive, sweat could be absorbed and the pressure from the sweat glands could be relieved. As a result, adhesion was maintained over a prolonged period of time. However, excessive swelling of the particles during sweat absorption led to rupture of the polymer matrix and strongly weakened the cohesion of the adhesives. Thereby, the effects of particle swelling were less detrimental for the stiff adhesive. In order to formulate new adhesives for prolonged wear situations, it is therefore paramount to balance the viscoelastic properties with the sweat absorption capabilities of the adhesive in order to ensure a good overall performance.

Acknowledgement

The authors thank Saeed Zajforoushan Moghaddam for the development of the procedure to establish the gelatine coating. Innovation Fund Denmark is gratefully acknowledged for financial support through the Grand Solutions Project #6151-00007B.

Supporting Information Available

The Supporting Information is available free of charge.

The Supporting Information includes additional rheological measurements, perspiration experiments at a pressure of 6 kPa, and additional measurements of the adhesive surface topography after perspiration.

References

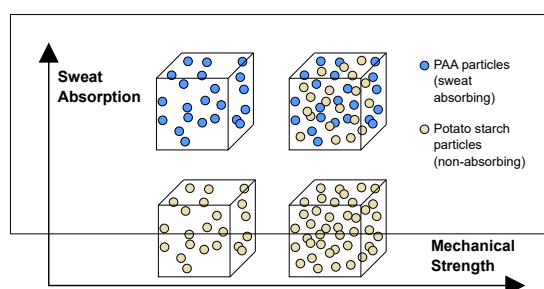
- (1) Boateng, J. S.; Matthews, K. H.; Stevens, H. N.; Eccleston, G. M. Wound Healing Dressings and Drug Delivery Systems: A Review. *Journal of Pharmaceutical Sciences* **2008**, *97*, 2892–2923.
- (2) Roy, S. H.; De Luca, G.; Cheng, M. S.; Johansson, A.; Gilmore, L. D.; De Luca, C. J. Electro-mechanical stability of surface EMG sensors. *Medical & Biological Engineering & Computing* **2007**, *45*, 447–457.
- (3) Hwang, I.; Kim, H. N.; Seong, M.; Lee, S.-H.; Kang, M.; Yi, H.; Bae, W. G.; Kwak, M. K.; Jeong, H. E. Multifunctional Smart Skin Adhesive Patches for Advanced Health Care. *Advanced Healthcare Materials* **2018**, *7*, 1800275.
- (4) Ferrari, F.; Bertoni, M.; Bonferoni, M. C.; Rossi, S.; Caramella, C.; Waring, M. J. Comparative evaluation of hydrocolloid dressings by means of water uptake and swelling force measurements: II. *International Journal of Pharmaceutics* **1995**, *117*, 49–55.
- (5) Rippon, M.; White, R.; Davies, P. Skin adhesives and their role in wound dressings. *Wounds UK* **2007**, *3*.
- (6) Woo, K. Y.; Sibbald, R. G.; Ayello, E. A.; Coutts, P. M.; Garde, D. E. Peristomal Skin Complications and Management. *Advances in Skin & Wound Care* **2009**, *22*, 522–532.

- (7) Venkatraman, S.; Gale, R. Skin adhesives and skin adhesion. *Biomaterials* **1998**, *19*, 1119–1136.
- (8) Creton, C. Pressure-Sensitive Adhesives : An Introductory Course. **2003**, 434–439.
- (9) Eisenhaure, J.; Kim, S. A Review of the State of Dry Adhesives: Biomimetic Structures and the Alternative Designs They Inspire. *Micromachines* **2017**, *8*, 125.
- (10) Yuk, H.; Varela, C. E.; Nabzdyk, C. S.; Mao, X.; Padera, R. F.; Roche, E. T.; Zhao, X. Dry double-sided tape for adhesion of wet tissues and devices. *Nature* **2019**, *575*, 169–174.
- (11) Lee, H.; Lee, B. P.; Messersmith, P. B. A reversible wet/dry adhesive inspired by mussels and geckos. *Nature* **2007**, *448*, 338–341.
- (12) Zhao, Y.; Wu, Y.; Wang, L.; Zhang, M.; Chen, X.; Liu, M.; Fan, J.; Liu, J.; Zhou, F.; Wang, Z. Bio-inspired reversible underwater adhesive. *Nature Communications* **2017**, *8*, 1–8.
- (13) Tiu, B. D. B.; Delparastan, P.; Ney, M. R.; Gerst, M.; Messersmith, P. B. Enhanced Adhesion and Cohesion of Bioinspired Dry/Wet Pressure-Sensitive Adhesives. *ACS Applied Materials & Interfaces* **2019**, *11*, 28296–28306.
- (14) Gu, Z.; Wan, X.; Lou, Z.; Zhang, F.; Shi, L.; Li, S.; Dai, B.; Shen, G.; Wang, S. Skin Adhesives with Controlled Adhesion by Polymer Chain Mobility. *ACS Applied Materials & Interfaces* **2019**, *11*, 1496–1502.
- (15) Chang, E. P. Viscoelastic Windows of Pressure-Sensitive Adhesives. *The Journal of Adhesion* **1991**, *34*, 189–200.
- (16) Yang, H. W. H. Water-based polymers as pressure-sensitive adhesives—viscoelastic guidelines. *Journal of Applied Polymer Science* **1995**, *55*, 645–652.

- (17) Krenczeski, M. A.; Johnson, J. F. Shear, tack, and peel of polyisobutylene: Effect of molecular weight and molecular weight distribution. *Polymer Engineering & Science* **1989**,
- (18) Novikov, M. B.; Gdalin, B. E.; Anosova, J. V.; Feldstein, M. M. Stress Relaxation During Bond Formation and Adhesion of Pressure-Sensitive Adhesives. *The Journal of Adhesion* **2008**, *84*, 164–190.
- (19) Pięłowski, J.; Kozłowski, M. Rheological properties of pressure-sensitive adhesives: polyisobutylene/sodium carboxymethylcellulose. *Rheologica Acta* **1985**, *24*, 519–524.
- (20) Eiler, J.; Simonsen, S. B.; Hansen, D.; Bingöl, B.; Hansen, K.; Thormann, E. Water Transport in Polymer Composites through Swelling-Induced Networks of Hydrogel Particles. *Soft Matter* **2020**,
- (21) Ferrari, F.; Bertoni, M.; Bonferoni, M. C.; Rossi, S.; Caramella, C.; Waring, M. J. Comparative evaluation of hydrocolloid dressings by means of water uptake and swelling force measurements: I. *International Journal of Pharmaceutics* **1994**, *112*, 29–36.
- (22) Cunningham, D. D.; Lowery, M. G. Moisture Vapor Transport Channels for the Improved Attachment of a Medical Device to the Human Body. *Biomedical Microdevices* **2004**, *6*, 149–154.
- (23) Renvoise, J.; Burlot, D.; Marin, G.; Derail, C. Peeling of PSAs on Viscoelastic Substrates: A Failure Criterion. *The Journal of Adhesion* **2007**, *83*, 403–416.
- (24) Kim, D. W.; Baik, S.; Min, H.; Chun, S.; Lee, H. J.; Kim, K. H.; Lee, J. Y.; Pang, C. Biomimetics: Highly Permeable Skin Patch with Conductive Hierarchical Architectures Inspired by Amphibians and Octopi for Omnidirectionally Enhanced Wet Adhesion (Adv. Funct. Mater. 13/2019). *Advanced Functional Materials* **2019**, *29*, 1970080.
- (25) Chen, F.; Ciok, D. Pressure Sensitive Adhesive Composition. 2002.

- (26) Stempel, E. Adhesive Skin Barrier Composition for Ostomy Appliance. 1996.
- (27) Fattman, G. F. Hydrocolloid Adhesive Compositions. 2004.
- (28) Kong, D.; Zhang, Q.; You, J.; Cheng, Y.; Hong, C.; Chen, Z.; Jiang, T.; Hao, T. Adhesion loss mechanism based on carboxymethyl cellulose-filled hydrocolloid dressings in physiological wounds environment. *Carbohydrate Polymers* **2020**, *235*, 115953.
- (29) Hou, L.; Hagen, J.; Wang, X.; Papautsky, I.; Naik, R.; Kelley-Loughnane, N.; Heikenfeld, J. Artificial microfluidic skin for in vitro perspiration simulation and testing. *Lab on a Chip* **2013**, *13*, 1868–1875.
- (30) Eiler, J.; Hansen, D.; Bingöl, B.; Hansen, K.; Heikenfeld, J.; Thormann, E. In Vitro Evaluation of Skin Adhesives during Perspiration. *International Journal of Adhesion and Adhesives* **2020**, *99*, 102574.
- (31) Hansen, D.; Zajforoushan Moghaddam, S.; Eiler, J.; Hansen, K.; Thormann, E. Performance of Polymeric Skin Adhesives during Perspiration. *ACS Applied Polymer Materials* **2020**, *2*, 1535–1542.
- (32) Choi, J.; Xue, Y.; Xia, W.; Ray, T. R.; Reeder, J. T.; Bandodkar, A. J.; Kang, D.; Xu, S.; Huang, Y.; Rogers, J. A. Soft, skin-mounted microfluidic systems for measuring secretory fluidic pressures generated at the surface of the skin by eccrine sweat glands. *Lab Chip* **2017**, *17*, 2572–2580.
- (33) Hansen, D.; Brewer, J. R.; Eiler, J.; Komjani, N. M.; Hansen, K.; Thormann, E. Water Diffusion in Polymer Composites Probed by Impedance Spectroscopy and Time-Resolved Chemical Imaging. *ACS Applied Polymer Materials* **2020**, *2*, 837–845.

Graphical TOC Entry



Supporting Information

**How the Viscoelastic and Sweat Absorbing
Properties of Skin Adhesives Affect their
Performance during Perspiration**

Johannes Eiler,^{†,‡} Daniel Hansen,^{†,‡} Bahar Bingöl,[‡] Kristoffer Hansen,[‡] and Esben
Thormann^{*,†}

[†]*Department of Chemistry, Technical University of Denmark, 2800 Kgs. Lyngby, Denmark*

[‡]*Coloplast A/S, 3050 Humlebæk, Denmark*

E-mail: esth@kemi.dtu.dk

1 Rheological Characterisation of the adhesives

Amplitude sweep experiments were carried out at a frequency of 1 Hz over a strain range of 0.002 - 50 % at a constant temperature of 32 °C. In Fig. S1 a - d, all amplitude sweep measurements are shown.

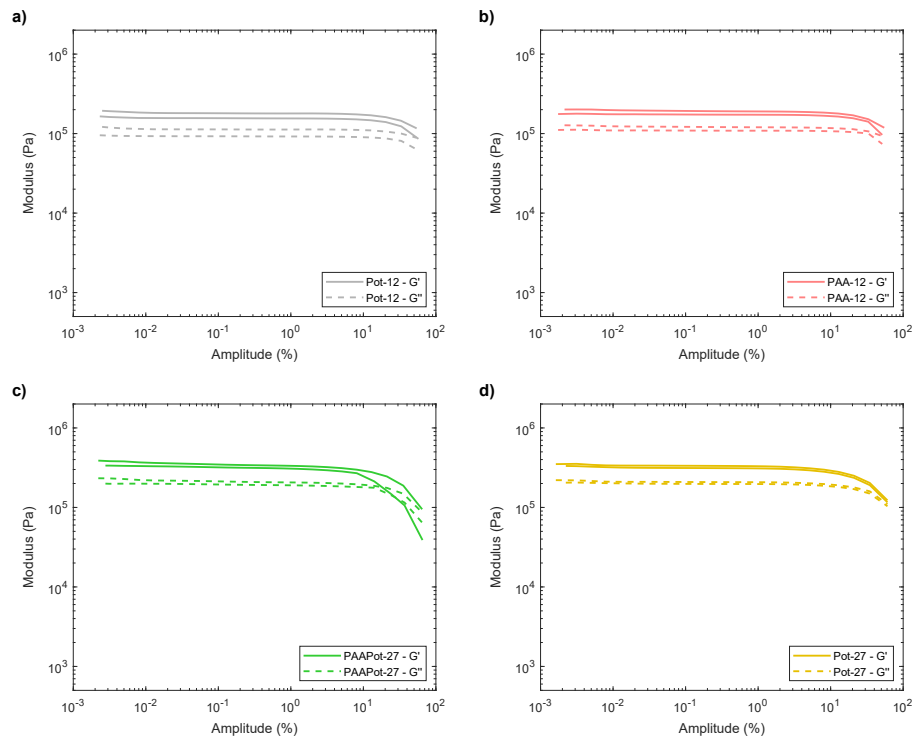


Figure S1: Amplitude sweep measurements of a) Pot-12, b) PAA-12, c) PAAPot-27, and d) Pot-27.

Frequency sweep experiments were carried out at a strain of 0.1 % over a frequency range of 0.0001 - 100 Hz at a constant temperature of 32 °C. In Fig. S2 a - d, all frequency sweep measurements are shown.

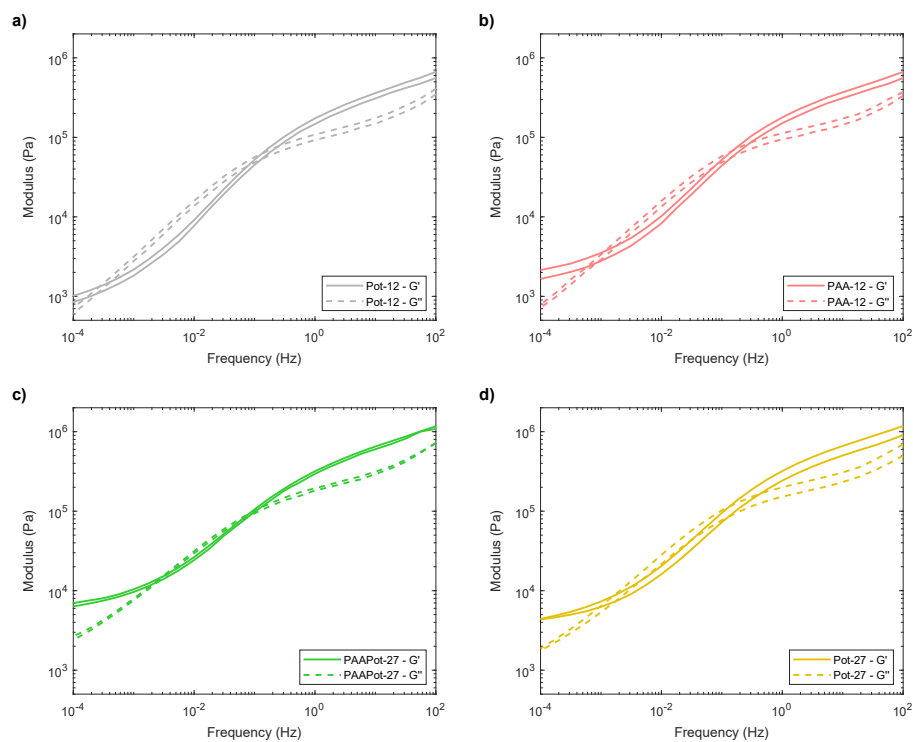


Figure S2: Frequency sweep measurements of a) Pot-12, b) PAA-12, c) PAAPot-27, and d) Pot-27.

2 Perspiration Experiments at 6 kPa

Perspiration experiments were additionally conducted at a constant pressure of 6 kPa, which corresponds to extreme sweating on human skin.¹ A 0.154 M NaCl solution was used as an artificial sweat composition. To ensure reproducible test conditions, the flow rate through the unoccluded perspiration simulator was measured over a period of 200 s prior to application of the adhesive. Thereby, the perspiration pressure of 3 kPa resulted in a free flow rate of $2.0 \pm 0.3 \text{ }\mu\text{L}/\text{cm}^2/\text{min}$. After drying the device, an adhesive with dimensions of 100 mm by 25 mm was applied to the artificial skin using a silicone pad with a pressure of 1770 Pa for 1 min. Thereafter, the flow was activated and the flow rate was monitored over the tested period (20 min and 60 min) until the experiment was finished with the measurement of the peel force of the adhesive. Triplicate analysis was performed for all experiments and an average with the corresponding standard deviation is reported. Two-sample T-tests with a significance level of 0.05 were performed to indicate differences between peel forces in dry conditions and after perspiration.

2.1 Non-Absorbing Adhesives

At an increased sweating pressure of 6 kPa, the difference in sweat flow became less apparent between Pot-12 and Pot-27. Here, the sweat flow rates gradually approached the free flow rate of the unoccluded substrate in both cases (see Fig. S3 a). Simultaneously, the peel force of Pot-12 decreased drastically with perspiration time and a shift from cohesively dominated failure to adhesive failure was observed again (see Fig. S3 b). In contrast, the peel force of Pot-27 remained moderately high over a perspiration period of 60 min and mixed failure modes were observed. The analysis of micrographs revealed the formation of cavities in Pot-12 as well as Pot-27 (see Fig. S3 c - h). An increased sweating pressure thereby also induced notable viscoelastic flow in the stiff adhesive Pot-27. Remarkably, its peel force after 60 min was higher at a sweating pressure of 6 kPa than it was at 3 kPa ($11.6 \pm 2.9 \text{ N}$

and 5.3 ± 2.3 N respectively). It is well-known that additional external work is required to detach the adhesive when viscoelastic flow occurs as energy is dissipated within the material during deformation.²⁻⁴ At a low sweating pressure of 3 kPa, only minimal viscoelastic flow was observed for Pot-27 and therefore the entire energy was transferred to the interface. We speculate that the increased viscoelastic flow at 6 kPa allows for dissipation of energy, thereby relieving pressure from the interface and thus enabling the maintenance of adhesion.

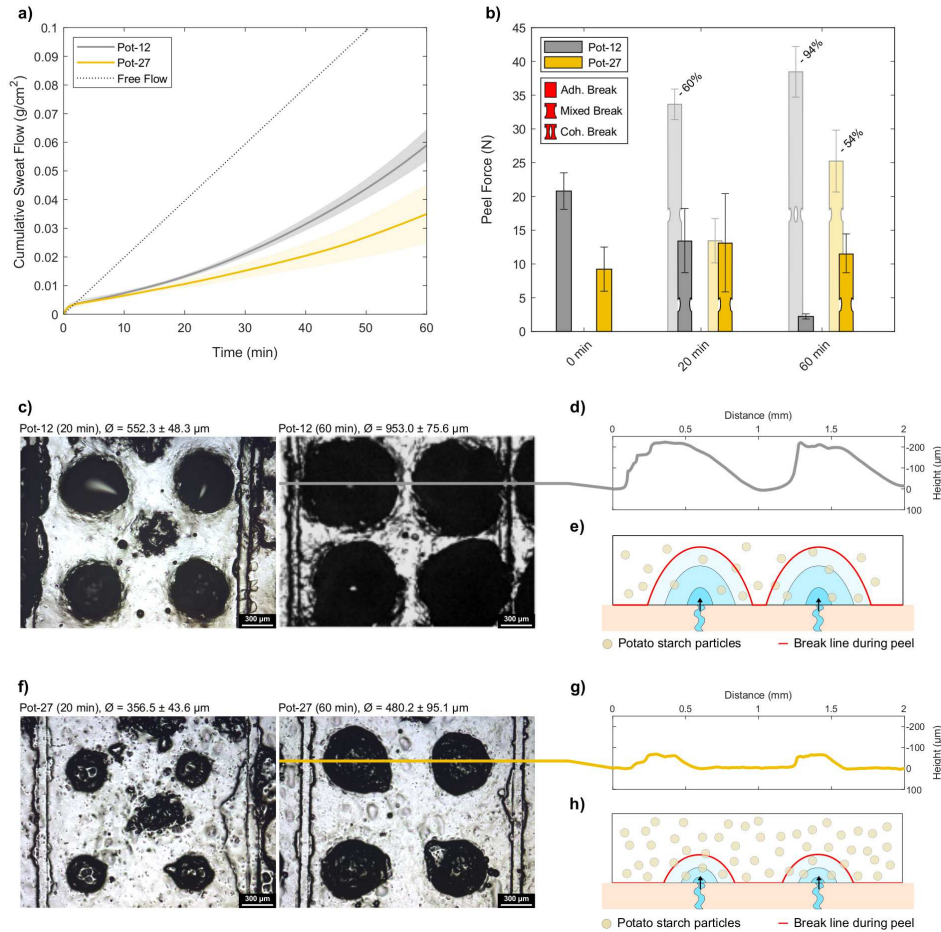


Figure S3: The effects of perspiration at a pressure of 6 kPa on the non-absorbing adhesives. a) The average cumulative sweat flow as a function of time with the standard deviation in the shaded area. A slightly higher flow of sweat is observed for the soft adhesive Pot-12. b) The peel force of Pot-12 decreases drastically during perspiration, while Pot-27 maintains adhesion at moderate levels. The shaded bars represent the corresponding peel forces under dry conditions. c) Micrographs of Pot-12 after 20 and 60 min of perspiration, showing the growth of cavities from the sweat pores. d) Line scan of the surface profile of Pot-12 after 60 min of perspiration. e) Schematic depiction of the failure mode of Pot-12 at a sweating pressure of 6 kPa. f) Micrographs of Pot-27 after 20 and 60 min of perspiration, showing the growth of cavities from the sweat pores. g) Line scan of the surface profile of Pot-27 after 60 min of perspiration. h) Schematic depiction of the failure mode of Pot-27 at a sweating pressure of 6 kPa.

2.2 Absorbing Adhesives

At an increased sweating pressure of 6 kPa, PAA-12 consistently exhibited flow rates as high as the free flow rate after approximately 30 min of perspiration (see Fig. S4 a). Cavity formation and growth as well as the absorption of artificial sweat were responsible for such high flow rates. Contrarily, the stiff adhesive behaved more occlusive and the flow rates were much lower in comparison as cavity formation was suppressed. This discrepancy was also observed in the peel forces after 60 min, where the peel force of PAA-12 decreased dramatically, while PAAPot-27 maintained similar peel forces to the dry condition (see Fig. S4 b). The failure of the absorbing adhesives was cohesively dominated after perspiration at 6 kPa in all cases (see schematics in Fig. S4 c and d).

The addition of absorbing particles did not yield any significant improvement for the stiff adhesive at a high sweating pressure of 6 kPa. The peel forces after perspiration at 6 kPa did not showed any significant differences between the soft adhesives, containing particles at a volume fraction $\phi = 0.12$, either. However, a smaller decrease in peel force after 20 min was observed for PAA-12 than Pot-12 (from 21.0 ± 6.8 N to 18.2 ± 2.3 N and from 33.7 ± 2.3 N to 13.5 ± 4.7 N respectively). It is likely that the pressure from the sweat pores was relieved through the absorption of artificial sweat into the particles and adhesion was therefore maintained. Conversely, the absorption of artificial sweat caused a weakening of the adhesive, leading to cohesive failure during peel.

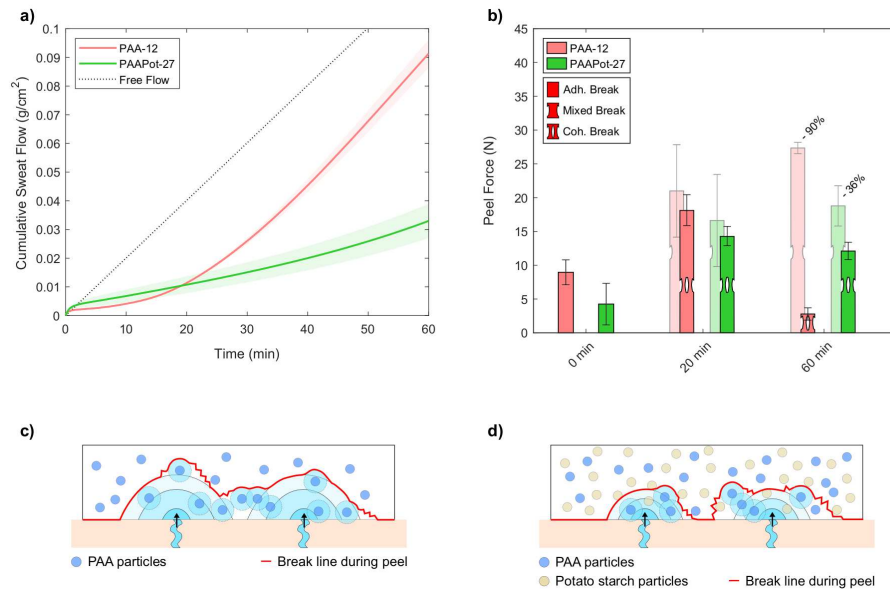


Figure S4: The effects of perspiration at a pressure of 6 kPa on the absorbing adhesives. a) The average cumulative sweat flow as a function of time with the standard deviation in the shaded area. A higher flow of sweat is observed for the soft adhesive PAA-12. b) The peel force of PAA-12 decreases drastically after 60 min of perspiration, while PAAPot-27 maintains high peel forces throughout the entire experiment. The shaded bars represent the corresponding peel forces under dry conditions. c) Schematic depiction of the failure mode of PAA-12 at a sweating pressure of 6 kPa. d) Schematic depiction of the failure mode of PAAPot-27 at a sweating pressure of 6 kPa.

3 Topography of the Adhesives after Perspiration

Line scans were performed with a mechanical profilometer to determine the topography of the adhesives after perspiration. The surface profile of the adhesives after perspiration at a pressure of 3 kPa over a period of 120 min is shown in S5 a and b.

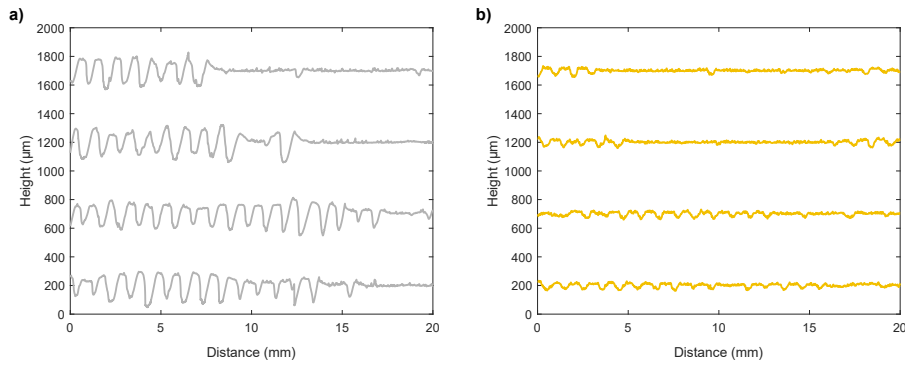


Figure S5: Surface profile after perspiration at a pressure of 3 kPa over a period of 120 min for a) Pot-12 and b) Pot-27.

The surface profile of the adhesives after perspiration at a pressure of 6 kPa over a period of 60 min is shown in S6 a and b.

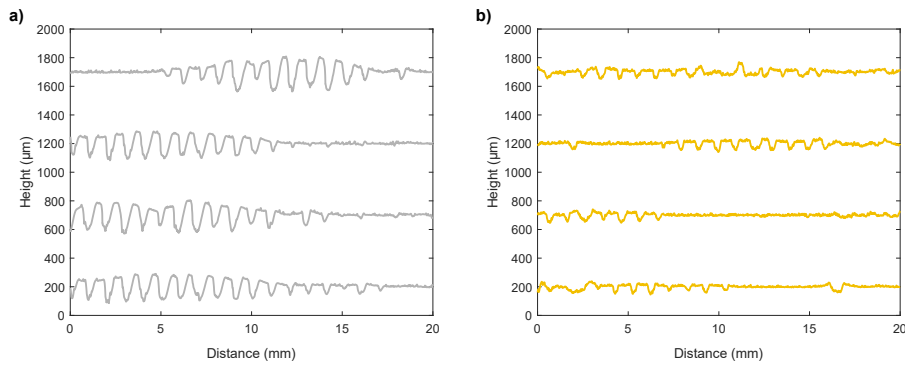


Figure S6: Surface profile after perspiration at a pressure of 6 kPa over a period of 60 min for a) Pot-12 and b) Pot-27.

The surface profile of the adhesives after sweating during the in vivo study is shown in S7 a and b.

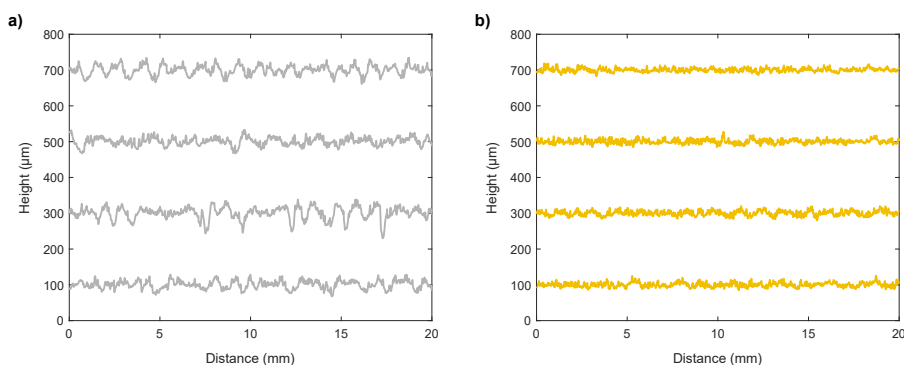


Figure S7: Surface profile after sweating during the in vivo study for a) Pot-12 and b) Pot-27.

References

- (1) Choi, J.; Xue, Y.; Xia, W.; Ray, T. R.; Reeder, J. T.; Bandodkar, A. J.; Kang, D.; Xu, S.; Huang, Y.; Rogers, J. A. Soft, skin-mounted microfluidic systems for measuring secretory fluidic pressures generated at the surface of the skin by eccrine sweat glands. *Lab Chip* **2017**, *17*, 2572–2580.
- (2) Chang, Y.-S.; Lai, Y.-H.; Dillard, D. A. The Constrained Blister - A Nearly Constant Strain Energy Release Rate Test for Adhesives. *Journal of Adhesion* **1989**, *27*, 197–211.
- (3) Wang, C. Measurements of interfacial strength from the blister test. *Journal of Applied Polymer Science* **1999**, *73*, 1899–1912.
- (4) Kappes, M.; Frankel, G. S.; Sridhar, N. Adhesion and adhesion degradation of a pressure sensitive tape on carbon steel. *Progress in Organic Coatings* **2010**,

Technical University of Denmark
Department of Chemistry
Group for Polymers and Functional Interfaces

Kemitorvet
Building 206
2800 Kgs. Lyngby
Denmark

Tel (+45) 45 25 24 19
www.kemi.dtu.dk

Coloplast A/S
Technology
Adhesives

Holtedam 1
3050 Humlebæk
Denmark

Tel (+45) 49 11 11 11
www.coloplast.com